Sponsor TBD Report No.:_____

AISI/DOE Technology Roadmap Program

Final Report

Behavior of Phosphorus in DRI/HBI During Electric Furnace Steelmaking

by

Richard J. Fruehan
Christopher P. Manning

October 5, 2001

Work Performed under Cooperative Agreement
No. DE-FC07-97ID13554

Prepared for
U.S. Department of Energy

Prepared by
American Iron and Steel Institute
Technology Roadmap Program Office
Pittsburgh, PA 15220

DISCLAIMER

"This report was prepared as an account of work sponsored by an Agency of the United States Government. Neither the United States Government nor any agency thereof, nor any of their employees, makes any warranty, express or implied, or assumes any legal liability or responsibility for the accuracy, completeness, or usefulness of any information, apparatus, product, or process disclosed, or represents that it use would not infringe privately owned rights. Reference herein to any specific commercial product, process, or service by trade name, trademark, manufacturer, or otherwise, does not necessarily constitute or imply endorsement, recommendation, or favoring by the United States Government or any agency therof. The views and opinions of authors expressed herein do not necessarily state or reflect those of the United States Government or any agency thereof."

"This report has been reproduced from the best available copy. Available in paper copy and microfiche"

Number of pages in report: 215

DOE and DOE contractors can obtain copies of this report
FROM: Office of Scientific and Technical Information, P.O.
Box 62, Oak Ridge, TN 37831. (615) 576-8401

This report is publicly available from the department of Commerce, National Technical Information Service, 5285 Port Royal Road, Springfield, VA 22161. (703) 487-4650.

TABLE OF CONTENTS

List of Figures

Chapter 2:

Chapter 3:

Chapter 4

Chapter 5

Chapter 6

List of Tables

List of Symbols

Lp	Slag-metal phosphorus distribution ratio, dimensionless
(%X)	wt% of species X in the slag phase
[%X]	wt% of species X in the metal phase
A	Slag-metal reaction area, cm^2 (unless otherwise noted)
A*ko	Mass transfer parameter, cm^3/s
a_x	Roultian activity coefficient of species a
C/S	wt%CaO/wt%SiO_s (B-ratio)
C_A	Concentration of Species A, moles or grams of species A per cm^3
δ	Thickness of theoretical stagnant film near interface, cm
D_A	Diffusion Coefficient of species A, cm^2/s
f_x	Activity coefficient species x in the 1wt% state
λ_x	Activity coefficient of species x assuming roultian standard state
J_A	mass or molar flux of species A, g/cm^2s or $moles/cm^2s$
Keq	Reaction equilibrium constant
Kp	Phosphate capacity
ks, km	Mass transfer coefficent of the slag and metal respectively, cm/s
ko	Overall mass transfer coefficient, including resistances in the slag and metal, cm/s
l	Characteristic length an element of liquid will travel at the interface before it is re-entrained into the bulk, cm
L	Characteristic thickness of an element of liquid at the interface, in which mass transport is controlled by steady state or non-steady state atomic or molecular diffusion, cm
η	Viscostiy
τ	Characteristic time to establish steady state diffusion across a surface element of liquid with characteristic thickness of L, seconds
θ	Residence time of an element of liquid at the interface before it is re-entrained into the bulk, seconds
v_l	Characteristic velocity of an element of liquid at the interface, cm/s
W_s, W_m	Mass of slag and metal respectively, g (unless otherwise noted)
x	Distance from the slag metal interface, cm

Executive Summary

In modern electric arc furnace (EAF) steelmaking, ore based scrap substitute materials are often used to control the chemistry of the steel produced and/or improve the efficiency of the process. At the present time, the most common forms of direct reduced scrap substitute materials are direct reduced iron (DRI) and hot briquetted Iron (HBI). DRI is produced from a combination of pelletized and lump ore, which is reduced by reformed natural gas in a shaft furnace such as the Midrex furnace. HBI is currently produced by hot pressing either reduced DRI pellets or reduced iron ore fines into dense metallic iron briquettes. Due to the great similarities of most direct reduced materials, this large group of materials will be referred to generically as DRI/HBI unless greater specification is required. Most commercially available forms of DRI/HBI contain significantly higher levels of phosphorus as compared with scrap. As increasing quantities of these materials are used in EAF steelmaking for the production of higher quality steels, control of phosphorus levels in the metal will become a concern. The goals of this research include the development of a more complete understanding of the behavior of phosphorus in DRI/HBI during EAF steelmaking. A thorough investigation of the kinetics and thermodynamics of phosphorus transfer in the EAF has been conducted based upon laboratory and plant experiments and trials.

Metallographic investigation of commercial DRI/HBI materials indicates that before melting, phosphorus in DRI/HBI is contained as a calcium phosphate phase in the unreduced oxide "gangue" portion of the material. Laboratory experiments have shown that phosphorus reversion from gangue to metal occurs significantly in less than one minute for all commercial direct reduced materials tested in this study.

Based upon the work of previous researchers and the experimental results of the present study, it was assumed that the kinetics of phosphorus transfer between slag and metal are limited by liquid phase mass transfer of phosphorus in the slag, metal, or both phases. An overall mass transfer coefficient, ko, was defined, which includes the effects of mass transfer in both the slag and the metal. Fundamental laboratory kinetic experiments indicate that either the slag-metal interfacial area, A, and/or the overall liquid phase mass transfer coefficient, ko, change during dephosphorization experiments.

Because the contributions of the reaction area and the mass transfer coefficient to the overall rate are difficult to separate, experimental results were analyzed in terms of the mass transfer parameter, A*ko. The liquid phase mass transfer parameter for dephosphorization was found to range between 10^{-1} to $1x10^{-3}$ cm^3/s for different experimental conditions.

Plant trials were conducted to directly evaluate the conditions of mass transfer in the electric furnace. Controlled mass transfer experiments were conducted on a 150 ton DC electric arc furnace. The mass transfer parameter, A*ko, for this furnace was determined to be between $1.7x10^4$ and $3.5x10^5$ cm^3/s. An additional series of plant trials were conducted on a 150 ton AC electric furnace to examine the effects of different scrap substitute materials upon the slag chemistry, the behavior of phosphorus in the steel, and upon furnace yield. The data from these trials were also used to develop empirical models for the slag chemistry and furnace temperature as functions of time during a single heat.

The laboratory and plant data were used to develop a numerical process model to describe phosphorus transfer in the EAF. The experimental data from this study and the results of previous researchers were used to test the process model and reasonable agreement was observed. The process model was used to evaluate the influence of various EAF operating parameters upon phosphorus mass transfer between the slag and metal.

ACKNOWLEDGEMENTS

The authors would like to acknowledge the AISI-DOE for financial support of this research. In addition, the member companies of the Center for Iron and Steelmaking Research at Carnegie Mellon University have supported this research both financially and with guidance and information. Specifically, BHP, Midrex, and Cliffs Reduced Iron supplied commercial material samples and invaluable information regarding commercial direct reduced iron and hot briquetted iron products. The plant trials conducted in conjunction with this project were among the most critical and truly interesting components of the research. This success of this project was due in large part to the cooperation of many individuals at North Star Steel - Texas and Pennsylvania Steel Technologies-Bethlehem Steel regarding these plant trials. The authors would also like to thank Dr. Sridhar Seetharaman and Dr. Alan Cramb of Carnegie Mellon University, and Bhaskar Yalamanchilli of North Star Steel for their participation on the thesis committee of the doctoral thesis, which resulted from this research. Their contribution to the direction and quality of this work is greatly appreciated.

CHAPTER 1

INTRODUCTION

Very often, large amounts of ore based scrap substitute materials such as direct reduced iron (DRI) pellets, hot briquetted iron (HBI), iron carbide, etc. are used when producing steels with low residuals via EAF steelmaking. At the present time, the most common forms of direct reduced scrap substitute materials are DRI and HBI. DRI is produced from a combination of pelletized and lump ore, which is reduced in a shaft furnace such as the Midrex furnace by reformed natural gas. The product DRI is therefore a pellet material with a large amount of internal porosity and a very low bulk density. HBI is currently produced via two major process routes. By one process route, reduced DRI pellets can be fed from the reducing furnace into a briquetting machine. Physically compacting the pellets into larger briquettes greatly decreases the porosity of the material and increases the bulk density. HBI is also produced directly from ore fines via processes such as Finmet and Circored in which the ore fines are reduced in a series of fluidized bed reactors and then compacted into dense briquettes. Generally, the chemical properties of DRI and HBI sold commercially today are very similar. Nearly all commercial direct reduced materials contain between 80 to 90 percent metallic iron, 5 to 10 percent iron oxide, 5 to 10 percent gangue, and 0 to 4 percent carbon. The term gangue is used to describe the unreduced components of the mineral ore, including silica, alumina, lime, magnesia, etc. Due to the great similarities of most direct reduced materials, this large group of materials will be referred to generally as DRI/HBI for most of this paper unless greater specification is required.

Whereas DRI/HBI products have low contents of copper, nickel, nitrogen, sulfur, etc., they can contain large amounts of phosphorus. Depending upon the quality of ore used to produce the DRI/HBI, these products can contain five to ten times as much phosphorus as scrap. Most commercially available DRI/HBI materials commonly contain between 0.03 to 0.09% phosphorus as compared with 0.015 to 0.02 % for scrap. DRI/HBI produced from lower grades of ore can contain as high as 0.15%P.

In normal EAF steelmaking, the phosphorus distribution ratio between slag and metal is low as compared to a BOF. The phosphorus partition ratio (Lp) can be defined as:

$$L_p = \frac{(\%P)slag}{[\%P]metal} \quad (1)$$

The L_p observed at tap for common EAF slag chemistries ranges from 5-50 as compared with 50-150 in oxygen steelmaking. The observed phosphorus partition ratios for both EAF and BOF steelmaking do not necessarily reflect the equilibrium Lp for the slag chemistries and furnace temperatures of the given system. In both processes, the approach toward equilibrium is limited by the kinetics of phosphorus transfer. In addition to relatively low observed phosphorus partition ratios, lower slag volumes are used in EAF steelmaking. Therefore, thermodynamics and a mass balance predict steels of high phosphorus content when using DRI/HBI. However, indications from steel producers are that phosphorus contents in actual practices are much lower than predicted.

One hypothesis has been presented in the literature as a possible explanation of the unexpectedly low metal phosphorus contents observed in industry. Previous researchers [1,2,3] have shown that the phosphorus contained in direct reduced iron products is present as an oxide component gangue phase. The fact that the phosphate in the gangue is not reduced is consistent with the thermodynamics for the conditions present during the common direct reduction processes, i.e. Midrex, Hyl III, Fior, etc. It was theorized that during melting, the phosphorus in the DRI/HBI gangue first physically separates to the slag phase creating an initially high phosphorus slag. It was believed that slow kinetics of phosphorus reversion as well as slag flushing resulted in the unexpectedly low phosphorus levels in the steel [1,2]. However, the kinetics of phosphorus transfer between the gangue and metal phases of DRI/HBI are unknown even on a microscopic scale. Furthermore, the thermodynamics and kinetics of phosphorus transfer between the bulk slag and metal phases have not been studied in detail for the electric arc furnace. Therefore, the above hypothesis relies upon several significant assumptions regarding the rate of phosphorus transfer within the DRI/HBI material during melting, and the rate of phosphorus transfer between the bulk slag and steel during EAF steelmaking.

1.2 RESEARCH OBJECTIVES

In order to efficiently control the phosphorus in ore based scrap substitutes in the EAF, a more sophisticated understanding of the phenomena of gangue-metal separation during melting and phosphorus transfer the EAF must be developed. The goals of this research are to contribute to a more complete understanding of both the behavior of phosphorus in DRI and the kinetics and thermodynamics of phosphorus transfer in metal - slag (or DRI/HBI gangue) systems. The end result of this work should be a simple real-time process model that can be used by the plant operator to design slag chemistry and flushing practices, which optimize phosphorus retention in the slag phase for any type or amount of DRI/HBI charge.

This study includes three major components: laboratory experiments, plant experiments and trials, and development of a process model. The laboratory experiments include the physical observation of the gangue - metal microstructure of several types of DRI/HBI via optical and scanning electron microscopy. Also, the precise distribution of phosphorus between the gangue and metal phases in DRI has been determined. The behavior of phosphorus, and the rate of gangue - metal separation in DRI upon melting was investigated. Also, phosphorus distribution is a strong function of the FeO content of the slag. Therefore, the effect of carbon content and degree of metallization of DRI/HBI upon slag make and phosphorus distribution is also examined.

The fundamental thermodynamics and kinetics of phosphorus transfer in slag - metal systems were reevaluated through a laboratory scale study in order to develop the appropriate rate equations. Plant experiments were conducted to examine the specific rates of mass transfer between slag and metal for the EAF. Both the stirring conditions and the slag - metal interfacial area present during electric furnace steelmaking are unknown. Therefore, it is extremely difficult to transfer data and observations obtained in the laboratory to the industrial scale. From the experimental work, a process model was developed, which can accurately model slag-metal phosphorus transfer in the EAF. The accuracy of the process model was tested using the plant trial data. The value of the process model in evaluating various operating conditions for the EAF is exhibited through several select examples.

LITERATURE REVIEW

2.1 The Behavior of Phosphorus in DRI/HBI - A joint investigation by BHP and CASIMA[1] examined the behavior of phosphorus in two types of HBI during EAF steelmaking. The study compared plant data regarding metal phosphorus levels achieved when using two types of HBI feed: HBI #1 produced from Mt. Newman, Australia fines via the FIOR process (0.065wt%P), and HBI #2 produced from Venezuelan ore via the Midrex process (0.095wt%P). The study reported that low phosphorus melts could be obtained using large amounts of both types of feed. Other steel producers have reported similar observations.[5] The BHP/CASIMA study included a SEM metallographic investigation of the two types of HBI. Elemental mapping of the HBI shown in Figures 1-3 indicates that the phosphorus is preferentially associated with the oxide phase present in the HBI rather than with the reduced iron.

Figure 1: Secondary electron image of HBI adapted from Trotter et al. [1]

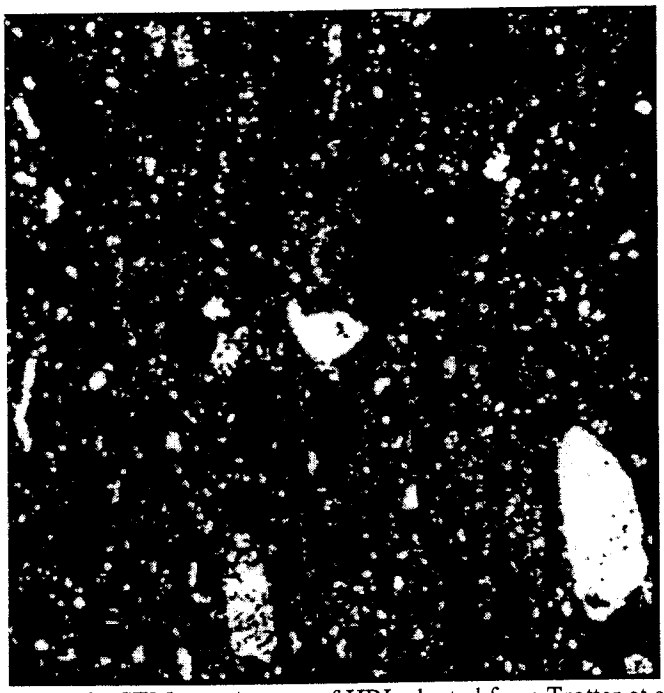

Figure 2: SEM oxygen map of HBI adapted from Trotter et al. [1]

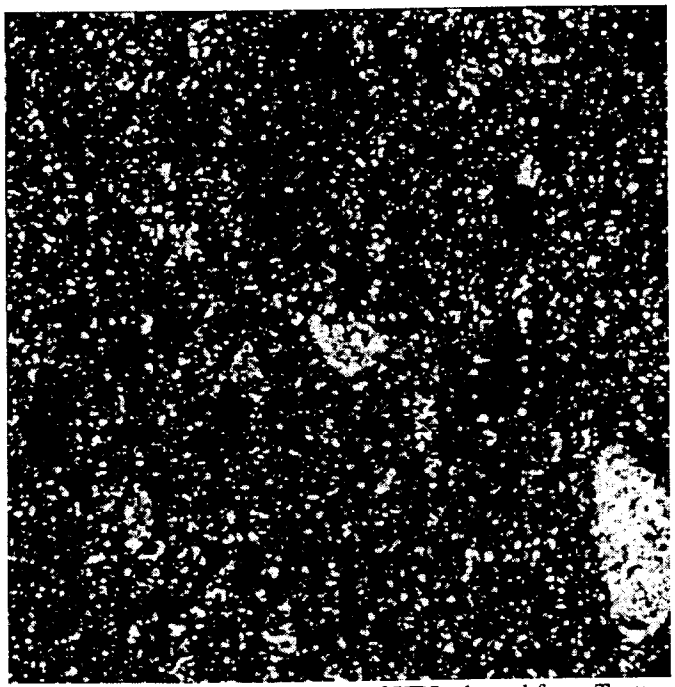

Figure 3: SEM phosphorus map of HBI adapted from Trotter et al. [1]

This finding is supported by chemical analysis performed by other investigators.[2] Unfortunately, no scale was provided with the original pictures to indicate the relative sizes of the imaged gangue features. However, based upon metallographic results of the present study, which will be presented later in this paper, these features are most likely on the order of 50 to 150 microns in size.

The BHP/CASIMA investigators concluded that the phosphorus present in the gangue initially enters the slag phase during melting. Slow kinetics of phosphorus reversion and slag flushing practices result in the observed unexpected low phosphorus levels in the metal. This basic theory represents the original hypothesis of the present work.

A much earlier study of phosphorus in direct reduced sponge iron by Queens [3], also concluded that phosphorus is not reduced during direct reduction. In the study by Queens, an electron microscope investigation of the gangue phase identified 20 to 30 micron particles containing 21%wt P - 37%wt%Ca. A component of the study includes a series of 2 ton bulk melting experiments with several grades of sponge iron containing up to 0.07wt%P. Queens concluded that with special fluxing modifications, which ensured a basic, oxidizing slag, the high phosphorus material could be used to produce low phosphorus steel. However, this researcher made no specific comments on the kinetics of phosphorus transfer either to or from the slag phase.

Between 1965 and 1975, Lukens Steel conducted an extensive series of trials with a number of scrap substitute materials, including Midrex DRI, Hyl DRI, Fior HBI, and various synthetic materials. Portions of the findings of that study were published in the open literature[5, 6, 7]. Review of internal literature describing this study, which was shared by Lukens with the present author, gives a much better notion of the true extent of the research conducted by Lukens. In that study, more than 800 trials of both batch and continuously fed electric furnace heats were conducted.[8 - 10] The effects of scrap substitute usage were evaluated with respect to a wide range of operating parameters. Of special interest to the present study were trial heats conducted with varying amounts of HyLSA prereduced pellets, which contained 0.362wt% phosphorus.[8] Ten trial heats were conducted in a 165 ton AC-EAF during which 17 tons of HyLSA pellets were continuously fed during refining. Incredibly, only one of the 10 heats was tapped with an unacceptably high phosphorus content of 0.022wt%P.

In addition to the heats with HyLSA pellets, a larger number of trials were conducted with Fior HBI produced by Esso from Venezuelan iron ore.[9] The reduced Fior material contained 0.14wt% phosphorus. For most of the trial heats, approximately 25 tons of briquettes were continuously fed into the furnace during the refining period. Chemical analysis of slag samples from before and after continuous feeding showed that the slag phosphorus increased from 0.294 wt% to 0.618 wt%. Despite the increase in slag

phosphorus, all heats were tapped at, or below 0.01wt% P in the steel. In 24 trials with a third material, 25 tons of HBI containing 0.096wt%P were continuously fed into the 165 ton furnace over a period of 35 minutes.[10] Metal samples were taken from the furnace immediately before and after continuous feeding. Comparison of the average before and after chemistries for the 24 heats revealed a 0.001% decrease in the metal phosphorus after the continuous feeding period. Despite these observations, it is unlikely that the low metal phosphorus contents measured by Lukens were the result of slow kinetics. Continuous feeding of a dense carbon and iron oxide containing material like the Fior HBI will greatly enhance slag metal mixing. Also, because these trials were conducted prior to the days of powerful UHP transformers, the tap to tap time on most of the trial heats exceeded 3 hours. It is far more likely that the observed low metal phosphorus contents were the result of favorable equilibrium conditions. With a low to medium powered furnace (by today's standard) producing steel in an ingot cast shop, it is very likely that most heats were tapped at much lower temperatures and lower FeO contents than are common today. For these conditions, is very likely that the high observed phosphorus partition ratios of Lukens trials are near or below the equilibrium distribution ratio. In such a case, reversion of phosphorus from the slag to the metal will not occur.

2.2 Slag-Metal Phosphorus Equilibrium – Although equilibrium thermodynamics is not the focus of this study, it is the deviation from the equilibrium phosphorus distribution between slag and metal that represents the driving force for any phosphorus transfer reaction. Therefore, a thorough understanding of the relevant equilibrium thermodynamics is necessary for an accurate evaluation of the kinetics of phosphorus transfer. The review that follows represents only a brief introduction to a long and extensive history of thermodynamic studies [refs. 11 - 33].

Winkler and Chipman [27], Suito et al. [18, 19] and others have carried out basic thermodynamic studies of phosphorus distributions over wide ranges of temperature and slag chemistry. Fuwa [11] and Wijk [26] provided overviews of the phosphorus problem in the steel industry and Stubbles [17] examined industrial practice in some detail. Turkdogan [20], Suito et al. [19], Zhang et al. [28], Ide and Fruehan [29] and others have provided interpretations of available data. The accurate prediction of the phosphorus partition ratio based upon readily accessible parameters such as temperature and slag

composition represents an extremely useful, yet difficult capability. The studies conducted so far have covered the range from very theoretical evaluations to very empirical modeling of experimental and industrial data. Most thermodynamic studies to date have attempted to evaluate phosphorus in the slag – metal system using either classical molecular thermodynamics or an approach that recognizes the ionic nature of molten slags.

Some of the earliest studies described the phosphorus reaction as:

$$2[P] + 5(FeO) = (P_2O_5) + 5Fe \qquad 2$$

Assuming low solute concentrations in the metal phase, the equilibrium constant for this reaction can be written:

$$K_{eq} = \frac{a_{P_2O_5}}{a_{FeO}^5 [\%P]^2} \qquad 3$$

In quantifying phosphorus equilibrium many researchers have used the concept of a phosphate capacity which contains experimentally accessible parameters. In the case of equation 3, many researchers have described the phosphate capacity as:

$$K_p = \frac{(\%P_2O_5)}{(FeO)^5 [\%P]^2} \qquad 4$$

Based upon laboratory data, Balajiva et al. [24] established the following empirical relationship between Kp and weight percent CaO in the slag:

$$\log K_p = 11.80 \log(\%CaO) - C \qquad 5$$

Where C is an experimentally determined, temperature dependant variable parameter.

Equation [5] can be expanded such that:

$$K_{eq} = \frac{N_{P_2O_5}}{[\%P]^2 N_{FeO}^5} \bullet \frac{\gamma_{P_2O_5}}{\gamma_{FeO}^5} \qquad 6$$

Where N_i is the mole fraction of species i and γ_i is the Roultian activity coefficient. Comparison of equations [4] and [6] suggests that the activity coefficient terms in equation [6] are the source of the compositional dependence of Kp.

Later studies [21] attempted to directly evaluate these activity coefficient terms assuming an imaginary pure liquid P_2O_5 as a standard state. Correlations have been developed for Kp by several researchers which include the compositional dependence of the activity coefficient terms on basic slag components, i.e. CaO, CaF_2, FeO, MgO, MnO, etc.

More recently, several attempts have been made to reevaluate phosphorus equilibrium, recognizing the true ionic nature of molten slags. [19, 23, 28] The most recent literature is in agreement that for basic slags, the slag metal phosphorus reaction can be written as equation [2]:

$$[P] + \frac{5}{2}[O] + \frac{3}{2}(O^{-2}) = (PO_4^{-3}) \qquad 7$$

The equilibrium constant (K_p) for this reaction can be expressed as:

$$K_p = \frac{a_{PO_4^{-3}}}{a_P * a_O^{5/2} * a_{O^{-2}}^{3/2}} \qquad 8$$

where a_i is the activity of species i. An important difference should be noted between equations 8 and 4. Due to the form in which the phosphorus reaction is expressed in equation 2, the activity (or weight percent) of phosphorus in the metal appears as a squared term in equation 4. However, due to the form of the phosphorus reaction in equation 7, the activity of phosphorus appears to the first power in equation 8. At low metal phosphorus contents, this represents a significant difference in the equilibrium constant.

If this expression is expanded:

$$K_{eq} = \frac{N_{PO_4^{-3}} \bullet \gamma_{PO_4^{-3}}}{f_P \bullet [\%P] \bullet f_O^{5/2} \bullet [\%O]^{5/2} \bullet N_{O^{-2}}^{3/2} \bullet \gamma_{O^{-2}}^{3/2}} \qquad 9$$

Where f_i represents the one-weight percent standard state activity coefficient of species *i*. When rearranged in the following manner:

$$\frac{N_{PO_4^{-3}}}{[\%P] \bullet [\%O]^{5/2}} = \frac{\gamma_{PO_4^{-3}}}{f_P \bullet f_O^{5/2} \bullet N_{O^{-2}}^{3/2} \bullet \gamma_{O^{-2}}^{3/2}} \bullet \frac{1}{K_{eq}} \qquad 10$$

Again, the terms that are most accessible experimentally are placed on the left hand side of the equation, and the terms remaining on the right represent a formidable collection of largely unknown quantities.

Several researchers have attempted to apply a formalism for describing ionic melts, established by Flood, Forland, and Grjotheim [30, 31] to the phosphorus system. By this method, an ideal anionic equilibrium constant for equation [7] is defined as:

$$K_{PO_4} = \frac{N_{PO_4^{-3}}}{[\%P] \bullet [\%O]^{2.5} \bullet N_{O^{-2}}^{1.5}} \qquad 11$$

It was shown by Flood and Grjotheim that:

$$\log K_{PO_4} = \sum_i (N'_{M_i} \log K_{M_i}) + f(\gamma) \qquad 12$$

Where N'_{Mi} is the equivalent cationic fraction of the cation *Mi* (i.e. Ca^{2+}, Fe^{2+}, Mg^{2+}, Mn^{2+}, etc.) and K_{Mi} is the equilibrium constant for the formation of pure $M_{i3}(PO_4)_2$ by the reactions:

$$2[P]+5[O]+3CaO=Ca_3(PO_4)_2$$
$$2[P]+5[O]+3MgO=Mg_3(PO_4)_2$$
$$2[P]+5[O]+3MnO=Mn_3(PO_4)_2$$
$$\cdots$$
$$2[P]+5[O]+3M_iO=M_{i3}(PO_4)_2$$

In equation [12], f(γ) represents the sum of all the activity coefficient terms. In order to convert K_{PO4} to a phosphorus distribution, equations [11] and [12] can be combined and rearranged such that:

$$\log\frac{N_{PO_4^{-3}}}{[\%P]}=\sum_i(N'_{M_i}\log K_{M_i})+f(\gamma)+\frac{5}{2}\log[\%O]+\frac{3}{2}\log N_{O^{-2}} \qquad 13$$

The term N'_{Mi} can be calculated from the slag chemistry. The K_{Mi} terms can be calculated from the experimentally determined free energies of formation for the different species present. In most cases it can be assumed that the dissolved oxygen content is controlled by the reaction:

$$Fe+[O]=(FeO)$$

Therefore, [O] can be correlated to the activity of FeO in the slag. Some researchers have developed empirical relations that describe N_O^{-2} as a function of SiO_2. [28] Other correlations have been developed which relate N_O^{-2} to optical bacisity or other compositional parameters.

The f(γ) term is unknown and can only be determined experimentally. Several researchers have also attempted to develop correlations that relate this term to some compositionally dependent term such as optical basisity. The f(γ) term can be defined as follows:

$$f(\gamma)=\sum_i N_i\ln\frac{\gamma^i_{PO_4^{-3}}}{(\gamma^i_{O^{-2}})^{1.5}} \qquad 14$$

Where γ_x^i refers to the activity coefficient of phosphate or free oxygen ions with respect to each cation, i. From equation [13] it is apparent that f(γ) is very similar to the $\gamma_{P2O5}/(\gamma_{FeO})^5$ term which was evaluated in earlier studies. Belton et al. [32] have shown an apparent henrian behavior of the phosphate ion in slags with basicities >1.3. These researchers were then able to develop a correlation that expressed f(γ) as a function of concentrations of ferrate ion and free oxygen ion and temperature. The researchers demonstrated that this correlation agreed fairly well with several independent data sets, though only for a limited range of slag basicities.

All correlations to date describing equilibrium phosphorus distribution have relied to some extent upon empirical evaluation of new or existing data sets. Systematic errors or differences within these data sets, as well as fundamental differences in the approaches of the various researchers, have resulted in significant quantitative disagreement between these different correlations. Despite this quantitative disagreement within the literature, there is general agreement upon which factors most strongly influence phosphorus equilibrium, namely:

- Increasing temperature reduces Lp.
- Highly basic slags increase Lp.
- Oxidizing conditions increase Lp.

Several correlations developed by different researchers for the prediction of phosphorus distribution are listed in Appendix A. Figures 4 and 5 highlight both the similar trends and numerical differences for four different correlations.

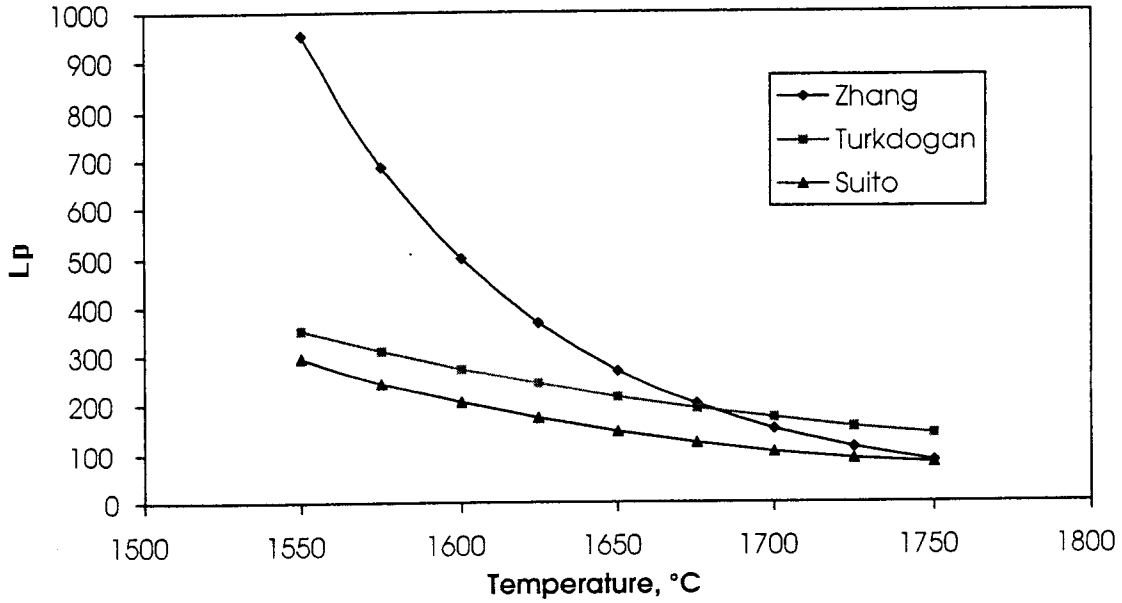

Figure 4: Equilibrium phosphorus partition ratio as a function of temperature as predicted by three correlations assuming a slag chemistry of: 25%FeO - 7%MgO – 46%CaO – 22%SiO_2

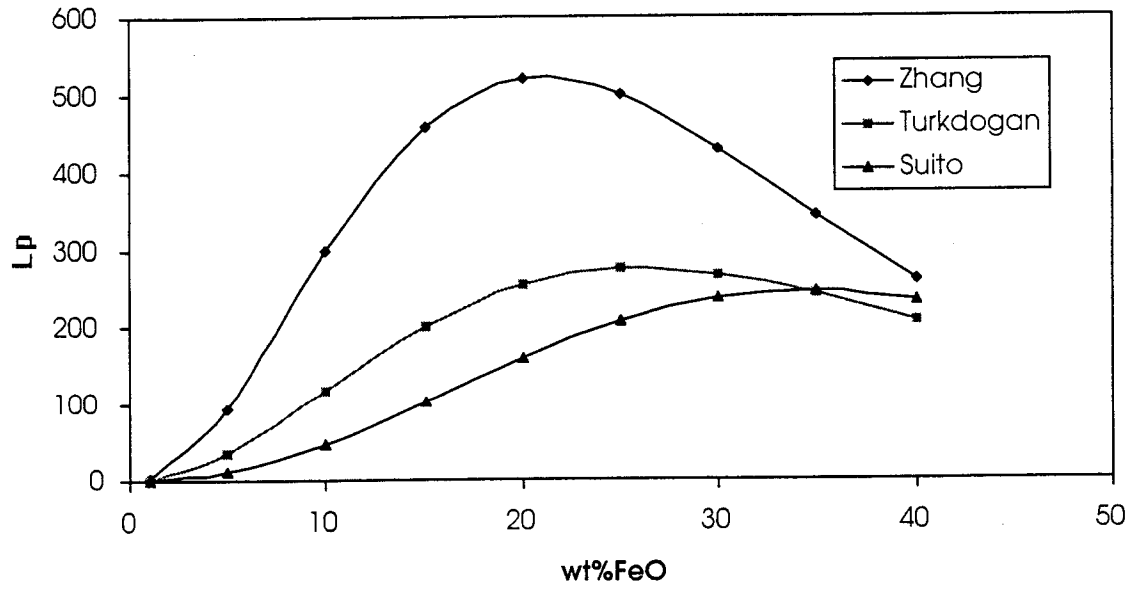

Figure 5: Equilibrium phosphorus partition ratio as a function of FeO as predicted by three correlations assuming T = 1600°C and constant basicity, CaO/ SiO_2 = 2.1.

Different correlations more accurately predict phosphorus equilibrium at different slag chemistries and temperatures. Therefore, when attempting to predict the equilibrium phosphorus distribution for a given slag – metal system, it is imperative to select the model which best describes the system of interest. A recent study by Ide and Fruehan [29] reevaluated the phosphorus equilibrium for the slag chemistries and temperatures directly applicable to this study. In that study, the basic framework of the correlation of

Suito et al. was used, and focused experiments were conducted to evaluate and refine some of the coefficients of the equation. The basic trends of the improved correlation follow those of Suito et al. The Ide et al. correlation is also listed in Appendix A.

2.3 Kinetics of Phosphorus Transfer- As with the results of thermodynamic studies, there is also some disagreement amongst the results of previous kinetic studies. This is due in part, to the fact that different equilibrium phosphorus distribution models have been used in these studies. As mentioned above, most kinetic studies to date have examined the rate of oxidation of phosphorus from metal to slag (dephosphorization). Mori et al. [34] and Motlagh [35] specifically looked at the kinetics of phosphorus reduction from slag to metal (phosphorus reversion or rephosphorization). Most previous studies of phosphorus transfer kinetics have attempted to identify the rate limiting step of this slag-metal reaction. All studies reviewed by the present author either concluded or assumed that the kinetics of the phosphorus reaction are limited by the rate of mass transfer of phosphorus from the bulk of either the slag or metal to the slag-metal interface. Such reactions are said to be controlled by liquid phase mass transfer in the slag, metal or both phases. The basic assumptions of this model are:

- The chemical reaction at the slag metal interface is rapid, thus the interface is always at equilibrium
- The driving force for mass transfer is the difference in the concentration of phosphorus in the bulk liquid phase and the equilibrium concentration at the interface
- The rates of physical transport of phosphorus atoms in the metal or phosphate ions in the slag are limited by some resistance

The liquid phase mass transfer model is typically expressed as:

$$J_A = -k_A\left(C_A^i - C_A\right) \qquad 15$$

Where J_A is the flux of species A, k_A is the mass transfer coefficient, and C^i_A and C_A are the concentrations of A at the interface and bulk respectively. Because various units of both flux and concentration are commonly reported in the literature, the mass transfer coefficient is often reported in inconsistent units. This confusion can be easily avoided by adding the appropriate terms to the flux equation, which are required for unit

conversion. However, these terms are often rolled into the mass transfer coefficient. In the present paper, 'mass transfer coefficients' will always be defined in units of cm/s. When equation 15 is rearranged, the simplest definition of the mass transfer coefficient is obtained:

$$k_A = \frac{J_A}{\left(C_A - C_A^i\right)} \qquad 16$$

This definition can be useful from an engineering stand-point, in the description of complex systems involving turbulent fluid flow. However, the nuances of the fundamental phenomena, which are described by the mass transfer coefficient is a topic of some debate within the literature. Several different physical and mathematical justifications of the mass transfer coefficient have been developed in the literature. A brief review of these arguments will be presented in the following.

One of the oldest theoretical descriptions of the mass transfer coefficient is often attributed to Lewis and Whitman [36]. This model, commonly referred to as the film theory, suggests that all of the resistance to mass transfer in a fluid phase is limited to a thin unmixed film of fluid near the fluid interface. This model is shown schematically in Figure 6.

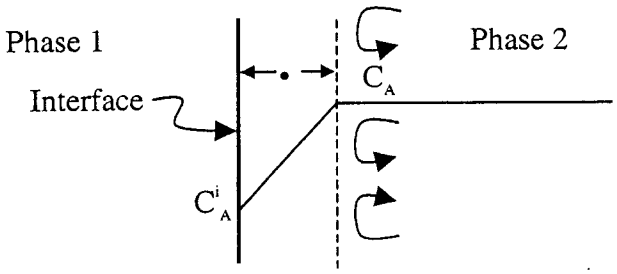

Figure 6: Schematic representation of the film model

The film region is bounded on one side by the interface and on the other by a completely mixed bulk region. Figure 6 fully depicts only one side of the two phase interface. In the case a slag-metal interface, films would exist on both sides of the interface in the slag and the metal. Mass transfer through the stagnant film region occurs purely by atomic or molecular diffusion. Diffusive flux can be described by Fick's first law, which can be written as:

$$J_A = -D_A\left(\frac{\partial C_a}{\partial x}\right) \qquad 17$$

Where J_A is again the flux of species A, D_A is the diffusion coefficient of species A, and $\partial C_A/\partial x$ is the concentration gradient of species A in the x direction. If steady state conditions are initially assumed, the film theory suggests that the entire concentration difference between the interface and the bulk fluid occurs across the length of the film thickness, ∂. By this argument the flux equation can be re-written as:

$$J_A = -D_A \frac{\left(C_A^i - C_A\right)}{\partial} \qquad 18$$

By rearranging equation 18 and combining it with our definition of the mass transfer coefficient in equation 16, we obtain:

$$k_A = \frac{D_A}{\partial} \qquad 19$$

Equation 19 suggests that if the mass transfer coefficient and diffusion coefficient of a species are known, a film thickness can be calculated, or if the film thickness and diffusion coefficient are known, the mass transfer coefficient can be calculated. However, as many researchers have pointed out, the existence of a truly stagnant film near the interface of a turbulent liquid is not likely to exist for most conditions. Regardless of the accuracy of the physical model used to justify the mathematics, the film theory suggests that the mass transfer coefficient is directly proportional to the diffusion coefficient.

Although it is not relevant to the present study, it is worth pointing out that under conditions of fluid flow past a solid, a laminar momentum boundary layer is likely to exist near the interface of the solid and fluid. [37] If the concentration boundary layer of Figure 6 is contained entirely within the laminar momentum boundary layer, it is probable that atomic or molecular diffusion would represent the dominant mechanism of mass flux normal to the solid-fluid interface. Although not entirely accurate, the basic model of Figure 6 is relevant for mass transfer across a solid-fluid interface. A significant effort has been made to develop correlations for the mass transfer coefficient based upon different combinations of dimensionless groups for various geometries of solid-fluid interfaces. Examples of such correlations can be found in many heat and mass transfer reference books. [37,38,39,40]

In contrast to a fluid-solid interface, a liquid-liquid interface such as a slag-metal interface, offers significantly less resistance to shear stresses. For this reason, momentum boundary layers near fluid–fluid interfaces are much less stable than near solid-fluid interfaces, and it is much easier for eddy currents to penetrate right up to the interface. Higbie [41] suggested that turbulent eddy currents continuously deliver new elements or packets of liquid from the well mixed bulk to the interface. The residence time, θ, of a liquid packet at the interface can be viewed in terms of the interfacial velocity, v_i, of the packet and a characteristic length, l, it travels across the interface before it is re-entrained into the bulk.

$$\theta = \frac{\ell}{v_i} \qquad 20$$

Because a given packet of liquid is only at the interface a short time, θ, before it is swept back into the bulk, the packet is subject to unsteady-state diffusion or penetration of species A while it is at the interface. This theory is generally referred to as the penetration theory and is represented schematically in Figure 7.

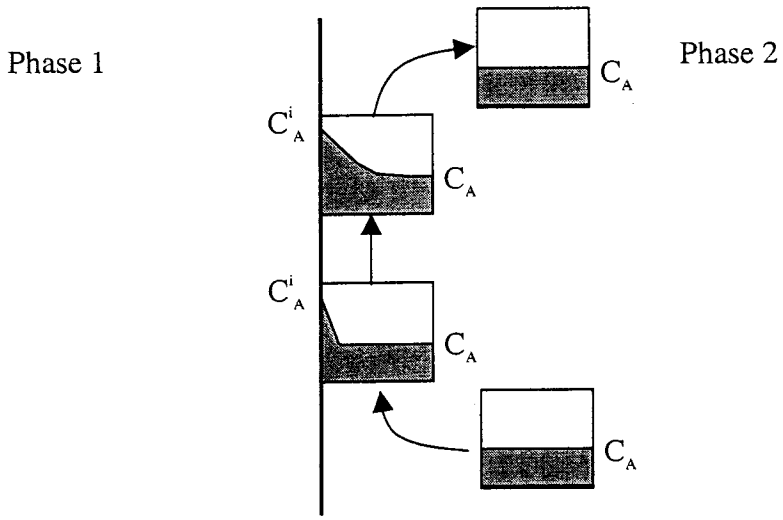

Figure 7: Schematic representation of the motion of a packet or element of fluid to and away from the interface according to the penetration theory.

A key assumption of the penetration theory is that the time a packet of fluid is at the interface, θ, is shorter than the time required to establish steady state diffusion across thickness of that packet. The solution for non-steady state diffusion into a semi-infinite body can be found in most mass transport text books. [37, 39] For the present case, non-

steady state diffusion into the liquid packet yields the following solution for the concentration of A as a function of time and distance from the interface:

$$\frac{\left(C_A^i - C_A\right)}{\left(C_A^i - C_{A\infty}\right)} = erf\frac{x}{2\sqrt{D_A t}} \qquad 21$$

Using Fick's first law to solve for the flux at interface (x=0):

$$J_A = -D_A\left(\frac{\partial C_A}{\partial x}\right)_{x=0} \qquad 22$$

The instantaneous flux at the interface is given by:

$$J_A = \left(C_A^i - C_{A\infty}\right)\left(\frac{D_A}{\pi t}\right) \qquad 23$$

The average flux across the interface during the residence time of a liquid packet at the interface can be calculated by integrating equation 23 with respect to time from t=0 to t=θ and dividing by θ:

$$\overline{J_A} = \frac{1}{\theta}\int_0^\theta \left(C_A^i - C_{A\infty}\right)\left(\frac{D_A}{\pi t}\right)^{\frac{1}{2}} dt \qquad 24$$

$$\overline{J_A} = 2\left(C_A^i - C_{A\infty}\right)\left(\frac{D_A}{\pi \theta}\right)^{\frac{1}{2}} \qquad 25$$

Therefore, in contrast to the film theory, which predicts a linear dependence of the mass transfer coefficient with the diffusion coefficient, the penetration theory predicts the mass transfer coefficient to be equal to:

$$k_A = 2\sqrt{\frac{D_A}{\pi \theta}} \qquad 26$$

Like the film thickness, •, in the film theory, the residence time, θ, of the penetration theory is a function of the stirring conditions and the physical properties of the interface, and is extremely difficult to quantify experimentally.

A variation of the penetration theory was introduced by Danckwertz.[42] This model, often termed the surface renewal model, includes a surface age distribution rather than a constant residence time, θ, for all surface elements. The mathematics of this model are more complex than the basic penetration model as it includes a probability

distribution function for the residence time rather than a simple constant. The surface renewal model results in the same proportionality of the mass transfer coefficient with the square root of the diffusion coefficient.

Experimental results from various fluid systems and different stirring conditions have indicated that the mass transfer coefficient is proportional to D^n where n ranges between 0.5 and 1.[37] This suggests that, at least mathematically, the film theory and penetration/surface renewal theories may represent the boundaries of a continuous relationship between D and k. Toor and Marchello [42] proposed the film-penetration model, which approaches the film and penetration models as limiting cases of a single phenomenon. The film-penetration model suggests that surface elements of an average thickness, L, are circulating between the interface and bulk fluid with some average residence time at the interface. Within the thickness, L, of the surface elements, mass transport normal to the interface is dominated by atomic or molecular diffusion. At distances greater than L form the interface, mass transfer is dominated by turbulent transfer and the concentration is approximately constant.

Toor and Marchello [42] suggest that elements of liquid at the interface are different from those in the bulk liquid as they are more stable due to the effects of interfacial tension. Because the rotational and translational motion of interfacial elements are more restricted relative to bulk elements, a concentration gradient and diffusional mass transfer can be established within the element. This suggests that the residence time of an element of liquid at the interface is somehow proportional to the interfacial tension; however, the authors make no speculation regarding the specifics of that relationship.

The time, τ, required to establish steady state diffusion within an interfacial element of thickness L can be roughly approximated as:

$$\tau = \frac{L^2}{D} \qquad 27$$

The film-penetration theory recognizes that the key difference between the film and penetration models lies in the relationship between the average residence time of the surface elements, θ, and the time required to establish steady state diffusion, τ. When the residence time, θ, is much greater than τ, diffusion across the interfacial elements proceeds in a steady state manner, and the mass transfer coefficient is proportional to the diffusion coefficient. When the residence time is much less than τ, diffusion into the

interfacial element proceeds in a non-steady state manner before the element is swept into the bulk. In the latter case, the mass transfer coefficient is proportional to the square root of the diffusion coefficient. Assuming a distribution of residence times about an average, when the average residence time and the time to establish steady state are similar, the mass transfer coefficient will be proportional to D^n, where n is between 0.5 and 1. Toor and Marchello offer a continuous graphical solution of the proportionality of the flux to the diffusion coefficient as a function of θ / τ with the solutions of the film and penetration theories as asymptotes.

The film-penetration theory offers a very interesting framework from a conceptional standpoint. However, the inaccessibility of θ and τ, limit the usefulness of this model in generating meaningful calculations. The conclusion one must draw from the literature, is that the precise physical and mathematical description of the mass transfer coefficient for liquid-liquid reactions remains somewhat unclear.

As mentioned above, Mori et al. [34] conducted an extensive fundamental study of slag-metal phosphorus transfer kinetics. These researchers employed a similar experimental approach as proposed in the present study to produce fairly internally consistent data. Figure 8 shows the experimental apparatus used by Mori et al. in that study.

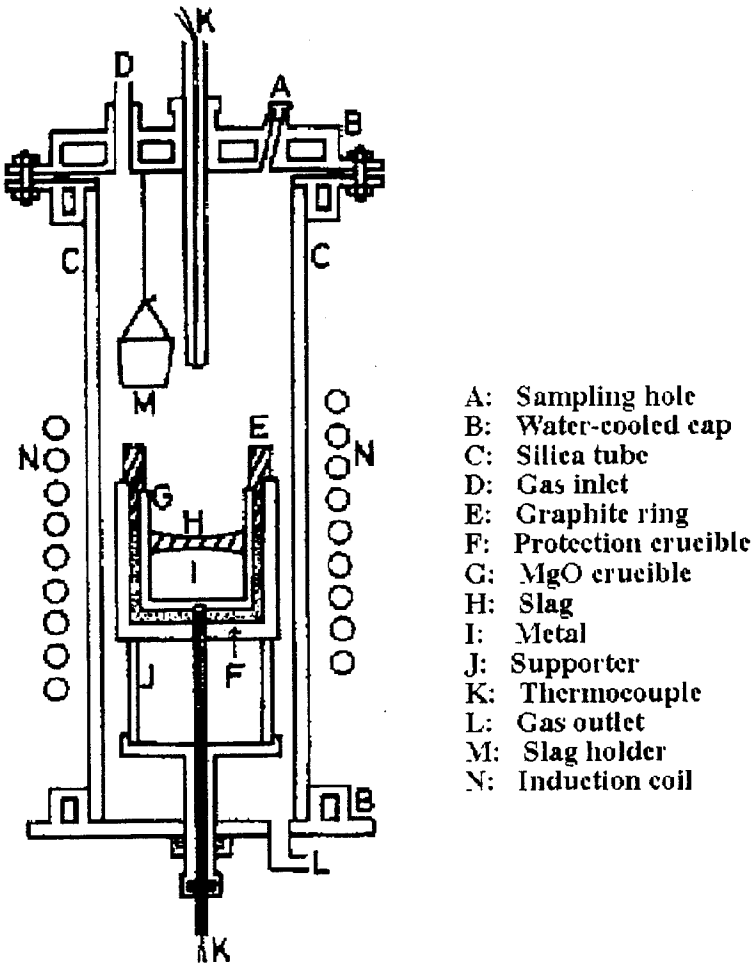

Figure 8: Experimental apparatus used for Phosphorus kinetic study by Mori et al. [34]

In their study, the researchers melted approximately 250 g of iron or iron-phosphorus alloy in a magnesia crucible in an induction furnace. Once the experimental temperature was reached, approximately 40 g of prefused synthetic slag contained in a pure iron slag holder (shown as item M in Figure 8) was lowered to the metal surface. The experiment was judged to begin when the slag holder melted and the slag flowed out onto the liquid metal surface. The slag chemistries and experimental temperatures studied by Mori et al. are listed in Appendix B. Samples were taken from the metal and slag repeatedly once the slag and metal were in contact. Metal samples were analyzed for oxygen and phosphorus, and slag samples were analyzed for CaO, SiO_2, FeO, MgO, and P_2O_5.

In the discussion of their results, these researchers noted some difficulty in choosing an adequate thermodynamic model that was consistent with their results. Without extensive justification, Mori et al. [34] assumed that liquid phase mass transfer in either

the slag or metal was controlling the kinetics of phosphorus transfer. The researchers developed the flux equations for phosphorus in the slag and metal assuming constant mass transfer coefficients in the slag and metal, a constant area of slag metal contact, and with concentrations in weight percent. The flux equations for phosphorus in the metal and the slag are given as equations 28 and 29 respectively:

$$\frac{\partial[\%P]}{\partial t} = -\frac{A\rho_m k_m}{W_m}\left[[\%P^i]-[\%P]\right] \qquad 28$$

$$\frac{\partial(\%P)}{\partial t} = -\frac{A\rho_s k_s}{W_s}\left[(\%P)-(\%P^i)\right] \qquad 29$$

Where, **A** is the slag - metal surface area,

$\mathbf{k_s}$ and $\mathbf{k_m}$ are the mass transfer coefficients in the slag and metal,

ρ_s and ρ_m are the slag and metal densities,

$\mathbf{W_s}$ and $\mathbf{W_m}$ are the weights of slag and metal, and

$(\%\mathbf{P^i})$ and $[\%\mathbf{P}]$ are the phosphorus contents of the slag and metal at the slag/metal interface.

Mori et al. reasoned that due to the conditions of their experimental apparatus, the kinetics of dephosphorization would be controlled entirely by mass transfer in the metal. Using a numerical solution to equation 28 to analyze their experimental results, the researchers calculated metal liquid mass transfer rates in the range of 0.33×10^{-2} to 1.09×10^{-2} cm/sec for the conditions studied. In Figures 9 and 10, Data from this study by Mori et al. [34] are replotted. In addition to the raw data, the solid lines shown were calculated based upon the liquid phase mass transfer model with the conditions stated above, i.e. constant k_m, constant A, etc.

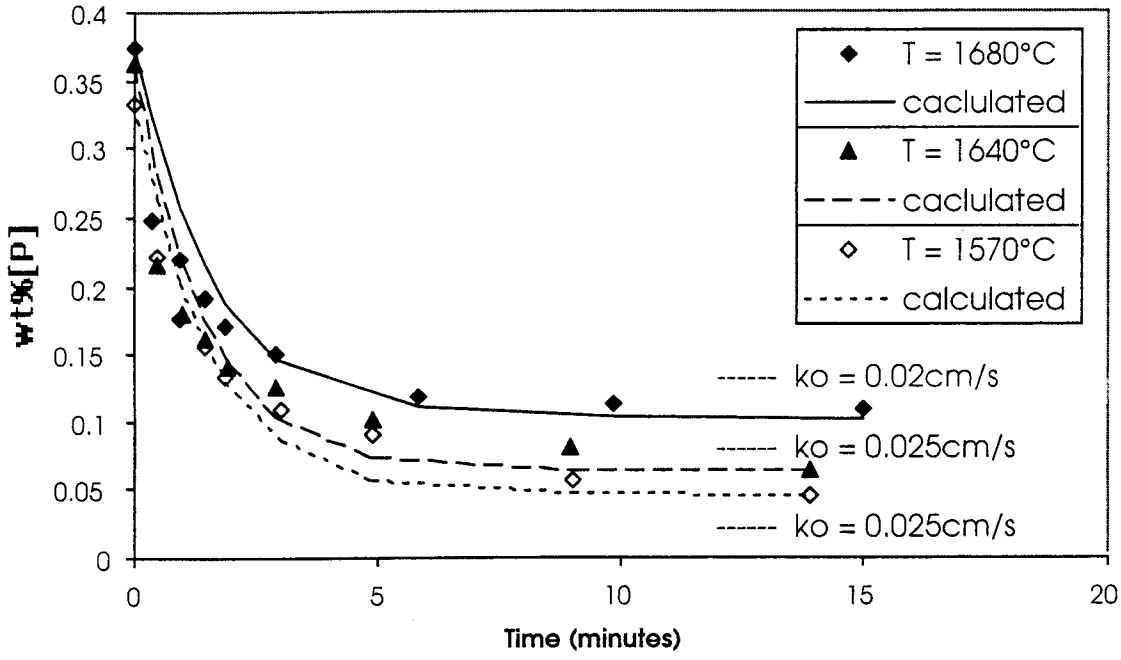

Figure 9: Dephosphorization kinetic data adapted from Mori et al. [34] plotted with calculated curves for best fit overall mass transfer coefficients, ko. The thee data sets shown were collected for approximately the same slag chemistry at different experimental temperatures.

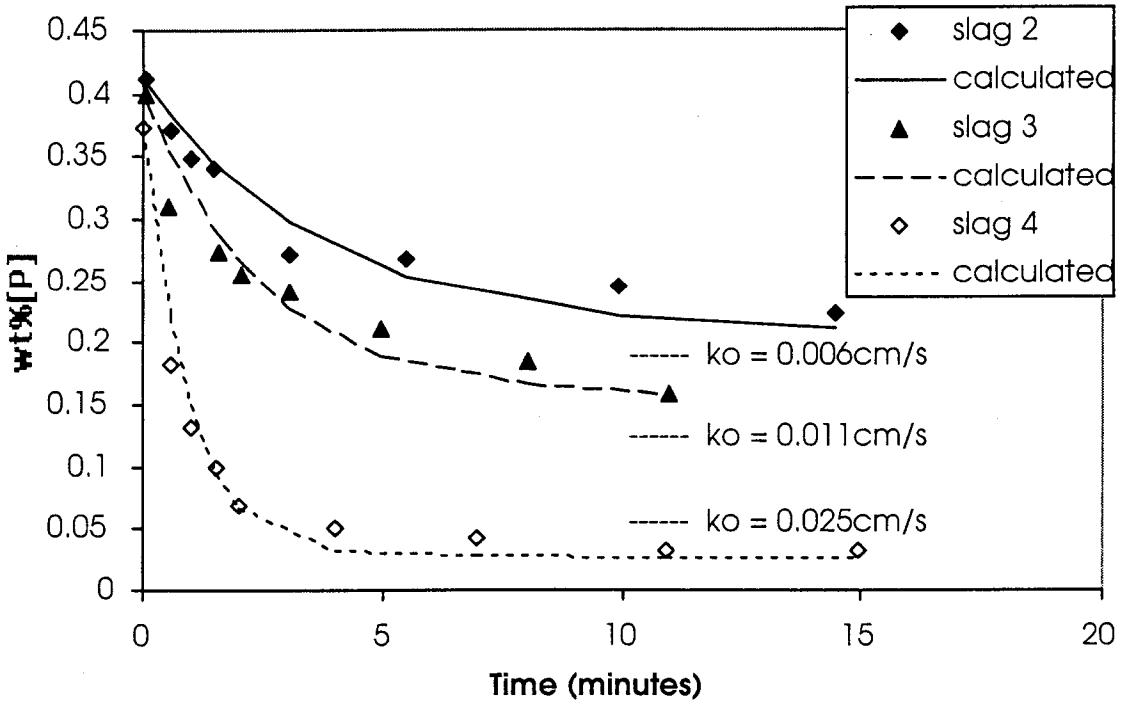

Figure 10: Dephosphorization kinetic data adapted from Mori et al. [34] plotted with calculated curves for best fit overall mass transfer coefficients, ko. The thee data sets shown were collected for different slag chemistries at the same experimental temperature(1640°C).

In Figures 9 and 10, the calculated continuous curves were generated assuming a constant driving force (e.g. constant Lp), a constant overall mass transfer coefficient, and constant slag metal area. For these calculations, it was assumed that the final slag and metal chemistries provided in the paper by Mori et al., and listed in Appendix B of this paper, represented the equilibrium phosphorus partition, Lp. Clearly, however, there are indications in these and other data presented by Mori et al. that at least some of the experiments had not yet reached equilibrium by the final sample.

In both Figures 9 and 10, the experimental data exhibit an initial fast rate, which is faster than the calculated curve at very short experimental times. After 3 to 5 minutes, the transfer rate appears to slow down, becoming slower than the calculated curve.

In Figures 11 and 12, rephosphorization data from the same study are replotted. Again the continuous curves represent the calculated metal phosphorus versus time assuming a liquid phase mass transfer model and a best fit overall mass transfer coefficient.

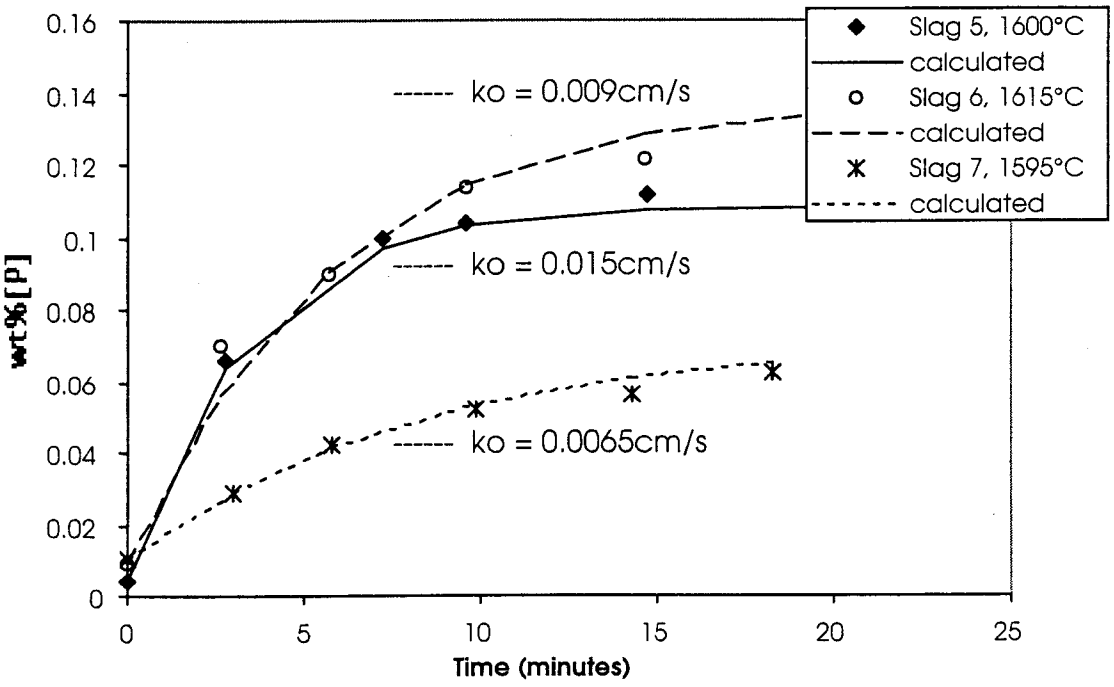

Figure 11: rephosphorization kinetic data adapted from Mori et al. [34] plotted with calculated curves for best fit overall mass transfer coefficients, ko. The thee data sets shown were collected for different slag chemistries at different experimental temperatures.

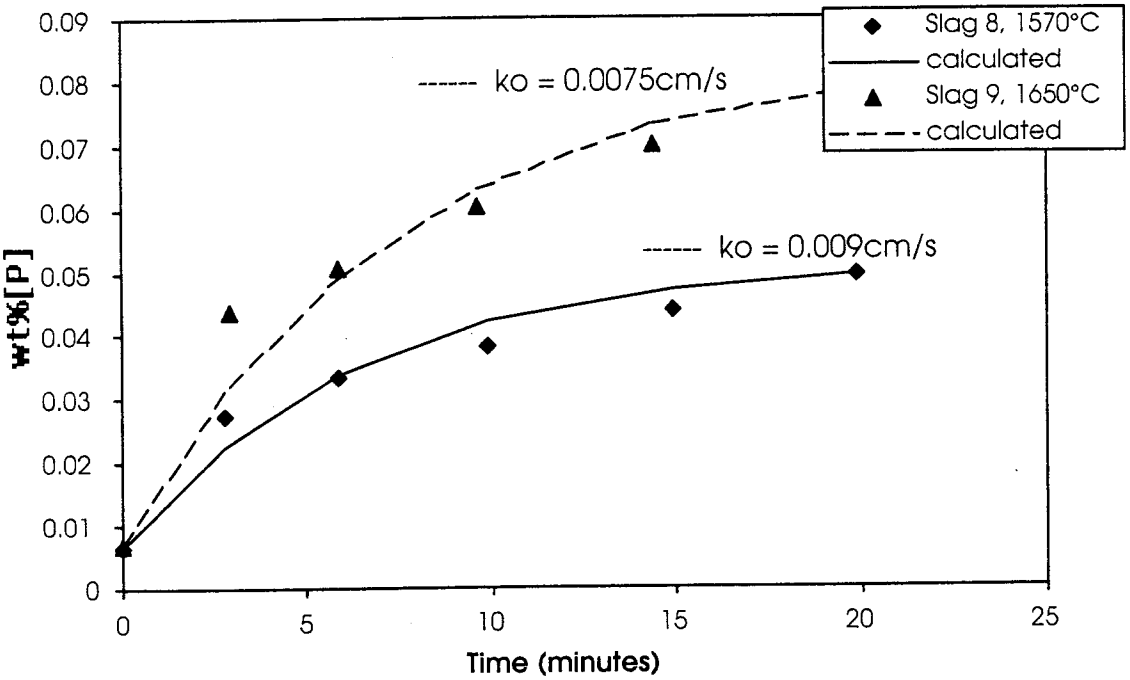

Figure 12: Rephosphorization kinetic data adapted from Mori et al. [34] plotted with calculated curves for best fit overall mass transfer coefficients, ko. The thee data sets shown were collected for the same slag chemistry at different experimental temperatures.

The general trends observed in the dephosphorization experiments regarding an initial fast rate followed by a slower rate, were also observed in the rephosphorization experiments. Mori et al. identified an apparent dependence of the mass transfer coefficient upon the equilibrium phosphorus distribution ratio, e.g. the driving force for mass transfer. However, none of the theoretical descriptions of the mass transfer coefficient presented earlier in this section even suggest a dependence of k upon concentration or driving force parameters. Despite these very interesting trends, Mori et al. did not offer an extensive discussion of these points in their analysis. The above mentioned trends in the data of Mori et al. [34] are also reflected in the data of the laboratory kinetic study presented later in this paper. Therefore, the data of these experiments by Mori et al. will be revisited in the discussion of the present data.

In the study by Mori et al. [34], most dephosphorization rates were observed to be fairly rapid, e.g. equilibrium was obtained within 15 minutes. Within the experimental technique used by these researchers a significant transient period existed at the start of each experiment. During dephosphorization and rephosphorization experiments, the experiment was judged to start when the slag holder, shown in Figure 8, melted, presumably near 1537°C, and the slag flowed out onto the liquid iron or Fe-P alloy. For

experiments at higher temperatures, a finite time must have passed before the slag reached the experimental temperature. This would result in an initially higher Lp, and hence driving force, which would decrease until the target temperature was obtained. The experiments conducted by Mori et al. were extremely well executed; however, the experimental technique employed by these researchers may have introduced some unnecessary complexity to an already difficult and dynamic system.

Several studies have been reported recently investigating the kinetics of phosphorus transfer between slag and either hot metal or high carbon iron. [43 - 47] Several attempts have been made to predict the behavior of highly complex systems involving multiple simultaneous multi-phase reactions. [44, 45] Several studies have been conducted where these models have been applied to experimental data collected for systems of various sizes. [43, 46] Generally, such multi-component models require the simultaneous fitting for a large number of experimental parameters. This can be very useful for modeling plant data. Also, if the fundamental mechanisms and rate constants for the separate reactions are known with a high degree of confidence, multicomponant kinetic models are a useful framework for evaluating overall rate constants in complex systems. It is the opinion of this researcher that the kinetics of phosphorus transfer are not well understood for even very simple and well-defined systems. Hot metal or high carbon phosphorus oxidation experiments can be very difficult to evaluate since the system never reaches true equilibrium. Most importantly, huge gradients in oxygen potential between the slag and metal, and a dynamic slag composition make it very difficult to accurately define the driving force for phosphorus transfer. Several dephosphorization studies have estimated the equilibrium phosphorus partition to be the final or maximum partition achieved during the study. Other studies have attempted to correlate the oxygen potential at the interface to the Fe^{2+}/Fe^{3+} ratio in highly oxidized slags. Both of these estimations require significant assumptions and may not reflect the true driving force for dephosphorization.

In a recent study, Wei et al. [44] examined the effects of stirring rate, slag chemistry, and experimental atmosphere on the rate of phosphorus transfer between slag and high carbon iron. In this study, both dephosphorization and rephosphorization kinetics were studied for an Al_2O_3 – CaO - SiO_2 – Li_2O – Fe_tO slag / Fe – 4.4%C system at 1300°C under an Ar-O_2 atmosphere. The system was mechanically stirred by an eccentric alumina stirrer at rotation speeds from 0 to 300 rpm.

The researchers attempted to develop a model to describe the various rates of the different simultaneous reactions of the system. In this model the researchers linked the multiple simultaneous reactions to the oxygen potential at the slag – metal interface. By assuming mass flux balance at the gas – slag and slag – metal interfaces, the researchers numerically solved the flux equations for the various components for short increments of time. For the calculations within the model, it was assumed that the phosphorus partition ratio, thus the driving force for phosphorus transfer, only varied with oxygen activity at the slag – metal interface. Although this allowed the authors to directly link the phosphorus reaction to the Fe^{2+}/Fe^{3+} ratio in the bulk slag, it neglects all other compositional variation of Lp. Since up to fifty percent of the starting FeO content of the slag was consumed during these experiments, the above assumption probably introduced some degree of error into the analysis. A mixed slag and metal liquid phase mass transfer controlled model was developed to describe the kinetics of phosphorus transfer. A numerical value was assigned to the overall mass transfer coefficient for phosphorus. However, the system evaluated by Wei et al. [44] was extremely complex and dynamic. Consequently, the overall model contained many variable parameters, which may have distorted the true mass transfer kinetics of phosphorus.

In the analysis of their results, Wei et al. [44] noted that the mechanical stirring rate had a negligible effect on the apparent rate of dephosphorization. It was proposed that this was the result of a balanced effect of a simultaneous increase in the metal phase mass transfer coefficient, ko, and a decease in Lp. Lp is decreased by an increased rate of decarborization resulting in a decrease in the oxygen activity at the interface. However, the unique balancing of these two terms seems unlikely. Two other more likely explanations include:

- Liquid phase mass transfer can not be accurately described as a constant mass transfer coefficient in the highly complex system studied by Wei et al. [37]
- Stirring in the slag phase, resulting from CO evolution due to the reaction of FeO in the slag and carbon in the metal, was dominating the mass transfer conditions for the system. That is to say that the additional stirring energy provided by the mechanical stirring was small relative to the stirring energy of the evolving gas.

If phosphorus transfer is controlled by slag phase mass transfer, and stirring conditions in the slag are controlled by the CO evolution mentioned above, increasing the mechanical

stirring rate would have only a small effect on the rate of phosphorus transfer. Furthermore, due to the large amount of mechanical and gas stirring during the experiments, it is unlikely that a constant slag-metal area based upon the crucible cross-sectional area accurately reflects the true slag – metal reaction area. The effects of mechanical stirring on the amount of slag metal mixing and rate of separation are uncertain at best. Despite this uncertainty, the apparent rate of phosphorus transfer observed by Wei et al. [44] is relatively fast. Almost all of the experimental data presented in that study appeared to reach a steady state phosphorus level within 5 to 10 minutes. Many of the observations reported by Wei et al. were admittedly the effect of various experimental parameters on the driving force for phosphorus transfer. Therefore, it is difficult to draw solid conclusions regarding the fundamental mechanism and rate of phosphorus transfer.

In a very recent study, Monaghan et al. [47] attempted to evaluate the kinetics of dephosphorization of carbon saturated iron. In these experiments, a highly oxidizing slag (up to 66wt% Fe_2O_3) was used. Like Wei et al. [44], these researchers assumed that oxygen activity at the slag metal interface dominated the driving force for dephosphorization. It was also assumed that the slag phase controlled the oxygen activity at the interface. This latter assumption, made by both Wei et al. and Monaghan et al. implies that either mass transfer of carbon in the metal or chemical kinetics of the reaction:

$$[C]_i + [O]_i = CO(g)$$

are slow. Subscripts i indicate oxygen and carbon at the interface. The fact that any dephosphorization occurs in these experiments validates this assumption to some extent, as the equilibrium oxygen activity in carbon saturated iron is very very low.

Monaghan et al. [47] attempted to evaluate phosphorus transfer kinetics by separating driving force effects from their experimental data. By assuming a liquid phase mass transfer controlled model, the researchers attempted to isolate driving force effects. An unfortunate limitation of the approached used by Monaghan et al. [47] is the inability to define the phosphorus partition ratio, thus the driving force, with a high degree of confidence. Despite this fact, several interesting observations were made. The researchers reported with some confidence that mass transfer in the slag phase controlled

the rate of dephosphorization. In conjunction with this conclusion, a correlation was demonstrated between slag viscosity and the apparent rate of mass transfer. Three slag components, Fe_2O_3, CaF_2, and $CaCl_2$, were varied to produce slags with a range of viscosities. In general, the rate of mass transfer decreased with increasing slag viscosity. Monaghan et al. assumed a penetration theory description of the slag mass transfer coefficient as described above:

$$k_s = 2\sqrt{\frac{D}{\pi\theta}} \qquad 30$$

Where k_s is the slag mass transfer coefficient, D is the diffusivity of phosphorus, and θ is the contact time of an element of slag with the slag – metal interface. Also, since diffusivity and viscosity, η, are inversely related:

$$D \propto \frac{1}{\eta} \qquad 31$$

It can be said that:

$$k_s \propto \left(\frac{1}{\eta}\right)^{1/2} \qquad 32$$

In the analysis of their results Monaghan et al. [47] included a plot of k_s versus $(1/\eta)^{1/2}$ adapted below as Figure 13:

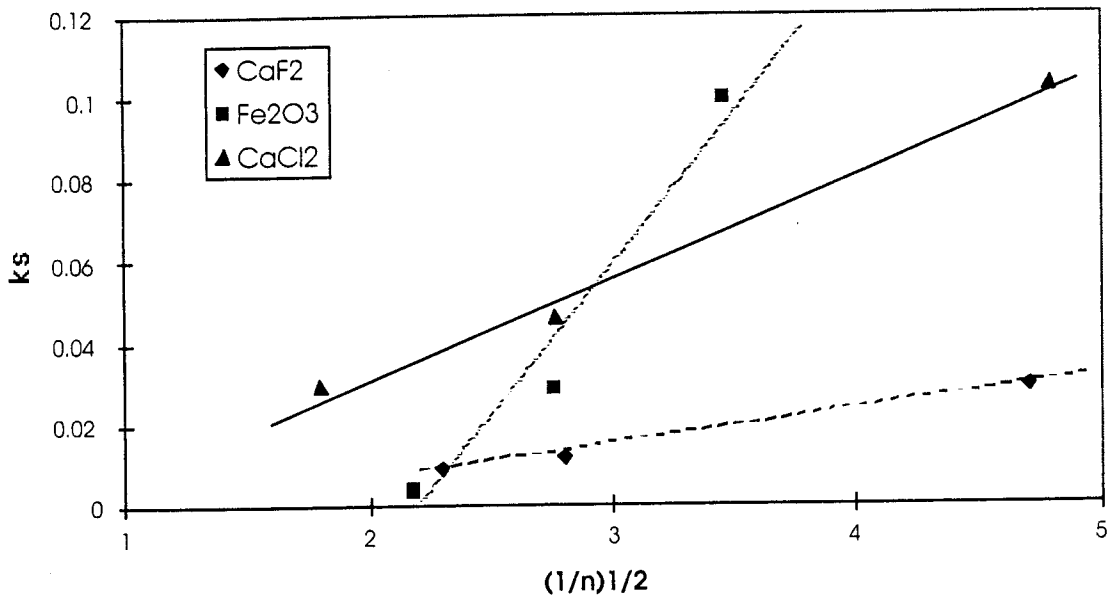

Figure 13: Calculated ks versus $(1/\eta)^{1/2}$. Adapted from Monaghan et al. [47].

Despite the apparent linear behavior expressed in this plot when only one slag component is varied, there is no overall trend relating slag viscosity and the calculated slag mass transfer coefficient. Furthermore, slag mass transfer coefficients on the order of 0.1 cm/s are extremely unusual. Based on these observations it is unlikely that the k_s term presented in Figure 13 is a true mass transfer coefficient containing only kinetic information. Several other parameters can also be correlated to slag viscosity, which are also likely to influence the plot in Figure 13. These include:

1. Slag foamability
2. Susceptibility to slag-metal mixing, and rate of droplet separation.
3. Slag composition and therefore Lp, i.e. the driving force.

Imprecise knowledge of the reaction area due to slag metal mixing, or uncertainty regarding the driving force for the reaction would significantly affect the calculated term k_s. Furthermore, little is known about the mass transfer of reacting species within a foamy slag. The trends reported by Monaghan et al. [47] are interesting, though they must be viewed with a high degree of skepticism. Investigation of a simpler system is necessary to truly understand their observations.

One important point of the phosphorus studies conducted on high carbon systems should be restated, as it is particularly relevant to process model developed later in the paper. The fact that dephosphorization of high carbon iron via an oxidizing slag can

occur suggests that the oxygen potential of the slag, not the metal dominates the oxygen potential at the interface. This suggests that in evaluating the equilibrium phosphorus distribution for slag – steel systems, the equilibrium can be calculated based entirely on the slag chemistry and temperature without detailed consideration of the bulk metal oxygen potential.

Chapter 3

Experimental Procedures

3.1 Metallographic Observations

It is an objective of this study to investigate the microstructures of several types of direct reduced iron products from various sources. A metallographic investigation has been conducted via optical and scanning electron microscopy examining several types of direct reduced products. These materials are listed in Table 1.

Table 1: Chemical Composition of Investigated Commercial Materials

Material	Method of Reduction	Fe_t	FeO	C	SiO_2	Al_2O_3	CaO	P
Midrex DRI	Midrex	93.13	5.87	1.89	1.92	---	1.59	0.028
Midrex HBI	Midrex	92	10	< 0.5	1.8	---	---	0.06
BHP - HBI	Finmet	92	8	1.3	1.6	---	0.1	0.045
Mobile DRI	Midrex	91.2	7	2.43	1.14	0.36	0.3	0.037
Circal HBI	Circored	97	12	0	1.03	0.32	---	0.028
Sidor DRI	Midrex	93.76	7.6	>3	1.67	---	2.11	0.054
Opco HBI	Midrex	91.5	8.4	0.8	~2	---	---	0.053

The analytical x-ray capabilities of the electron microscope were used to provide rough estimates of the chemistries of the different phases, which were observed.

3.2 DRI Fast Melting Experiments

Several experiments were designed and conducted where DRI material was quickly melted and quenched. The goal of these experiments was to allow the gangue and metal phases to physically separate while in the liquid state, but to quench the material before significant phosphorus transfer could occur. . A standard procedure for these experiments was developed, which allowed for:

1. Reasonable Temperature Control – Phosphorus equilibrium is a strong function of temperature. Poor temperature control after melting could introduce significant error.

2. Efficient Phase Separation – The micrographs of HBI and DRI shown in the results section, illustrate the heavily intermingled nature of the metal and gangue. Gas evolved upon melting DRI/HBI also tends to re-entrain gangue particles. Efficient phase separation is necessary to ensure that the true metal phosphorus content is being measured.
3. Accurate Analysis – The chemical analysis for these experiments was conducted by the author, with special attention paid at all stages to ensure accurate analysis of phosphorus contained in the metal phase only.

In these experiments 20 to 30 grams of either HBI or DRI were lowered into a hot empty magnesia crucible in a high purity argon atmosphere. The MgO crucible was heated within a molybdenum crucible via an induction furnace. For all experiments, the temperature was held at 1600±10°C as measured by a two color optical pyrometer aimed at the bottom of the MgO crucible. The accuracy of the pyrometer was initially checked for this system against a type B thermocouple and found to be accurate within ±10°C. A schematic of this apparatus is shown Figure 14. Once the material was in the furnace, heating to the melting temperature took between 30 and 120 seconds depending upon the density and gangue composition of the material. The time from when liquid was first observed to form until melting was completed took 20 to 40 seconds for all materials. For all materials containing carbon, rapid gas evolution resulted in a completely emulsified melt for the first 30 seconds after melting. Pin samples were taken from the melt via a 3 mm I.D. quartz tube as a function of time as measured from first observed melting. After 5 minutes had passed the furnace was shut off and the melt was cooled at approximately 300°C/min. The final sample, the slug of metal remaining in the crucible, was estimated to be solid at 6 min.

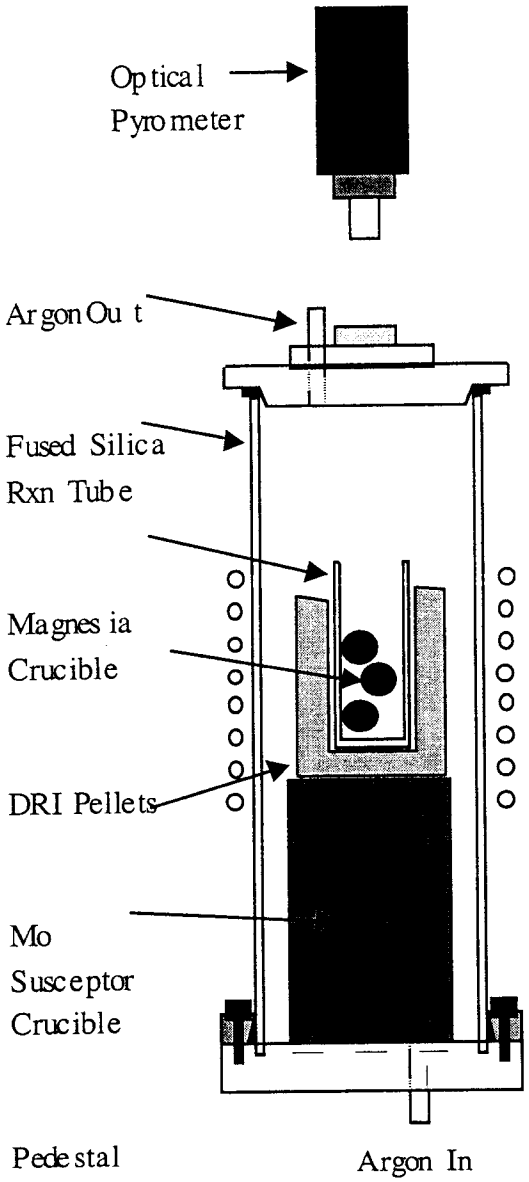

Figure 14: Experimental apparatus used for quick melting and quenching of DRI and HBI.

It was found that some of the samples, particularly those from early in the experiment, were a mixture of slag and metal. Significant effort was made to separate the oxide and metal prior to analysis. Approximately 0.3 to 0.5 grams of oxide free metal was isolated from each sample for analysis via the phospho-molybdenum-blue photometric method.

Several additional fast melting experiments were conducted where HBI material was dropped into a liquid slag phase instead of an empty crucible. For these experiments 30 grams of HBI were dropped into 15 grams of magnesia saturated liquid slag with a basicity of 1 and zero initial iron oxide at 1600°C. The intended purpose of the slag

phase was only to capture and dilute the early melting components of the gangue, prior to bulk melting of the HBI material. For this reason the slag initially contained no iron oxide, and thus had no phosphorus capacity. If the early melting portion of the gangue contained significant amounts of phosphorus, and could effectively separate to an external slag prior to bulk melting, the initial metal samples should show a relatively low phosphorus content, which would increase with time.

One final set of fast melting experiments were conducted where the gangue chemistry of the Circal material was altered by adding CaO or $CaCO_3$ to the material. For these experiments, several hundred grams of the Circal HBI was crushed to powder of less than 40 mesh. The crushed HBI was then blended with small amounts of reagent grade CaO or $CaCO_3$ powder. Both the CaO and $CaCO_3$ were very fine powders. The material was then repressed to a density of approximately 5 g/cm3. The Circal material contains approximately 1% silica, 5 to 12% FeO, and very little else other than pure iron. In the modified material, just enough lime was added to give a basicity of 1 and 1.5. Rapid melting experiments were subsequently conducted where 30 grams of material were lowered into a hot empty crucible. The fast melting procedure was the same as described above.

3.3 Controlled Melting Observations

In order to develop a better understanding of the behavior of DRI/HBI during melting, several controlled melting experiments were conducted. A hot stage confocal microscope was used to observe two HBI materials microscopically during melting. In the microscope, 4mm diameter samples of either Midrex HBI or BHP-HBI were heated until complete melting occurred. Samples of each material were prepared with a single polished surface. The temperature was controlled manually, and increased from room temperature to approximately 1550°C at a rate of roughly 10 to 25 °C per minute. The entire heating and melting cycle was recorded on a S-VHS cassette via a CCD camera for subsequent review.

Both DRI and HBI materials were also observed macroscopically during melting in an induction furnace. For these experiments, sectioned and polished samples of either DRI or HBI were placed in MgO crucible contained within a molybdenum crucible. The Molybdenum crucible was heated via the induction furnace at approximately 10 °C per

minute as measured by a two color optical pyrometer aimed at the polished surface of the DRI or HBI sample. The heating and melting cycle was recorded via a CCD camera and S-VHS videocassette recorder.

3.4 Laboratory Kinetic Experiments

It was originally hypothesized that the phosphorus in DRI is primarily present in the oxidized state in the gangue. It was believed that slow kinetics coupled with frequent slag flushing resulted in the lower than expected metal phosphorus levels, which have been reported by some EAF steel producers. Thus, a fundamental investigation of the kinetics of phosphorus reversion was originally planned as an integral part of this study. The present understanding is that, even if phosphorus is initially present exclusively in the oxide phase, phosphorus reversion from gangue to metal will be very rapid upon melting due to the enormous metal - oxide interfacial area present in DRI pellets. If this is the case, the kinetics of both phosphorus reversion and removal are important to understanding the observed industrial phenomenon.

Laboratory experiments designed to elucidate the rate controlling mechanisms and rate parameters of phosphorus transfer were conducted. These experiments are designed to measure the rate of transfer from slag to metal and metal to slag as a function of slag chemistry and temperature. It was initially assumed that the rate of phosphorus transfer is controlled by liquid phase mass transfer in both the slag and the metal. Dephosphorization experiments were conducted for slag chemistries representative of common EAF practices:

CaO	-	30 – 55%
SiO_2	-	10 – 30%
MgO	-	8 –12%
FeO	-	5 – 40%

In addition, phosphorus reversion experiments were conducted using a slag phase representative of typically observed DRI gangue chemistries, e.g. low basicity, high phosphate, and variable FeO. The temperature of kinetic investigations ranged from 1550°C to 1650°C. The experiments were conducted in a 10 kW induction furnace under known stirring conditions for the metal. Experiments were conducted in 3 cm I.D. high purity, high density magnesia crucibles unless otherwise specified. Samples of the metal were taken via a 3mm I.D. quartz tube as a function of time and analyzed for phosphorus.

Slag samples were take using a cold iron rod and were analyzed for CaO, MgO, SiO_2, Fe_tO, and phosphorus. Phosphorus in both the slag and metal was analyzed by the phospho-molybdenum-blue photometric method. The specific results and method of analysis for slag samples taken from kinetic experiments appear in Appendix D. Initially, in these laboratory experiments the simplest case was studied, where no carbon is present, and the reaction:

$$(FeO) = [Fe] + [O]$$

controls dissolved oxygen in the metal. Due to the extreme complexity of coupled slag metal reactions such as the phosphorus reaction, it is necessary to reduce of the number of system variables present in a real EAF environment to a manageable few. Under these controlled experimental conditions, basic mass transfer and kinetic parameters can be determined and then applied to more realistic systems.

The experimental apparatus for these experiments is shown in Figure 15.

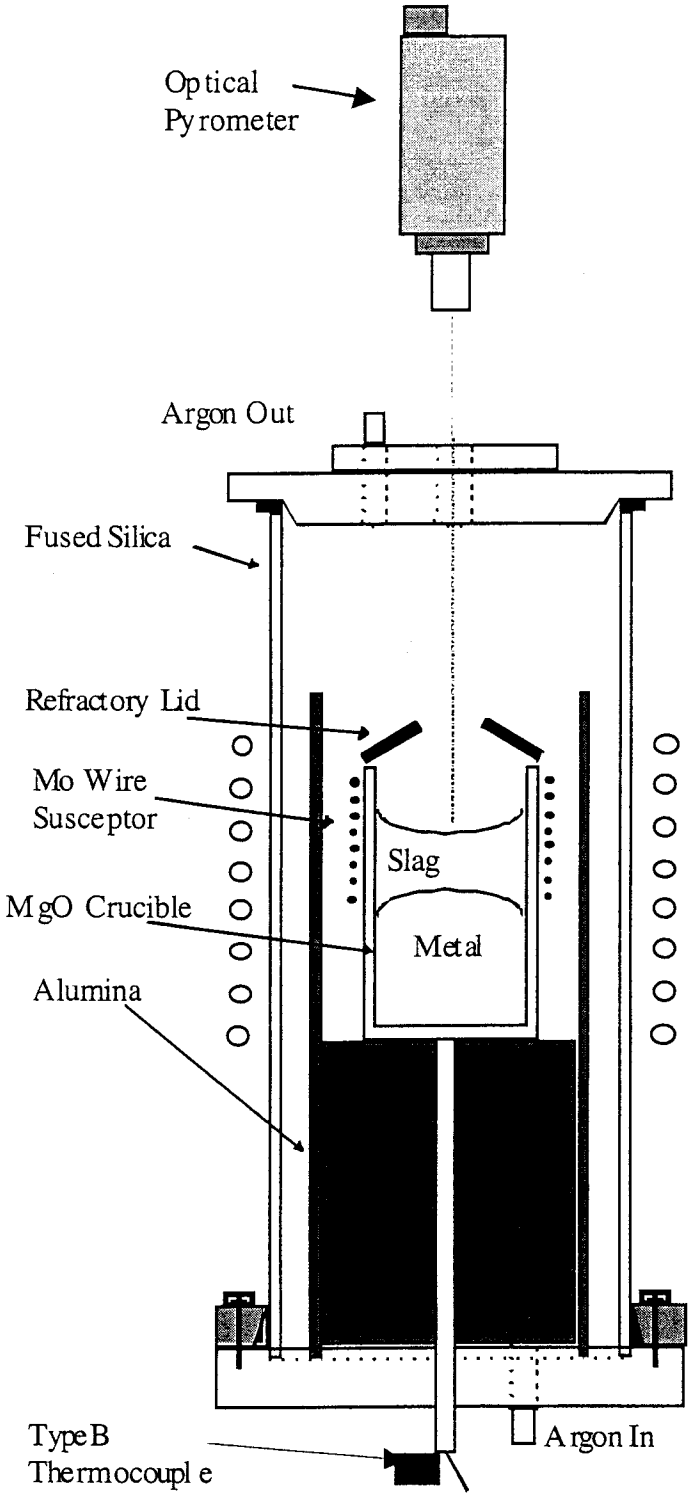

Figure 15: Experimental apparatus for kinetic experiments.

For these experiments, the iron metal (approximately 150 to 200 grams) was inductively heated and stirred. However, the slag (approximately 60 to 80 grams) was indirectly heated via a molybdenum susceptor. In order to be sure thermal gradients were

minimized, the surface temperature of the slag was continuously measured using a two color optical pyrometer and the metal temperature was measured via a type B thermocouple in contact with the bottom of the magnesia crucible. The pyrometer was calibrated for the slags used in the experiments with a type B thermocouple. Special attention was paid to ensure that the slag and metal temperatures stayed within 10 degrees of one another. Because the molybdenum susceptor coupled very efficiently with the induction coil, the temperature of the slag could be adjusted by ±50°C by altering the vertical position of the experimental apparatus within the coil, and/or by making subtle changes to the spacing of the coils. Continuous monitoring and adjustment of the temperature in this manner ensured a fairly isothermal system.

Several experimental techniques were explored initially for dephosphorization and rephosphorization kinetic experiments. It was found that the addition of small, high phosphorus additions, which dissolved rapidly in either the slag or metal allowed for the shortest transient period at the start of each experiment. For dephosphorization experiments, pure electrolytic iron and the experimental slag were allowed to equilibrate at the experimental temperature for 30 minutes. At that time, an addition of 2 to 4 grams of a Fe-9.5%P alloy was made to the metal. The ferrophosphorus addition was made by attaching the material to a 2 mm diameter pure iron wire, which was submerged through the slag layer to the bottom of the crucible until the wire and the ferrophosphorus melted. The experiment was judged to begin at the moment the iron wire began to collapse into the melt. For rephosphorization experiments, phosphorus additions were made to the slag in the form of a partially sintered calcium phosphate pellet. Experiments were judged to begin when the pellet was visually observed to melt into the slag phase. For both dephosphorization and rephosphorization experiments, the temperature of the slag and/or metal phase were observed to fluctuate by less than 10 °C at the time of addition.

Chapter 4

Results and Discussion

4.1 Metallographic Observations

Although the chemistries, densities, and other physical properties of the materials investigated in this study differ greatly, several common features were observed. The "gangue phase" is actually a complex mixture of several discrete oxide phases. Phosphorus was observed to be associated only with the oxide phases containing significant amounts of lime. In general, the oxide feature sizes observed in the two Midrex based materials were very small, generally less than 50 μm. The oxide particles found to contain measurable amounts of phosphorus were extremely small, usually less than 5μm. Figures 16 and 17 are micrographs of Midrex pellet materials, which were sectioned, polished, and observed via scanning electron microscopy.

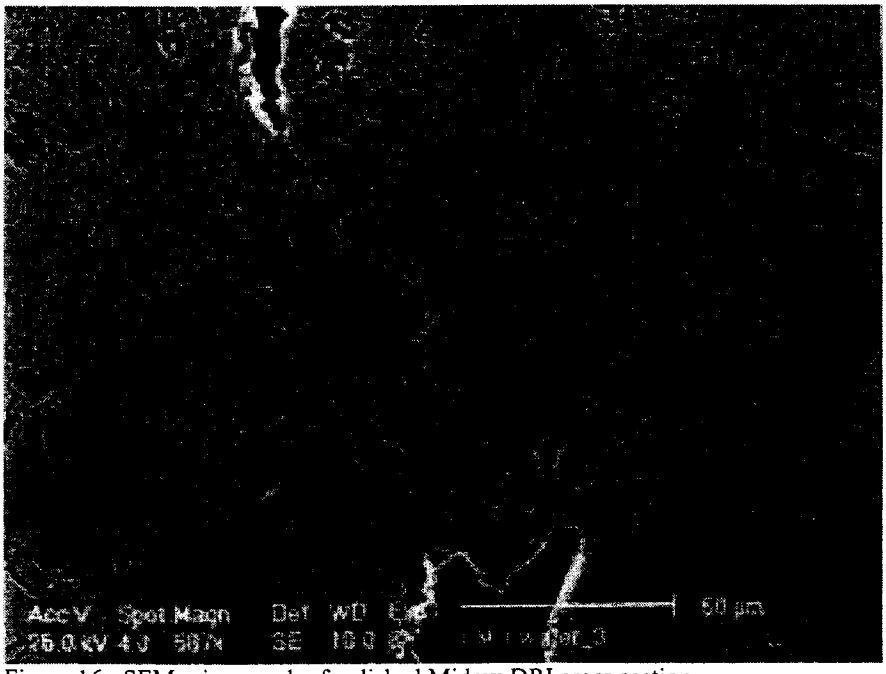

Figure 16: SEM micrograph of polished Midrex DRI cross section.

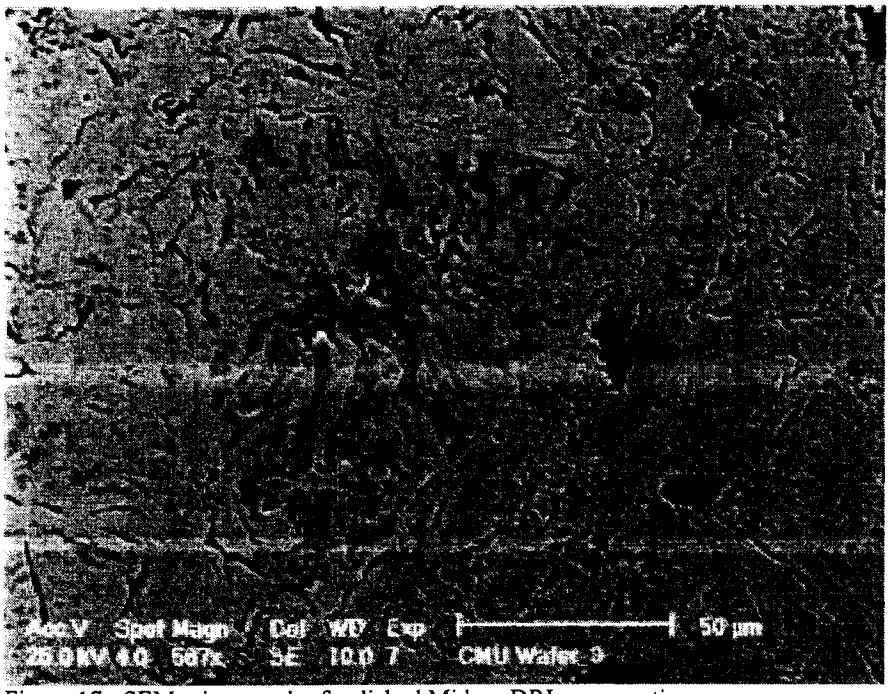

Figure 17: SEM micrograph of polished Midrex DRI cross section.

Figures 18 – 20 are micrographs of Midrex HBI material, which was sectioned, polished, and observed via scanning electron microscopy.

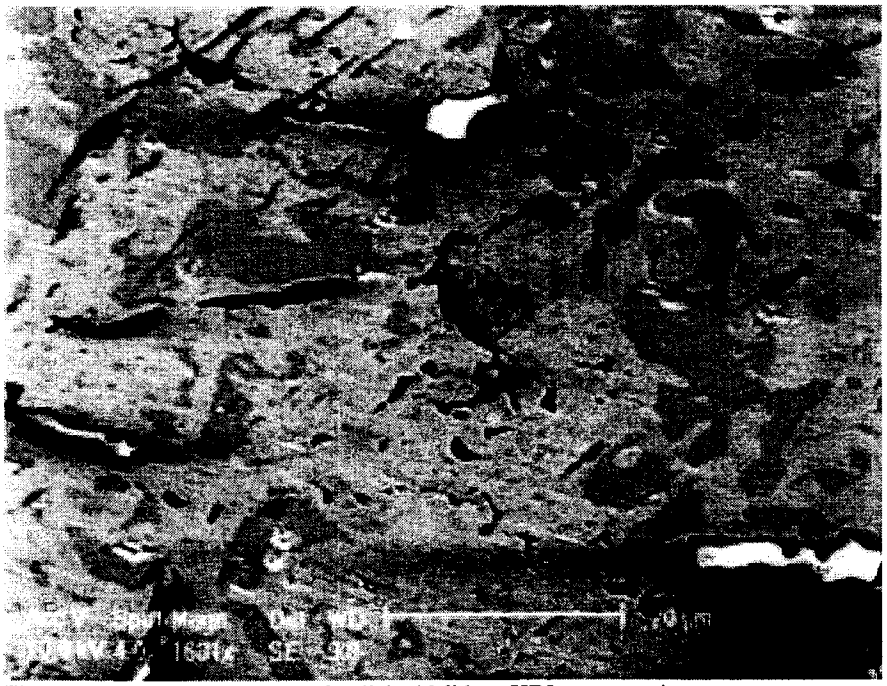
Figure 18: SEM micrograph of polished Midrex HBI cross section.

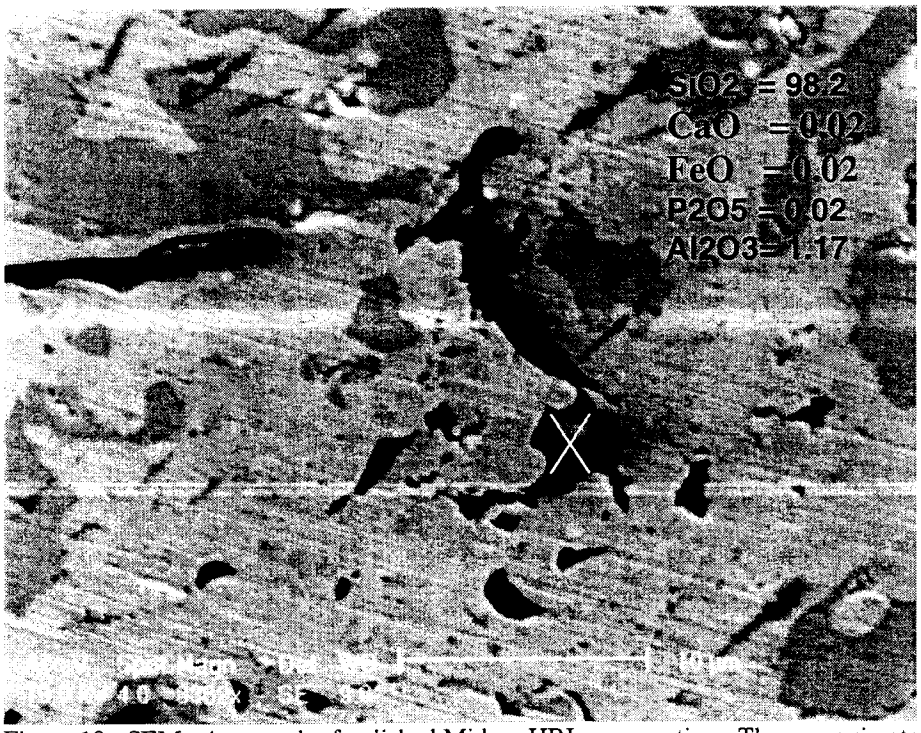

Figure 19: SEM micrograph of polished Midrex HBI cross section. The approximate chemical composition of the indicated oxide feature was measured via EDS.

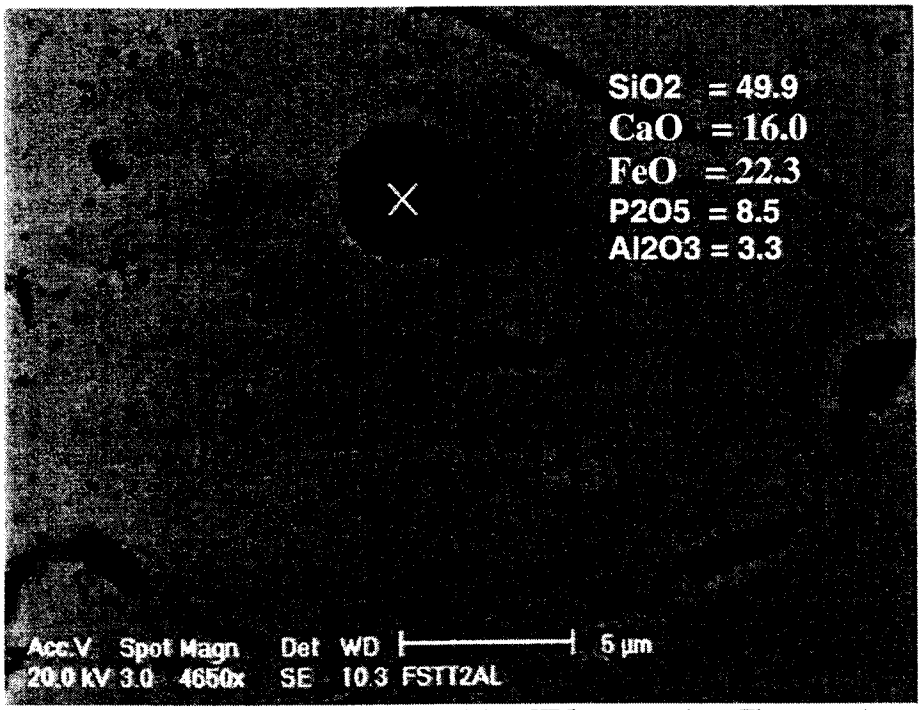

Figure 20: SEM micrograph of polished Midrex HBI cross section. The approximate chemical composition of the indicated oxide feature was measured via EDS.

For both the DRI and HBI materials examined, three general types of oxide features are observed in Figures 16 - 20:

1. The darker gray areas embedded in the lighter gray iron matrix were found to be primarily unreduced iron oxide.
2. The larger black particles, indicated in Figure 19, were primarily SiO_2 with only trace amounts of other oxides and no elevated concentration of phosphorus
3. The very fine oxide features, indicated in Figure 20, were found to be a mixture of several oxide components, including significantly elevated levels of phosphorus and lime.

Samples of BHP HBI produced via the Finmet process were also examined. Microstructurally, this material is very different than Midrex based materials. This is due to the fact that the Finmet process uses a series of fluidized beds to reduce ore fines. Alternatively, in the Midrex process, a combination of lump ore and pelletized ore are reduced in a shaft furnace. The Midrex pellets produced from pelletized ore were generally observed to have a very fine grain structure, whereas the briquetted fines based Finmet material exhibited a much courser structure. Figure 21 is optical micrograph of BHP HBI, which was sectioned and polished.

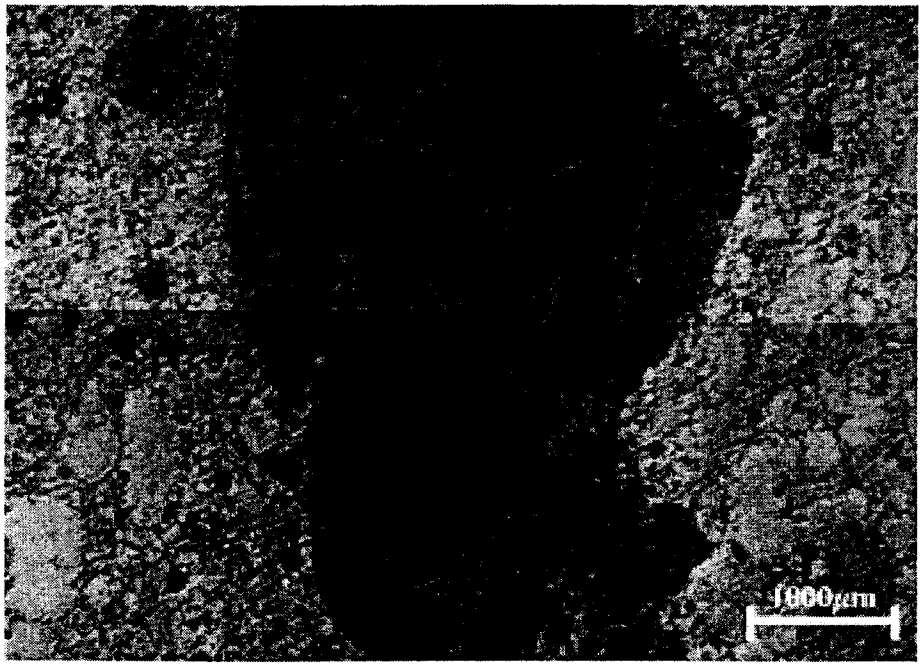

Figure 21: Optical micrograph of polished BHP HBI cross section.

Clearly, the largest gangue features observed in this material are on the order of thousands of microns as opposed to tens of microns as seen in Figures 16-20. However, when these very large particles are examined in closer detail in the SEM, one finds that they are in fact a composite of several oxide phases. Figure 22 is an SEM micrograph of the same sample of BHP-HBI. An approximate overall chemistry is listed for the large particle shown in the image as measured via the EDS unit of the microscope.

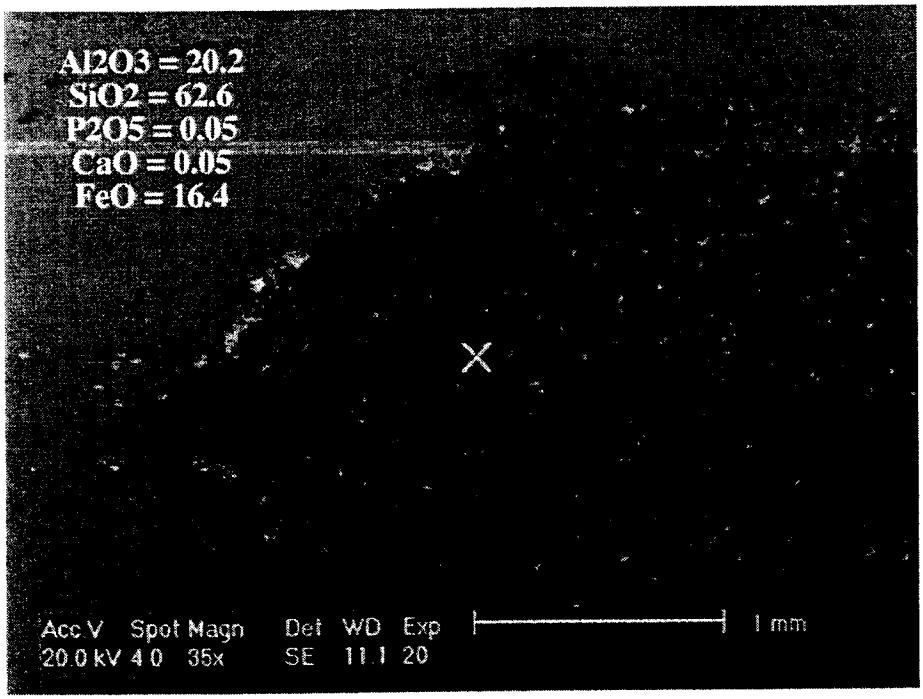

Figure 22: SEM micrograph of polished BHP HBI cross section.

As mentioned, this "macro" particle is actually a composite of various phases, thus the chemistry listed does not reflect the composition of a single specific phase. With the exception of these very large oxide features, which were not observed in pellet based materials, the finer gangue particles were similar to what was observed in the Midrex DRI and HBI. The larger and most common oxide features, excluding unreduced iron oxide, include a very high silica - alumina phase. One such particle is shown in Figure 23.

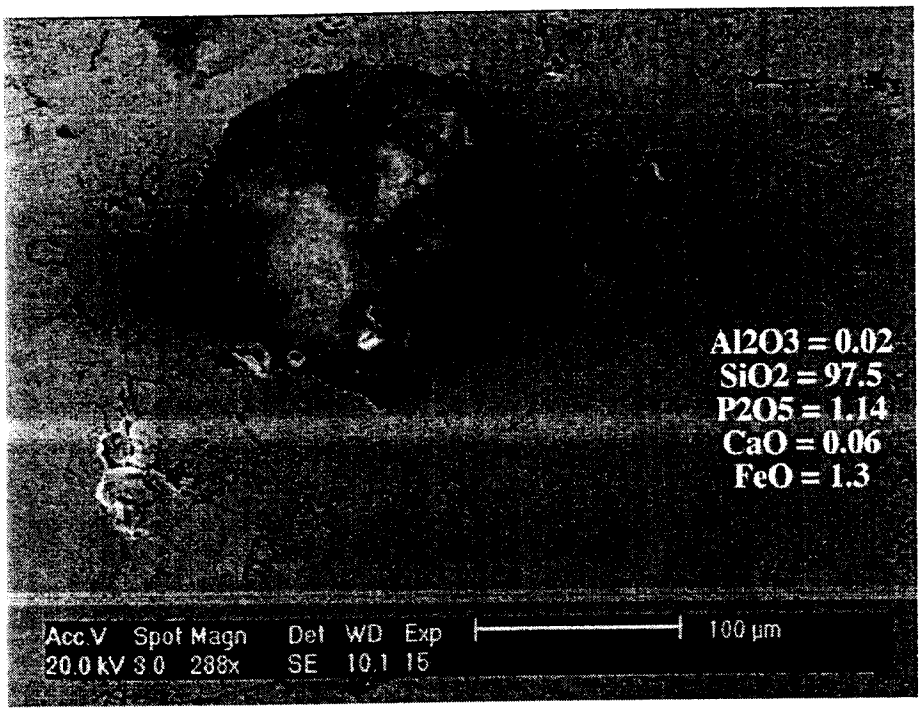

Figure 23: SEM micrograph of polished cross section of BHP HBI. The approximate composition of the large oxide feature was measured via EDS.

In general, these high silica particles, as well as the regions of unreduced FeO, and the "macro" composite particles do not appear to contain elevated levels of phosphorus as compared with the surrounding metal matrix. As with the Midrex based materials, particles containing significant amounts of phosphorus also exhibited much higher contents of lime, supporting the conclusion that the phosphorus in direct reduced materials is most likely in the form of a calcium phosphate phase. Although the high phosphorus particles identified in the BHP-HBI are 2 to 5 times larger than those identified in the pellet based materials, even the largest of these particles were no larger than 50 microns in diameter. A typical high phosphorus particle found in the BHP-HBI material and the approximate chemical composition of the particle is shown below in Figure 24.

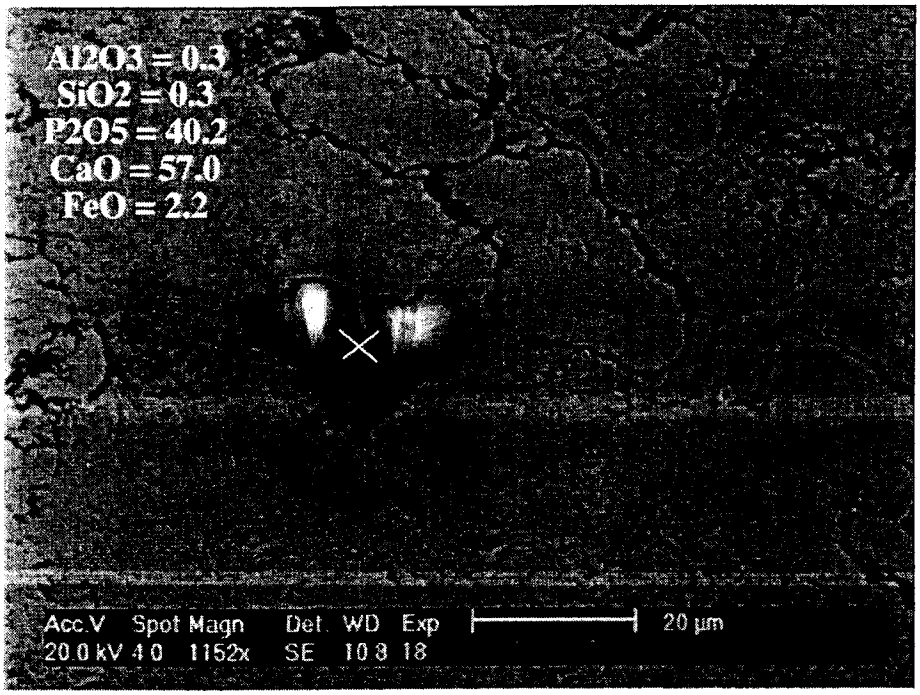

Figure 24: SEM micrograph of polished cross section of BHP HBI. The approximate composition of the large oxide feature was measured via EDS.

It should be noted that the various discrete phases observed in the solid state are unlikely to separate from the metallic iron phase as discrete particles.. The CaO-P_2O_5 pseudo-binary system exhibits phases, which melt well below 1200°C. The FeO rich side of the FeO-SiO_2 system also contains low melting phases. During controlled melting experiments reported below, first melting was observed to occur at 1100°C or less. For the most part, the various discrete oxide phases contained in DRI/HBI material are loosely connected by strings of unreduced or reoxidized FeO. It is unlikely that a gangue particle of the chemistry shown in Figure 24 would still exist as a discrete phase at the time of bulk melting.

4.2 Fast Melting Experiments

The results of fast melting experiments with six commercial DRI and HBI materials are shown in Figure 25.

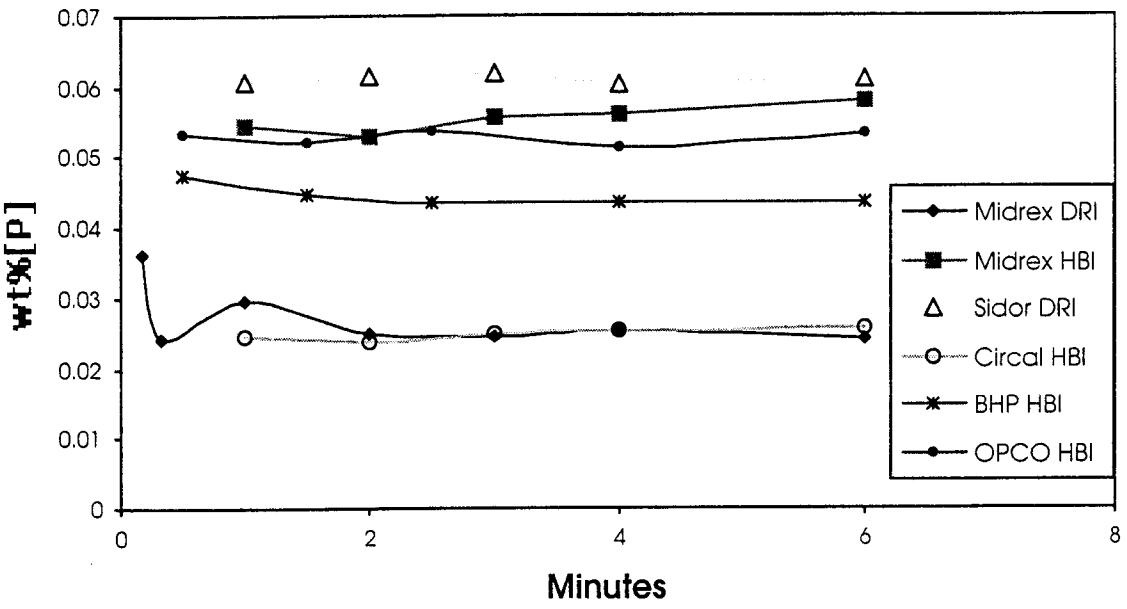

Figure 25: Results of fast melting experiments with six commercial DRI and HBI materials.

Table 1 from Section 3.1 listing the chemical compositions of the materials used in the fast melting experiments is shown again below:

Table 1: Chemical Composition of Investigated Commercial Materials

Material	Method of Reduction	Fe_t	FeO	C	SiO_2	Al_2O_3	CaO	P
Midrex DRI	Midrex	93.13	5.87	1.89	1.92	---	1.59	0.028
Midrex HBI	Midrex	92	10	< 0.5	1.8	---	---	0.06
BHP - HBI	Finmet	92	8	1.3	1.6	---	0.1	0.045
Circal HBI	Circored	97	12	0	1.03	0.32	---	0.028
Sidor DRI	Midrex	93.76	7.6	>3	1.67	---	2.11	0.054
Opco HBI	Midrex	91.5	8.4	0.8	~2	---	---	0.053

If the data in Figure 25 are compared with the total phosphorus values for each material (shown in Table 1) it is clear that nearly all the phosphorus is transferred from the gangue to the metal in less than a minute after melting. Furthermore, only modest fluctuations in the metal phosphorus occur at times longer than a minute.

The reason for this rapid reversion can be better understood by making some fundamental calculations. The metallographic investigation of DRI/HBI indicated that the oxide gangue features are on the order of tens of microns or less in dimension.

Therefore, the area of contact between the gangue particles and the surrounding iron matrix is enormous. An extremely conservative estimate of this area of contact can be calculated based on the mass fractions of metal and oxide provided by chemical analysis and assuming a dispersion of spherical oxide particles 50 microns in diameter. The assumption of spherical gangue particles significantly underestimates the contact area as this geometry represents the lowest possible surface area to volume ratio. Such a very conservative calculation predicts an area of contact on the order of 120 cm^2/cm^3 of HBI material or roughly 600 cm^2/gram of HBI. This estimate of metal - oxide interfacial area, combined with calculated estimates for the equilibrium phosphorus distribution for the gangue material (Lp ~1) and the overall mass transfer coefficient (ko~10^{-3}), can be used in the kinetic model derived later in this paper to predict an equilibration time of significantly less than one second. Based upon these approximations, Figures 26 and 27 show the calculated change in metal and gangue phosphorus levels respectively assuming all of the phosphorus is initially contained in the gangue phase.

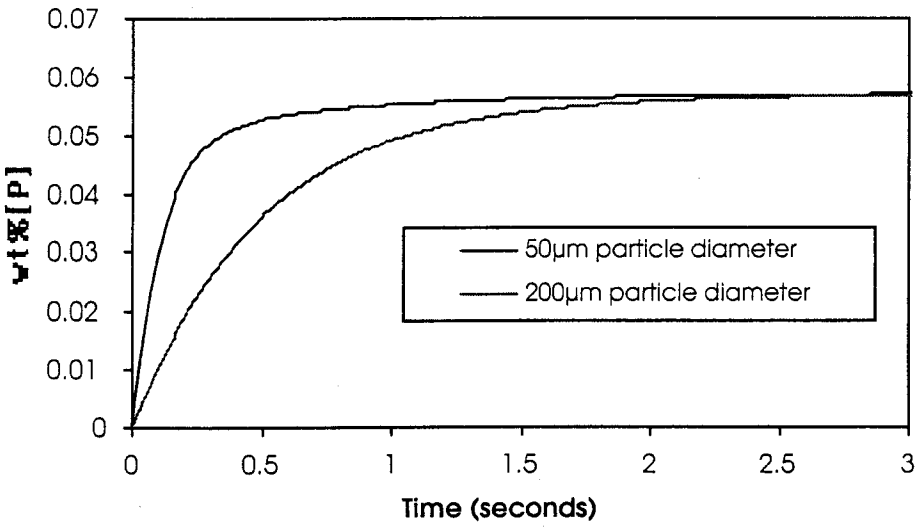

Figure 26: Calculated metal phosphorus content versus time assuming a liquid phase mass transfer controlling model.

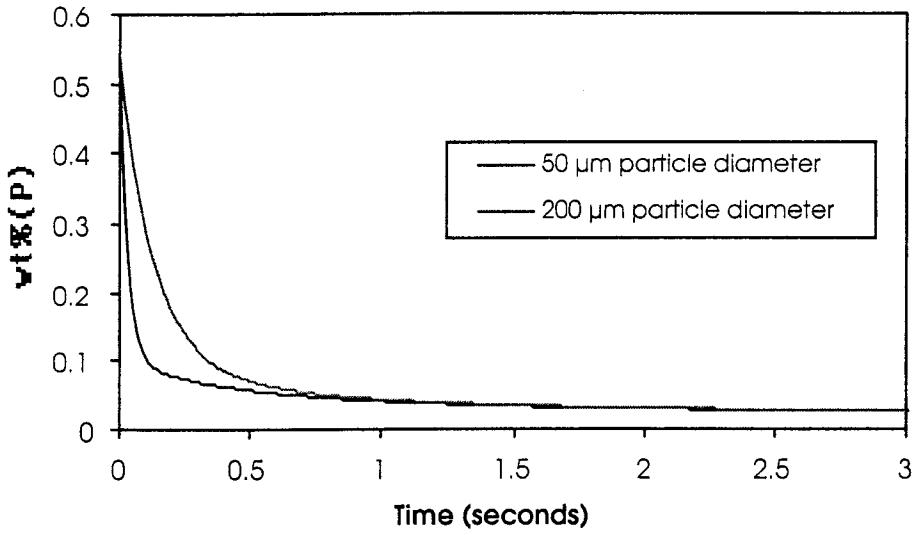

Figure 27: Calculated gangue phosphorus content versus time assuming a liquid phase mass transfer controlling model.

In Figures 26 and 27 two cases were modeled, assuming:

1. An average gangue particle size of 50 µm.
2. And, an average gangue particle size of 200 µm.

These calculations agree with the experimental observation that all of the phosphorus is transferred from the gangue phase to the metal within the time scale required for melting.

Fast melting experiments in which a liquid slag was present were conducted with the Circal and BHP – HBI materials. Figure 28 shows the results of a fast melting experiment where 30 grams Circal was added to 15 grams of liquid magnesia saturated liquid slag with a basicity of 1 and zero initial iron oxide at 1600°C.

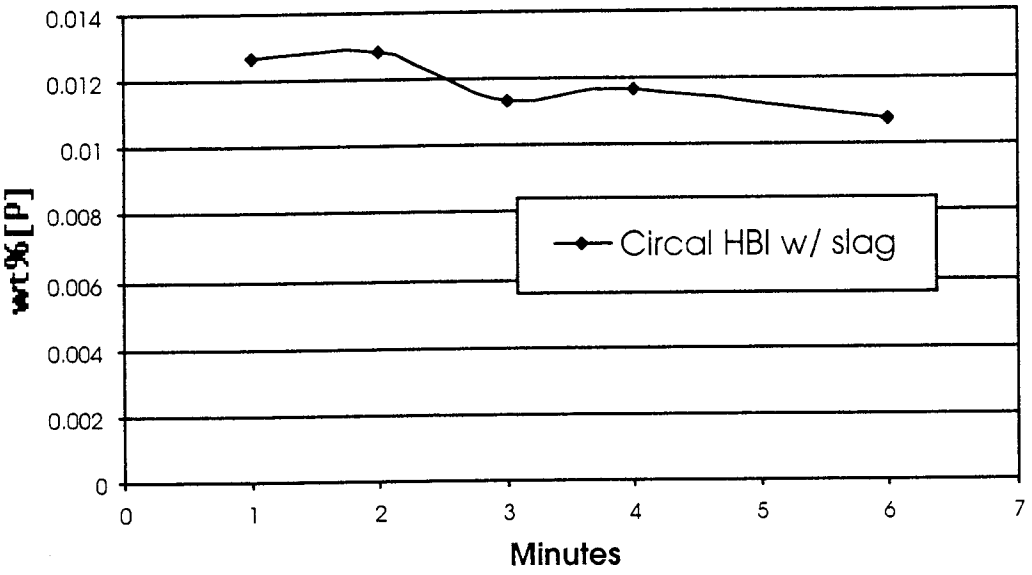

Figure 28: Metal phosphorus as a function of time for Circal HBI melted into a magnesia saturated liquid slag with basicity =1 at 1600°C.

The results shown in Figure 28 are very interesting for several reasons. Because this material contains no carbon, the FeO contained in this material reported to the slag generating a slag with some phosphorus capacity. The indication of the data is that phosphorus transfer kinetics are fast in this system and that the system is near equilibrium in under 1 minute. The data suggest that the phosphorus is slightly decreasing with time. This would imply that full reversion occurs simultaneously with melting and that the phosphorus is then transferred from the metal to the slag until equilibrium is approached (or the experiment is terminated.)

The results of the fast melting experiments with the BHP – HBI material in slag are shown in Figures 29.

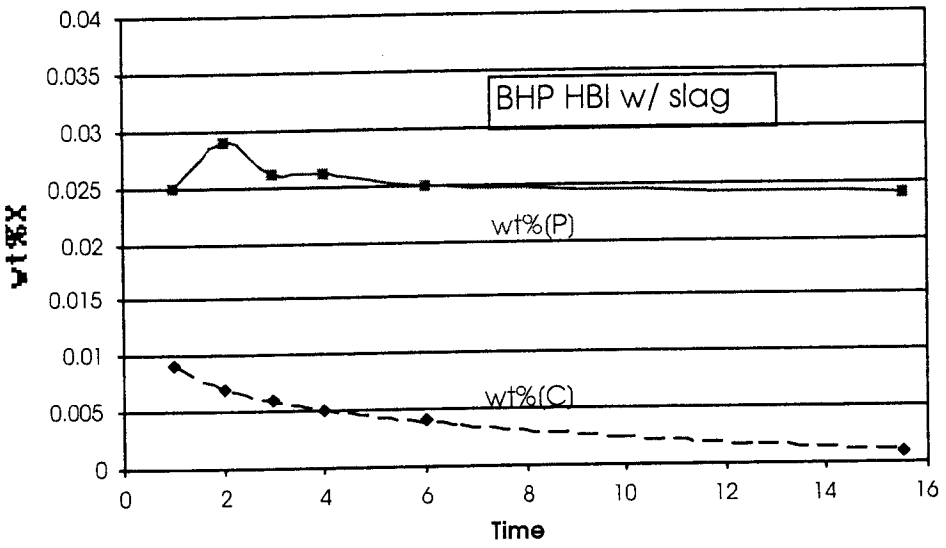

Figure 29: Metal phosphorus as a function of time for BHP - HBI melted into a magnesia saturated liquid slag with basicity =1 at 1600°C.

At the time of the experiment shown in Figure 29, the degree of metallization of the BHP material had degraded somewhat from the time at which chemical analysis in Table 1 was completed. Therefore, the 1.38wt% carbon contained in the material was not sufficient to consume all of the iron oxide present. Therefore, like the Circal material, the BHP – HBI contributed some FeO to the liquid slag upon melting, generating a slag with some phosphorus capacity. As was seen with the Circal material, roughly half of the phosphorus in the material had transferred to the slag by the time of the final sample.

The metal samples from the experiment in Figure 29 were also analyzed for carbon. The data from the experiment with the BHP material indicate that by the time of the first sample 99% of the carbon contained in the material has been consumed. The continued reaction between the remaining carbon and the FeO in the slag is apparent in the data.

The results of the fast melting experiments with the modified Circal material to which lime was added are shown below in Figure 30.

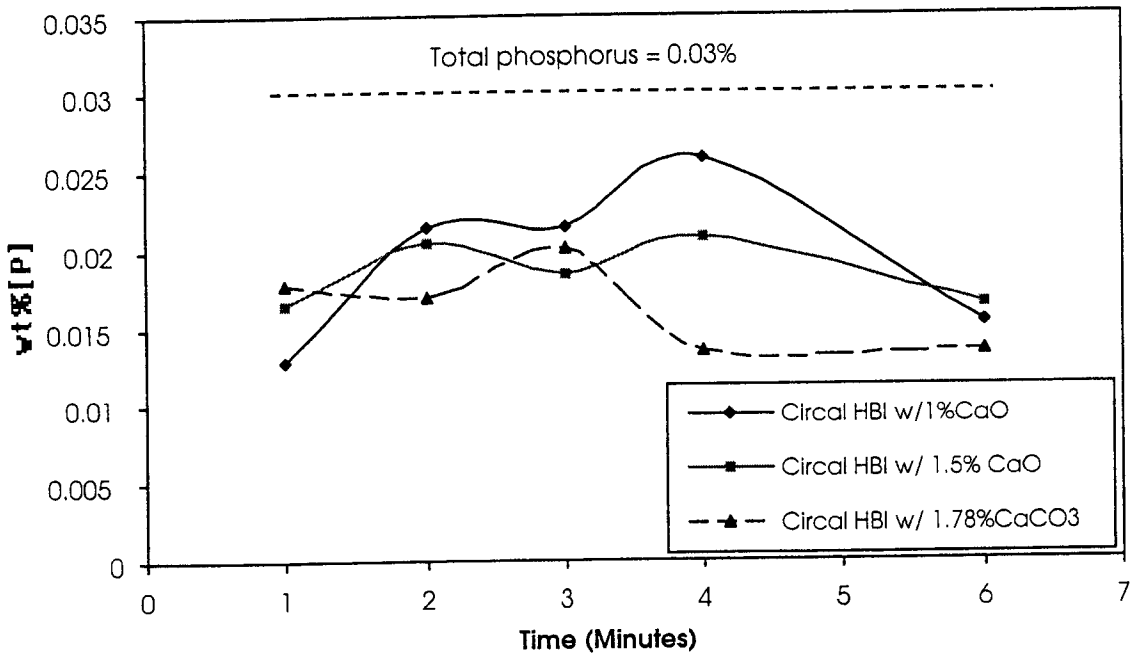

Figure 30: Fast melting experiments with Circal HBI with additions of 1 % and 1.5 % CaO and 1.78% $CaCO_3$.

As the Circal material contains approximately 1wt% silica, additions of 1 wt% CaO and 1.5 wt% CaO should have resulted in a gangue chemistry with a V-ratio of 1 and 1.5 respectively. The 1.78% $CaCO_3$ should have given the molar equivalent of 1% CaO. None of these additions were found to significantly affect the metallic iron yield of the HBI (around 86%.)

There are several interesting results in the data of Figure 30.

1. Small additions on the order of 1 % cut the melt-in metal phosphorus in half.
2. Although the both the Sidor and Midrex DRI materials exhibit gangue chemistries with V-ratios greater than 1 (see Table 1) the carbon in these materials consumes the residual iron oxide upon melting. The resultant gangue upon melting contains almost no iron oxide and will therefore have a very low phosphorus capacity.
3. The data in Figure 30 show a lot of scatter. This is because a high phosphorus gangue actually forms when enough lime is added to give the gangue some phosphorus capacity. Small amounts of gangue entrained in metal samples strongly affected the analysis.
4. There appears to be little difference whether the lime is added in the form of CaO or $CaCO_3$. The compromise presented with $CaCO_3$ is that a greater mass of material is required for the same number of moles of Ca.

5. There also seems to be little difference between the experiments with additions of 1% and 1.5% CaO. This is most likely due to the fact that, in the case of the Circal material the gangue, which is formed will be more than 80% FeO. At such a high iron oxide contents, small shifts in the V-ratio will have much less of an effect on phosphorus equilibrium than is normally expected.

The use of prefluxed or basic ore pellets in Midrex type reactors or the addition of small amounts of lime into fines based reactors may represent a simple and cost effective way of controlling the phosphorus in direct reduced materials. However, in materials with very high carbon content, the effect upon melt-in phosphorus will be negligible. Although, the metallic yield of a fluxed material will be reduced by 1 or 2%, several benefits may be generated by the added components. Most electric furnace producers modify their standard furnace flux practice when using large amounts of DRI/HBI to account for the additional silica in the material. A DRI/HBI material, which melts in with a gangue chemistry similar to the target slag chemistry, is more easily substituted in to the standard scrap melting practice. Furthermore, large flux additions in the form of lime or dolomite often dissolve slowly in the furnace and may not be effective in controlling the furnace chemistry until late in the heat. Lime contained within DRI or HBI will melt-in far more quickly than top charged lime and may generate a good steelmaking slag more efficiently than conventional fluxing practices. Ultimately, a pre-fluxed material would reduce the number of operating variables when using DRI, guaranteeing greater consistency in the furnace slag chemistry from heat to heat and during individual heats. Greater consistency offers many operational benefits, which will not be elaborated upon here.

4.3 Controlled Melting Observations

Several important observations were made based on the controlled melting experiments:

1. First melting of the oxide gangue phase occurs long before the melting temperature of the bulk metal phase is approached. First melting has been observed to occur on a microscopic scale at approximately 1050°C for the HBI material. A liquid phase can be observed on a macroscopic scale at approximately 1200°C. Most or all of the oxide phase appears to be molten at approximately 1350°C.
2. The molten gangue appears to react with the surrounding metal to form a gaseous product at temperatures as low as 1050°C. This can be verified by the formation and release of bubbles in the liquid oxide phase.
3. When the material is heated slowly (10 - 20°/min) from 1000 °C to the metal melting temperature at approximately 1530°C, the reaction between the metal and gangue appears to be complete before the sample reaches 1200°C. When the sample is heated rapidly (50 - 100°/min), the reaction resulting in bubble formation in the gangue continues until the entire sample is molten.

The analytical software package Thermocalc was also used to model the melting behavior of an oxide phase with a chemistry representative of DRI/HBI gangue. The model predicted first melting to occur at 1051°C and complete melting to occur at 1233°C. This prediction is supported by the above mentioned physical observations. These findings are of interest as they may offer a possible mechanism by which gangue – metal separation might occur during an EAF heating cycle. When melted in the presence of a liquid slag phase, the phosphorus in the low melting gangue might be physically "captured" and diluted in the slag phase long before bulk melting of the metal phase occurred. Both the driving force and kinetics of reversion from a bulk slag to the metal would be reduced as compared with the direct reaction between the gangue and metal. However, the efficiency of the escape of the gangue from the solid metal matrix is controlled by several factors:

1. The inter-connectivity of the oxide phase within the metal matrix.
2. The driving force for phase separation, both surface tension effects and gas pressure from internal reaction within the material.
3. The precise melting temperatures of both the oxide and the metal phases.

In spite of the above arguments, the results of the fast melting experiments with and without a liquid slag present suggest that the achieved degree of gangue separation at low temperatures is not sufficient to result in significantly reduced metal phosphorus levels at the time of bulk melting.

4.4 Kinetics of Phosphorus Transfer

4.1.1 Mathematical Model of Phosphorus Transfer – In order to evaluate the experimental results, it is necessary to introduce the framework of the mathematical model used in this study to describe the kinetics of phosphorus transfer. Most recent literature is in agreement that the slag-metal phosphorus reaction is correctly expressed in the form:

$$[P]+\frac{5}{2}[O]+\frac{3}{2}(O^{-2})=(PO_4^{-3}) \qquad 33$$

Where [ ] indicates metal phase and ( ) indicates slag phase. The thermodynamics of phosphorus transfer was discussed in detail in Section 2.2. If this reaction is accepted, several possible rate controlling steps become apparent. In the case of dephosphorization these steps include:

1. Metal phase mass transfer of [P] to the slag metal interface
2. Metal phase mass transfer of [O] to the slag metal interface, or supply of [O] from the slag to the interface via the reaction: **(FeO) = Fe + [O]**
3. Slag phase mass transfer of (O^{2-}) to the interface
4. Slag phase mass transfer of the (PO_4^{-3}) away from the interface
5. Chemical reaction of the formation of (PO_4^{-3}).

The possible rate limiting steps of rephosphorization are obviously linked, differing only in the direction of the transferred species and the dissociation rather than the formation of (PO_4^{-3}). Based upon the fact that most slag - metal chemical reactions are rapid at high temperatures, most previous researchers have assumed the kinetics of phosphorus transfer to be limited by liquid phase mass transfer. Since [O] can be supplied to the interface both from the bulk metal and via the dissociation of FeO at the slag-metal interface, it is most likely that the kinetics of phosphorus oxidation are limited by the mass transfer of

phosphorus either in the slag or in the metal. Previous researchers have shown that the oxidation of phosphorus from high carbon iron via a highly oxidized slag is possible. [44-47] This suggests that the oxygen potential of the interface is controlled by the slag phase and that the rate of oxygen delivery to the interface by the slag is faster than the rate of mass transfer in the metal phase. As a result, it is likely that the kinetics of phosphorus transfer are controlled by mass transfer of phosphorus in the slag, metal, or both phases. The results of previous researchers are divided as to whether mass transfer in the slag or metal is the rate controlling step. This is due to the fact that it is experimentally difficult to separate the individual effects of mass transfer in the two phases. Therefore, it was initially assumed that phosphorus transfer between the slag and metal is controlled by liquid phase mass transfer in both phases.

Several analytical and numerical models of phosphorus transfer have been developed by other researchers and were discussed within the literature review of this study. For this study, kinetic expressions for phosphorus transfer from slag to metal and metal to slag were developed based upon liquid phase mass transfer correlations developed for sulfur transfer by Fruehan [4] and others.

In order to account for the effects of mass transfer in both the slag and the metal an overall mass transfer coefficient, ko, must be defined. Assuming that phosphorus is conserved within the slag-metal system, the flux of phosphorus out of the metal must equal the flux into the slag and vise versa. This can be expressed mathematically as:

$$\frac{\partial(\%P)}{\partial t} W_s = -\frac{\partial[\%P]}{\partial t} W_m \qquad 34$$

Where the flux equations for phosphorus in the metal and the slag are respectively:

$$\frac{\partial[\%P]}{\partial t} = -\frac{A\rho_m k_m}{W_m}\left[[\%P^i]-[\%P]\right] \qquad 28$$

$$\frac{\partial(\%P)}{\partial t} = -\frac{A\rho_s k_s}{W_s}\left[(\%P)-(\%P^i)\right] \qquad 29$$

Then equations 28,29, 34 can be combined to give:

35

$$\rho_s k_s \left[(\%P) - (\%P^i)\right] = \rho_m k_m \left[[\%P] - [\%P^i]\right]$$

Within the liquid phase mass transfer model, it is assumed that the chemical reaction is fast. Therefore, the phosphorus contents of the slag and metal at the interface are given by the equilibrium phosphorus distribution ratio, according to:

$$(\%P^i) = L_P[\%P^i] \qquad 36$$

By combining equations 34 and 35, it is possible to solve for $[\%P^i]$ as a function of the bulk concentrations:

$$[\%P^i] = \frac{\rho_m k_m [\%P] + \rho_s k_s (\%P)}{\rho_m k_m + \rho_s k_s L_P} \qquad 37$$

If this definition of $[\%P^i]$ is put back into the flux equation for phosphorus in the metal:

$$\frac{\partial[\%P]}{\partial t} = -\frac{A\rho_m k_m}{W_m}\left[[\%P] - \frac{\rho_m k_m [\%P] + \rho_s k_s (\%P)}{\rho_m k_m + \rho_s k_s L_P}\right] \qquad 38$$

Equation 38 can be simplified and rearranged to give the result:

$$\frac{\partial[\%P]}{\partial t} = -\left(\frac{A\rho_m}{W_m}\right)\frac{1}{\left(\frac{\rho_m}{k_s \rho_s L_p} + \frac{1}{k_m}\right)}\left[[\%P] - \frac{(\%P)}{L_P}\right] \qquad 39$$

Equation 39 suggests that an overall mass transfer coefficient, ko, can be defined such that:

$$k_o = \frac{1}{\left(\frac{\rho_m}{k_s \rho_s L_p} + \frac{1}{k_m}\right)} \qquad 40$$

As defined by equation 40, ko has the units of cm/s. A similar exercise can be performed to arrive at and expression for the flux in the slag phase:

$$\frac{\partial(\%P)}{\partial t} = -\left(\frac{A\rho_s}{W_s}\right)\frac{1}{\left(\frac{1}{k_s} + \frac{L_p \rho_s}{k_m \rho_m}\right)}\left[(\%P) - [\%P]L_P\right] \qquad 41$$

In this case, ko, is defined as:

$$k_o = \frac{1}{\left(\frac{1}{k_s} + \frac{L_p}{k_m}\frac{\rho_s}{\rho_m}\right)} \qquad 42$$

The two definitions for ko expressed in equations 40 and 42 differ by the ratio of the densities of the metal and slag. Although it is a nuisance to have two definitions for ko, it is necessary to maintain the units of ko as cm/s. Because the independent contributions of the slag and metal mass transfer coefficients are difficult to separate experimentally, the flux equations for phosphorus in the slag and metal will generally be expressed in terms of an overall mass transfer coefficient in the present work.

Under some conditions, it is possible to obtain an analytical solution to the flux equations for phosphorus in the slag and/or metal. The phosphorus content of the metal and slag are related through the mass balance:

$$\left[(\%P) - (\%P^0)\right] = -\left[[\%P] - [\%P^0]\right]\frac{W_m}{W_s} \qquad 43$$

For the rephosphorization experiments of this study, the initial metal phosphorus [$\%P^0$] level will be essentially zero. Thus, equation 43 can be combined with equations 41 and 42 such that:

$$\frac{\partial(\%P)}{\partial t} = -\frac{A\rho_s k_o}{W_s}\left[(\%P) - \left[(\%P^0) - (\%P)\right]\frac{L_p W_s}{W_m}\right] \qquad 44$$

And then integrated to produce an expression, which computes **(%P)** as a function of time:

$$-\frac{A\rho_s k_o}{W_s}t = \frac{1}{1+\frac{L_p W_s}{W_m}}\ln\left[\left(1+\frac{L_p W_s}{W_m}\right)\frac{(\%P)}{(\%P^0)} - \frac{L_p W_s}{W_m}\right] \qquad 45$$

An equivalent expression for dephosphorization can also be developed. In the case of phosphorus transfer from metal to slag, the expression takes the form:

$$-\frac{A\rho_m k_o}{Wm}t = \frac{1}{1+\frac{W_m}{L_p W_s}}\ln\left[\left(1+\frac{W_m}{L_p W_s}\right)\frac{[\%P]}{[\%P^0]} - \frac{W_m}{L_p W_s}\right] \qquad 46$$

From this equation, the metal phosphorus level can be calculated directly as a function of time. Within the solution of equation 45 and 46 it is assumed that neither the mass transfer coefficient, ko, nor the interfacial area, A, are functions of time or concentration. However, it will be shown in the experimental results of this work and of previous studies, that either A or ko do vary as a function of time. This point will be discussed in the following section.

Figures 31 and 32 show metal phosphorus and slag phosphorus levels versus time as calculated by the above equations for conditions, which are relevant to this study.

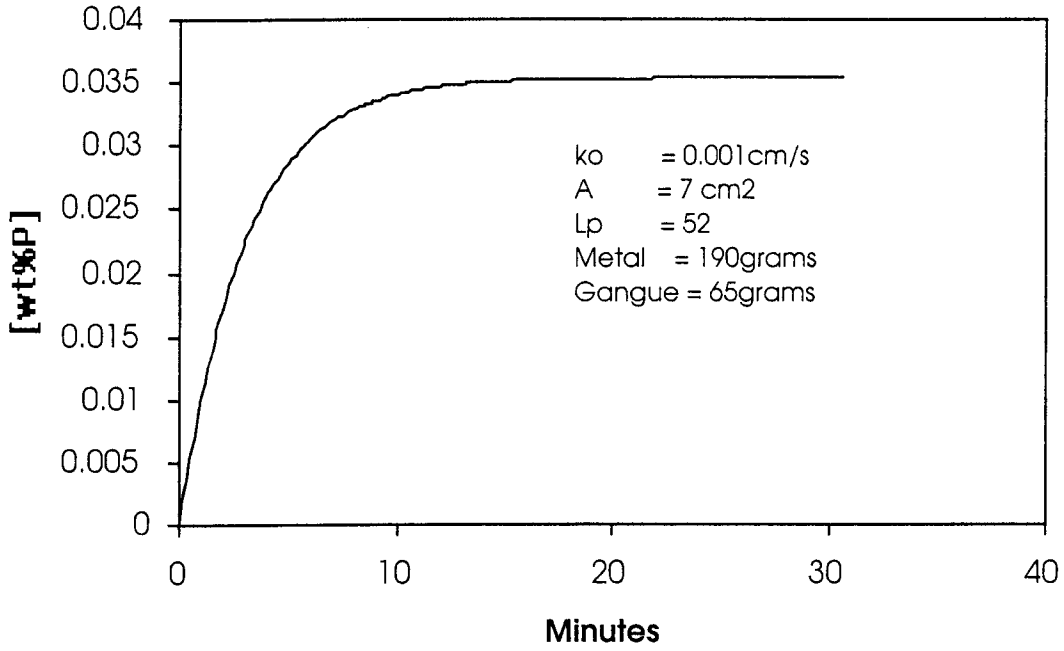

Figure 31: Calculated metal phosphorus versus time for the experimental parameters of this study assuming an overall mass transfer coefficient equal to 0.001cm/sec.

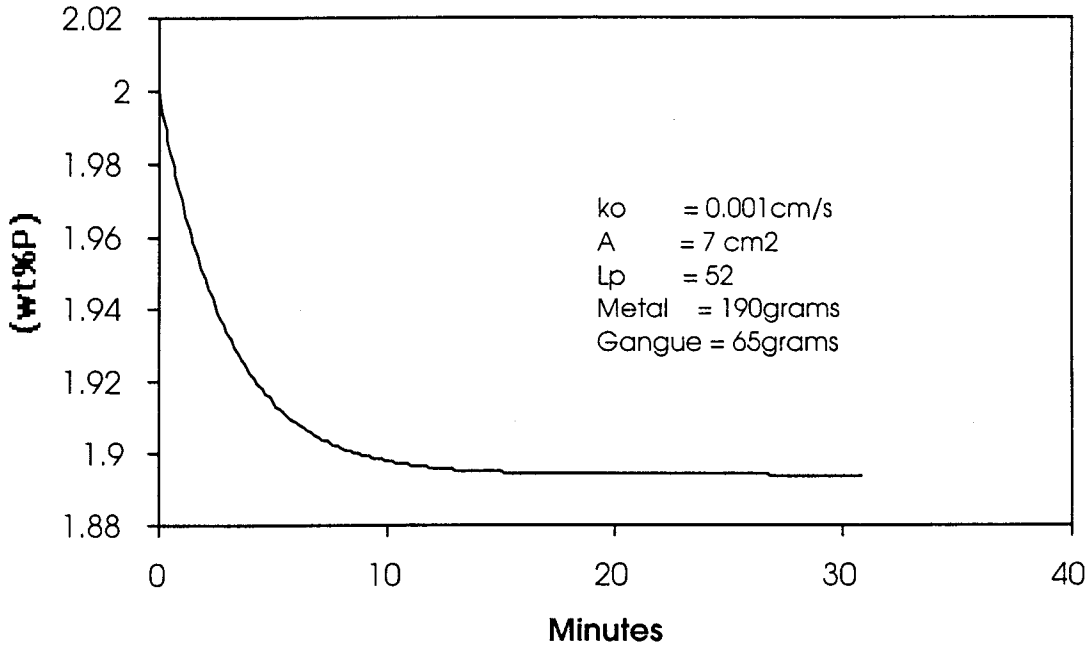

Figure 32: Calculated slag phosphorus versus time for the experimental parameters of this study assuming an overall mass transfer coefficient equal to 0.001cm/sec.

Equations 45 and 46 are also very useful for analyzing experimental data. When slightly rearranged as shown below:

$$-Ak_o t = \frac{W_s}{\rho_s} \frac{1}{1+\frac{L_p W_s}{W_m}} \ln\left[\left(1+\frac{L_p W_s}{W_m}\right)\frac{(\%P)}{(\%P^0)} - \frac{L_p W_s}{W_m}\right] \qquad 47$$

And:

$$-Ak_o t = \frac{Wm}{\rho_m} \frac{1}{1+\frac{W_m}{L_p W_s}} \ln\left[\left(1+\frac{W_m}{L_p W_s}\right)\frac{[\%P]}{[\%P^0]} - \frac{W_m}{L_p W_s}\right] \qquad 48$$

All of the driving force or constant terms can be isolated to the right hand side or RHS of these kinetic expressions. When this RHS of equation 47 is plotted versus time, the result should be a straight line with a constant slope equal to **koA.** This product has been previously termed the "mass transfer parameter."[4] It is often necessary to group the interfacial area and the mass transfer coefficient together in this way, because it can be very difficult to calculate either term independently under some experimental conditions. Specifically, under circumstances where significant slag-metal intermixing or emulsification occurs, it is impossible to calculate a meaningful interfacial area.

In previous evaluations of steelmaking vessels, the entire term:

$$\frac{A\rho_m k_o}{W_m} \qquad 49$$

has also been used a convenient kinetic parameter. In oxygen steelmaking vessels, the oxygen blowing rate often scales linearly with the size of the vessel or the weight of the contained metal, W_m. Also, both the slag-metal area, A, due to intermixing and the mass transfer coefficient, ko, tend to increase with increasing blowing rate. Therefore, the term expressed in equation 49 remains relatively constant for different oxygen steelmaking vessels of varying size. However, this balancing relationship between reactor size and gas usage is not expected to hold for electric arc furnace vessels, and may be less useful

in describing this system. The term in equation 49 has the units of reciprocal time and is very similar to a reaction rate constant. Defining this term as a 'mass transfer rate constant,' however, is an inaccurate description of the properties of the parameter as it likely to vary significantly as a given furnace heat proceeds. During both oxygen steelmaking and electric arc furnace steelmaking the physical conditions, which influence equation 49, i.e. the stirring conditions, slag-metal area, and liquid slag and metal masses, are functions of time during any given heat. Therefore, the term in equation 49 should not be expected to remain constant for the duration of an entire heat.

4.4.2 Laboratory Kinetic Experiments

A large number of dephosphorization and rephosphorization experiments were conducted. Early dephosphorization experiments were conducted by a slightly different technique than the standard method described in Chapter 3. Initially, an Fe-0.6%P alloy and a slag containing no iron oxide were melted and allowed to equilibrate at the experimental temperature. In theory, a slag containing no iron oxide should have a phosphorus partition ratio near zero. The experiments were initiated when an addition of FeO was made to the slag, thus increasing Lp. The large slag addition required for these experiments raised some concerns regarding the transient period near the beginning of the experiments. However, some reproducible results were obtained. Below, Figures 33, 34, and 35 show the results of three dephosphorization experiments plotted as weight percent phosphorus in the metal versus time. The continuous curve shown in the plot was calculated via equation [46] for the experimental conditions assuming a best fit ko.

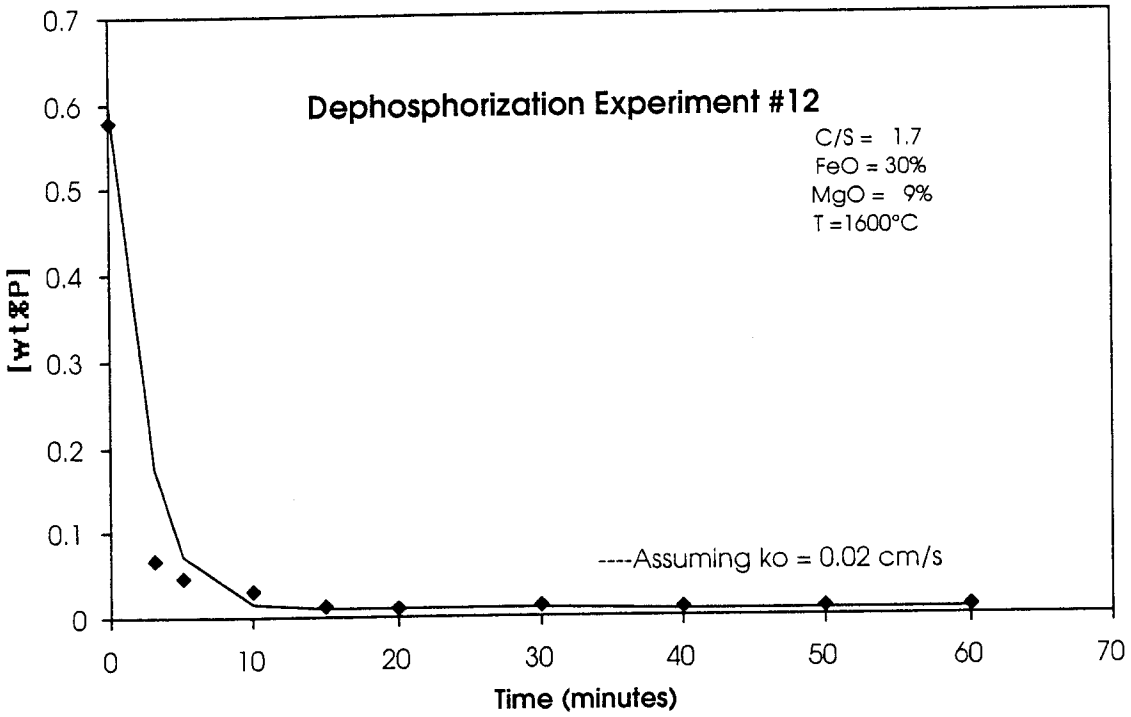

Figure 33: Metal phosphorus versus time for dephosphorization experiment #12. Continuous curve calculated via equation [46] assuming a best fit ko.

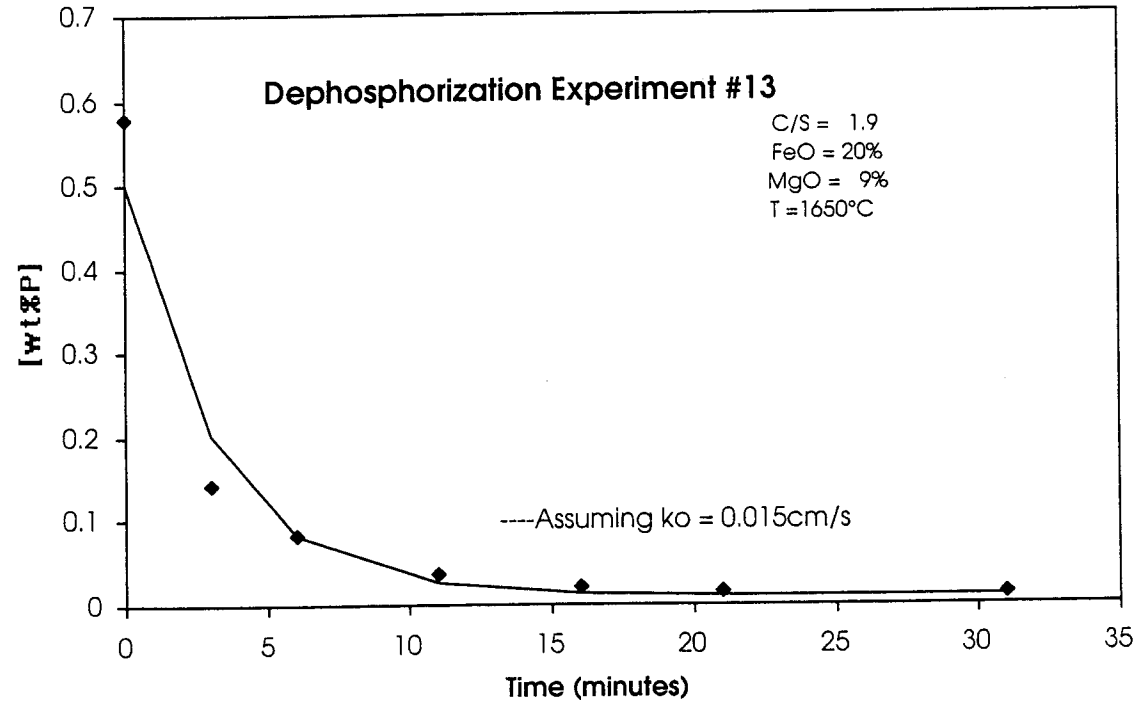

Figure 34: Metal phosphorus versus time for dephosphorization experiment #13. Continuous curve calculated via Equation [46] assuming a best fit ko.

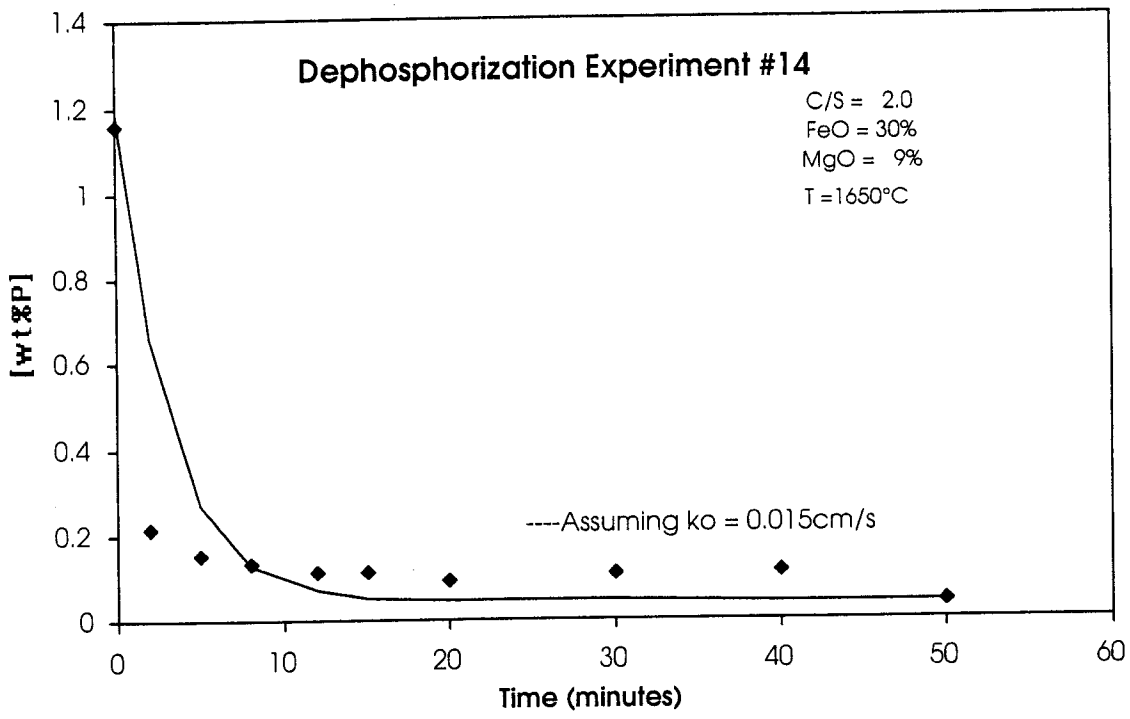

Figure 35: Metal phosphorus versus time for dephosphorization experiment #14. Continuous curve calculated via Equation [46] assuming a best fit ko.

These three experiments (12 – 14) are typical of the general trends, which were observed for early experiments. The relatively high initial metal phosphorus level decreased quickly. After 10 to 15 minutes, very little phosphorus transfer was observed. This initial fast rate followed by a slower rate of phosphorus transfer is consistent with the results of Mori et al. [34] In Figures 36 – 38, the data from experiments 12-14 are replotted as the right hand side, RHS, of equation [48] versus time. Therefore, the slope of the data in these RHS versus time plots is equal to the mass transfer parameter A*ko with the units cm^3/s

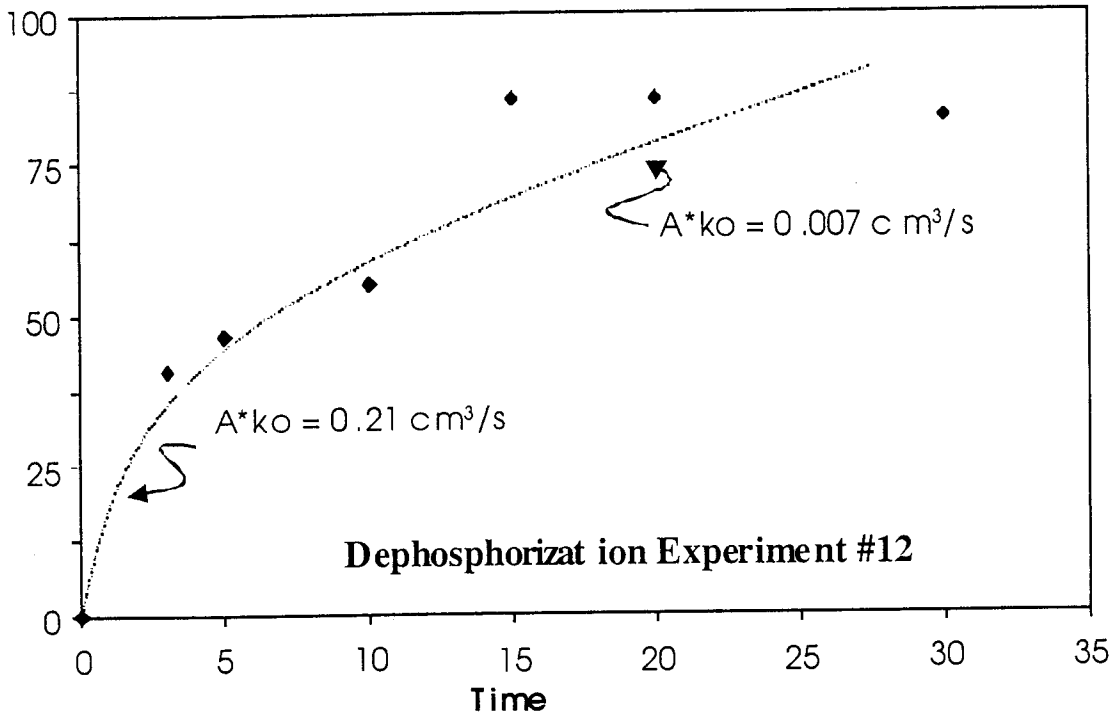

Figure 36: Data from dephosphorization experiment #12 replotted as the RHS of equation [48] versus time.

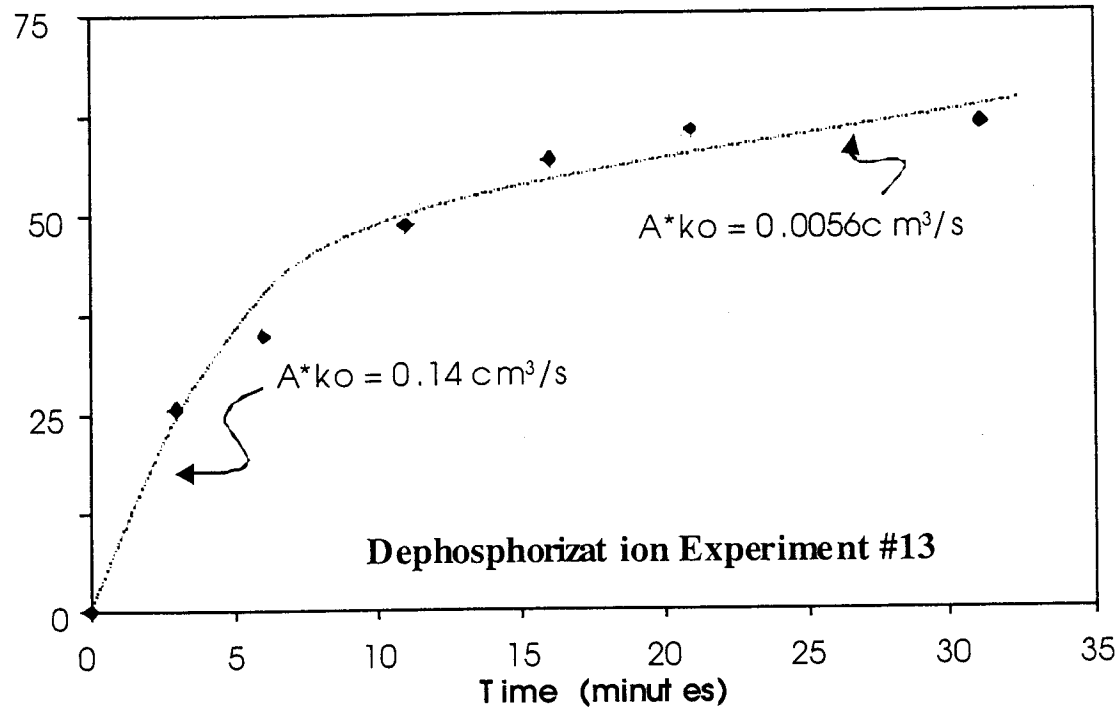

Figure 37: Data from dephosphorization experiment #13 replotted as the RHS of equation [48] versus time.

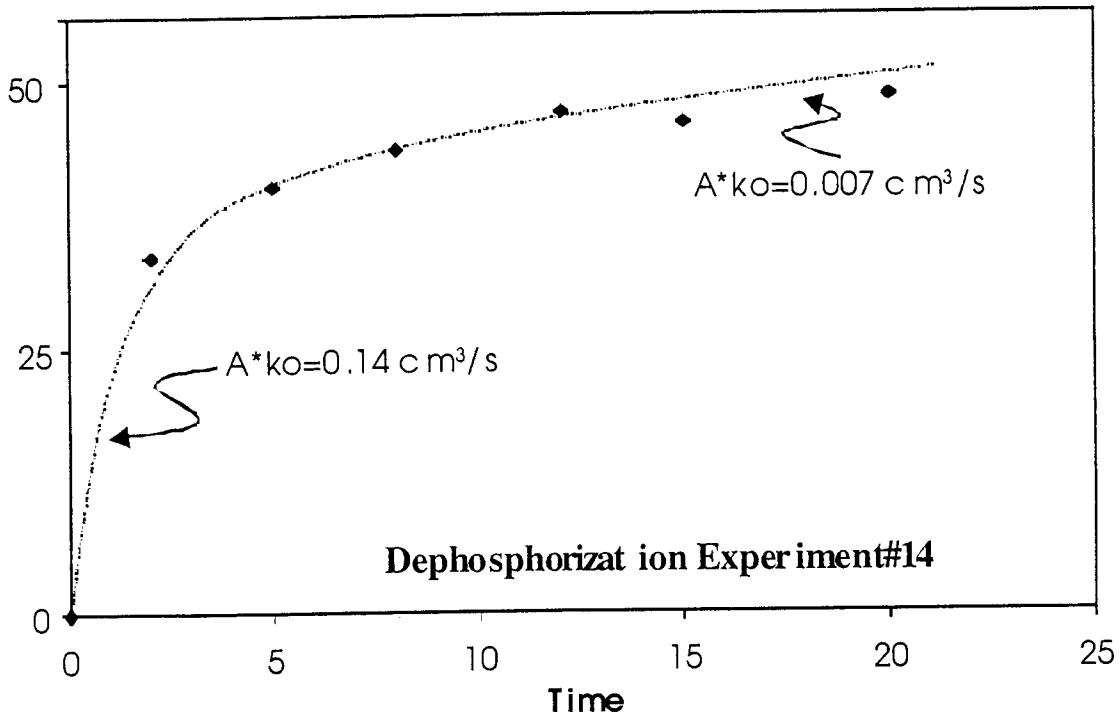

Figure 38: Data from dephosphorization experiment #14 replotted as the RHS of equation [48] versus time.

Although there is some scatter in the data presented in Figures 36 – 38, it is clear that the apparent rate of reaction is changing. Because it is difficult to determine whether the observed trend is the result of a systematic change in the reaction area or in the mass transfer coefficient, the results are analyzed in terms of the mass transfer parameter. The continuous curve indicates the general trend of the data but has no quantitative significance. The two rates near the beginning and end of the experiments are only meant to indicate the magnitude of the mass transfer parameter at these times. The author does not intend to suggest that these two rates indicate two separate regions with different mass transfer mechanisms and rates. All three experiments display a decrease in the mass transfer parameter by a factor of 20 to 30 from the start of the experiment to the end. In Figures 39 and 40 the kinetic data of two experiments from Mori et al. [34] which were presented in Chapter 2.3, are replotted as the RHS of equations 48 and 47 respectively.

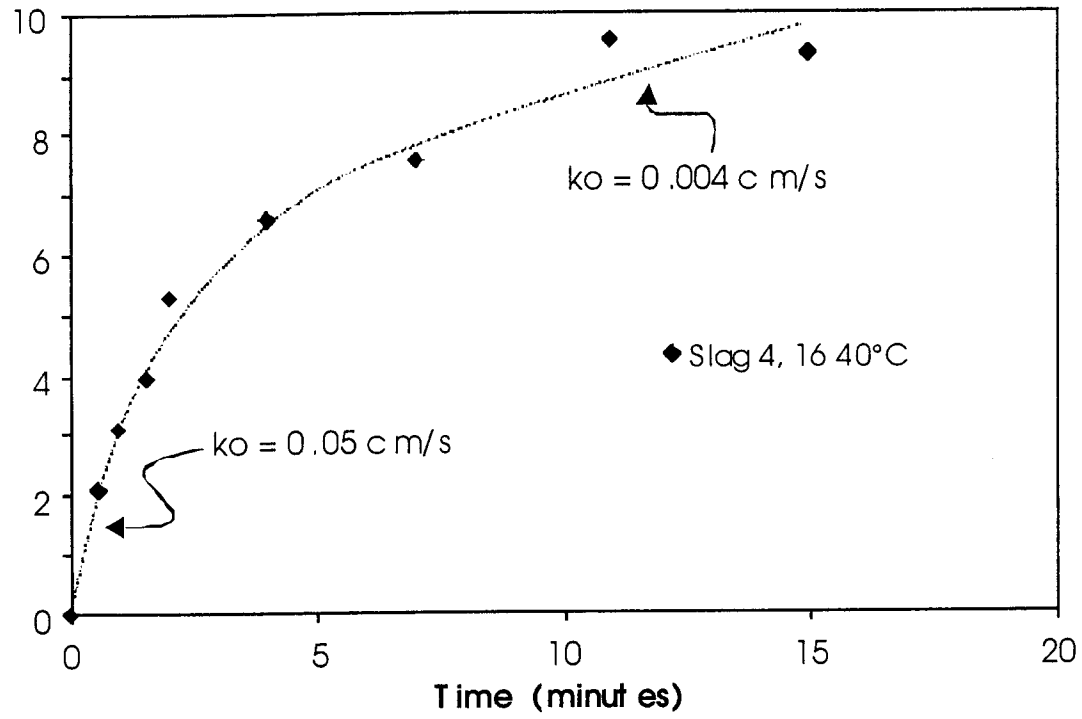

Figure 39: Adapted from Mori et al. [34]. Data from dephosphorization experiment shown in Figure 10 replotted as the RHS of equation 48 versus time.

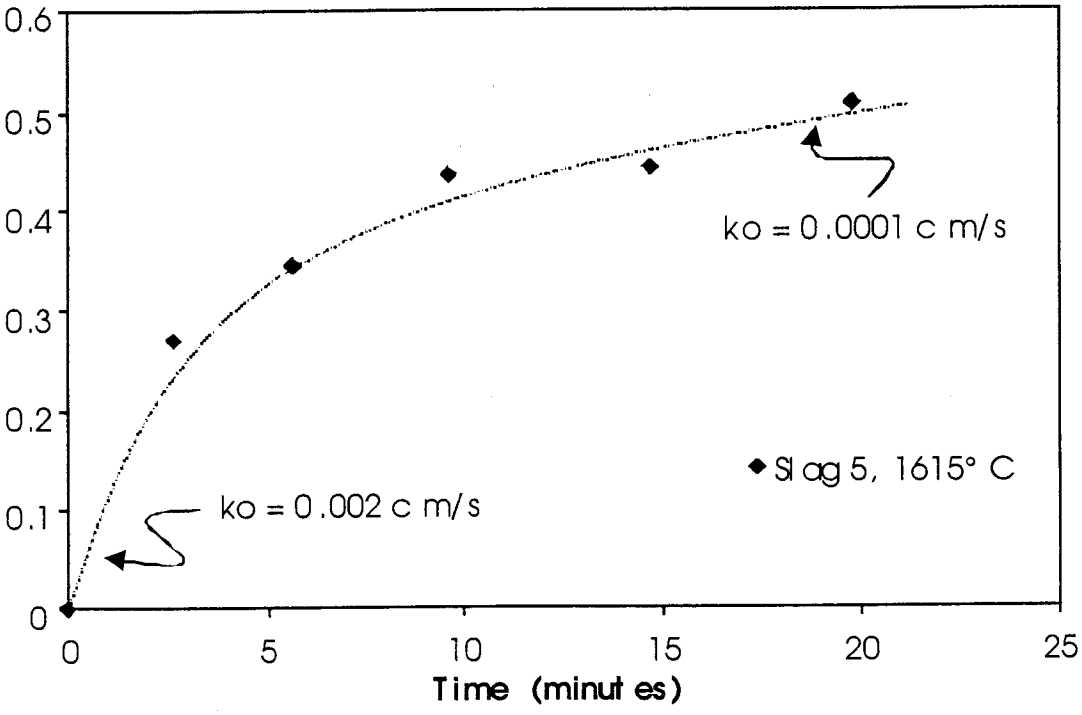

Figure 40: Adapted from Mori et al. [34]. Data from rephosphorization experiment shown in Figure 11, and replotted here as the RHS of equation 48versus time.

The trends of the present study are in agreement with those observed in the data of Mori et al. [34]. Both the general decrease in the apparent rate and the numerical values of the initial and final rates (when crucible size differences are accounted for) are very similar for the present work and the work of Mori et al. [34].

However, the experimental procedure followed in early experiments was very similar to that of Mori et al. [34] and therefore shared many of the problems of those experiments. In these initial experiments, the slag and metal temperatures were not measured independently. The experimental temperature was monitored only by the optical pyrometer. Later calibrations suggested that a significant temperature gradient may have existed between the slag and metal phases. Also, there was some concern that the relatively large slag additions (20 to 30 wt%) were resulting in an unacceptably long transient period at the start of the reaction. Furthermore, due to the apparently discontinuous change in the reaction rate at short experimental times, as displayed in Figures 36 and 38, it was desired to develop an experimental technique, which would allow for a precise reaction start time, a minimum transient period, and accurate sampling at short times. For these reasons, the standard method described in Section 3.4 was adopted.

The results of four dephosphorization experiments are shown below in Figures 41 – 44. Again, the continuous curves were calculated via Equation [46] assuming a constant, best fit ko.

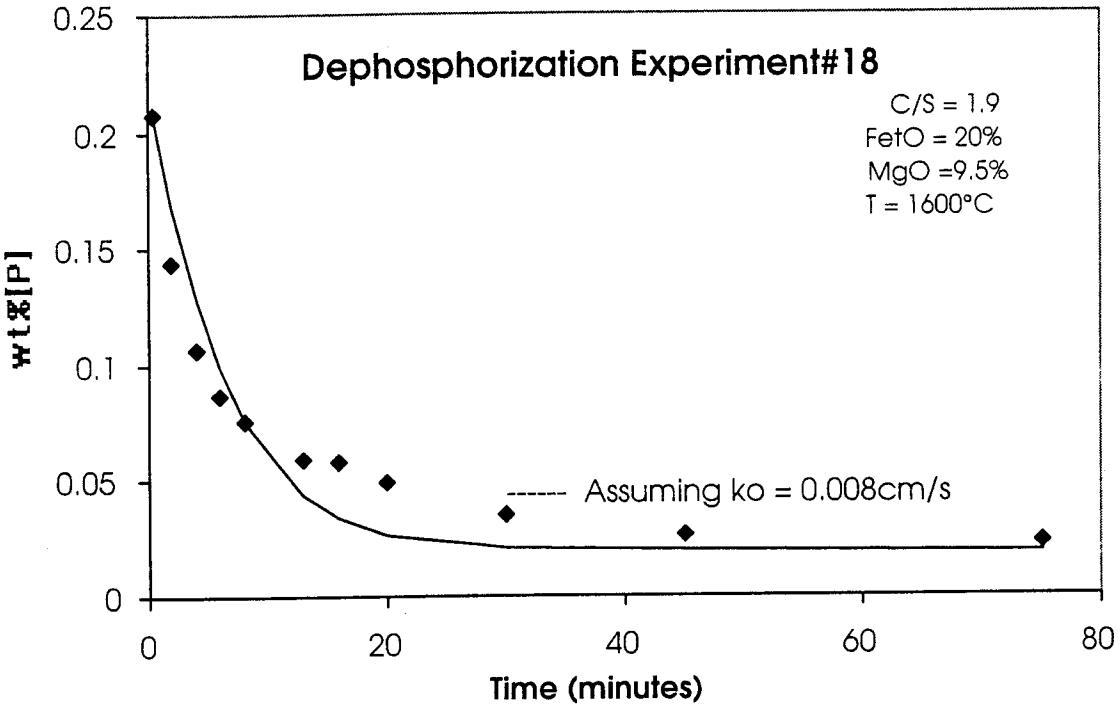

Figure 41: Metal phosphorus versus time for dephosphorization experiment #18. The solid line was calculated via Equation [46] assuming a constant, best fit ko.

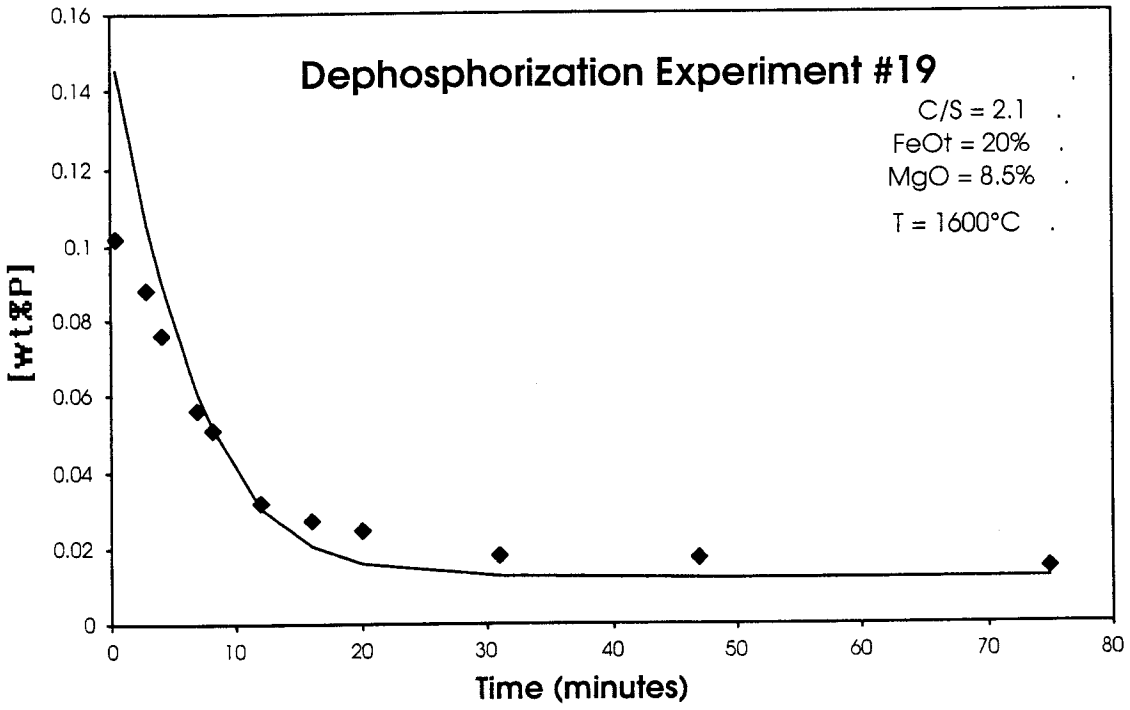

Figure 42: Metal phosphorus versus time for dephosphorization experiment #19. The continuous curve was calculated via Equation [46] assuming a constant, best fit ko.

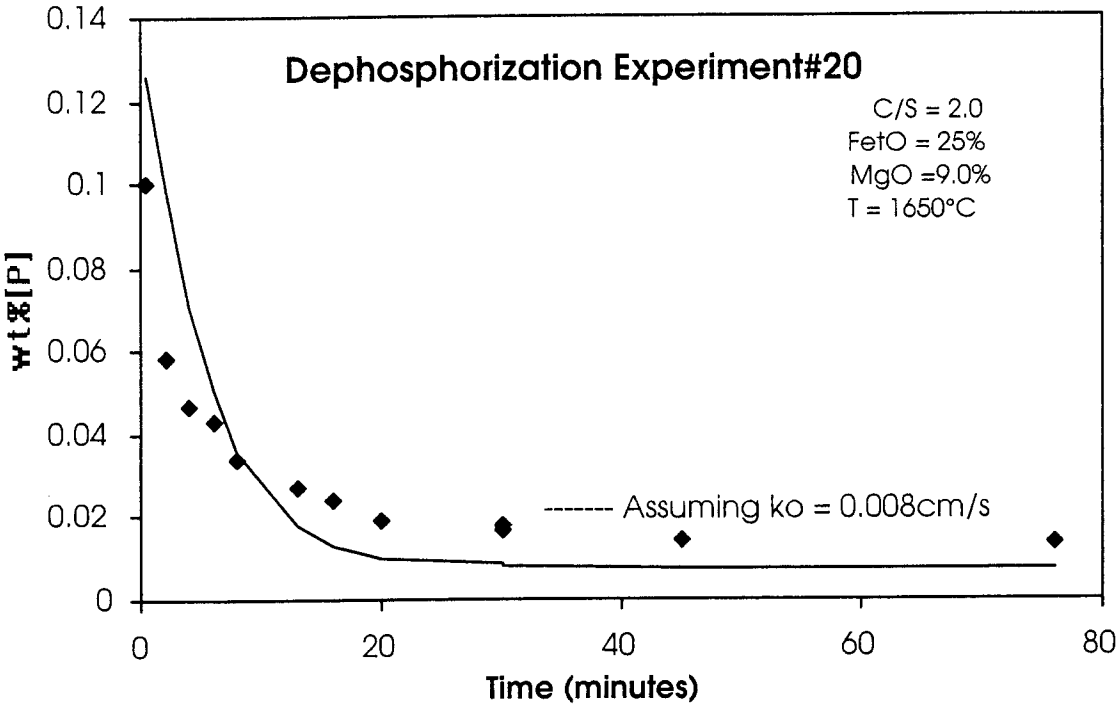

Figure 43: Metal phosphorus versus time for dephosphorization experiment #20. The continuous curve was calculated via Equation [46] assuming a constant, best fit ko.

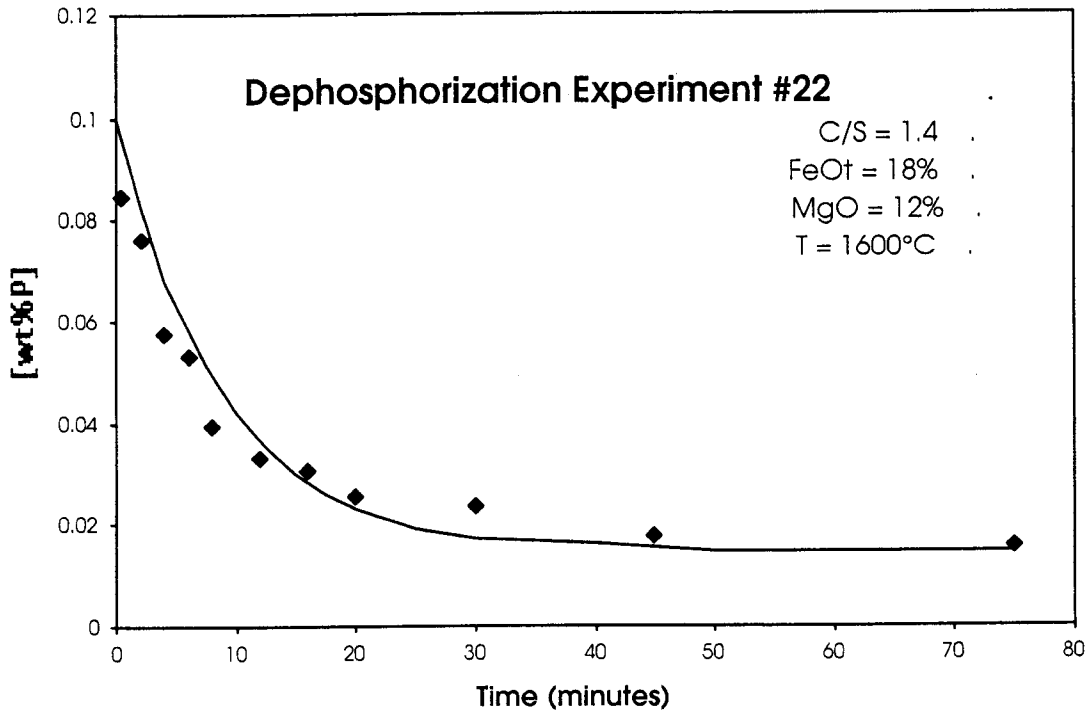

Figure 44: Metal phosphorus versus time for dephosphorization experiment #22. The continuous curve was calculated via Equation [46] assuming a constant, best fit ko.

Again, the data from these experiments were replotted as the right hand side of equation [48]. The resulting graphs are shown below as Figures 45 –47:

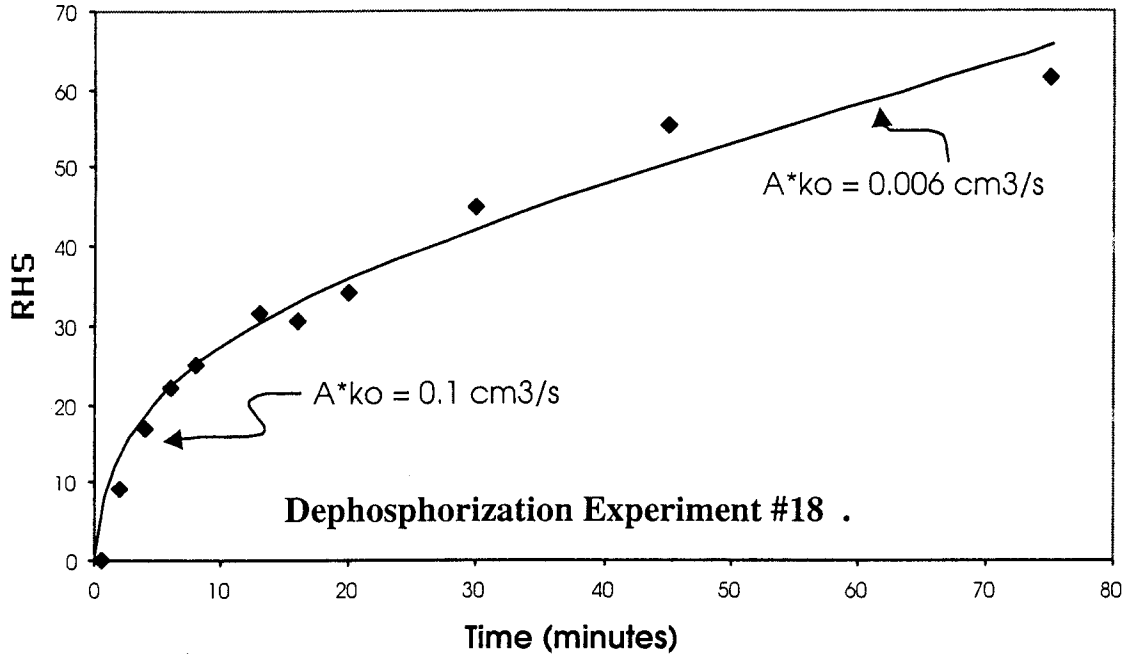

Figure 45: Data from dephosphorization experiment #18 replotted as the RHS of equation [48] versus time.

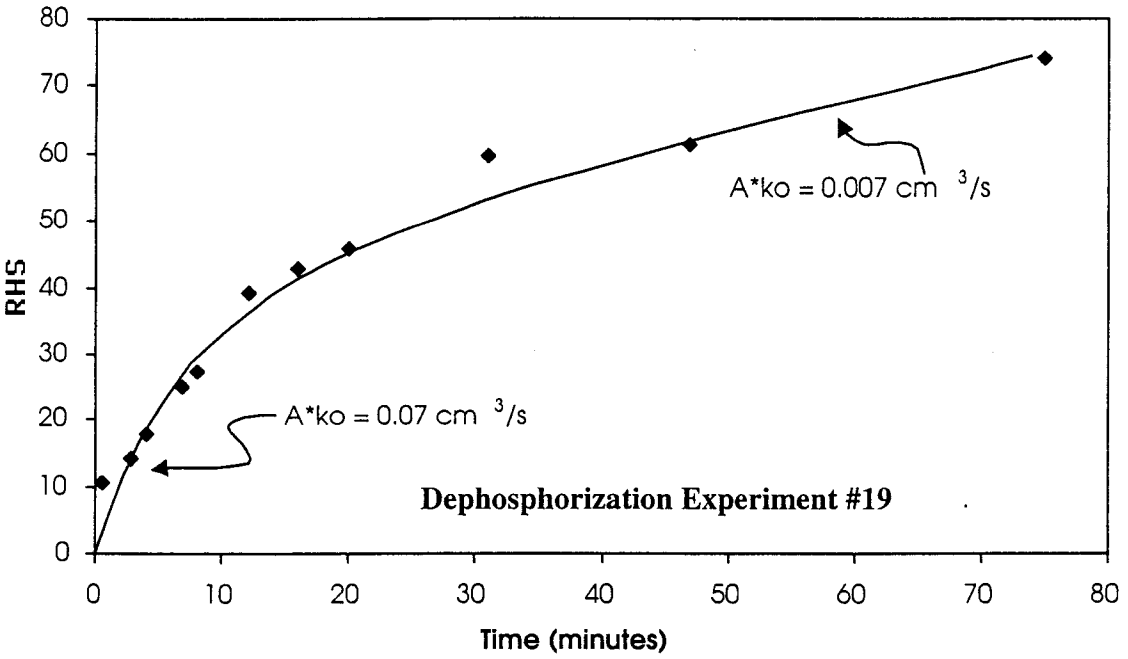

Figure 46: Data from dephosphorization experiment #19 replotted as the RHS of equation [48] versus time.

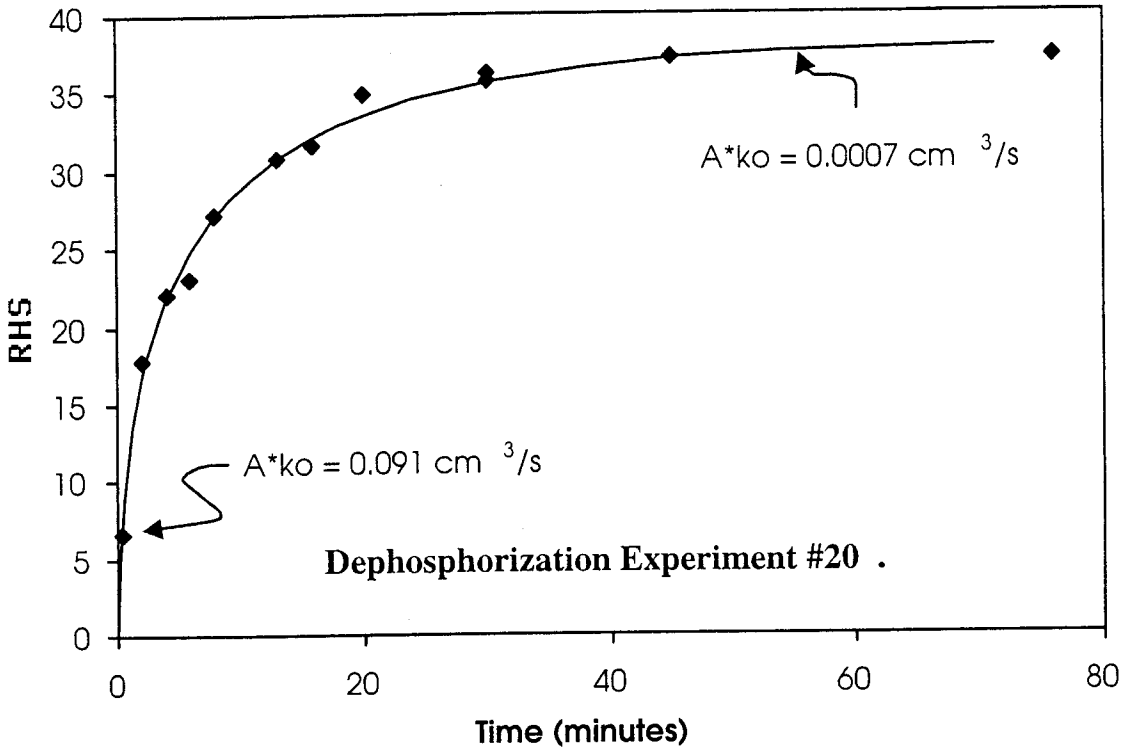

Figure 47: Data from dephosphorization experiment #20 replotted as the RHS of equation [48] versus time.

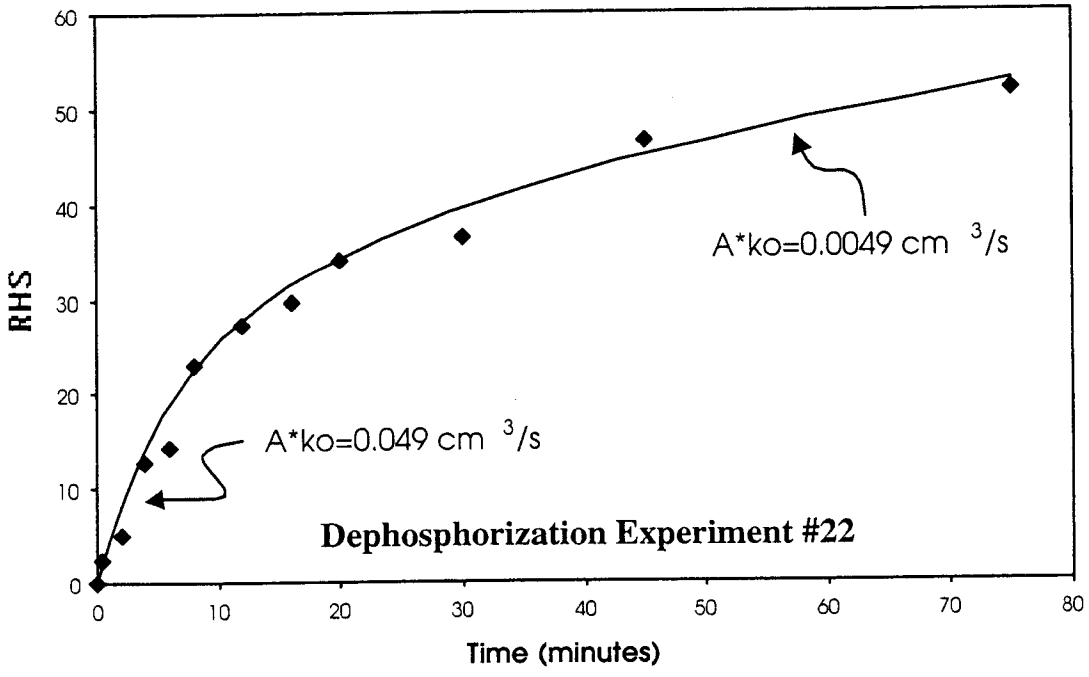

Figure 48: Data from dephosphorization experiment #22 replotted as the RHS of equation [48] versus time.

These results clearly confirm the trends observed in early experiments and also in the data of Mori et al [34]. Figures 45 –48 show that what appeared to be a discontinuous rate change in early experiments is actually a continuous decrease in the rate as a function of time. Again, experiments showed a reproducible drop in the apparent mass transfer parameter by approximately one to two orders of magnitude. For most dephosphorization experiments the average overall mass transfer parameter for the first 4 minutes was found to be approximately 0.07 cm/s. For the final 45 to 60 minutes of the experiment the average A*ko was typically 0.007 cm/s for dephosphorization experiments.

In addition to the dephosphorization experiments reported above, several rephosphorization or phosphorus reversion experiments were conducted. The results of a phosphorus reversion experiment are shown in Figure 49. In this experiment, a slag chemistry representative of DRI gangue was used:

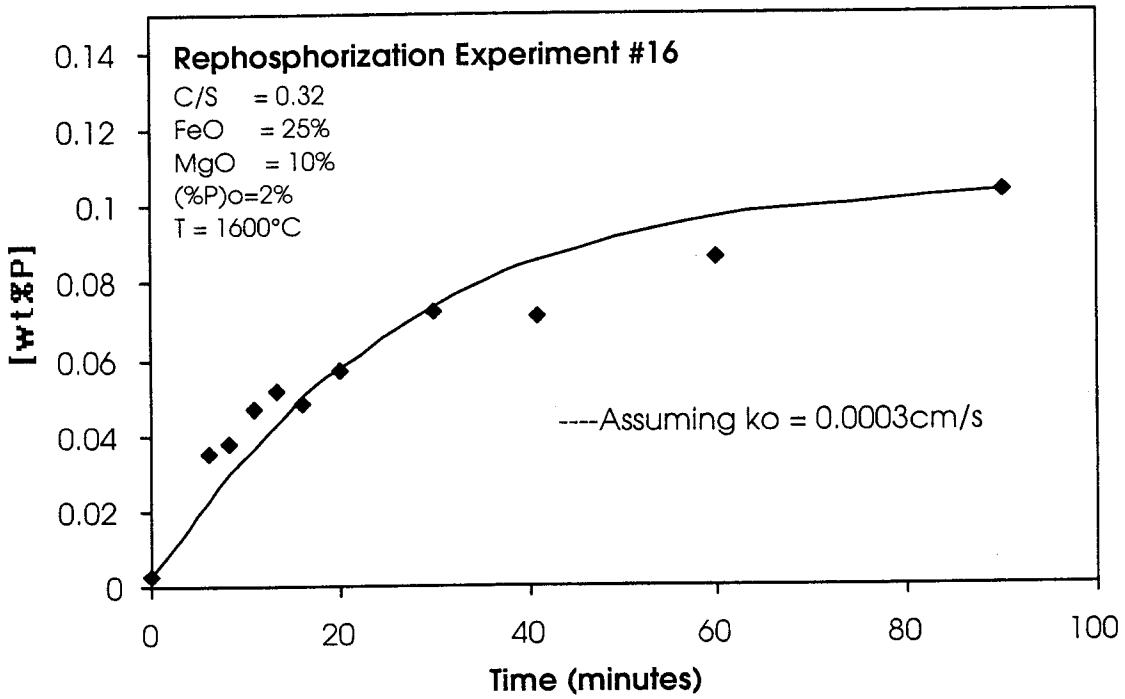

Figure 49: Results of rephosphorization experiment #16 plotted as metal phosphorus versus time. The continuous curve was calculated via equation [45] assuming a best fit ko.

In agreement with the results of Mori et al.[34], it was found that rephosphorization proceeded at a slower rate than dephosphorization under seemingly similar experimental conditions. The experiment shown in Figure 49 had not reached a clear equilibrium

phosphorus distribution after 90 minutes. The data from Experiment #16 are replotted as the RHS of equation [47] in Figure 50 below:

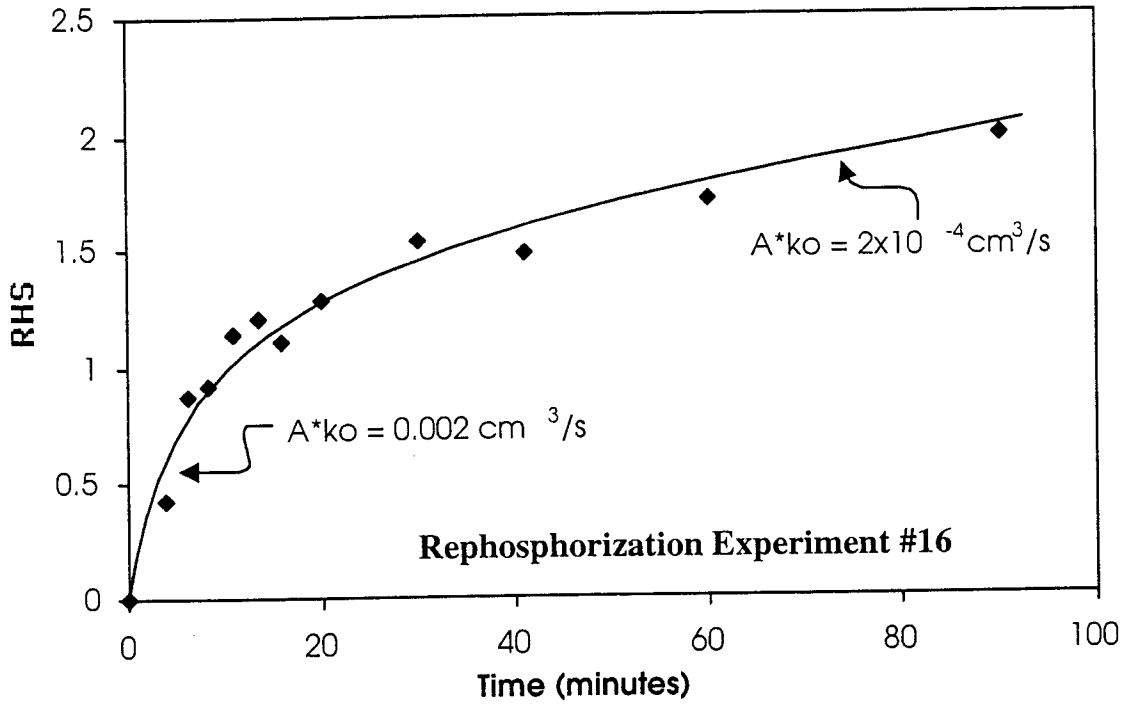

Figure 50: Data from Rephosphorization Experiment #16 plotted as the RHS of equation [47] versus time.

Although the average rate in Figure 50 is significantly slower than the rates of dephosphorization presented earlier, the data exhibits a pronounced bend toward a slower rate at longer times. Again the initial and the final rates differ by approximately one order of magnitude. As was discussed in Section 4.4.1, the overall mass transfer coefficient for rephosphorization should differ from that of dephosphorization by the ratio of the slag density over the metal density, approximately 0.5 in this case. The data of the present study indicate that the rate of rephosphorization is 20 to 50 times slower than the observed rates of dephosphorization.

Two significant differences exist between the conditions of the rephosphorization and dephosphorization experiments, which should be noted. The pre-logarithmic terms in equations 47 and 48 are artifacts of the integration of the flux equations. For the conditions of the experiments conducted in the present study as well as the experiments of Mori et al. [34], the pre-logarithmic terms were consistently different for dephosphorization and rephosphorization experiments. As a result of the experimental

conditions, the pre-logarithmic term of equation 47 was consistently a factor 2 to 8 greater than that for equation 48. As a result, the RHS of equation 48 develops two to eight times faster than the RHS of equation 47 increasing the slope by the same amount.

The second inconsistency between the dephosphorization and rephosphorization experiments lies in the physical properties of the slags used in the different experiments. In the present study, rephosphorization experiments were conducted with slags with very low basicities. As a result, the slags used in those experiments consistently exhibited much higher viscosities as compared with the slags used in dephosphorization experiments. Several models of the mass transfer coefficient were presented in Section 4.4.1. In each model, slag viscosity is likely to have some inverse proportionality with the mass transfer coefficient; however, the exact form of the proportionality is not precisely known. Each model explicitly describes the proportionality of the mass transfer coefficient to the diffusion coefficient. However, the film thickness of the film theory and/or the surface residence time of the penetration theory are also likely to be functions of the slag viscosity.

For the reasons outlined above, it is believed that observed slower rate of rephosphorization relative to dephosphorization was the result of the experimental conditions and not a fundamental difference in the mass transfer mechanism. The observation of a variable mass transfer parameter during both dephosphorization and rephosphorization experiments supports the hypothesis that the two reactions are fundamentally similar.

Variable Mass Transfer Parameter:

The apparent overall mass transfer parameter was calculated as a function of time for dephosphorization experiments 18 – 22. This calculation was made by determining the slope in the RHS versus time plots (Figure 45-48) for each increment of time. Where local scatter in the data produced physically meaningless values, the slope was calculated over a longer time increment, which was representative of the overall trend. Figure 51 shows the result of this calculation:

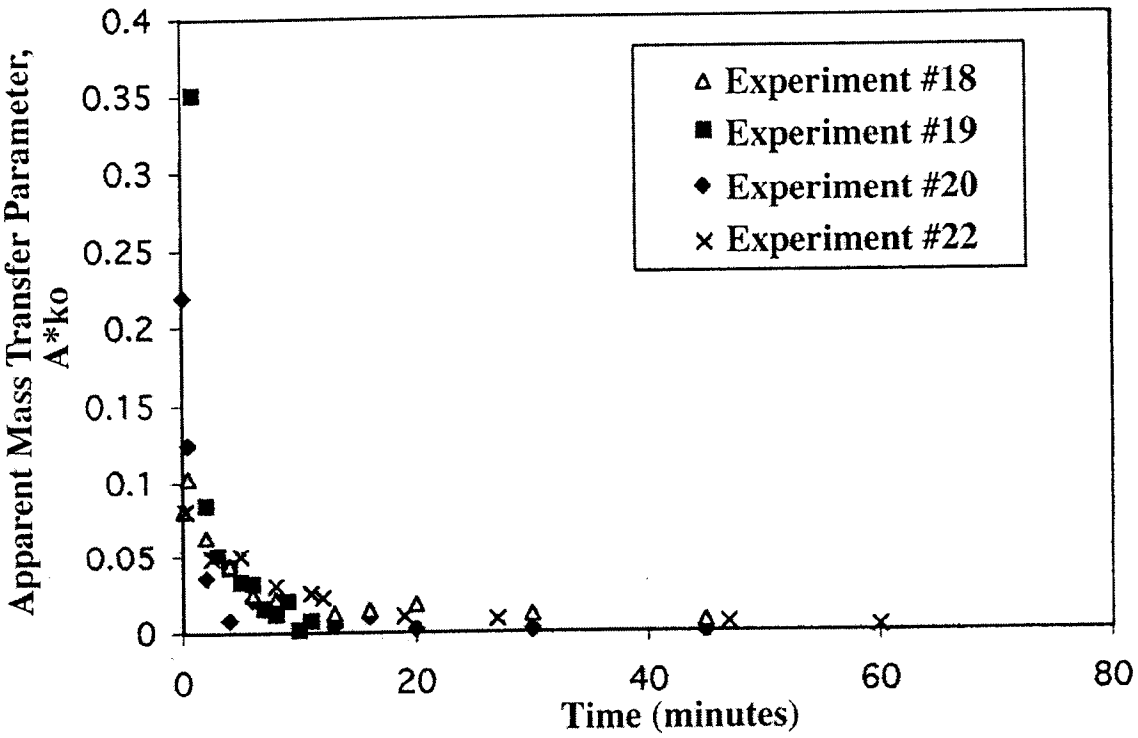

Figure 51: The apparent mass transfer parameter, A*ko, as a function of time for dephosphorization experiments 18 – 22.

The very near correlation of the instantaneous mass transfer coefficients for experiments 18 – 20, suggests that the observed phenomenon is consistent and reproducible. Furthermore, the fact that a similar trend can be observed in the data of Mori et al. [34] suggests that this is not a systematic error inherent to the experimental design. This observed change in the apparent mass transfer parameter, suggests one or a combination of several things:

1. The reaction area is not constant, i.e. some dynamic interfacial phenomenon such as emulsification is occurring.
2. The overall mass transfer coefficient is changing as a function of time.
3. The driving force for the reaction expressed in equations 47 and 48, does not correctly reflect the true system.

Dynamic Interfacial Phenomena:

It is possible that the observed change in reaction rate is not caused by a change in the overall mass transfer coefficient, but by a change in the slag-metal interfacial area. It is possible that some dynamic interface phenomenon is causing a distortion of the interface

such that at short times, when the driving force and mass flux are large, the reaction area is temporarily increased. It is widely accepted that emulsification can occur during periods of intense mass transfer between two immiscible liquids.[39] The mechanisms and criteria for emulsification and other interfacial phenomena between liquid iron-slag systems have been studied by a number of researchers.[48, 49]. Cramb and Chung[48] and Gaye et al. [49] and others have shown that high rates of mass transfer of surface active elements can result in a deep reductions in slag-metal interfacial tension, γ. These researchers have also shown that as the mass transfer reaction approaches equilibrium and the mass flux at the interface decreases, the interfacial tension again returns to a higher equilibrium value. This is shown schematically in Figure 52.

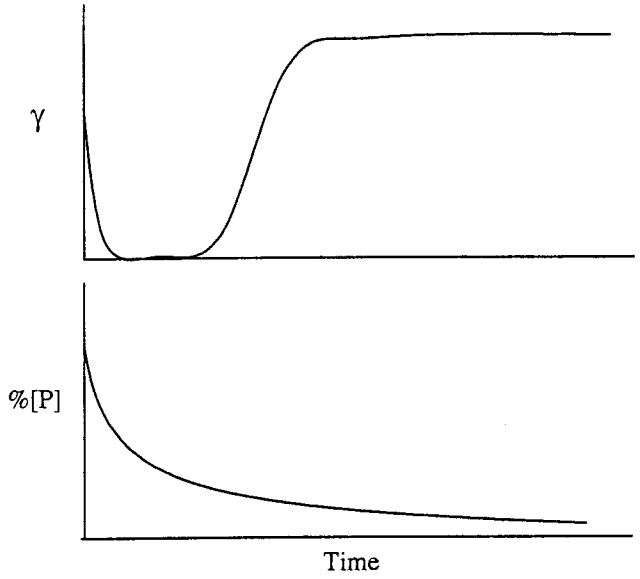

Figure 52: Adapted from Gaye et al. [49]. A schematic representation of the interfacial tension, γ, (upper graph) and metal phosphorus content (lower graph) as functions of time.

It has been proposed that during this transient period of reduced interfacial tension, turbulent interfacial fluid flow, driven by Marangoni forces can result in emulsification. Under less dramatic conditions, intensified local stirring at the interface and a distortion of the slag-metal meniscus without complete emulsification could significantly enhance the rate of mass transfer.

Gaye et al. [49] measured the dynamic interfacial tension during a wide range slag-metal reactions including dephosphorization. For the various oxidation reactions studied, Gaye et al. established criteria for dynamic interfacial tension reduction in terms of the associated oxygen flux across the interface. In the case of the dephosphorization

reaction, these researchers found that when the oxygen flux due to the phosphorus reaction exceeded 0.03 g atom.$m^{-2}.s^{-1}$ the interfacial tension was reduced form an initial high equilibrium value (1200mJ /m^2) to a very low value < 300 mJ/m^2. Furthermore, when the oxygen flux exceeded 0.5 g.atom.$m^{-2}.s^{-1}$ the interfacial tension was reduced to such a value very near zero. The metal alloy studied by Gaye et al. initially contained from 1 to 4 percent phosphorus. Also, the slags used in that study were ternary calcium-alumina-wustite slags. Therefore, the slag-metal systems examined in the present study differed somewhat from those used by Gaye et al. Despite these differences, the initial oxygen flux due to the phosphorus reaction was calculated for the first five minutes of the experiments shown in Figure 51. The results of those calculations are tabulated below.

Table 2: Calculated Oxygen Flux Due to Phosphorus Transfer

	Initial Oxygen Flux (g.atom.$m^{-2}.s^{-1}$) Due to the Measured Rate of Phosphorus Transfer
Experiment #18	1.38
Experiment #19	0.83
Experiment #20	1.1
Experiment #22	0.43

According to the criteria established by Gaye et al., all of the dephosphorization experiments shown in Figure 51 were likely to under go a large reduction in the interfacial tension during the first 10 to 12 minutes of reaction. Interestingly, Experiments 19 and 22 resulted in the smallest initial oxygen fluxes. These experiments also exhibited a smaller difference between the initial and final mass transfer parameters relative to Experiments 18 and 20. These results suggest that the mass transfer parameter is related to the mass flux through the interfacial tension. However, it remains unclear whether the dynamic interfacial tension is affecting the slag-metal reaction area or the mass transfer coefficient itself.

An attempt was made to find clear evidence of slag metal interfacial distortion during dephosphorization. Cramb and Chung [48] examined the effect of silica reduction via Fe-Al droplets upon the slag-metal interface. Several experiments were conducted by those researchers in which Fe-Al droplets were allowed to react with the slag for various

lengths of time before the experiment was quenched. After cooling, the samples were sectioned, polished and examined metallographically for indications of slag-metal emulsification. From these experiments, the researchers were able to obtain clear visual evidence of slag penetration into the metal phase and metal droplet separation into the bulk slag phase.

In attempt to produce similar results for the slag metal system of the present study, several experiments were conducted with essentially the same slag metal system as experiment #18, but were terminated after approximately 4 minutes by quenching to room temperature. Unfortunately, the slag chemistry of these experiments undergoes 'slag falling' or spontaneous disintegration due to low temperature phase transformations as it is cooled. Thus, a large portion of the bulk slag phase could not be recovered. However, in the vicinity of the slag-metal interface, the several millimeters of the slag phase remained as a monolithic solid. The remaining slag and metal were then sectioned vertically, polished, and examined under the optical microscope for evidence of emulsification. Figure 53 shows the slag-metal interface at approximately 50x magnification.

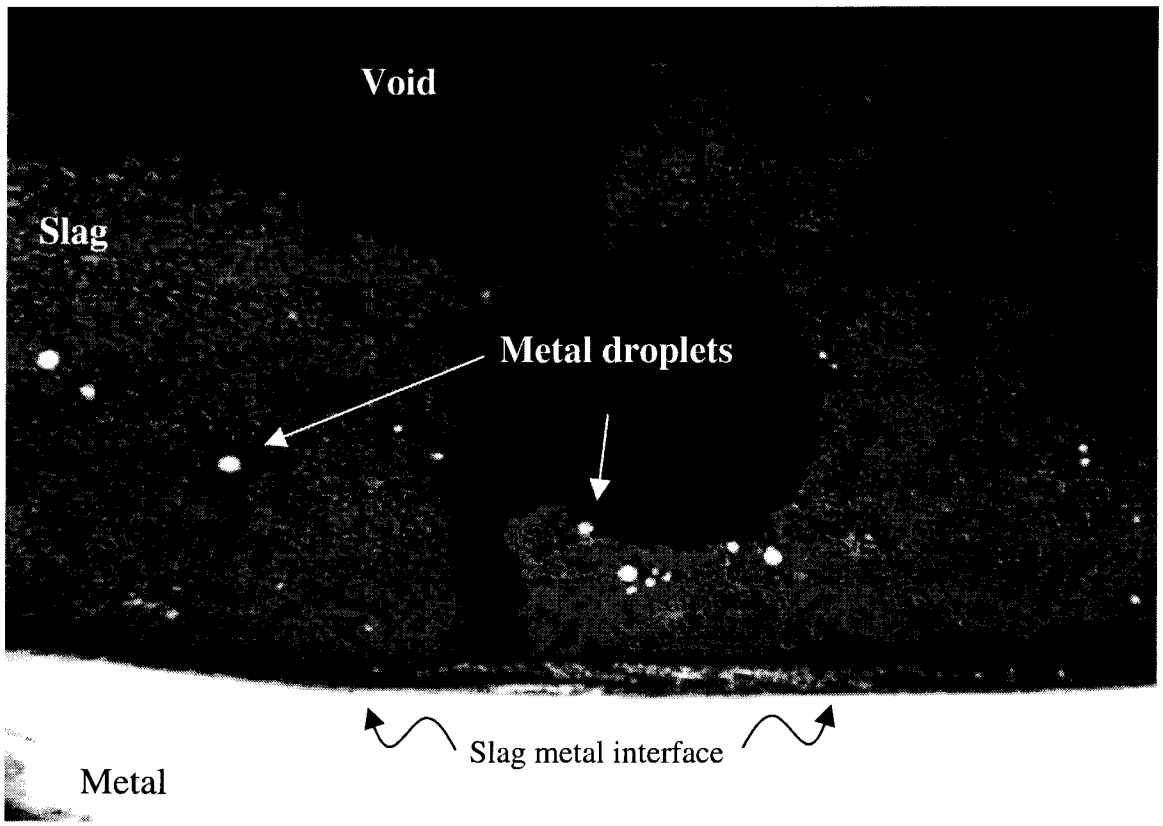

Figure 53: Optical micrograph of the slag-metal interface, quenched 4 minutes after the start of dephosphorization. White spots are metal droplets suspended in the slag.

Figure 54 is a composite of several micrographs showing the slag metal interface.

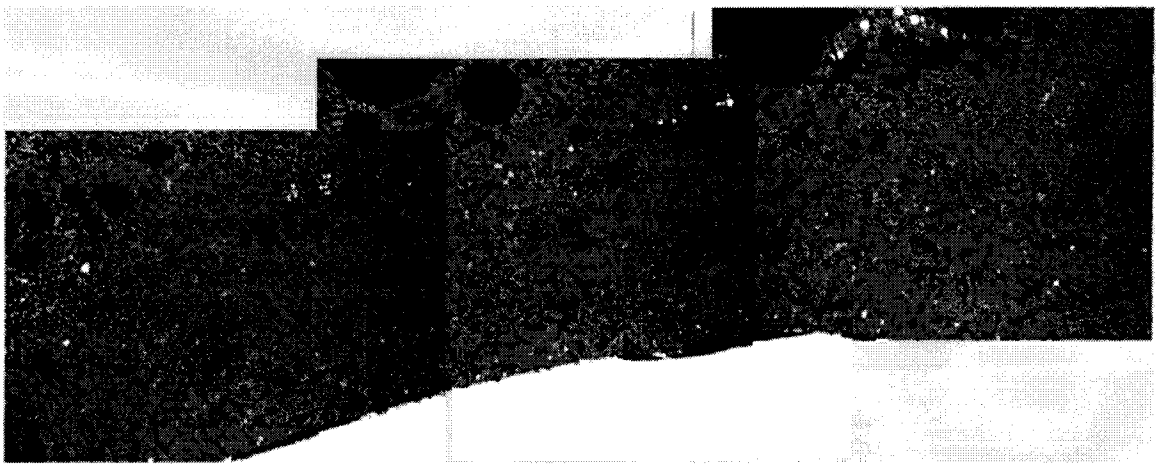

Figure 54: Composite of several optical micrographs of the slag metal interface quenched 4 minutes after the start of dephosphorization. White spots are metal droplets suspended in the slag phase.

Metal droplets can be observed in the slag phase in the micrographs shown in Figures 53 and 54. Investigation of the entire interface revealed that a "halo" of metal droplets had formed at a constant distance above the interface in the slag phase. No evidence was found of slag entrainment into the metal. The observation of metal droplets in the slag phase supports the hypothesis that the slag metal interface is unstable during dephosphorization. However, this investigation cannot be substituted for an in situ observation of the interface while the reaction is occurring.

In a recent study, Seetharaman et al. conducted a series of sessile drop experiments with Fe-P droplets in a highly dephosphorizing slag.[50,51] During these experiments, the behavior of the slag-metal interface was observed in situ during dephosphorization via x-ray radiography. In these experiments, an Fe-0.1%P sample of 3 – 7 grams was placed in an MgO crucible. The sample was allowed to equilibrate at 1550°C. A pellet of slag weighing approximately 3 grams with the initial composition:

CaO 40%

SiO_2 30%

Fe_2O_3 30%

was then added to the furnace. After the slag addition, X-ray images were taken of the sessile drop at a rate of 1 second per minute for a ten minute period. X-ray images from

one of the sessile drop experiments conducted by Seetharaman et al. [50] are reproduced in Figure 55:

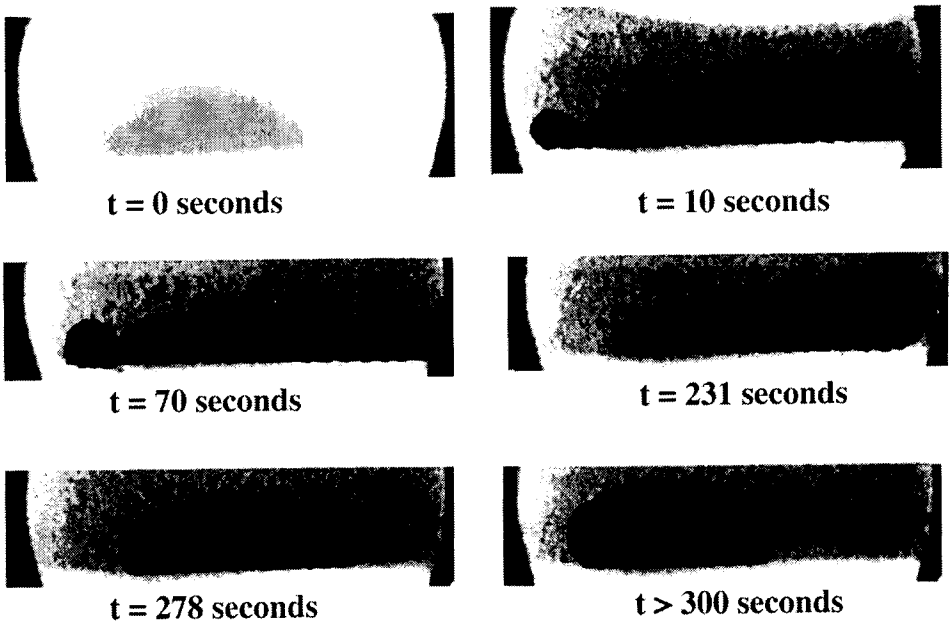

Figure 55: X-ray images adapted from sessile drop experiments with Fe-0.1%P conducted by Seetharaman et al. [50].

In Figure 55, the first frame at t = 0 shows the Fe-0.1%P droplet before the slag addition. The second frame shows the sample 10 seconds after the slag addition. The droplet has clearly changed shape dramatically, significantly increasing the surface area of the drop. The third image, taken at t = 70 seconds, shows that the droplet has formed a neck on the left-hand side. At this stage, of the experiment, the interfacial tension between the droplet and the slag appears to be very low. Under conditions of more energetic fluid flow, partial emulsification of the slag and metal is quite possible. By t = 231 seconds the droplet has begun to pull back together, and at times greater than 278 seconds the drop returns to a shape with a high contact angle, indicating an increase in the interfacial tension.

As component of their study, Seetharaman et al. [51] conducted a dephosphorization experiment similar to those of the present study, for the same slag-metal system of the sessile drop experiments. The results of one dephosphorization experiment from that study are shown blow.

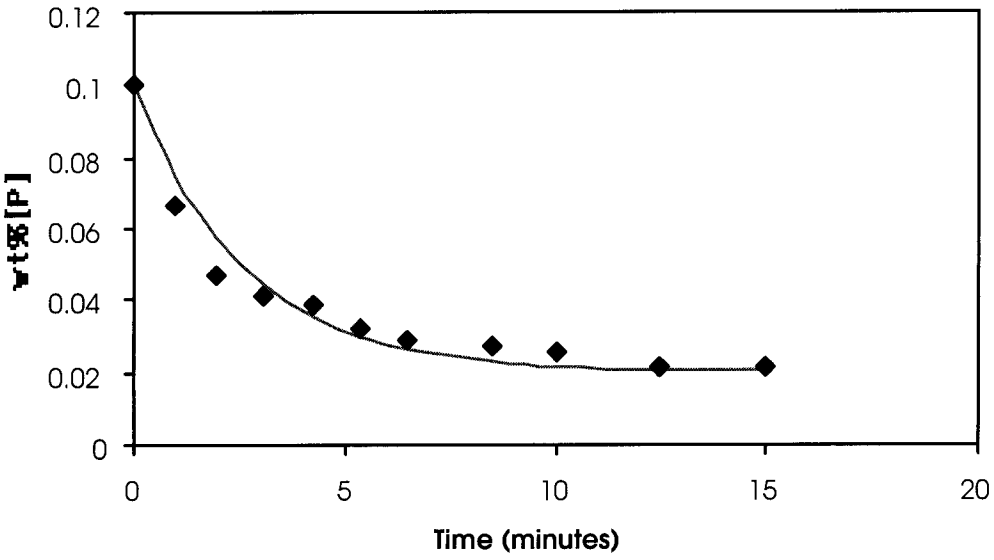

Figure 56: Metal phosphorus versus time data for dephosphorization experiment conducted by Seetharaman et al. [51]

The data in Figure 56 show similar trends as were observed in the present study, i.e. a best fit ko under predicts the rate of dephosphorization at short times and over estimates the rate at longer times. The data in Figure 56 were replotted as the RHS of equation [48] versus time in Figure 57.

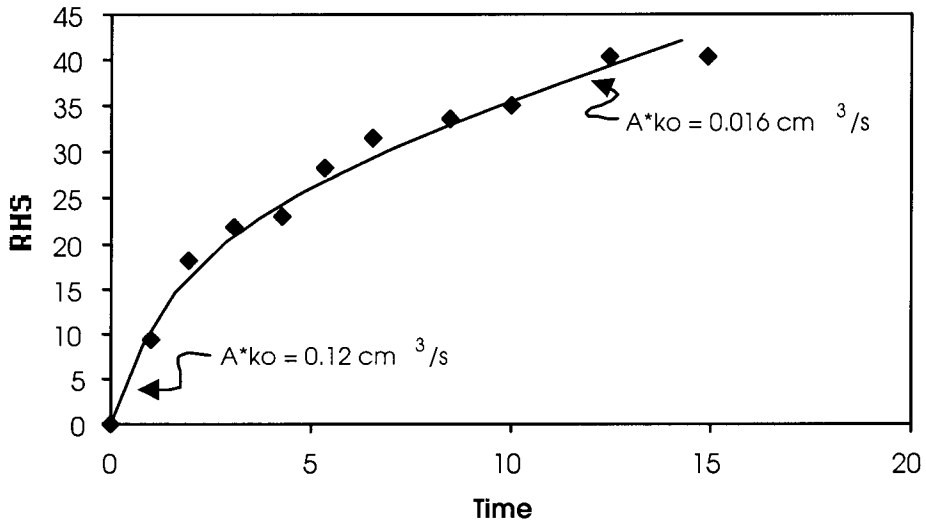

Figure 57: Experimental dephosphorization data from Figure 51, replotted as the RHS of equation [48] versus time. Data are adapted from Seetharaman et al. [43]

The mass transfer parameter in Figure 57 is consistent with the results of the present study both in magnitude and the observed behavior. In the calculation of the RHS of

equation [48] the final slag chemistry for the experiment, as reported by Seetharaman et al., [51] was used to calculate the equilibrium phosphorus distribution ratio for the system.

From the data in Figure 57, and the reported cross sectional area of the crucibles used by Seetharaman et al., an average apparent mass transfer coefficient was calculated to be 0.011 cm/s. An attempt was made to roughly calculate the rate of phosphorus transfer from the sessile drop shown in Figure 55. For this simulation, several important assumptions were made. First, the change in reaction area relating to the shape change of the droplet was ignored. The observed shape change would result a change in a reaction area by roughly a factor of four. The intent of this simulation is only to generate an order of magnitude calculation. Other sources of error, including temperature and slag chemistry variation near the beginning of the experiment will easily result in fluctuations of the driving force for phosphorus mass transfer of least a factor of four. Also, a constant and average mass transfer coefficient was assumed. In the calculation, a hemispherical cap of 5 grams of Fe-0.1%P alloy was brought into contact with 3 grams of slag of the experimental chemistry at t = 0. The numerical phosphorus mass transfer model, described in Chapter 6, was used solve for the phosphorus content of the metal droplet as function of time. The result is shown in Figure 58.

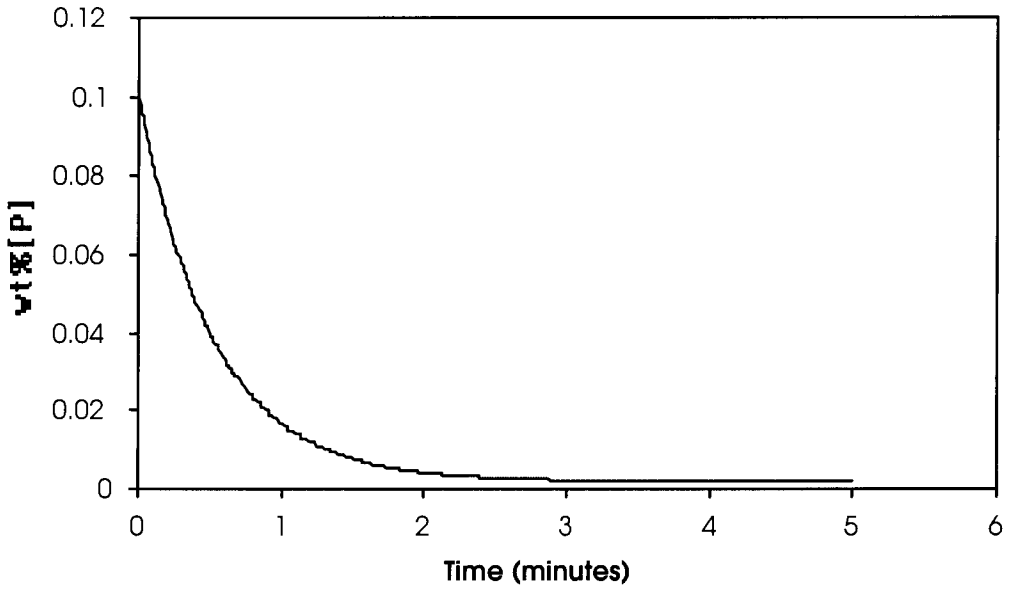

Figure 58: Simulated phosphorus mass transfer during the sessile drop experiments of Seetharaman et al. [51]

The results of the simulation in Figure 58 coincide very well with the observed changes in the shape of the sessile drop shown in Figure 55. Most of the phosphorus transfer is completed within 3 minutes for the conditions of the sessile drop experiments. During the sessile drop experiments, the contact angle of the drop was observed to begin increasing again at times greater than 120 seconds.

These results strongly support the hypothesis that a deep reduction of the interfacial tension will occur for the conditions of phosphorus mass transfer studies in the present work. The observed variation of the mass transfer parameter, may be tied to actual changes in the reaction area due to slag metal emulsification or some less dramatic form of interfacial distortion. However, this is not the only possible explanation for observed change in the mass transfer parameter.

In Section 2.3 several physical and mathematical descriptions of the mass transfer coefficient were discussed. The film theory proposes that mass transfer occurs via molecular diffusion across a stagnant film of thickness:

$$\partial = \frac{D}{k} \qquad 50$$

Based upon the calculated mass transfer coefficients for the present experiments, a theoretical film thickness of approximately 10^{-2} to 10^{-3} cm can be calculated to exist in both the slag and metal phases. The time required to establish steady state diffusion across such a small film thickness would be significantly less than a second. Therefore, the transition from non-steady state to steady state diffusion could be ignored. However, as was discussed in section 2.3, the instability of the slag-metal interface makes it unlikely that the film theory will provide an accurate description of the mass transfer coefficient. Alternatively, the film-penetration model [42] predicts that when the average residence time of an element of liquid at the interface is short, mass transfer will proceed via a combination of non-steady state diffusion into the surface elements and turbulent mixing between the interface and bulk.

Toor and Marchello [42] suggest that the residence time of elements of liquid at the interface is some function of the interfacial tension. Interfacial elements of liquid are different from those in the bulk liquid because they are more stable in position and orientation with respect to the interface. This added stability and the residence time of a liquid element at the interface are related to the interfacial tension. Therefore, the

observed dynamic reduction of the interfacial tension during dephosphorization [49, 50] could have a direct effect upon the mass transfer coefficient. During periods of high mass flux and low interfacial tension, the average residence time of interfacial elements could be reduced by several orders of magnitude. During periods of low mass flux and high interfacial tension, the residence time would also increase. According the penetration model, the mass transfer parameter is proportional to the inverse square root of the residence time. In the extreme case, the film-penetration model predicts the possibility of transition from non-steady state diffusion at low interfacial tension and short surface residence times to steady state diffusion at high interfacial tension and long surface residence times. Such a transition would result in a change in the proportionality of the mass transfer coefficient with the diffusion coefficient from a square root dependence to a linear dependence. Such a shift could easily cause an order of magnitude or greater change in the mass transfer coefficient.

The above argument regarding the effect of a dynamic interfacial tension upon the mass transfer coefficient is very hypothetical in nature. Explicit relationships between key parameters such as the interfacial tension and the surface residence time have not been established in the literature. Although it is difficult to quantify these effects, a mechanism can be imagined by which a dynamic interfacial tension could result in a dynamic mass transfer parameter without emulsification or a change in the slag-metal area.

Variable Driving Force for Phosphorus Transfer:

The observed decrease in the apparent rate of mass transfer could also be the result of an inadequately or incorrectly defined driving force or mechanism for phosphorus transfer. Mori et al. [34] noted a dependence of the overall rate upon the equilibrium partition ratio, Lp. In order to reproduce this effect in the present study, an experiment was conducted using slag with a significantly lower Lp than for the slags of previous experiments. Figure 59 shows the results of dephosphorization experiment #21 plotted as metal phosphorus versus time.

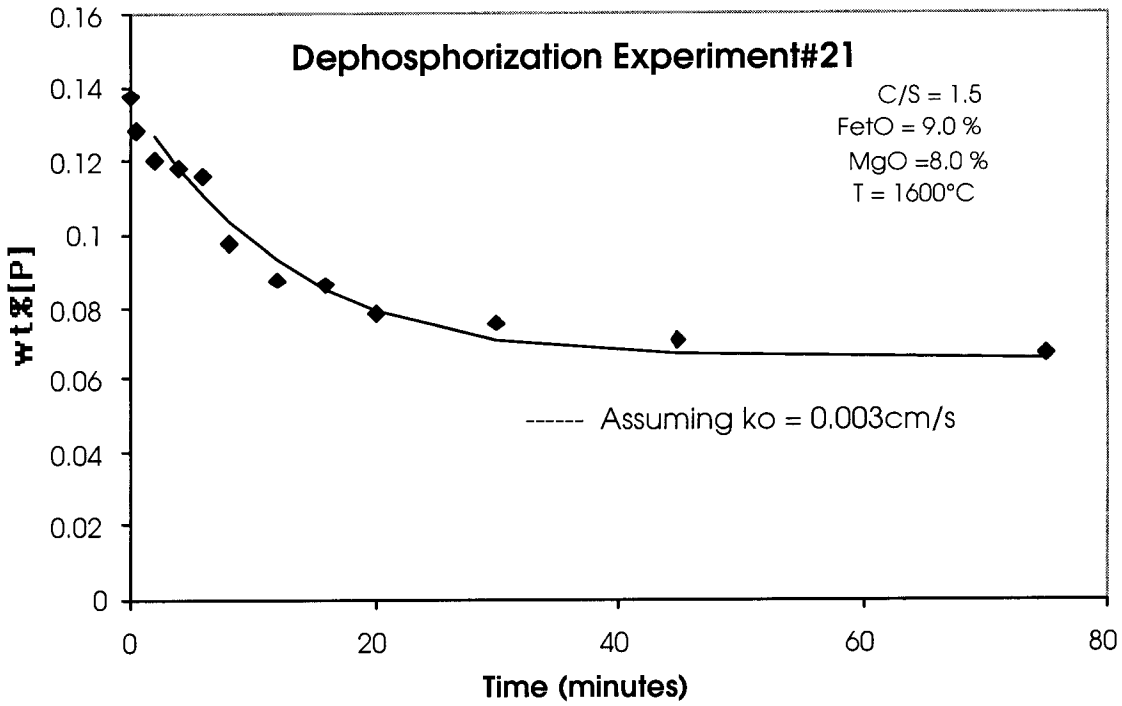

Figure 59: Metal phosphorus versus time for dephosphorization experiment #21. Continuous curve calculated via Equation [46] assuming a constant, best fit ko.

The rate and extent of phosphorus transfer was clearly less in experiment #21 than for other experiments. Figure 60 replots the data of experiment #21 as the RHS of equation[48] versus time.

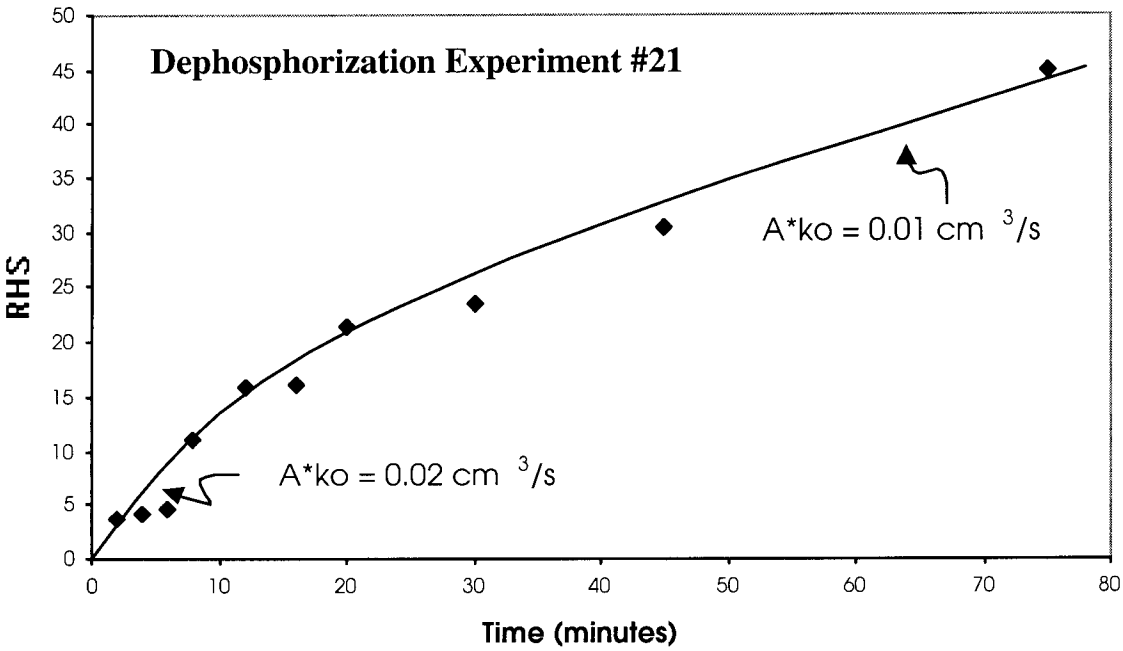

Figure 60: Data from dephosphorization experiment #21 replotted as the RHS of equation [48] versus time.

It is apparent from Figure 60, that both the average overall rate and the change in the rate are significantly less in experiment #21 as compared with other dephosphorization data presented above. However, although it is only by a factor of two, there is an unmistakable bend in the data toward a slower rate. The mass flux of oxygen associated with the phosphorus transfer shown in the first 12 minutes of Figure 59 is on the order of 0.2 g.atom.m^{-2}.s^{-1}. According to Gaye et al. [49] this flux is within the range where a reduction of the interfacial tension is likely to occur, but the interfacial tension will not necessarily go to zero.

In review of the data of Mori et al. [34] for phosphorus transfer, these same trends are also observed. Those researchers observed an apparent dependence of the average mass transfer coefficient upon Lp. Although Mori et al. did not comment specifically on the systematic change in rate, the degree to which the mass transfer coefficient changed from beginning to end of those experiments appears to be related to the driving force for dephosphorization as well. In experiments where the Lp was large, ko showed a large decrease from the beginning to the end of the experiment. In dephosphorization experiments where Lp was low, ko showed much less variation from start to finish.

In the study by Mori et al., samples taken from the bulk metal for phosphorus analysis were also analyzed for oxygen. For most dephosphorization experiments the oxygen content of the metal increased from an initial value typically below 50 ppm to a final value in excess of 1000 ppm. As reported by Mori et al. [34], the bulk metal oxygen content increased faster, but on the same time scale as the rate of change of phosphorus. Despite this fact, these researchers assumed that oxygen mass transfer was significantly faster than phosphorus such that the slag metal interface was always at equilibrium with respect to oxygen. In Figure 61, metal oxygen data from the dephosphorization experiment shown in Figures 9 and 39 are replotted.

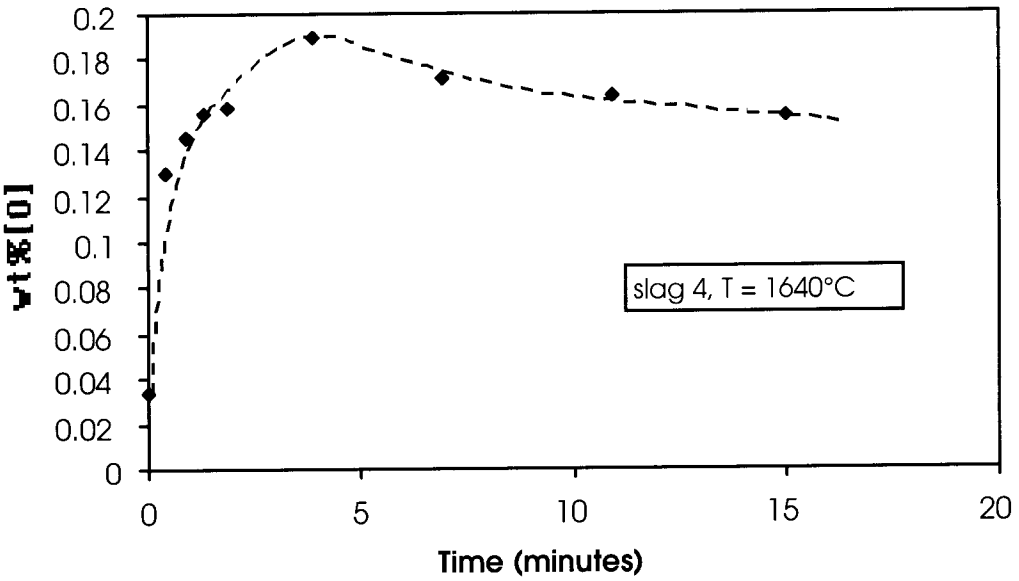

Figure 61: Oxygen transfer kinetic data adapted from Mori et al. [34] The continuous curve indicates only the trend not a fundamental calculation.

The data in Figure 61 show an interesting peak in the metal oxygen at approximately 5 minutes. This also correlates to the time in Figure 39, shown below, when the phosphorus mass transfer coefficient appears to slow down.

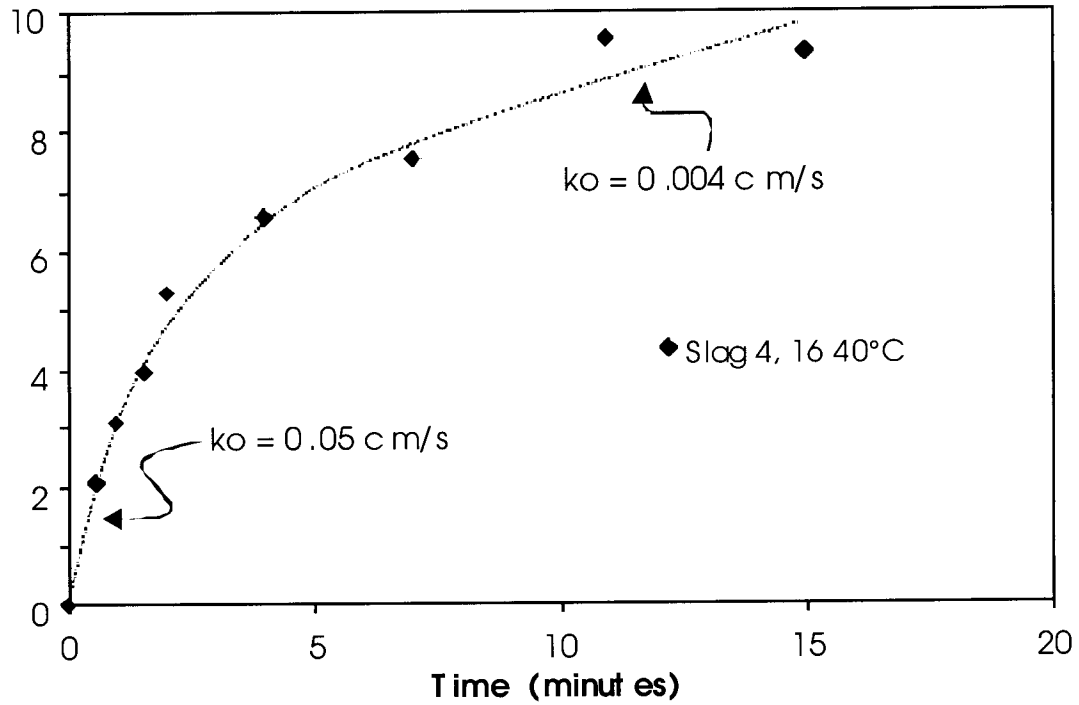

Figure 39: Adapted from Mori et al. [34]. Data from dephosphorization experiment shown in Figure 10 replotted as the RHS of equation 48 versus time.

This trend of a peak in metal oxygen followed by a decay was common to all dephosphorization experiments conducted with slags, which exhibited a large equilibrium phosphorus distribution ratios. The experiments in which Lp was large were also the experiments, which exhibited the largest changes in the phosphorus mass transfer coefficient. The Lp for the experiment shown in Figures 10 and 39 was equal to 69. By comparison, the Lp for the experiment conducted with slag 1 at 1540°C shown in Figure 9 was 34. The data from this experiment are replotted as the RHS of equation 48 in Figure 62.

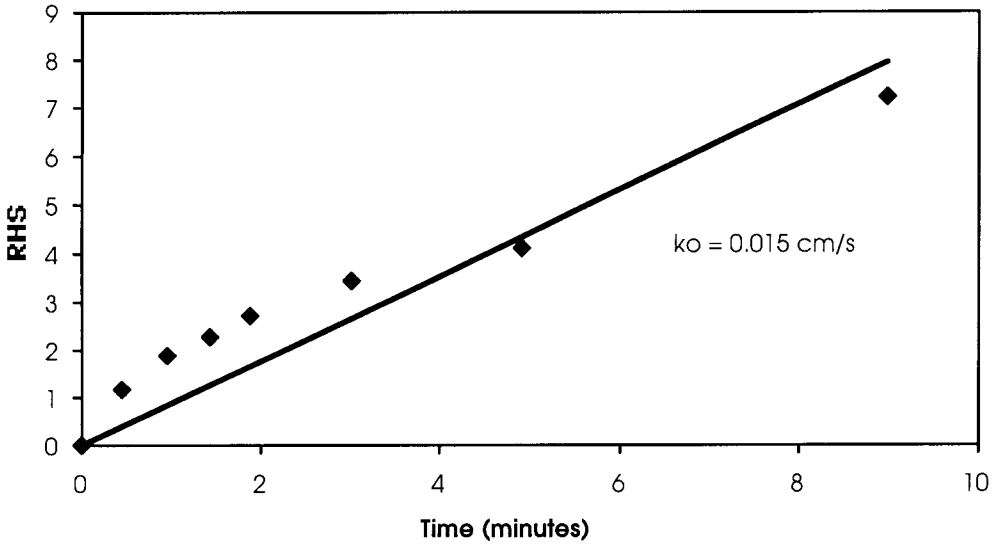

Figure 62: Adapted from Mori et al. [34]. Data from dephosphorization experiment shown in Figure 9 replotted as the RHS of equation 48 versus time.

The mass transfer coefficient in Figure 62 only varies from 0.033 cm/s at the beginning of the experiment to 0.011 cm/s toward the end. The data for the oxygen content of the metal for this experiment are replotted in Figure 63.

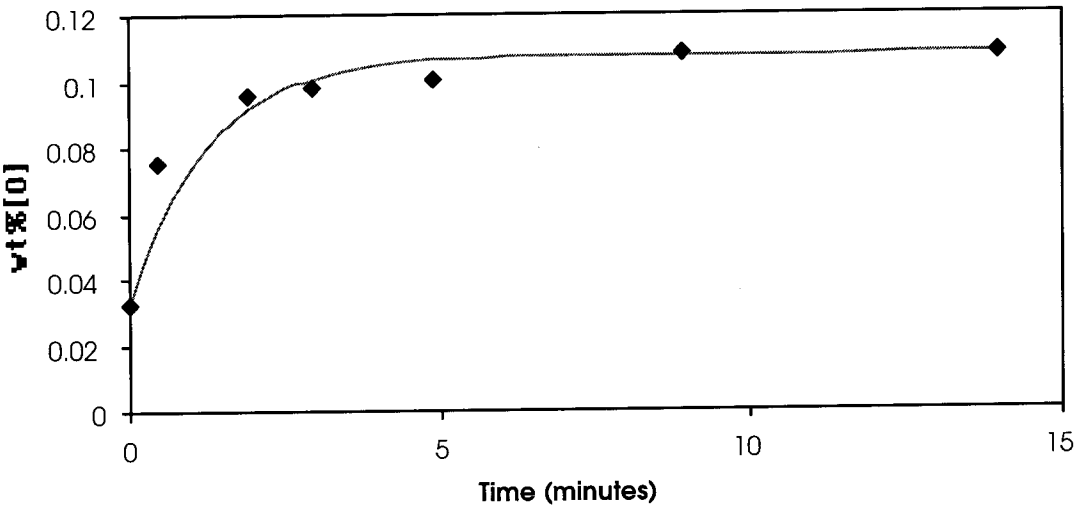

Figure 63: Oxygen transfer kinetic data adapted from Mori et al. [34] The continuous curve was plotted assuming liquid phase mass transfer controlled kinetics and a best fit mass transfer parameter.

The data in Figure 63 do not show the peak in the metal oxygen content, which was observed in Figure 61. In order to calculate the continuous curve in Figure 63, it was assumed that liquid phase mass transfer was controlling oxygen transfer into the bulk metal, and that the final metal oxygen content represented equilibrium. Under this assumption, the flux equation for oxygen is given by:

$$\frac{d\%[O]}{dt} = -\frac{Ak_o\rho}{W_m}\left([\%O]_i - [\%O]\right) \qquad 51$$

The term $[\%O]_i$ in equation 51is the oxygen content of the metal at the slag metal interface. Assuming that the interface is at equilibrium, and that the final metal oxygen represents that equilibrium, equation 51 can be rewritten in terms of the final metal oxygen:

$$\frac{d\%[O]}{dt} = -\frac{Ak_o\rho}{W_m}\left([\%O]_f - [\%O]\right) \qquad 52$$

Equation 52 can be integrated analytically to give the equation:

$$-k_o t = \frac{W_m}{A\rho} \ln\left(\frac{[\%O]_f - [\%O]}{[\%O]_f - [\%O]_o}\right) \quad 53$$

The continuous curve in Figure 63 was calculated according to equation 53. The data of Figure 63 were replotted as the RHS of equation 53 versus time in Figure 64.

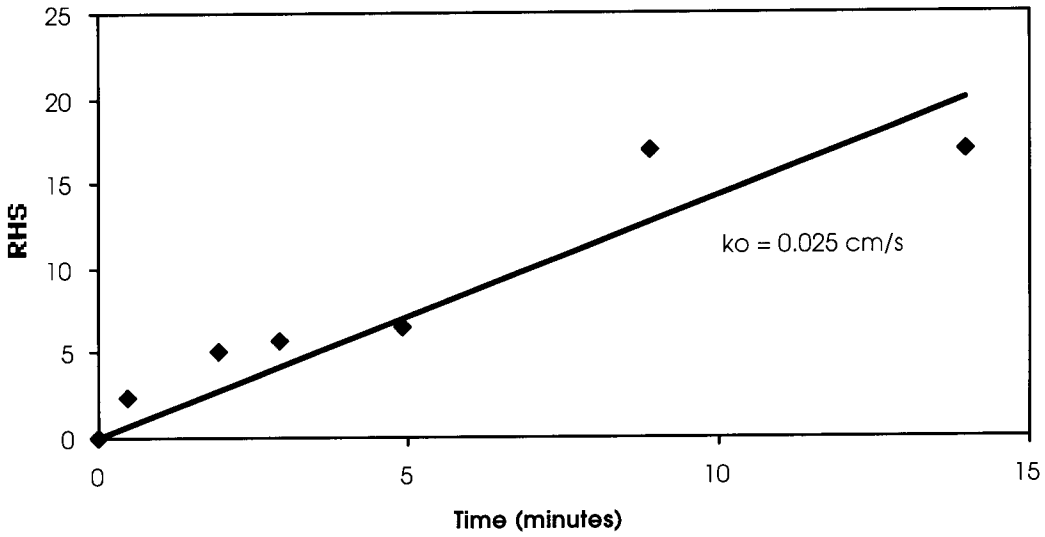

Figure 64: RHS of equation 53 versus time.

Figure 64 is typical of the results for oxygen transfer in the metal for dephosphorization experiments conducted by Mori et al. with low phosphorus distribution ratios. Clearly, the assumptions necessary for equations 52 and 53 to be used are not true for experiments that exhibited a peak and decline in the metal oxygen. Equation 51 should still be valid; however, the interfacial metal oxygen is changing during the heat, and the final bulk metal oxygen content does not describe the condition at the interface at all times during the experiment.

The focus here by the author on oxygen is for several reasons.

1. The oxygen potential at the slag-metal interface is one of the strongest influences of the equilibrium phosphorus reaction.
2. Oxygen is surface active in iron, where as phosphorus is not particularly so. Accordingly, previous researchers examining the effects of phosphorus transfer upon the interfacial tension have done so with respect the associated oxygen flux, not the phosphorus flux. [49] The mechanism by which oxygen is exchanged across the slag-metal interface should have a significant effect upon the properties of the interface during the reaction.

3. Clearly, the data of Mori et al. [34] show that something unexpected is occurring with respect to oxygen. If it is real, the peak and decay in metal oxygen content for dephosphorization experiments with a large Lp, cannot be explained by conventional hypotheses regarding the transfer of reactants to and products away form the interface during dephosphorization.

One simple explanation of the observed peak and decay in metal oxygen content can be rationalized. In the experiments for which this phenomenon was observed, the initial oxygen mass flux, calculated directly from the oxygen data, was on the order of 8 $g.atom.m^{-2}.s^{-1}$. This is a massive flux and would undoubtedly result in significant emulsification. Therefore, metal samples taken during the first 5 minutes of reaction may have contained large amounts of entrained slag, which would significantly elevate the observed total oxygen content. The decay in oxygen content after 5 minutes can be rationalized as resulting from the separation of entrained slag inclusions from the metal phase. This explanation is as likely or more likely than any other.

Chapter 5

Plant Trials

Laboratory experiments can be an effective tool in evaluating the fundamental equations, mechanism, and rate parameters for chemical reactions, which occur during steelmaking. However, the mass transfer conditions of the EAF or any industrial reactor differ significantly from conditions, which can be effectively simulated in the laboratory. Differences in the stirring conditions and degree of slag metal mixing in the EAF versus those in laboratory experiments can result in variations in the mass transfer parameter by several orders of magnitude. Therefore, a number of plant trials were conducted in order to gain a better understanding the parameters, which influence mass transfer during EAF steelmaking. The results of these industrial scale experiments, as well as the results of previous researchers, will be discussed in the following sections.

5.1 Pennsylvania Steel Technologies, Inc-Bethlehem Steel Mass Transfer Trials

Several controlled trial heats were conducted in order to evaluate the mass transfer parameter for the EAF. It should be noted that differences in specific melting practices from one plant to the next will lead to variations in the mass transfer parameter for different operations. The degree of slag foaming and amount of slag metal mixing are most strongly effected by the evolution of gas, primarily carbon monoxide, within the steel melt, at the slag metal interface, and/or within the slag layer. The location, extent, and rate of gas evolution is affected by several furnace operating parameters, such as:

- Amount and physical characteristics of charge carbon and injected carbon
- Bath carbon at melt-in, e.g. scrap mix plus additional carbon
- Slag chemistry at melt-in, e.g. flux practice, scrap characteristics, melting practice
- Amount, characteristics, and method of addition of DRI/HBI materials
- Amount and method of oxygen injection
- Use of bottom stirring

The mass transfer parameter of a given furnace will be influenced by the amount of slag-metal mixing, the physical dimensions of the furnace, the furnace power and melting rate, as well as the electromagnetic characteristics of the arc. Irons et al. [52, 53] have attempted to evaluate the relative influence of these parameters on stirring in the steel

bath through computational fluid dynamic modeling of the EAF. Due to the extreme complexity of a high temperature three (or more) phase system with moving boundaries, multiple simultaneous multi-phase chemical reactions, and large chemical, temperature, and surface tension gradients it is extremely difficult to precisely characterize the EAF through fluid dynamic modeling. As a parametric comparison, the fluid dynamic modeling of Irons et al. indicates that, in the absence of bottom stirring, CO evolution within the bath is the most significant driver for fluid flow in the steel in an AC furnace. Also, the evolution of gas bubbles at or below the steel-slag interface significantly increases the slag-metal interfacial area by enhancing the amount of slag-metal inter-mixing. For this reason, it is assumed that, in the absence of bottoms stirring, the degree of slag-metal mixing effected by the various influences listed above, will dominate the mass transfer parameter. Therefore, the mass transfer parameter should scale with some proportionality to the superficial gas velocity at the imaginary flat-bath slag-metal interface. However, gas generated within or above the slag layer will have limited effect on the mass transfer parameter. For the above reasons, it is recognized that no universal mass transfer parameter can be defined for all electric furnaces. However, the results of the trials reported here should be characteristic of a modern electric furnace of similar physical dimensions with an effective foamy slag practice.

Controlled industrial scale mass transfer experiments were conducted on a 150 ton DC electric furnace by Pennsylvania Steel Technologies, Inc-Bethlehem Steel (PST). Some important operating parameters of the furnace used are given below:

Table 3: Operating Parameters of PST - EAF

Power	UHP-DC		
Capacity	150 tons	-	3 bucket charge
Diameter	23 feet		
Tap to Tap	Approx. 60 minutes		
Typical Oxygen Usage	Melting – 89,040 SCF		
	Refining – 46,200 SCF		
	Total – 1200 SCF/Ton		
Injected Carbon*	600 – 800 lbs		
Charge Carbon	9000 lbs in 3rd bucket charge		
Flux – Pre-blended*	77.2%CaO –	6562 lbs	
	14.6%MgO –	1241 lbs	
	4.6% SiO_2-	391 lbs	
	Total -	8500 lbs	*Addition completed by melt-in of 2nd bucket
Slag Flushing	During Melting ≈ 0		
	During Refine – variable…0 to 10,000 lbs		
Hot Steel Heel	37 tons		
Slag Heel	4 to 12 inches ≈ 8600 lbs to 22,000 lbs		

For these plant trials, temperature readings and samples were taken of the slag and metal as a function of time as soon as a reliable temperature reading could be made (approximately 10 to 15 minutes after the final charge.) This resulted in the collection of approximately 4 slag, metal, and temperature samples during the 10 to 15 minute refining period. The slag and metal samples were then analyzed. Due to the focus of this study, it was intended to examine the rate of phosphorus transfer between the metal and slag in order to determine the mass transfer parameter for this furnace. As was discussed at length earlier, the equilibrium phosphorus distribution is a strong function of temperature and slag chemistry. Therefore, even in the unlikely case where the slag and steel melt in at the equilibrium phosphorus distribution, the dynamic variation of that equilibrium with changes in bath temperature and slag chemistry during refining will drive further phosphorus mass transfer. The lag in the actual measured phosphorus distribution behind the calculated dynamic equilibrium distribution should give a good indication of the phosphorus mass transfer parameter for this furnace.

In order to calculate the dynamic phosphorus equilibrium, the slag chemistry and bath temperature must be known as functions of time during the period of interest. Figures 65 and 66 show the actual temperatures and slag chemistries, which were measured for one experimental heat.

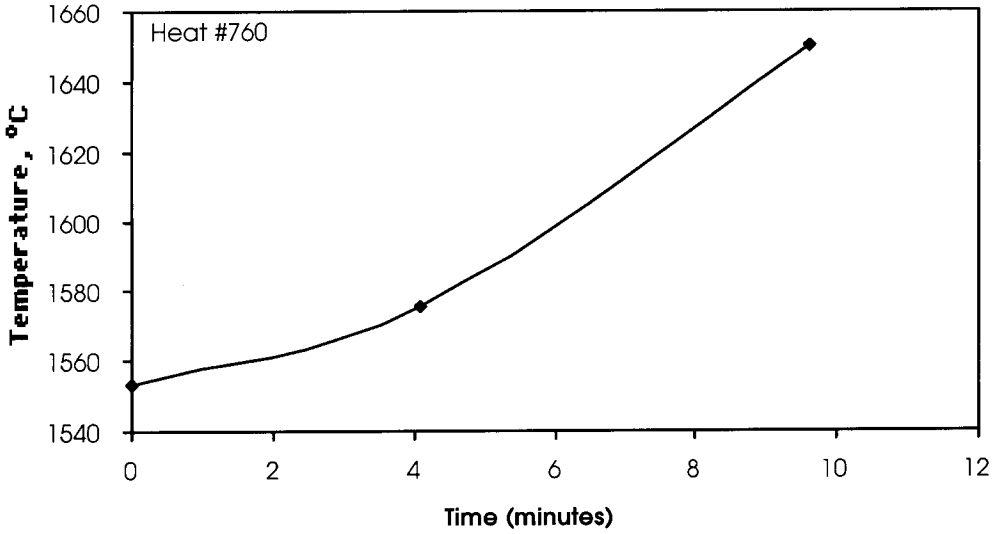

Figure 65: Bath temperature versus time.

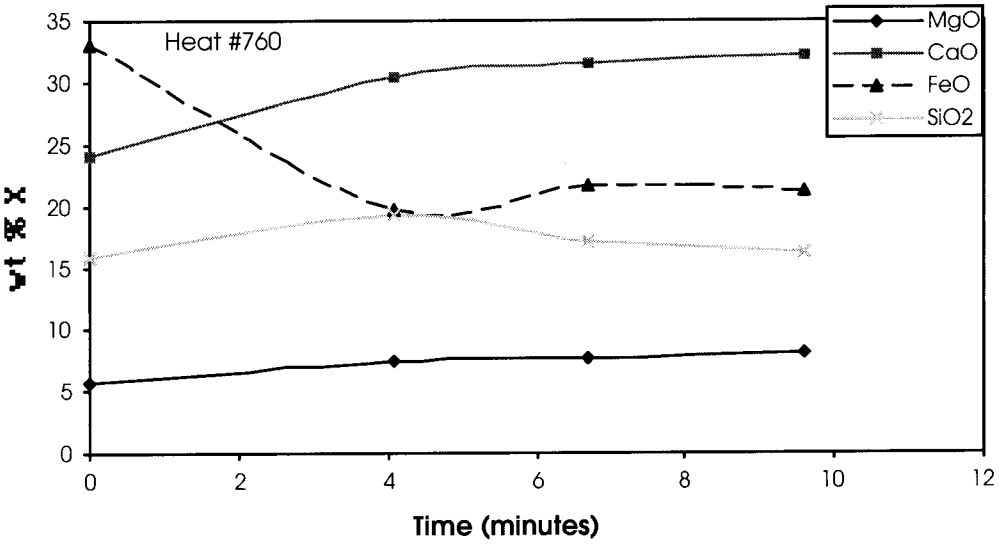

Figure 66: Slag chemistry versus time. All components are in weight percent.

The temperature profile shown in Figure 65 is fairly typical. As melt-in of the final charge nears completion, the temperature of the bath begins to increase rapidly. The slag chemistry profile indicated in Figure 66 shows similar trends to those seen in other furnaces, as will be discussed in the following sections. The initial slag formed during melting is high in FeO due to rapid oxidation of the scrap pile by injected oxygen. The

FeO content of the slag subsequently decreases due to chemical reduction via bath carbon, charge carbon, and injected carbon, as well as due to dilution by late melting components of the slag. Although all flux additions are made to the furnace prior the addition of the third scrap bucket, a significant portion of the slag can be expected to freeze off when the final charge is dropped. The continuous increase in the V ratio of the slag in Figure 66 indicates the continuous dissolution of solid lime. Both the reduction of iron oxide from the slag and the continuous dissolution and melting of solid slag components in the furnace will result in a dynamic total slag mass during the refining period. This point is further complicated by slag flushing.

Figure 67 shows the measured slag and metal phosphorus for the above heat.

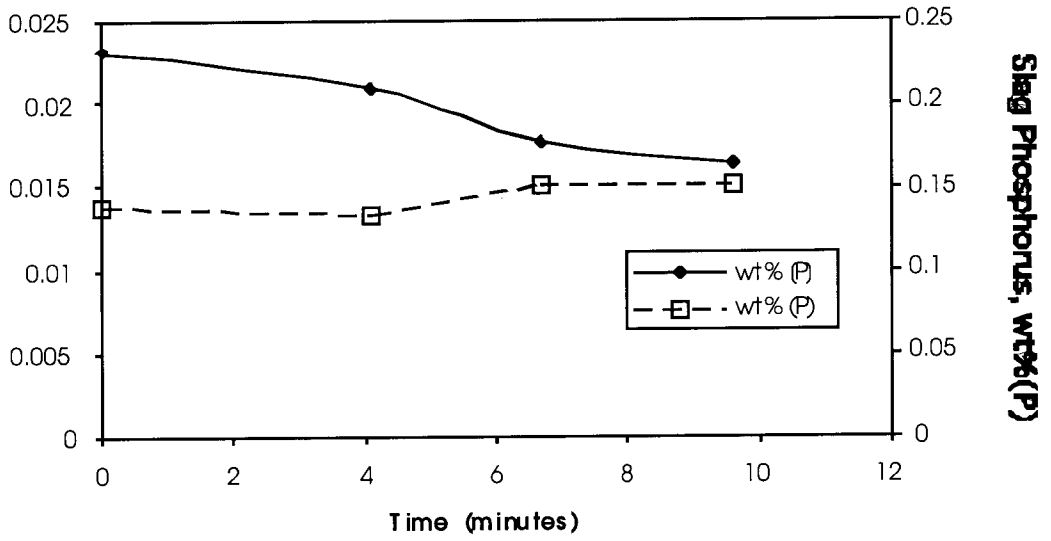

Figure 67: Slag and metal phosphorus content versus time.

Clearly, the metal phosphorus content is decreasing during the refining period for this heat. However, if negligible phosphorus losses to the gas phase are assumed, the initial simultaneous decrease in the slag and metal phosphorus content confirms that the slag weight and possibly the metal weight are increasing. In Figure 68, the slag chemistry and temperature data of Figures 65 and 66 were used to calculate the equilibrium phosphorus distribution according to two different correlations. The observed slag-metal phosphorus distribution is also shown.

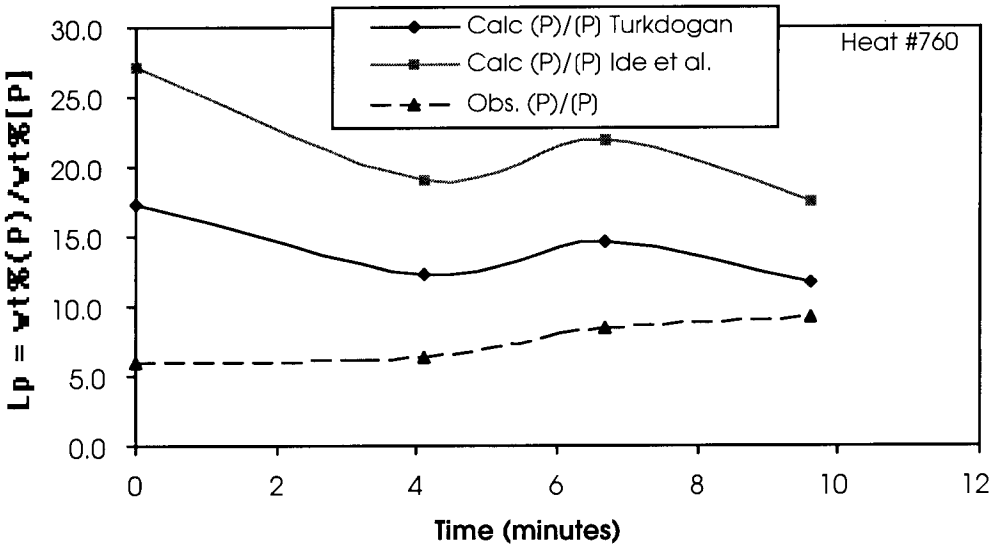

Figure 68: Calculated equilibrium and observed slag-metal phosphorus distribution versus time

Figure 68 indicates that the observed slag-metal phosphorus distribution is below the equilibrium value during the entire heat. The flux equation for phosphorus in the metal is given by equation 28:

$$\frac{\partial[\%P]}{\partial t} = -\frac{A\rho_m k_m}{W_m}\left[[\%P] - [\%P^i]\right] \qquad 28$$

Where the driving force for mass transfer is proportional to the difference between the bulk phosphorus content and the phosphorus at the metal-slag interface. It can be assumed that the slag-metal phosphorus distribution at the interface will be at the equilibrium dictated by the temperature and slag chemistry as calculated in Figure 68. In order to calculate the actual interfacial phosphorus values, some assumptions must be made regarding the masses of liquid steel and slag, which are present and regarding the total amount of phosphorus in the system. As a first approximation, it was assumed that all of the steel, 150 tons, is liquid and 10 tons of liquid slag is present. Based upon the scrap charge, it was estimated that the 150 tons of steel carried 69 pounds of phosphorus into the furnace, and the slag heel contained an additional 32 pounds of phosphorus. Based upon these assumptions the interfacial metal phosphorus content was calculated

according to the Ide et al. equilibrium correlation. The results of this calculation and the measured bulk metal phosphorus content are shown in Figure 69.

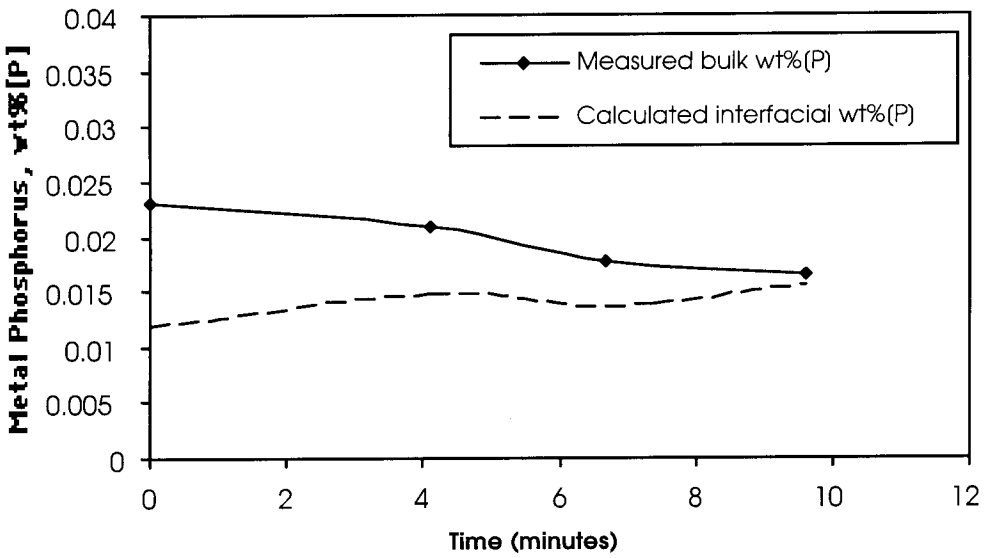

Figure 69: Measured bulk metal phosphorus and calculated metal interface phosphorus versus time

As discussed earlier, due to the variation of the equilibrium interfacial phosphorus value, the flux equation for phosphorus transfer in the steel can not be integrated analytically. However, the flux equation can be integrated numerically as a sum of integrals over discrete time intervals according to the following equation:

$$-\frac{A\rho_m k_o}{W_m} t = \sum_n \int_{[\%P]_n}^{[\%P]_{n+1}} \left[\frac{[\%P]_{n+1} - [\%P]_n}{[P]_{n+1} - [\%P]_i} \right] d[\%P] \qquad 54$$

As with the analytical solution presented in Chapter 4, equation 54 can be rearranged such that the mass transfer parameter is isolated on the left hand side of the equation:

$$Ak_o t = -\frac{W_m}{\rho_m} \sum_n \int_{[\%P]_n}^{[\%P]_{n+1}} \left[\frac{[\%P]_{n+1} - [\%P]_n}{[P]_{n+1} - [\%P]_i} \right] d[\%P] \qquad 55$$

Therefore, by plotting the right hand side of equation 55 versus time, the slope of the resulting line should be equal to the mass transfer parameter. As mentioned in Section 4.4.1, the term on the left hand side of equation 54 has been used in previous kinetic evaluations of oxygen steelmaking vessels. The term:

$$\frac{A\rho_m k_o}{W_m}$$ 49

has been shown to remain roughly constant for different oxygen steelmaking vessels. This is due to the scaling effect of vessel size and oxygen blowing rate in oxygen steelmaking vessels. The same scaling effect is not expected to hold for electric arc furnaces. Thus, this term is not as useful in defining mass transfer in the EAF.
In Figure 70, the summation expressed in equation 55 was plotted versus time.

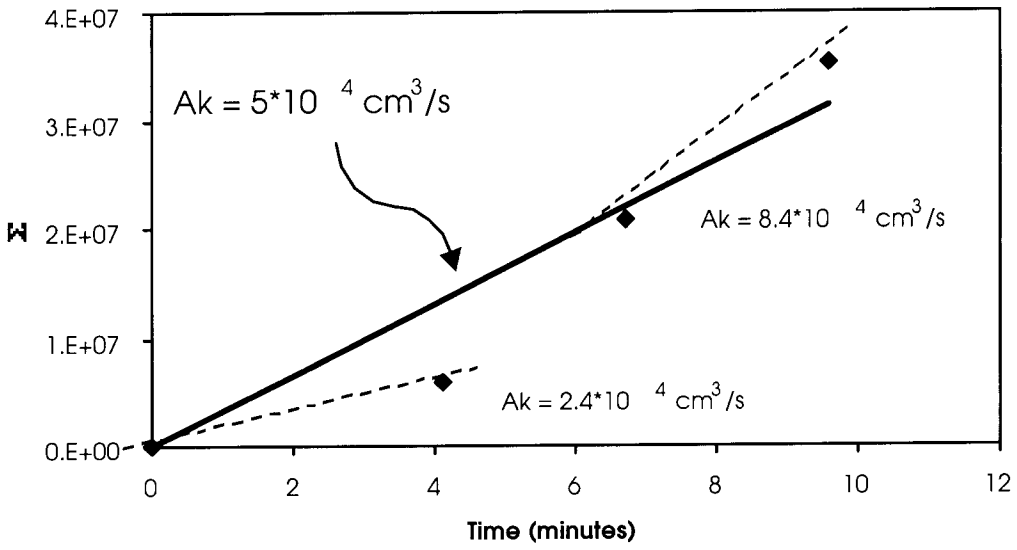

Figure 70: RHS of equation 55versus time. The observed slope is seen to vary between $2.4*10^4$ cm^3/s and $8.4*10^4$ cm^3/s.

When mass transfer parameters calculated in Figure 70 are converted to the form of the rate parameter expressed in equation 49, it is found that rate ranged between 0.066 min^{-1} and 0.24 min^{-1}. By comparison, equation 49 has been evaluated for the BOF and was found to be on the order of 1 min^{-1}. The average value of 0.15 min^{-1} for this trial is in good agreement with the prediction that stirring in a modern EAF will be similar to, but less than that in a BOF. When the interpolated continuous curves in Figure 70 are considered in addition to the discrete experimental points, the resultant plot is given in Figure 71.

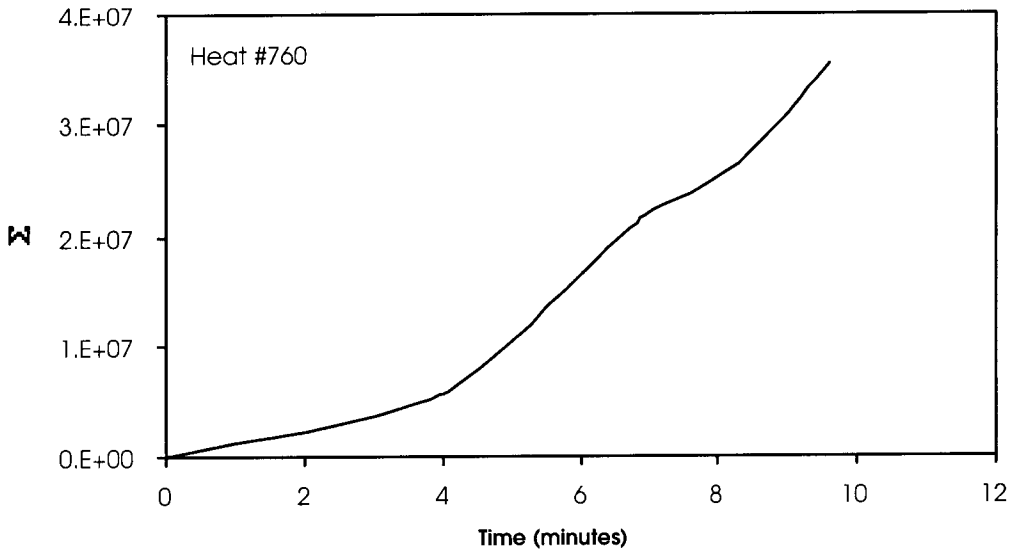

Figure 71: Continuous evaluation of equation 55 along continuous curves in Figure 69.

The curve in Figure 71 suggest that in the late stages of melt-in and in the early stages of the refining period, mass transfer is significantly slower as compared with later in the heat. This is expected as the slag viscosity is continually decreasing as the temperature is increasing. Unmelted solids in both the steel and slag will inhibit fluid flow in both phases. In addition, the rate of oxygen injection is increased by approximately 30% during the refining period as compared with during melting. The oxidation of carbon in the melt by FeO in the slag and injected oxygen will be enhanced by a more fluid slag and increased oxygen blowing. Increased carbon monoxide generation will in turn further increase fluid flow and slag metal mixing leading to a self amplification of the mass transfer parameter.

The temperature and slag chemistry profiles of a second heat are shown in Figures 72 and 73.

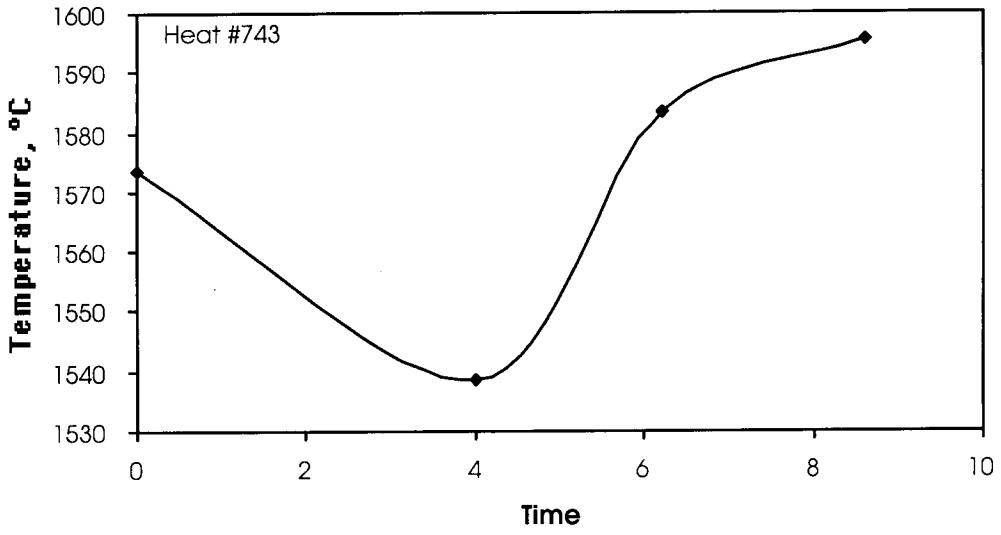

Figure 72: Bath temperature versus time

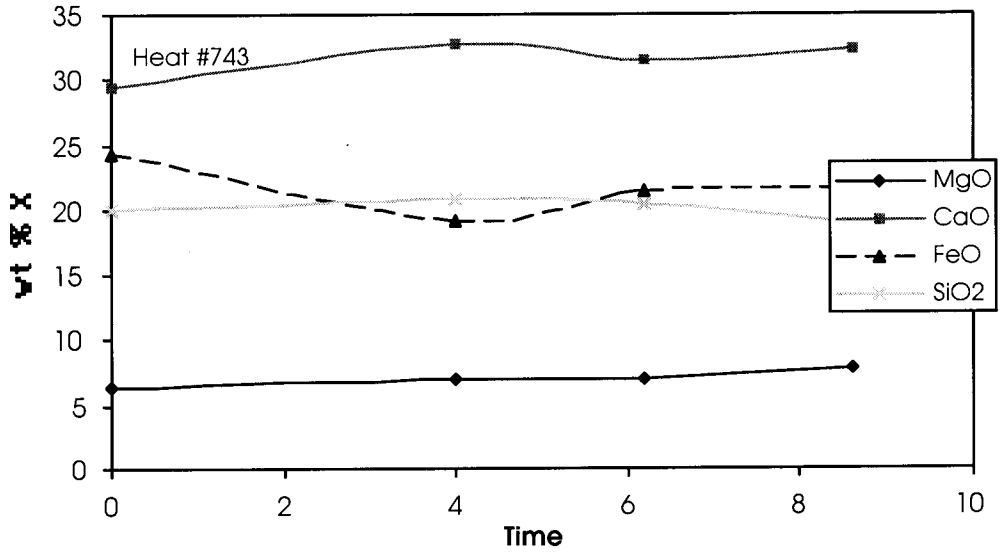

Figure 73: Slag chemistry versus time. All components are in weight percent.

The temperature profile in Figure 72 indicates an additional complication of these experiments. The 35 °C drop in temperature between the first and second sample is most likely the result of a cave in of unmelted 'cold' scrap, which had been stuck against the side wall of the furnace. For many common grades produced by PST, up to 12% iron is included in the scrap mix. This material is typically among the more dense components of the scrap mix and can contain up to 0.1wt%P. The effect of late melting scrap on the

bath temperature and chemistry will also have a secondary effect on the slag chemistry. This is shown in Figure 73. The lower V ratios indicated in Figure 73 as compared with Figure 65, suggest that a greater portion of the lime remained solid within the furnace until later in the heat. Based upon a heat balance of only the solid and liquid steel phases (neglecting the slag phase), the observed temperature drop correlates to approximately 14,000 lbs of late melting scrap. The metal and slag phosphorus are plotted as a function of time for this heat in Figure 74.

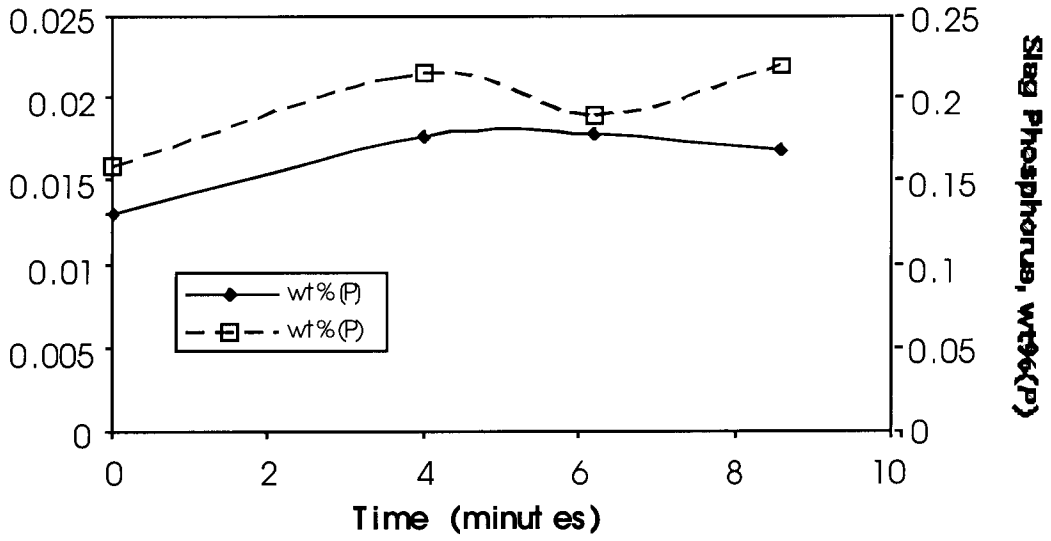

Figure 74: Slag and metal phosphorus versus time.

The slag and metal phosphorus increase between the first and second samples in Figure 74 is consistent with the melt-in of approximately 14,000 lbs of scrap or iron with 0.1wt%P. The equilibrium interfacial metal phosphorus content was calculated assuming a constant slag mass but with a changing liquid steel mass. In the calculation of the first point, 14,000 lbs of scrap with 0.1%P were not included in the phosphorus balance for the furnace. It was assumed that all scrap and the contained phosphorus was melted in at the second data point at 4 minutes. The results of the interfacial phosphorus calculation are shown in Figure 75.

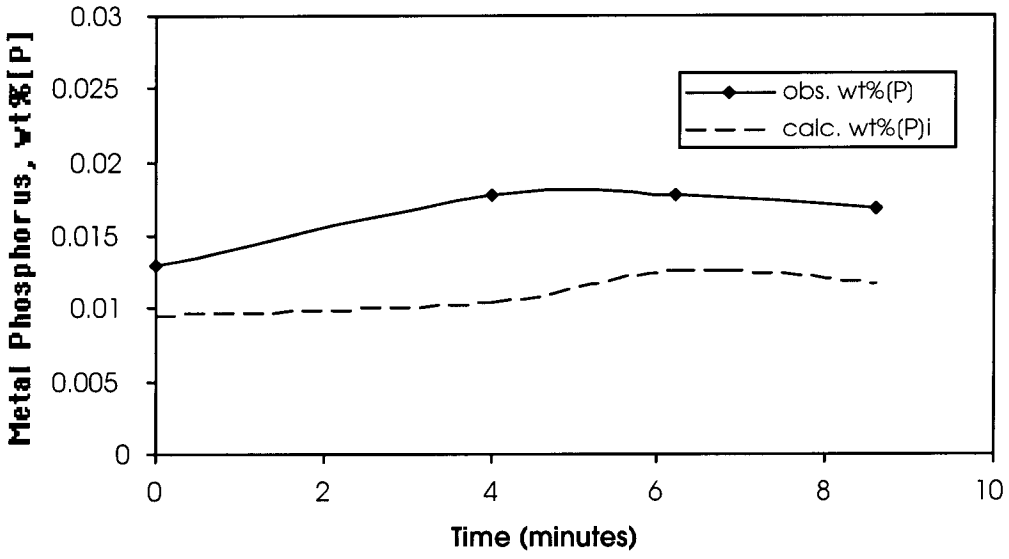

Figure 75: Measured bulk and calculated interfacial metal phosphorus versus time.

Clearly, the uncertainties in the masses of the liquid steel and slag introduce significant error in the first 4 minutes of Figure 75. The metal phosphorus increases between the first and second samples despite the clear driving force for dephosphorization, i.e. the interfacial phosphorus is lower than the bulk phosphorus. The continuous smoothed curves in Figures 74 and 75 above are probably poor representations reality. It is more likely that the initial metal phosphorus increase, due to the late melting slag, was actually greater than is shown, and that some phosphorus transfer to the slag had already occurred by the time of the second sample. It is possible to develop a more complex scrap melting model in order to accurately evaluate these data. However, such a complex model will not be used here in the determination of an experimental parameter.

For one trial heat, a controlled addition of 100 lbs of commercial ferrophosphorus was made to the furnace shortly after melt-in of the final bucket. Temperature readings and samples were taken of the slag and metal immediately prior to the addition and as a function of time thereafter. The added material in this trial was an Fe-22%P lump material, which was expected to cause an instantaneous increase of 0.007 wt%P in the metal bath. The temperature and slag chemistry profiles for this heat are shown in Figures 76 and 77.

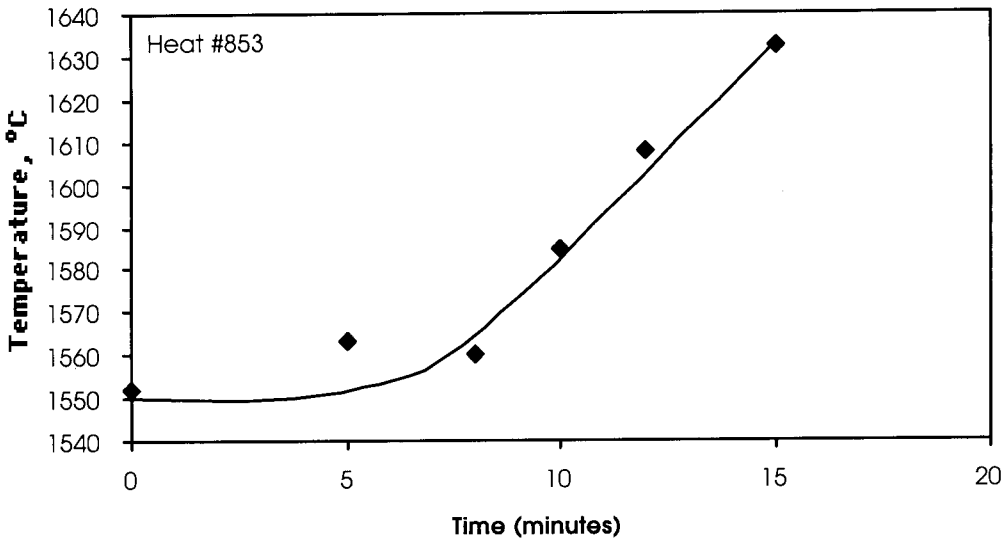

Figure 76: Temperature versus time.

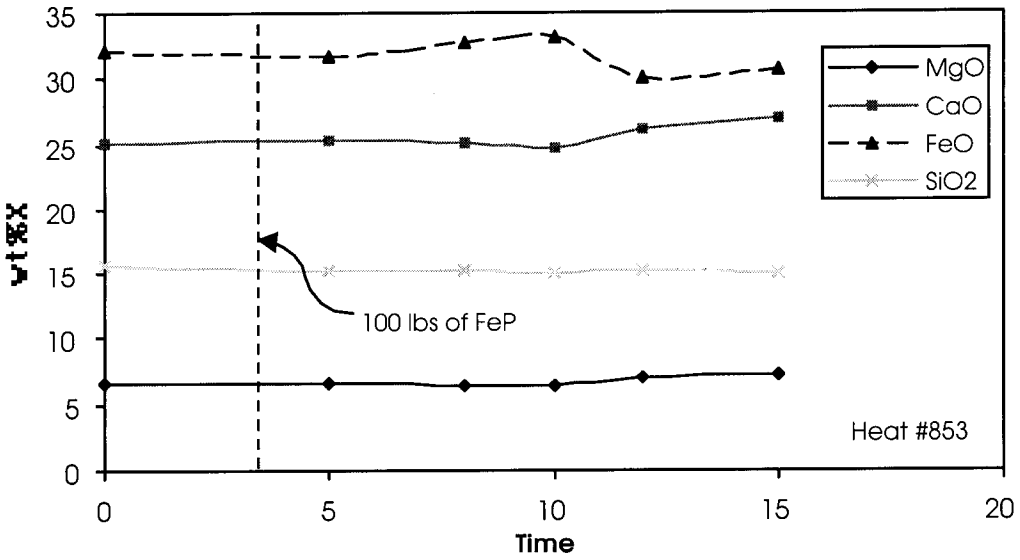

Figure 77: Slag chemistry versus time. An addition of 100 lbs was made at t = 3 minutes.

The measured slag and metal phosphorus contents are plotted versus time in Figure 78.

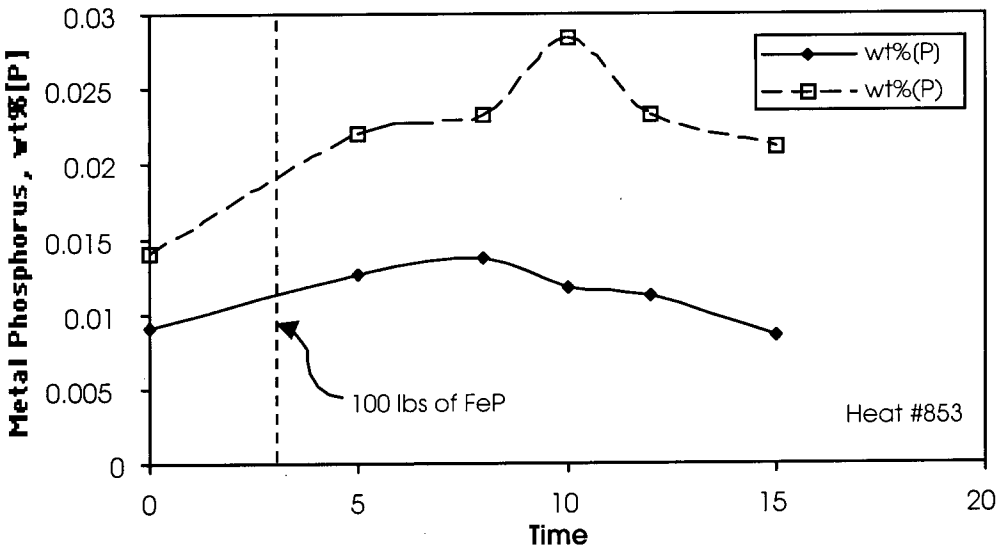

Figure 78: Measured bulk slag and metal phosphorus content versus time.

The variations in the slag and metal phosphorus shown in Figure 78 are somewhat unexpected and indicate that continuous melting of solids in both the slag and metal was occurring after the addition. From the temperature profile in Figure 76, it is likely that a significant amount of unmelted scrap was present until the time of the third sample at t = 8 minutes. The simultaneous decrease in the slag and metal phosphorus after t = 10 minutes suggests that continuous dissolution of unmelted slag is leading to the dilution of the slag phosphorus. During this particular heat, very little slag flushing occurred. Therefore, an approximate conservation of mass for phosphorus can be assumed for the furnace for this heat. In order to maintain a constant total mass of phosphorus in the furnace across the final 4 samples, the assumed mass of slag was increased by 25% in each of the last two points. The behavior of the melt in the first 8 minutes is too complex to model at this time without making significant assumptions. Therefore, only the final four samples were used in evaluating the mass transfer parameter during this heat. The measured bulk and calculated equilibrium interfacial metal phosphorus contents are plotted versus time in Figure 79.

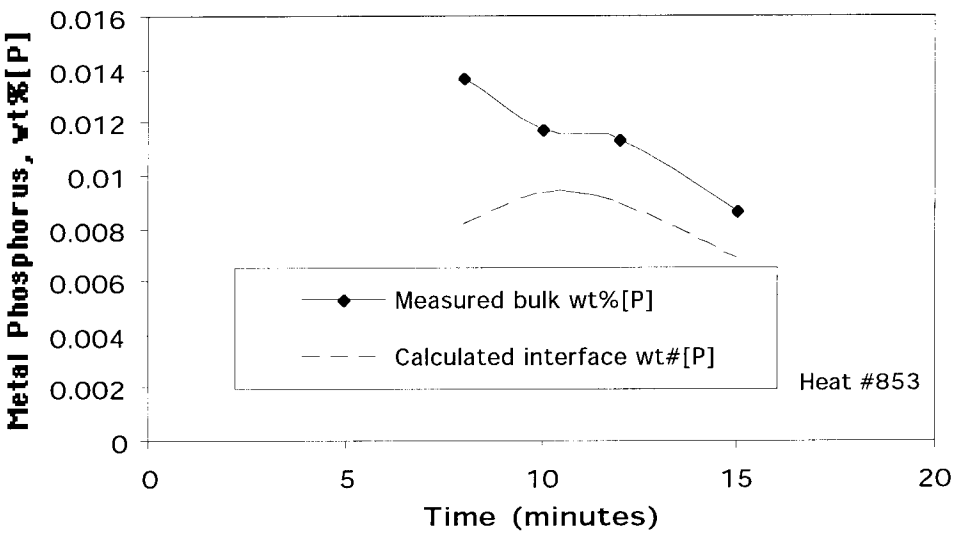

Figure 79: Measured bulk and calculated interfacial phosphorus content versus time. Only the final four samples of this heat are considered due to uncertainties in the amounts of solids in the steel and slag phase.

The calculated phosphorus content at the steel-slag interface shown in Figure 79 is significantly influenced by the assumption of a varying slag weight. Furthermore, the ability to accurately determine the deviation of the bulk phosphorus from that at the interface is critical in determining the driving force for mass transfer. Uncertainty in the driving force for mass transfer leads to obvious difficulties in determining the mass transfer parameter. In Figure 80 the RHS of equation 5[illegible] is plotted versus time assuming the concentrations indicated in Figure 79.

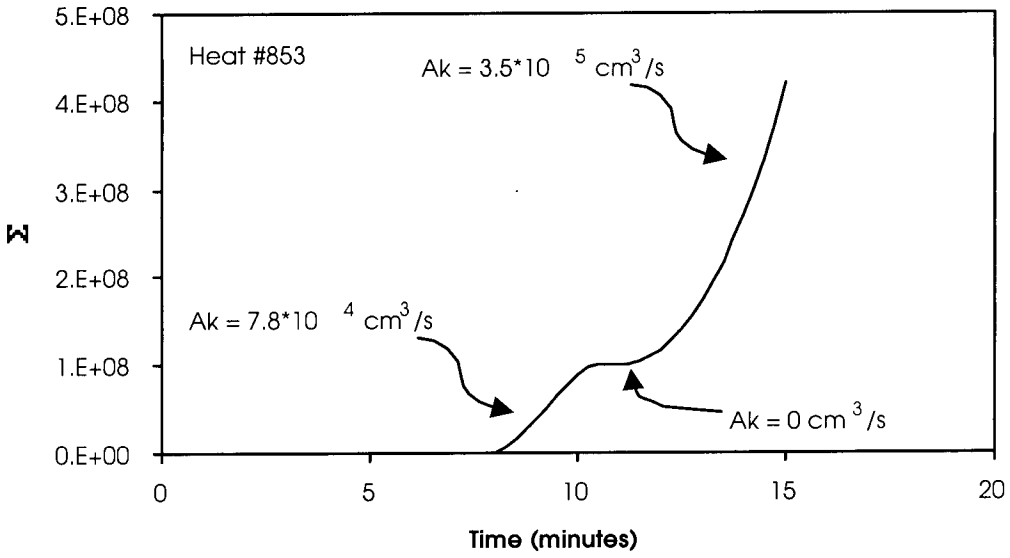

Figure 80: Continuous evaluation of equation 55 according to the data in Figure 79.

As in Figures 70 and 71, Figure 80 shows a continuously varying mass transfer parameter. It is believed that the nearly all of the steel charge was liquid during the period, which is evaluated in Figure 80. Thus, the initial mass transfer parameter is higher than was calculated in the early stages of Figure 80. Between 10 and 12 minutes the rapid increase in temperature results in a drop in the equilibrium phosphorus distribution and interfacial metal phosphorus. Thus, there is a temporary slowing of the rate of mass transfer as the bulk and equilibrium metal phosphorus contents converge. In the final portion of the sampling period, the temperature increase leads to an in crease in both the lime content of the slag and in the total slag mass. In this final period, the calculated mass transfer parameter is very rapid, approaching that which is observed during oxygen steelmaking.

However, this calculation should be viewed with a high degree of skepticism. The equilibrium interfacial metal phosphorus content is inversely proportional to the liquid slag mass. The deviation of the bulk metal phosphorus from that at the interface defines the driving force for mass transfer. Under estimation of the liquid slag mass, and thus the driving force, would tend to exaggerate the mass transfer parameter. Therefore, the stated uncertainty in the precise amount of liquid slag in the furnace is likely to cause some degree of uncertainty in the calculations shown in Figure 80.

Table 4 lists the results of the trials at PST in terms of the three measures of mass transfer kinetics, which have been used in the present study, the apparent mass transfer coefficient, the mass transfer parameter, and mass transfer time constant of equation 49:

Table 4: Results of Mass Transfer Trials at PST

	Mass Transfer Coefficient, ko (assuming furnace area) cm/s	**Mass Transfer Parameter, A*ko** cm^3/s	$\frac{A\rho_m k_o}{W_m}$ min^{-1}
High Value	0.99	$3.5*10^5$	1
Low Value	0.05	$1.7*10^4$	0.05
Best Fit Value	0.25	$8.7*10^4$	0.25
BOF Laboratory Expts.	--- ≈ 0.01	--- ≈ 0.07	1 ≈ 0.16

In Table 4, the apparent mass transfer coefficient was calculated for the trials at PST assuming a slag-metal area equal to the cross sectional area of the furnace. The calculated apparent mass transfer coefficient for the PST furnace ranged between 0.05 and 1 cm/s. The laboratory kinetic experiments performed according to the procedure outlined in Section 3.4 were conducted in a very well mixed system. It is likely that the bulk fluid flow in the EAF is much lower than that in the laboratory scale experiments. Based on this consideration and the calculated values in Table 4, it is likely that the actual slag-metal area is roughly 50 to 100 times greater than the cross sectional area of the furnace. Considering the volume of gas, which is injected and/or produced in the furnace, it is reasonable to expect that slag-metal mixing will result in a two order of magnitude increase in the slag-metal area.

5.2 North Star Steel - Texas EAF Trials with DRI/HBI

A series of plant trials with various scrap substitute materials were completed at North Star-Texas. The purpose of the trials at NSST was to determine the effects of DRI/HBI metallization and carbon content, upon slag chemistry, and thus upon phosphorus control during EAF steelmaking. The primary influence of these factors was predicted to be upon the melt-in FeO content of the slag. Although, the contribution of unreduced iron oxide from DRI/HBI to the EAF slag would result in a larger total slag mass and highly oxidizing conditions, excessive amounts of FeO in the slag can dilute the basic components of slag resulting in a low equilibrium phosphorus distribution. The thermodynamics of the phosphorus reaction were discussed in detail in previous sections.

In addition, excessive amounts of iron oxide in the slag can interfere with slag foaming, increase electrode consumption, accelerate refractory wear, and result in costly yield losses.

All commercial direct reduced materials contain some amount of unreduced iron oxide within the final product. In addition, most conventional materials contain some quantity of carbon, deposited late in the direct reduction process, in the form of either graphite and/or iron carbide. Both the amount of metallization obtained, and the specific amount of deposited carbon vary from one commercial product to the next. Most materials are engineered such that the minimum quantity of deposited carbon will balance the moles of unreduced iron oxide in the material. Additional carbon beyond what is required for the final reduction of unreduced iron oxide will either enter the liquid steel melt, react with the slag, or be available for combustion depending upon the method of addition and melting in the electric furnace.

Goldstein and Fruehan [54], as well as others, have conducted investigations of the final reduction of unreduced iron oxide by deposited carbon in commercial direct reduced pellet products. Qualitatively, this reaction has been shown to be very fast at temperatures above 1100°C. Goldstein et al. concluded that the rate of this final reduction during rapid heating was most likely limited by heat transfer. In the experiments of Goldstein et al., both commercial and more homogenous repressed pellets were dropped into a liquid slag or a hot empty crucible. The rate of the reaction was measured by measuring the rate of evolved gas. Under all conditions studied, this reduction took between 10 to 20 seconds, which is similar to the time required for the heating of the pellets from 800 to 1500 °C. Figure 81 shows the results of two experiments by Goldstein et al.[54] where the fraction of conversion of the unreduced iron to metallic iron is measured as a function of time. Figure 82 shows the results of the heat transfer model used by Goldstein et al. showing that the heating rate is very close to the rate of final reduction within the pellets during heat up.

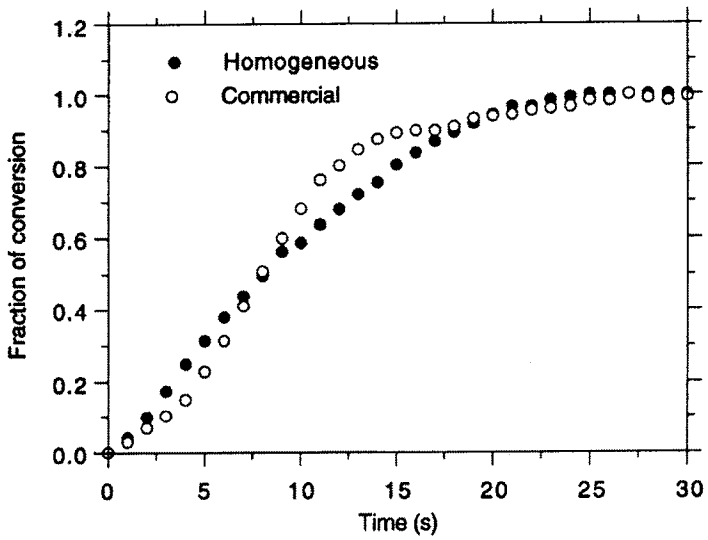

Figure 81: Degree of final reduction of residual iron oxide and deposited carbon in commercial DRI. Data adapted from Goldstein et al. [54]

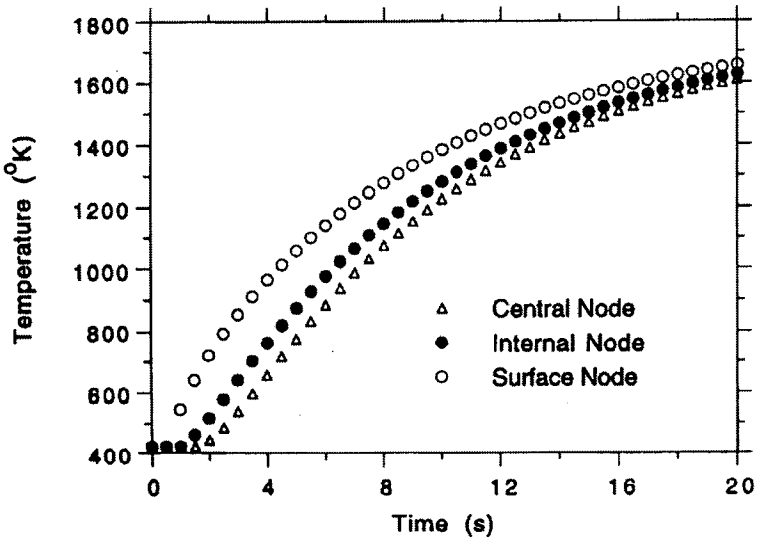

Figure 82: Temperature profile within DRI pellets as modeled by Goldstein.[54]

From the results of Goldstein and Fruehan [54], it can be concluded that the final reduction of iron oxide by deposited carbon in DRI will occur prior to melting during either batch or continuous charging into the electric furnace. Therefore, for materials, which are oxygen limited or contain enough carbon to balance the quantity of unreduced iron in the material, no iron oxide should remain in the material at the time of melting. The fate of excess deposited carbon in direct reduced materials is somewhat less clear.

For the conditions of continuous charging, excess carbon contained in DRI may react directly with FeO contained in the slag. For batch charging practices, the excess carbon will most likely first enter the liquid steel melt and then react with the slag layer or injected oxygen during the refining period.

The Circal HBI material produced by Cliffs Reduced Iron, contains no carbon as it is reduced via hydrogen. However, this material contains unreduced iron oxide similar to other conventional direct reduced materials. Due to the quality of the ore from which it is produced, the total number of iron units available in this material is very high (>97% total iron.) However, the total number of recoverable units may be lower than for carbon containing material. As described in Chapter 4, several laboratory experiments were conducted where Circal HBI was melted in a high purity argon atmosphere. In these melts, the Circal material produced a metallic yield of approximately 85%. The remaining 15% of the material formed a very high FeO slag layer, which did not react appreciably with the metal. Based on the discussion above, it is likely that when the Circal material is melted in the electric furnace, the residual FeO in the material will first report to the slag phase to be reduced and/or flushed from the vessel during melting and refining. The potential contribution of additional FeO to the slag by DRI/HBI, and the subsequent rate and degree of reduction of those iron units by carbon in the steel bath and injected carbon comprised the focus of the trials at NSST.

Similar to the trials at PST, slag and metal chemistry and temperature data were collected as a function of time during the refining period for the trials at NSST. Data were collected for heats with the following scrap charges:

Table 5: Trial Heats Conducted at NSST

# of Trial Heats	Scrap	Pig Iron	AIR-DRI	Circal HBI
2	100%	0%	0%	0%
10	75%	0%	25%	0%
10	72%	14%	0%	14%
5	70%	10%	0%	20%
5	80%	0%	0%	20%

The portion of the charge referred to generically as 'scrap' was a combination of plate and structural, #2 shredded, and #2 heavy melting scrap steels. Within each set of trials, the source and ratios of the different scrap materials were held constant in attempt to maintain some consistency within the trials. The pig iron, DRI, and HBI materials used in these trials possessed significantly different carbon and phosphorus contents. The chemistries of these materials are listed below:

Table 6: Chemistries of Scrap Substitute Materials used in NSST Furnace Trials.

Material	Fe_t	FeO	C	SiO_2	Al_2O_3	CaO	P
AIR-DRI	91.96	5.79	2.3	1.65	0.61	0.74	.025
Circal-HBI	97	12	0	1.03	0.2	0.1	0.028
	Fe_t	FeO	C	Si	S	CaO	P
Pig Iron	95.1	0	4	0.5	0.04	0	0.08

The AIR-DRI contains more than twice as much carbon as is required for the reduction of the contained FeO. A one to one weight ratio mixture of Circal HBI to Pig Iron also provides twice the amount of carbon required for the reduction of the FeO contained in the Circal. A two to one weight ratio of Circal HBI to pig iron results in an approximate molar balance of the iron oxide in Circal with the carbon in the pig iron.

For the two trial heats with a 100% scrap charge and the 10 trial heats with 25% DRI, a minimum of three slag samples were taken during the refining period. A minimum of two metal samples and two temperature readings were taken as soon as the most of the metallic charge had melted in. For some heats, more samples were obtained. In all cases the sampling period ranged from 10 to 35 minutes in duration with 3 to 8 minutes between samples. For the 20 trial heats with HBI and Pig Iron, only two samples were obtained from both the metal and slag. Some important operating parameters of the furnace used in the NSST trials are listed below:

Table 7: Operating Parameters of NSST - EAF

Power	AC	
Capacity	150 tons -	3 bucket charge
Diameter	23 feet	
Tap to Tap	Approx. 85 minutes	
Typical Oxygen Usage	42,000 SCF Total ≈ 300 SCF/Ton	
Injected Carbon*	2000 lbs	*Injected during refining period
Charge Carbon*	2000 lbs	*charged after 1st bucket
Flux	CaO- 7000lbs –	added during melt-in of 1st, 2nd and 3rd buckets
	MgO-2800lbs –	1/2 back charged during turn around and 1/2 charged during refining period
Slag Flushing	Highly variable ≈ 10,000 to 18,000 lbs	
Hot Steel Heel	5 to 10 tons	
Slag Heel	4 to 6 inches ≈ 8600 lbs to 11,000 lbs	

As explained above, the purpose of the trials at NSST was to attempt to determine the effects of DRI/HBI metallization and carbon content, upon slag chemistry. Multiple slag samples during each heat were desired in order to determine the bulk changes in the slag chemistry from melt-in until tap. Typically, the power on time between the dropping of the third bucket and the time at tap is on the order of 40 minutes. A bulk liquid slag phase is formed approximately 10 to 15 minutes after the dropping of the third bucket. As was exhibited for the trial heats with 100% scrap and a scrap – DRI charge, the maximum length of the slag sampling period is on the order of 20 to 30 minutes. Unfortunately, for the trial heats with HBI and Pig Iron, the time interval between the two samples ranged from 3 to 15 minutes. Therefore, the heats with Circal HBI and Pig Iron were not as useful in evaluating the dynamics of the slag system as had been hoped. In addition, it should be pointed out that a significant modification of the furnace oxygen injection system was made between the completion of the trials with DRI, and the trials with HBI and Pig Iron. This unfortunately complicates direct comparison of the DRI and HBI heats. The equipment modification was also accompanied by an upgrade of the control and monitoring system, which allowed for the detailed recording of the oxygen and natural gas usage for each heat.

Some very interesting observations were made from the first sets of trial heats conducted with 100% scrap and 25%DRI – 75%scrap. In contrast to a BOF, the data from these heats indicate that the particular furnace practice used at NSST melts-in at a fairly high FeO level in the slag, which is reduced as the heat proceeds. A similar trend can be seen clearly in the data from PST shown in Figure 66. This decline in the FeO content of the slag is a combination of actual reduction of the FeO from the slag via reaction with the steel melt and injected carbon, as well as continuous flushing and dissolution of lime and MgO additions. The slag chemistries of two heats as are plotted versus time are shown in Figures 83 and 84.

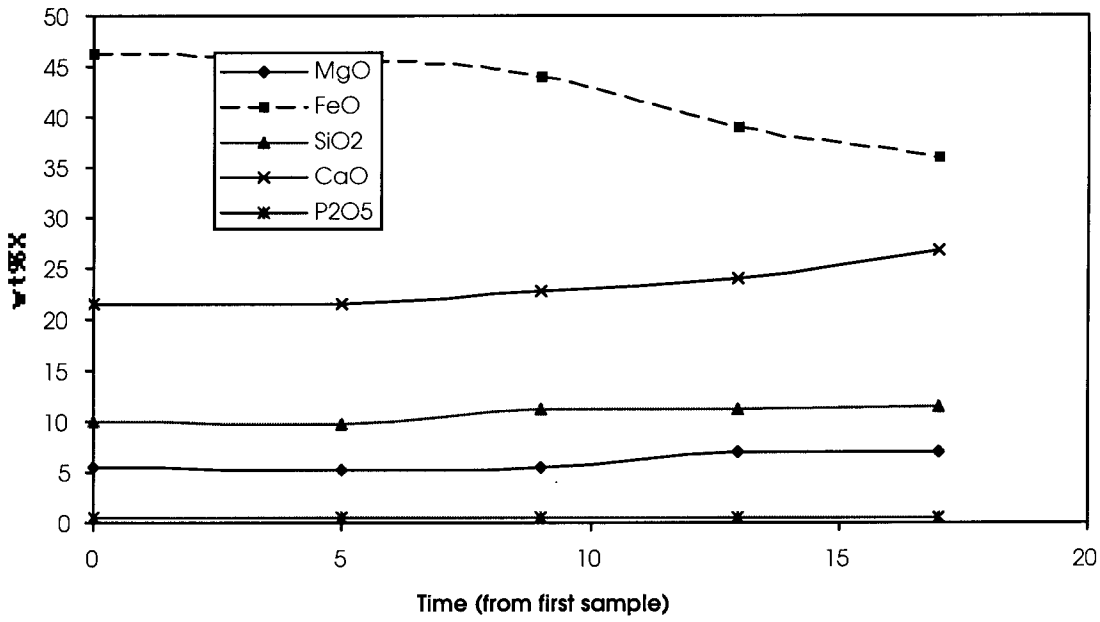

Figure 83: Wt% of slag component X versus time for a 100% scrap heat. The first sample was taken 15 minutes after the dropping of the third bucket.

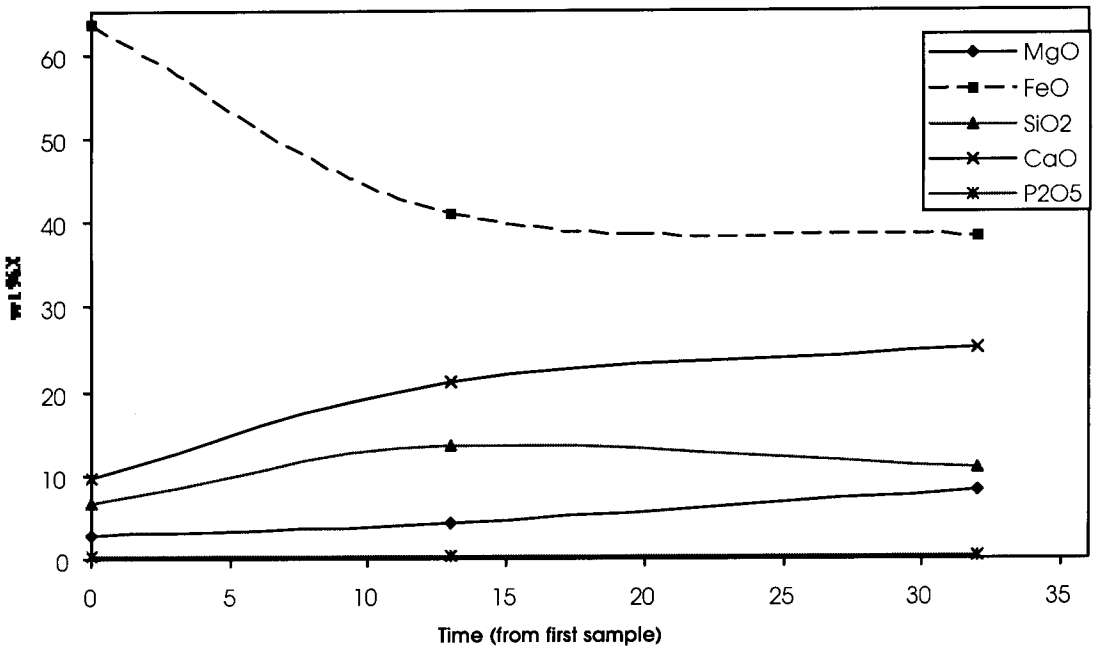

Figure 84: Wt% of slag component X versus time for a 25% DRI – 75% scrap heat. The first sample was taken 7 minutes after the dropping of the third charge.

The trends observed in Figures 83 and 84 will be discussed in greater detail in a later section of this paper. These data are presented here only to give the reader an indication of the trends, which were observed in these trials. Toward the end of the refining period, the slag chemistry appears to approach a steady state composition. No flux additions were made late in the refining period for any of the heats at NSST. It is likely that all of the metallic charge, and most of the flux additions were molten by the time of the final slag sample. Also, due to the consistent availability of final slag chemistry data for all trial heats, an attempt was made to identify trends in the final FeO contents of the slags for the different scrap charges. The average yield and average final FeO content of the slag for each of the different charge mixes are shown in Table 8.

Table 8: Average Cast Tons Yield and Final Furnace FeO for the Various Scrap Charge Mixes of the NSST Trials

Scrap Mix	Yield	Final wt% FeO in the Slag	Ratio of Carbon : FeO in Scrap Substitute Materials
100% Scrap	91.6 %	42.5 wt%	N/A
25% AIR-DRI - 75% Scrap	89.5 %	37.4 wt%	2:1
14%Circal - 14%Pig Iron - 72% Scrap	86.4 %	37.4 wt%	2:1
10%Pig Iron - 20% Circal – 70% Scrap	79.5 %	42.1 wt%	1:1
20% Circal – 80% Scrap	85.12 %	46.5 wt%	0:1

The yield listed in Table 8 was calculated as the number of quality cast tons per ton of charge material. However, significant additional yield losses can occur between the furnace and the billet yard, as suggested by the apparent lack of correlation between iron loss to the slag and cast ton yield. A yield term based upon cast tons of good billets, averaged over a large number of heats, is a very good indicator of overall steel plant performance. However, this term will not be useful in evaluating the relative performance of the electric furnace for different charge materials, unless the study is conducted over a large number of heats in a single sequence. For a study such as the present one, a much better indicator of furnace performance is the number of tons of liquid steel tapped to the ladle per ton of charge material. Unfortunately, ladle weights could not be measured during these trials.

Another furnace performance parameter, which is closely related to furnace yield is the FeO content of the slag. Loss of iron units to the slag during melting that are not later recovered, represents the largest single source of yield loss for the electric furnace. Therefore, in Table 8, there does appear to be a correlation between the final FeO content of the slag with the scrap charge mix. As mentioned earlier, additional oxygen injection capacity was added to the furnace between the trials with DRI and those with HBI. However, a simultaneous increase in the amount of charge carbon should have more than compensated for the extra oxygen in the system. Due to these inconsistencies between the trials, only qualitative comparisons will be made between these trials. According to the data in Table 8, as the molar ratio of carbon to iron oxide decreases from 2:1 to 1:1 to 0:1, the amount of iron oxide in the slag increases. In this ratio, only additional carbon introduced with the metallic charge, either in the DRI itself or in pig iron, is considered.

For all of the trial heats with Circal HBI, the same charge carbon practice was used. Therefore, charge carbon was not considered a variable in evaluating these trials. The amount of injected carbon, which was used in each heat was regulated by the furnace operator. Although this was a variable in these trials it is not a quantity, which is measured at NSST. Therefore, the amount of injected carbon was assumed to be approximately constant from heat to heat. It will be demonstrated later, injected carbon, may not play a major role in determining final FeO content of the electric furnace slag. Therefore, it was assumed that by neglecting the variations in the amount of injected carbon significant error would not result. On average, the 10 heats with 25% AIR-DRI and the 10 heats with 14% HBI-14% pig iron showed a decrease in the in the final FeO content of the slag as compared to the heats with a 100% scrap charge. Due to the scatter in the data and the described changes in furnace equipment and practice, the fact that these two scrap mixes showed the same average final FeO content should be considered coincidental. However, the decrease in final FeO content as compared with heats with 100% scrap can be explained. Both DRI and HBI will significantly densify batch charges of loose scrap. A more dense scrap charge will be much less susceptible to excessive oxidation by injected oxygen during melting. Also, these scrap mixes provided an excess of more than 200 pounds of carbon per ton of scrap substitute material, and should have significantly increased the melt-in carbon content of the steel bath.

Also of interest is the fact that the heats with 10% pig iron and 20% Circal HBI exhibited a very similar final FeO content as the heats with a 100% scrap charge. Although the HBI and pig iron should have helped to densify the scrap charge, this combination should have contributed almost no excess carbon to the steel bath.

The heats with 20% Circal HBI and no pig iron showed an increase in the final FeO content of the slag as compared with all other heats. The four percent increase in FeO for these heat compared with the heats with 100% scrap shown in Table 8, actually under represents the increase in the loss of iron units to the slag. For the heats with 20% HBI and no pig iron, the flux additions were increased from 7000 lbs of CaO and 2800 lbs of MgO to 9700 lbs of lime and 3000 lbs of MgO. This modification in flux practice was made in order to prevent excessive refractory wear by a highly fluid slag, and to ensure sufficient lime was present to control phosphorus and sulfur levels in the steel. Ignoring the effects of slag flushing, the increase in the wt% of FeO in the slag and the increase in

the total slag weight result in an increase in the actual pounds of iron oxide in the slag by nearly forty percent! The assumption of no slag flushing is a poor representation of the actual system. Therefore, the calculated 40% increase in iron units in the slag represents an upper limit of the possible change. Again, the apparent lack of correlation between the quality cast tons yield, which is listed in Table 8, and the iron losses to the slag suggests that this calculated yield is a poor indicator of furnace performance.

Because the 20 trial heats containing HBI were conducted in a sequence, and very few parameters were varied, an attempt was made to evaluate these data in a more quantitative manner. In Figure 85, the final iron oxide content of the slag is plotted versus the actual pounds of Circal HBI, which were charged in the furnace for each heat.

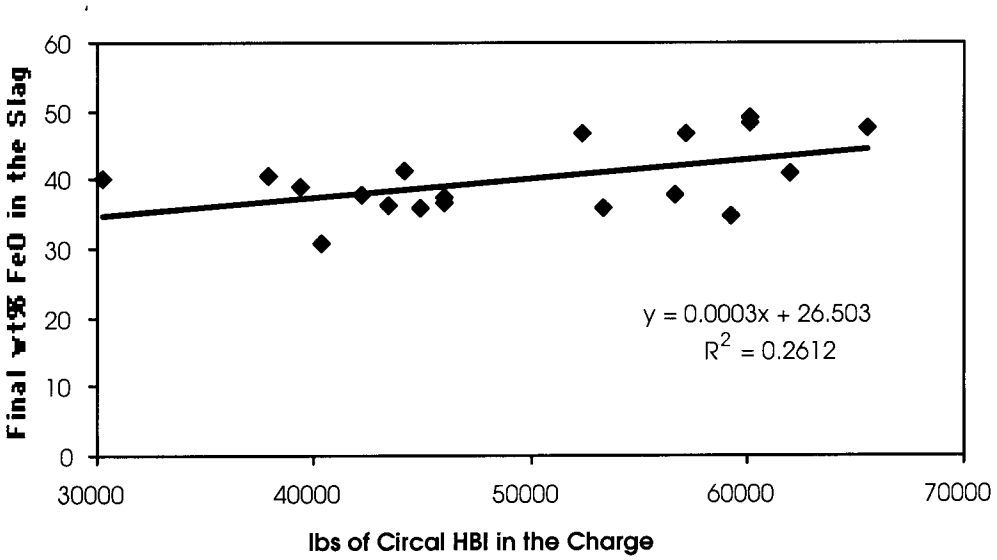

Figure 85: Final wt% FeO in the slag versus pounds of Circal in the charge.

A distinct increase in the final FeO content of the slag as a function of HBI in the charge can be detected. However, the large amount of scatter in the data suggest that other factors are influencing the slag chemistry.

In most modern electric furnace operations oxy-fuel burners and direct oxygen injection are used to supplement electrical energy input in order to increase melting rate and furnace productivity. At NSST both oxy-fuel burners and direct oxygen injection are used. Oxygen is injected during melting and refining via a door lance and a super sonic oxygen injector. In Figure 86, the final iron oxide content of the slag is plotted versus the amount of oxygen injected via the door lance and super sonic burner for each heat.

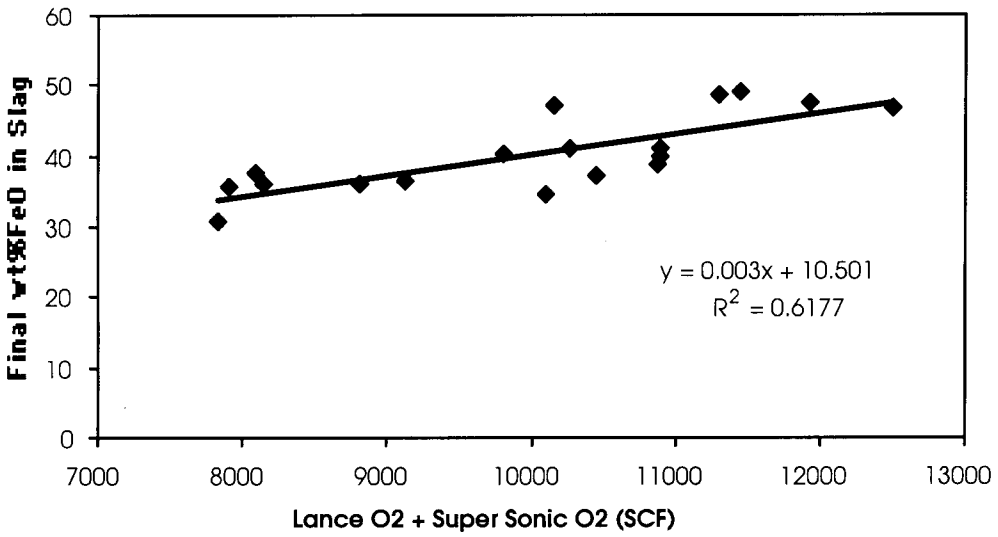

Figure 86: Final wt% FeO in the slag versus oxygen injected through the door lance and super sonic injector.

In Figure 86, oxygen injected through the oxy-fuel burners was neglected. Although the oxidizing combustion products of these burners would contribute to oxidation of the scrap, the gas usage through these burners was fairly consistent from heat to heat. Clearly, the correlation between injected oxygen and the FeO content of the slag is much tighter than the relationship between HBI in the charge and the slag chemistry. A comparison of Figures 85 and 86 suggests that the quantity of injected oxygen has a much greater effect upon the FeO content of the slag, than the amount of oxygen introduced by the FeO in the Circal material.

In addition to the amount of oxygen entering the furnace with the HBI and the injected oxygen, the amount of carbon introduced into the furnace via the pig iron also varied for the trial heats. In an attempt to account for this variation in carbon, the moles of carbon contained in the charged pig iron were subtracted from the moles of oxygen atoms contained in the HBI and the injected lance and super sonic oxygen. In Figure 87, final iron oxide content of the slag is plotted versus the resultant 'excess oxygen,' which was not balanced by carbon in the pig iron.

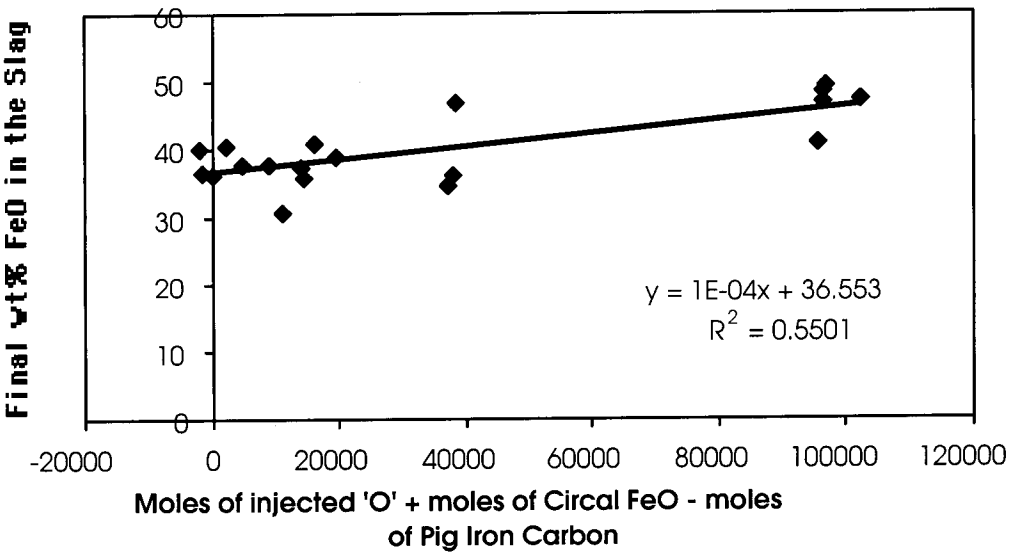

Figure 87: Final wt% FeO in the slag versus the moles of iron oxide in Circal plus the moles of injected oxygen minus the moles of carbon contained in the pig iron for the trial heats with Circal HBI.

Clearly, a great deal of scatter still remains in the data as plotted in Figure 87. For some of the intermediate points in Figure 86, representing the heats with the 10% pig iron – 20% Circal charge, significant furnace delays occurred during the trial heats. For these heats, it can be assumed that significant oxidation of the partially melted scrap pile occurred during the delays. This explains some of the scatter in the data of Figures 85 through 87. Another significant source of scatter is related to slag flushing. The time and amount of slag flushing was highly variable during the 20 trial heats with Circal HBI. The data of Figures 69, 83, and 84 suggest that electric furnace slags typically melt in with fairly high FeO contents. As will be argued later, the FeO content of the slag decreases as the heat proceeds as a result of chemical reduction of the iron oxide and dilution by continuously dissolving lime and magnesite. Flushing during early melting, high FeO slag from the furnace early in the heat will remove proportionately more iron units from the furnace as compared with flushing later in the heat. Therefore the timing and amount of slag flushing can have significant effects on the FeO content of the slag at tap. Another important goal of the trials at NSST was to evaluate any possible effects of the different scrap substitute materials upon the behavior of phosphorus in the furnace. Generally, all the mixes studied melted in at fairly low metal phosphorus levels 0.003wt%P to 0.014wt%P.). During the refining period, the metal phosphorus content either increased or decreased by no more than 0.004 wt% for all heats and usually by less

than 0.001wt% for most heats. It was also desired to determine, which equilibrium phosphorus distribution correlation best matched the data from the NSST trials. In Figures 88, 89, and 90 the observed phosphorus distribution at tap is plotted versus the calculated equilibrium distribution based on the correlations of Ide et al.[29], Turkdogan[20], and Zhang et al.[28] respectively.

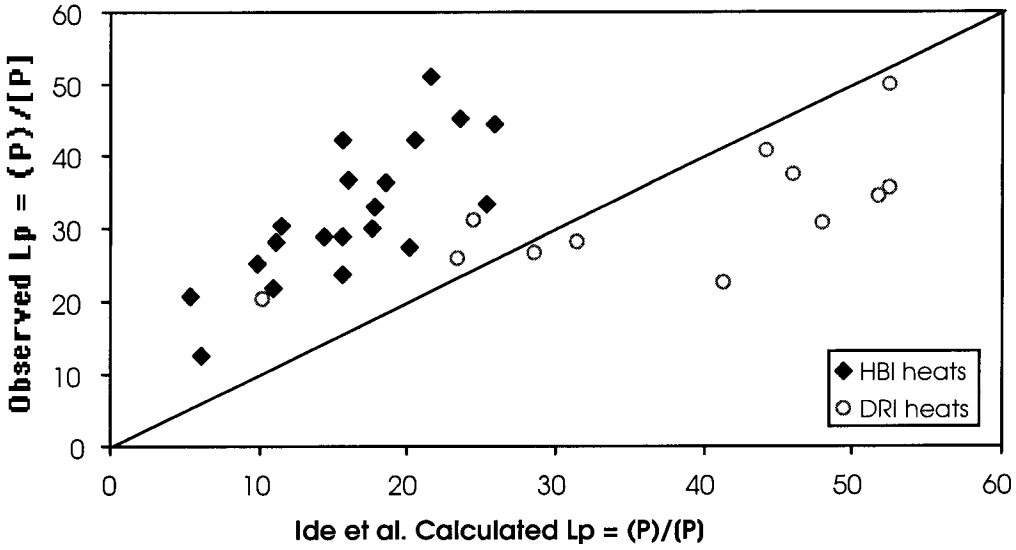

Figure 88: Observed phosphorus distribution at tap versus the equilibrium distribution as calculated by the Ide et al. correlation.

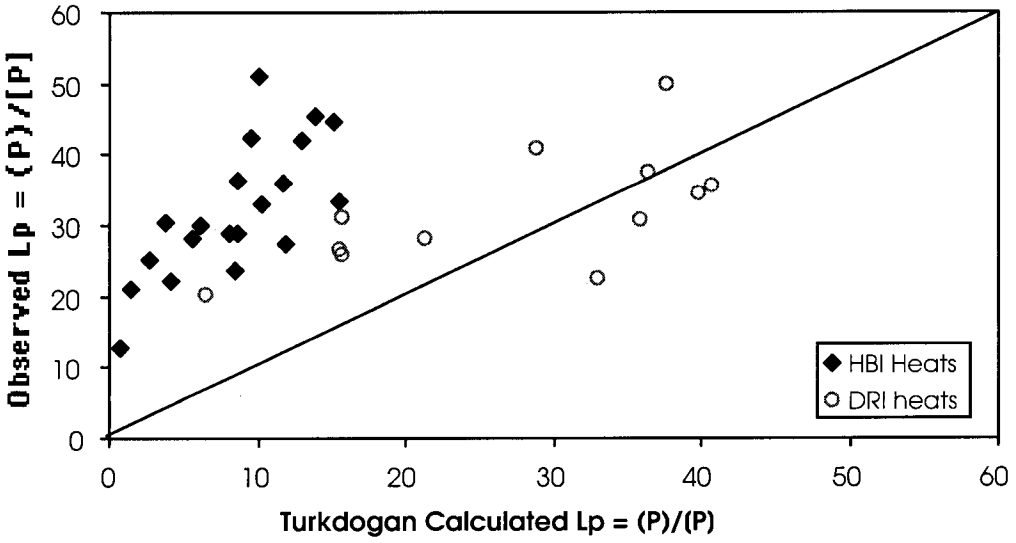

Figure 89: Observed phosphorus distribution at tap versus the equilibrium distribution as calculated by the Turkdogan correlation.

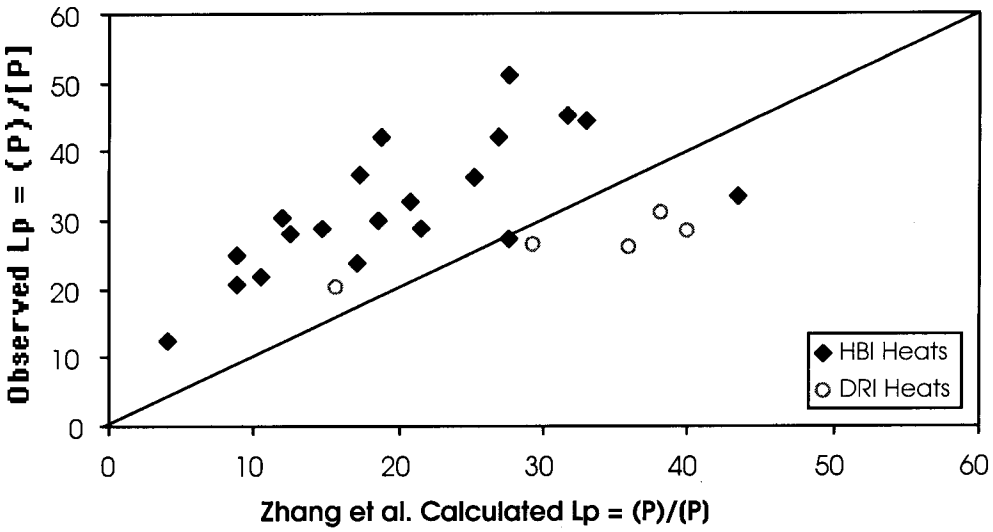

Figure 90: Observed phosphorus distribution at tap versus the equilibrium distribution as calculated by the Zhang et al. correlation.

As plotted in Figures 88 through 90, the experimental data show a great deal of scatter. As explained in section 6.1, the equilibrium phosphorus distribution is extremely dynamic during the course of a single heat. Therefore it is not expected that the furnace should reach equilibrium at the time of tap. However, because many of the equilibrium correlations in the literature can either over or under predict equilibrium by several orders of magnitude for some temperatures and slag chemistries, it is a worthwhile exercise to plot the data versus these correlations to confirm that they are close. A major limitation of both the Ide et al. and the Turkdogan correlations is the fact that neither can account for the effect of manganese oxide in the slag upon phosphorus equilibrium. All of the slag samples for the trials at NSST contained from 6 to 9 percent manganese oxide. These slags also contained up to 3 percent alumina. Both alumina and manganese will have an effect on the free oxygen activity in the molten slag and will, therefore have some effect on the equilibrium phosphorus distribution. The Zhang et al. correlation does contain a term, which accounts for manganese oxide dependence of phosphorus equilibrium. Although the data in Figure 90 does show a consistent deviation from equilibrium, the data are somewhat more coherent and less scattered than in Figures 88 and 89. Despite this apparent improvement, this correlation significantly over predicts equilibrium for some of the heats with DRI with higher basicities. These data are not shown in Figure 90 as the calculated equilibrium is clearly in error.

There is a consistent discrepancy between the data from the trials with HBI and those with DRI. Nearly all the trials with HBI showed an observed final phosphorus distribution, which was higher than the equilibrium value as calculated by any of the correlations. However, the observed final phosphorus distribution from the trials with DRI consistently fell nearer or below the calculated equilibrium. An actual measured phosphorus distribution, which is below equilibrium describes the conditions necessary for phosphorus reversion from slag to metal. In agreement with this fact, 11 out of 20 heats with HBI showed phosphorus pick up in the metal from the first to final sample. Of the remaining 9 heats, only one showed a decrease in metal phosphorus and the rest showed no change between the two samples. The trials with AIR-DRI melted in at very low metal phosphorus values and showed only minor fluctuations during the heats. Four heats showed a minor 0.001 wt% decrease in metal phosphorus, two heats showed an increase, and six showed no change. Overall, these observations are in best agreement with Figure 88, suggesting that out of these choices, the Ide et al. correlation is the most accurate.

An attempt was made to evaluate the conditions of phosphorus mass transfer for the trials at NSST as was done for the trials at PST. In Figures 91 and 92, the slag chemistry and temperature are plotted as a function of time for one of the trial heats.

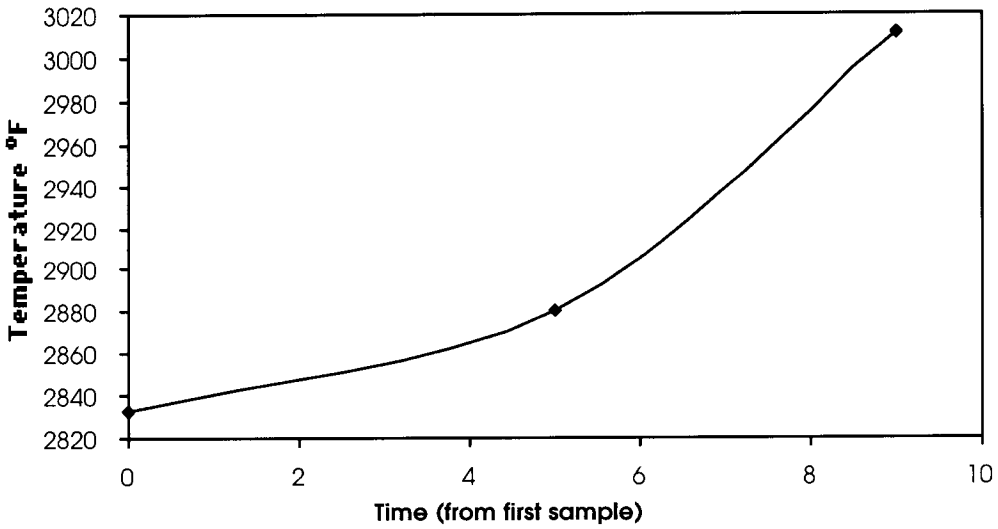

Figure 91: Furnace temperature versus time during the refining period for one heat with 25% DRI – 75% scrap.

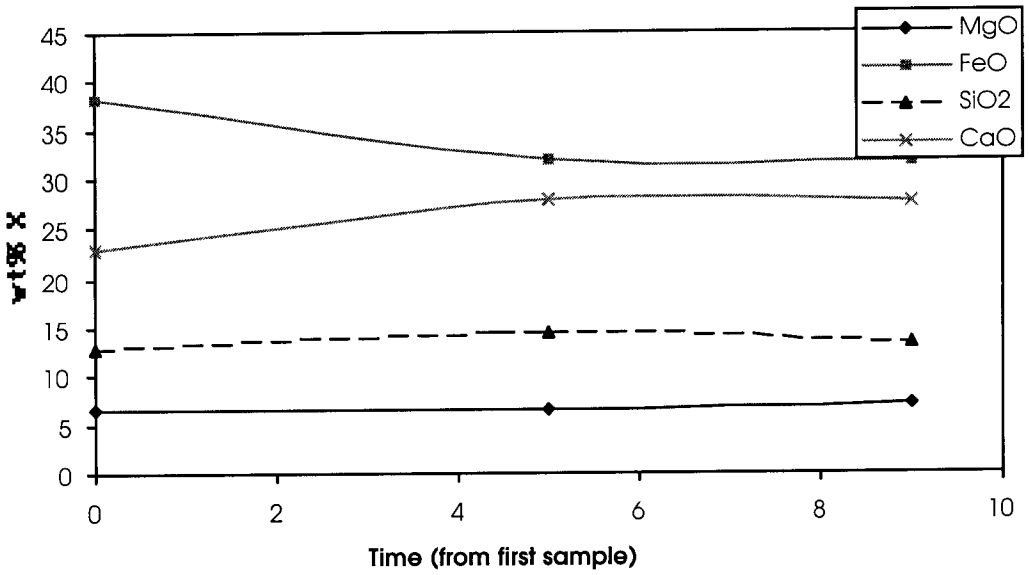

Figure 92: Slag chemistry versus time during the refining period for one heat with 25% DRI – 75% scrap.

In Figure 93, the observed slag-metal phosphorus distribution and the equilibrium phosphorus distribution according to the Ide et al. correlation are plotted versus time.

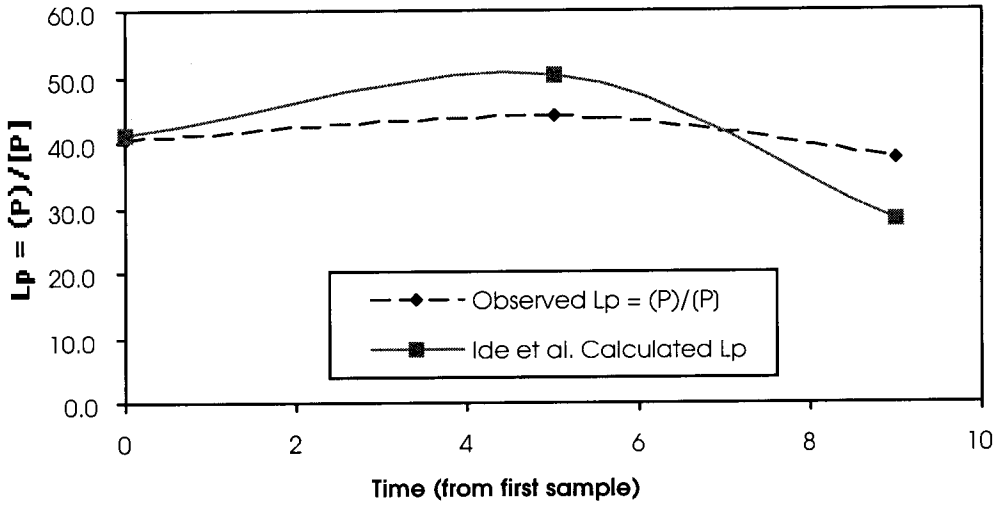

Figure 93: Calculated equilibrium and observed slag-metal phosphorus distribution versus time

The general behavior of both the calculated equilibrium and observed phosphorus distribution shown in Figure 93, is fairly representative of the trends observed for most of the trial heats with AIR-DRI. The equilibrium phosphorus distribution initially increases during the refining period in response to the increasing lime content of the slag, but then

decreases with the rapid increase in temperature toward the end of the heat. In Figure 94, the measured bulk and calculated interfacial metal phosphorus contents are plotted versus time.

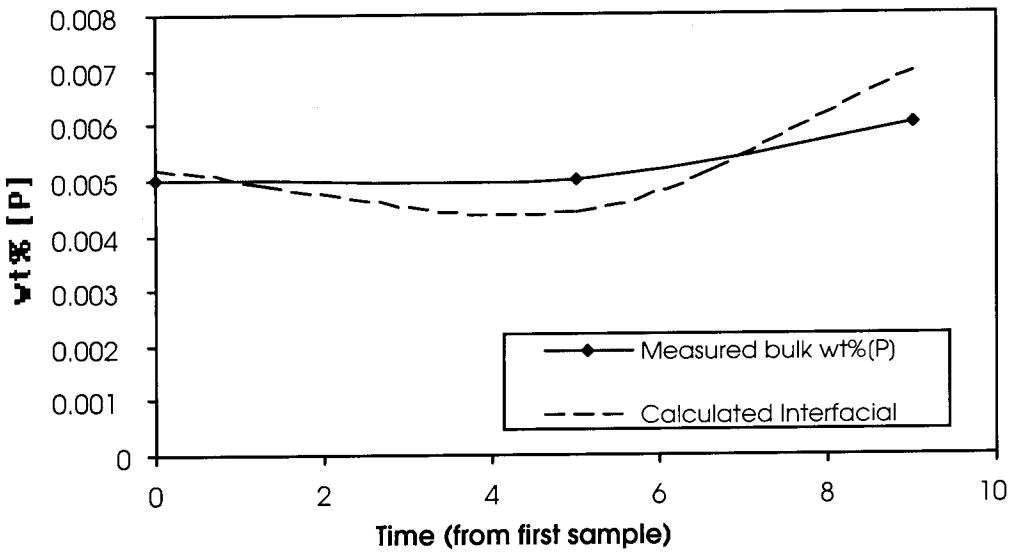

Figure 94: Measured bulk metal phosphorus and calculated metal interface phosphorus versus time

The behavior of the measured bulk metal phosphorus plotted in Figure 94 is very typical of what was observed for all the trial heats with AIR-DRI. The first metal sample in Figure 92 was taken 27 minutes after the dropping of the third bucket. By the time of the first metal sample, the bulk metal had reached a very low metal phosphorus content for all heats, which varied by only ± 0.001 wt% during the refining period. Because the measured metal phosphorus content, as well as the deviation from the calculated interfacial phosphorus content were very low, the driving force for phosphorus transfer, as calculated by equation 54, is also very small. Under these conditions, the calculation of the mass transfer parameter becomes very susceptible to errors in the estimated slag mass and calculated equilibrium, as well as errors in the chemical analysis. For the heats where the experimental data allowed evaluation of equation , the term:

$$\frac{A\rho_m k_o}{W_m} \qquad 49$$

was found to be on the order of 0.05 – 0.15 min^{-1}. This result is in fair agreement with the complimentary results from the electric furnace at PST. It is not unreasonable that the mass transfer parameter of the furnace at NSST is lower than that of the furnace at PST.

For various reasons, the standard furnace practice at PST results in a much higher melt-in carbon content than is used at NSST. As a result, much less injected carbon is used by PST to maintain a foamy slag. Carbon monoxide evolved at the slag-metal interface as a result of metal decarborization will generate more slag-metal stirring than gas evolved from solid injected carbon suspended in the slag layer. The higher rate of oxygen usage at PST relative to NSST should also result in better mixing conditions in the furnace.

Because only two slag and metal samples and one temperature reading were obtained for the trial heats with HBI, quantitative evaluation of the mass transfer parameter during these heats is not permitted. However, qualitative evaluation of the slag and metal chemistry data, indicate reasonable agreement with the calculations above for the heats with DRI.

5.3 BHP – Sydney Steel Mill EAF Trials with HBI

Researchers at BHP [1], previously conducted a large number of electric furnace trials with HBI. A great deal of the data from those trials were shared with the present author. Similar to the trials conducted at PST and NSST for this study, the BHP researchers examined the fluctuations of the slag and metal chemistries during the course of the trial heats. In fact, the amount of slag sampling performed during the BHP trials was far more extensive than that of either the PST or NSST trials. Samples were taken of the liquid slag at various stages during the melting and refining sequence for those heats. Table 9 lists some of the operating parameter of the BHP – Sydney furnace in which these trials were conducted.

Table 9: Operating Parameters of BHP - EAF

Power	AC
Capacity	80 tons - 2 bucket charge or 1 bucket + continuously fed HBI
Diameter	??
Tap to Tap	Approx. 70 minutes
Typical Oxygen Usage	Total – 81 0 SCF/Ton
Injected Carbon*	As required for slag foaming
Charge Carbon	0 – 2000 lbs
Flux	As required to maintain a V ratio = 2.5 Typical usage: Lime - 4400 – 6600 lbs Dolomite - 3300 – 4400 lbs
Slag Flushing	???
Hot Steel Heel	???
Slag Heel	???

In Figure 95, the slag chemistry of one heat from the BHP trials is plotted as a function of time. In this figure, the first slag sample was taken immediately before the final scrap charge was dropped.

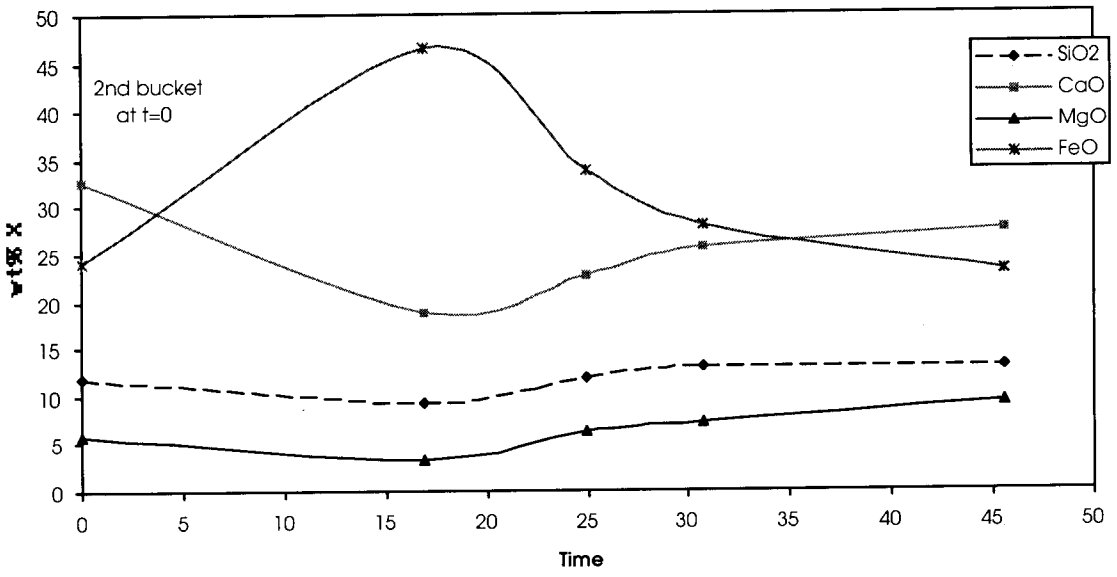

Figure 95: Slag chemistry versus time for a single two bucket batch charged EAF heat. The initial sample was taken between the first and final scrap charges to the furnace.

The data in the last 30 minutes of Figure 95 show very similar trends to the data from PST and NSST. The slag sample at t = 0 was taken between melt down of the first bucket and the addition of the second and final scrap charge. The changes in slag

chemistry from the first to the second sample in Figure 95 highlight the sharp increase in slag FeO during melt down. Also, the decrease in slag basicity between the first and second samples suggests that a portion of the lime has re-solidified due to the sharp temperature decrease, which results from the cold scrap addition. As was seen in the data from NSST, a continuous increase in the basicity of the liquid slag is observed, even when no flux additions are made late in the heat. This is due to the continuous dissolution of solid lime and MgO into the liquid slag as the furnace temperature increases. The solubility of CaO and MgO both increase with decreasing iron oxide in the slag, however, the temperature increase is more likely the dominant influence.

The BHP trials also included several heats where HBI was continuously fed into the furnace. The material used in these trials had the following chemical composition:

Table 10: Chemical composition of HBI used in the BHP – Sydney trials

Total Iron	92.6%
FeO	9%
Carbon	1.38%
Phosphorus	0.053%
SiO_2	1.52%
Al_2O_3	0.69%
MgO	0.21%

During the continuously fed heats, approximately 60 tons were continuously fed into furnace at a target rate of 1.5 tons per minute. Lime and dolomite were fed concurrently with the HBI to balance the silica content of the material and maintain a V ratio of 2.5. The slag chemistry for one of the continuously fed heats is plotted versus time in Figure96.

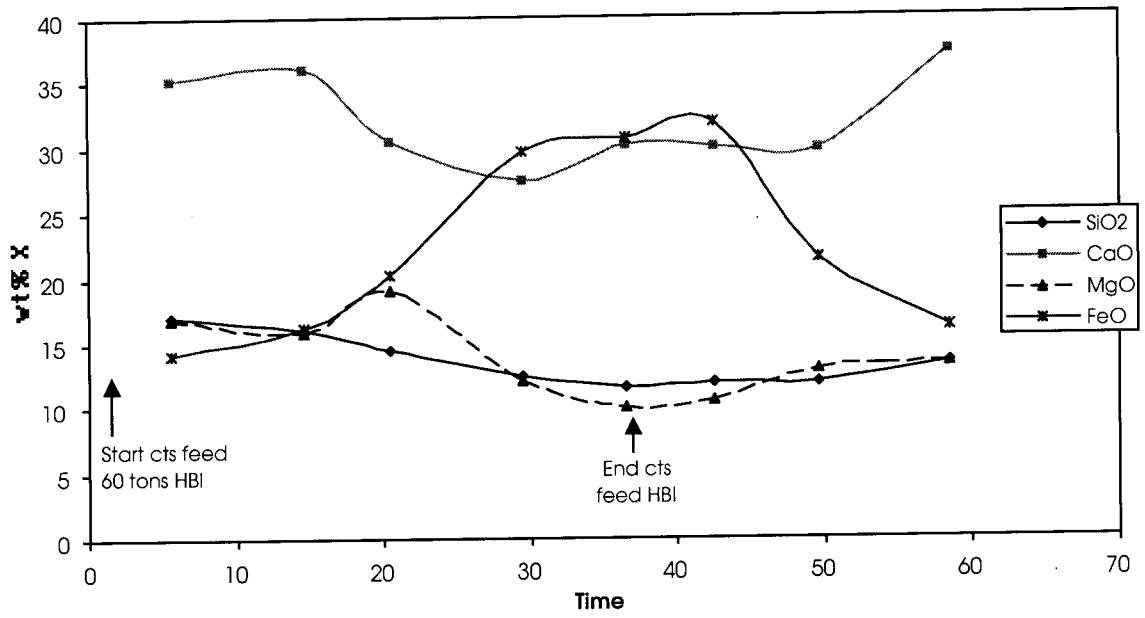

Figure 96: Slag chemistry versus time for a trial heat with 60 tons of continuously fed HBI.

In Figure 97, the slag FeO increases by nearly 20 wt% as a result of the continuously fed HBI. Based on the compositional data in Table 10, the continuously fed HBI material contains slightly less carbon than is required to reduce the iron oxide in the material. The imbalance results in an excess 7.2 kg of FeO per ton of HBI. For the 60 tons of charged HBI this generates a total of 430 kg of FeO, which must be absorbed by the slag. Based on the observed change in the FeO content of the slag, the actual contribution of FeO to the slag by the HBI was probably more than 7.2 kg per ton. It is quite possible that the chemistry reported in Table 10 did not account for degradation of the metallization of the HBI due to aging or possible moister pickup. Either source of oxygen would further shift the carbon – oxygen ratio away from the stoichiometric balance.

The continuously fed HBI heats are somewhat parallel, though on a much larger scale, to the fast melting experiments of the present study, which were reported in Chapter 4. Unfortunately, data regarding the metal chemistry were not available to the present author. However, data regarding the phosphorus content of the slag for the heat shown in Figure 96 are plotted in Figure 97 versus time.

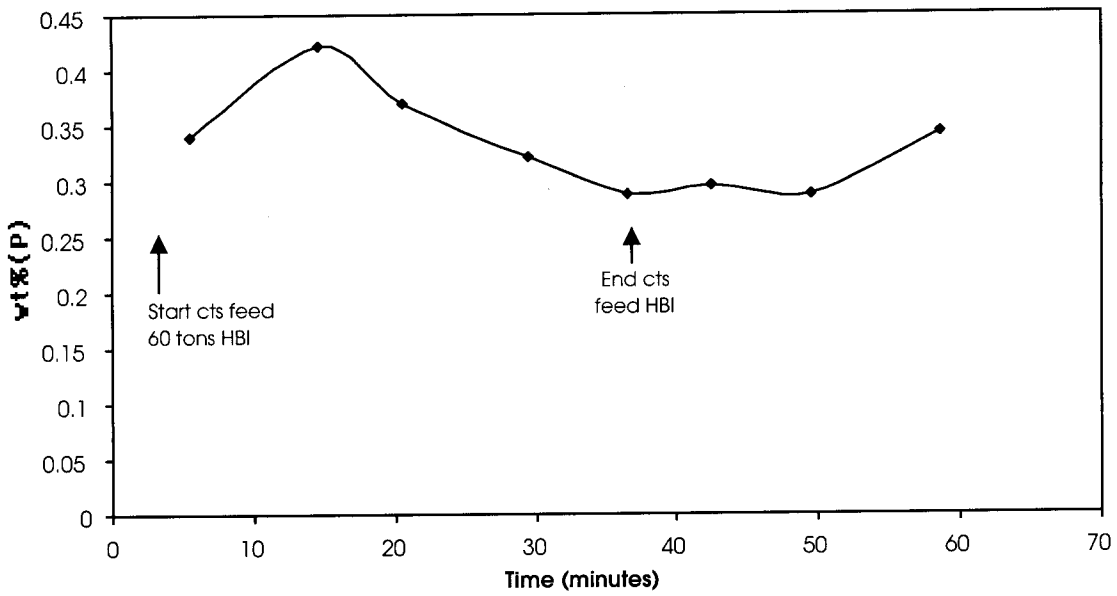

Figure 97: Phosphorus content of the slag versus time for the trial heat with 60 tons of continuously fed HBI shown in Figure 96.

In Figure 97, after an initial increase, the phosphorus content of the slag decreases during the period of continuous feeding. When continuous feeding is terminated, the slag phosphorus begins to increase again, despite a rapid increase in furnace temperature. During the continuous feeding period, the slag volume increases significantly due to the contribution of the HBI gangue material and the balancing flux additions. Also, a large amount of iron oxide reports to the slag as a result of the melting HBI. The BHP researchers estimated that the slag weight would increase by 25% at the level of HBI usage of this heat. If the phosphorus in the HBI material reported directly to the slag with the gangue material, 31 kg of phosphorus would enter the slag. This much phosphorus would more than double the amount of phosphorus in the slag. Therefore, even accounting for the diluting effects of the increased slag weight, the slag phosphorus content should increase significantly. The fact that the phosphorus content of the slag decreases for a significant portion of the continuous feeding period supports the earlier conclusion that the phosphorus in HBI does not remain in the gangue during melting. The increase in the slag phosphorus content after continuous feeding is stopped suggests that the slag metal phosphorus distribution is below the equilibrium value, and the dephosphorization of the metal is occurring. For these reasons, the data in Figure 97 are consistent with the theory that phosphorus reversion from HBI gangue to the surrounding

metal is rapid, and that the phosphorus in the steel is then transferred to or from the external slag according to the equilibrium of the slag chemistry and furnace temperature.

Chapter 6

Process Model

6.1 Slag and Temperature Model

In the previous chapter, experimentally determined temperature and slag chemistry data were used to evaluate the mass transfer conditions of two electric arc furnaces. The end goal of this project is to develop a process model, which can be used in a predictive manner to evaluate various raw materials and operating conditions. An electric arc furnace represents an extremely complex and dynamic reactor. During EAF steelmaking almost all system parameters are varying simultaneously with varying degrees of interdependency. Continuous oxygen and carbon injection, flux addition and dissolution, slag foaming and flushing, as well as continuous variation of the temperature are just a few of the complexities of the EAF environment. Continuous dissolution and/or melting of scrap and slag materials, cause difficulties in determining even some of the most basic system parameters such as the steel and slag weight. A process model should be useful in designing flux practice such that phosphorus retention in the slag is optimized without compromising yield considerations. The slag-metal system during electric steelmaking is an extremely dynamic system, which is sensitive to many operating parameters. In order to model specific chemical reactions such as decarborization or dephosphorization, the dynamics of the slag chemistry and furnace temperature must be known with a fair degree of accuracy. The slag chemistry can change dramatically during the course of a single heat as the result of several factors:

- Oxidation of metallic charge materials during melting
- Reduction of FeO from the slag
- Continuous addition of CaO and MgO as well as dissolution of undissolved slag components as a result of temperature increase and changes in FeO
- Changing slag mass due to the above factors, as well as due to slag flushing

A basic understanding of the general trends in temperature and slag chemistry during EAF steelmaking and the fundamental phenomena, which govern these changes, must be established before a predictive model can be developed for this system. In the previous

chapter a large amount of industrial data from three different electric arc furnaces was introduced. Some common trends were identified in the behaviors of the slag chemistry for all three furnaces. In this section, an attempt will be made to roughly model some of the basic phenomena, which influence the behavior of the bulk slag chemistry during electric furnace steelmaking.

6.1.1 Iron Oxide Formation and Reduction During EAF Steelmaking

Like most modern electric furnace shops, the three electric furnaces evaluated in Chapter 5 operate with high melting efficiency and shorter tap to tap times as priorities. As a result of aggressive melting practices using large amounts of injected oxygen, the slag-make at melt-in generally contains large amounts of iron oxide. Assuming relatively constant slag and metal heal weights, the total amount of iron units lost during a given heat will be a function of the iron oxide content of the slag, as well as the period, rate, and quantity of slag flushing obtained for a given slag practice. In Section 5.2, correlations were identified between the final iron oxide content of the slag and the amount of injected oxygen and the carbon – oxygen balance of the charge materials. Although the melt-in chemistry of the slag could not be evaluated due to a lack of data, it is most likely that the melt-in iron oxide content of the slag is most strongly affected by:

- The amount of iron oxide in the slag heal
- The amount of injected oxygen
- The physical characteristics of the scrap charge, i.e. bulk density
- The amount of unbalanced oxygen in direct reduced iron materials
- Furnace delays occurring partially through the melting sequence

For a furnace employing a hot heal practice, rapid oxidation of the very low carbon liquid steel heal will occur during the turn-around period while the furnace roof is off. A slag heal of 5 tons could easily contain 3 tons of iron oxide. The amount of iron oxide formed as a result of injected oxygen is related to both the quantity of oxygen used and the characteristics of the scrap. A scrap charge with a low bulk density will have a large amount of surface area available for oxidation. Ignoring other influences, the data from NSST trials indicated an approximate linear relationship between the final FeO content of the slag and the amount of injected oxygen according to the relationship:

$$wt\%(FeO) = 0.003 * (SCFof\ injected\ O_2) + const. \quad 56$$

A similar relationship is expected to exist for the melt-in FeO content of the slag. The value of an expression like equation 56 and the analogue for melt-in FeO, can not be understated. Such expressions are unique to the particular furnace and operating practice for which they are developed. In order to optimize a furnace for all parameters, it is necessary to know, at least empirically, the relationships between the various operating variables and performance indicators. If the empirical relationships, which link the different parameters, can be established for a given furnace, it is simple to develop a matrix analysis technique to optimize the furnace practice with respect to the different performance indicators.

Scrap substitute materials like the Circal HBI, which contain insufficient carbon to reduce the iron oxide contained within them will also contribute iron oxide units to the slag at melt-in. In the specific case of the Circal material, roughly 240 pounds of FeO per ton of HBI or 120 kg of FeO per metric ton of HBI will be added to the slag when this material is melted.

After melt-in, iron oxide in the slag will be reduced via:

- Reaction with injected carbon
- Reaction with the steel bath
- Reaction with entrained liquid steel droplets in the slag

Additional oxygen injected during refining to promote slag foaming and bath decarborization will form new iron oxide units. However, the summation of the various oxidation and reduction reactions most often results in a net reduction of FeO from the slag. For a given melt-in FeO content, the total amount of iron units recovered from the slag will be dependant upon a large number of variables including:

- The specific details of the slag flushing practice
- The melt-in steel carbon content, which is a function of the scrap mix and amount of charge carbon
- The mass transfer conditions of the furnace
- The amount and efficiency of injected carbon

Most modern electric furnace operations employ a foamy slag practice. After the majority of the scrap pile is melted down and the arc is no longer surrounded by scrap,

the quantity of heat radiated to the furnace side-walls increases and heat transfer efficiency to the steel decreases. By burying the arc in a foamed slag, radiation to the furnace walls is reduced and heat transfer to the steel bath is greatly increased. Furthermore, increased arc stability during foamy slag operation allows for higher furnace power settings among many other benefits. For many furnace operations, foamy slag practice is directly related to slag flushing. A slag with good foamability will increase in volume by a factor of four. For furnaces with an insufficient amount of free board, the rapid increase in slag volume associated with foaming will result in large amounts of slag flushing. If excessive slag foaming and flushing occur early in the heat, many otherwise recoverable iron oxide units may be unnecessarily lost from the furnace.

It is extremely difficult to separate the precise contributions of the various mechanisms of iron oxide reduction from the slag for actual plant data. Slag flushing, coupled with continuous lime and magnesia addition and/or dissolution make it very difficult to track either the precise slag volume or the exact causes of observed changes in slag chemistry. However, comparison of the fundamental reactions to actual plant data, can give a good indication of the limitations of the various reduction mechanisms. The slag chemistry data from the NSST electric furnace trials, which were introduced in Chapter 5 are reprinted below.

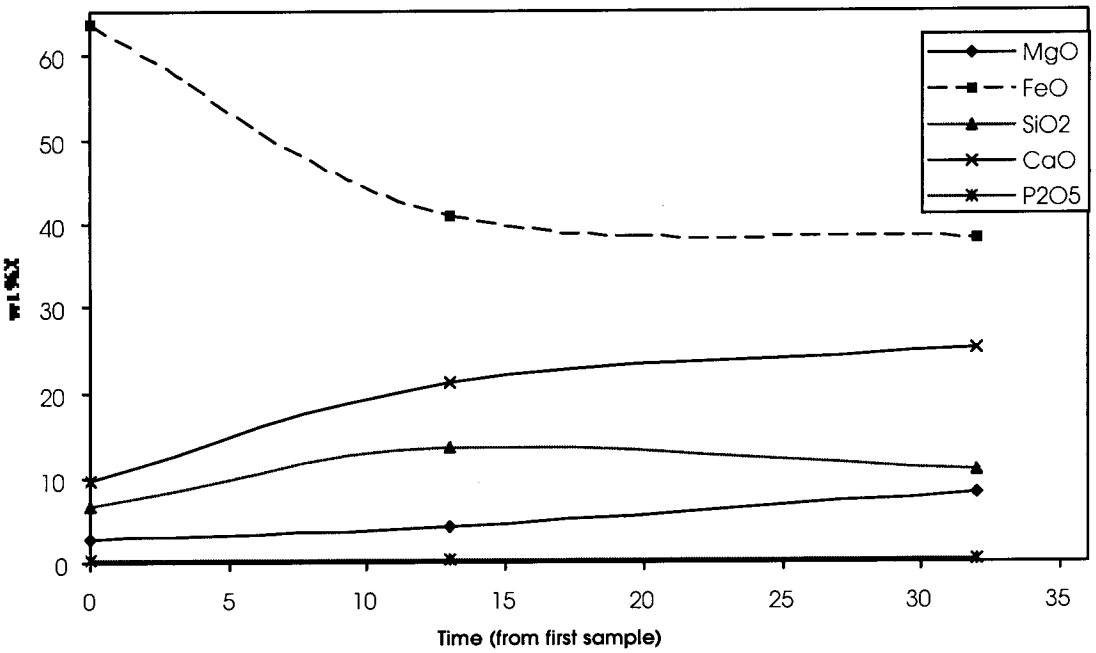

Figure 84: Wt% of slag component X versus time for a 25% DRI – 75% scrap heat. The first sample was taken 7 minutes after the dropping of the third charge.

As mentioned in Chapter 4, the trends observed in the slag chemistry from the NSST trials are very similar to those in the final 30 minutes of the BHP data. For all the trial heats at NSST, significant slag flushing commenced approximately 5 minutes after the time of the first slag sample. In addition, the continuous dissolution of lime and magnesite added during melt-in of the first two buckets, contributed to the dilution of the iron oxide present at the time of the first sample. Therefore, uncertainty in the total slag weight, as well as the precise amount of dissolved lime and MgO at any given instant, make it difficult to determine a reliable rate of iron oxide reduction from these numbers. Very careful inspection of the changes in the slag FeO with comparison to changes in the basicity suggest that some reduction of FeO from the slag does occur during the refining period.

The first sample obtained from the metal, correlating to the second slag sample in Figure 84, contained 0.026 wt% carbon. Based upon the composition of the scrap charge, which included 25% AIR-DRI, the theoretical melt-in carbon content of the steel is around 0.5 wt% C. This assumes that approximately half of the carbon in the DRI material is consumed by the iron oxide contained within the pellets and half reports to the steel melt. This calculated melt-in carbon probably represents an upper limit, and the

actual value is likely to be lower. Under these conditions, the rate of reaction between the slag and either entrained steel droplets or the bulk metal bath will most likely be limited by mass transfer of carbon to the slag metal interface. The rate of decarborization is therefore likely to be governed by the equation:

$$\frac{d[\%C]}{dt} = -\frac{Ak_o\rho}{W_M}\left([\%C] - [\%C]_i\right) \qquad 57$$

Where $[\%C]_i$ designates the carbon content at the slag metal interface. If it is assumed that the chemical reaction rate is fast, the $[\%C]_i$ can be assumed to be in equilibrium with the FeO content of the slag. Under the oxidizing conditions of this system, the equilibrium and interfacial carbon content would be effectively zero. Therefore it is very simple to integrate equation 57 giving the result:

$$-\frac{Ak_o\rho}{W_M}t = \ln\left(\frac{[\%C]}{[\%C]_o}\right) \qquad 58$$

This integration implicitly assumes that the mass transfer parameter is a constant. Both laboratory and plant experiments have shown, that the mass transfer parameter is not constant and may be a function of time and/or concentration. Under some conditions, these variations can be ignored, and a best fit, constant value can be assigned to the mass transfer parameter. At the extreme limits of the reaction, when the bulk concentration is very far from equilibrium and as the bulk concentration becomes very near equilibrium, the assumption of a constant mass transfer parameter may result in significant error. For the calculation of the reaction rate at intermediate times a constant mass transfer parameter may be acceptable. In such a case the term:

$$\frac{A\rho_m k_o}{W_m} \qquad 49$$

should be the same order of magnitude as the value calculated in Chapter 5 for phosphorus transfer. Therefore, it is a simple matter to calculate the amount of iron oxide reduction, which will occur as a result of reaction with carbon in the steel bath. Figure 98 shows the calculated change in wt% FeO in the slag versus time according to equation 58.

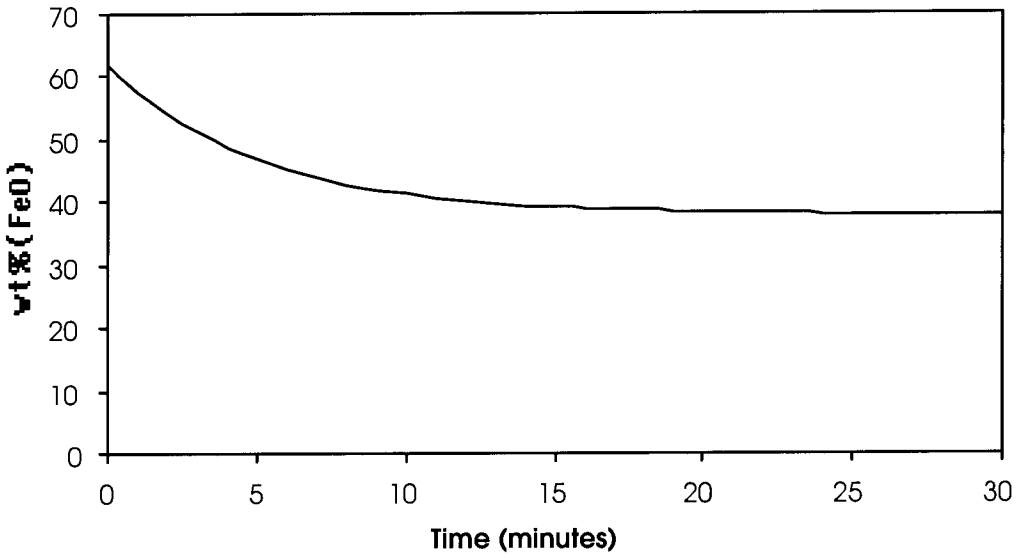

Figure 98: Iron oxide content of the slag versus time according to equation 58.

Despite the many assumptions made in the calculation of Figure 98, the agreement of the calculation with the experimental data shown in Figure 84 is remarkably good.

At NSST, slag foaming is significantly enhanced by the direct injection of carbon into the slag layer via a door lance. Carbon injected directly into the slag during the refining period should have a significant effect on the FeO in the slag. The reduction of FeO in slag by solid carbon will proceed via the gaseous intermediates CO/CO_2. At high FeO levels in the slag, this reaction is most likely limited by the combustion of CO at the gas carbon interface. The reactivity of the specific type of carbon used and the surface area available for reaction, will have a strong effect on the observed rate of reduction of FeO from the slag. Typically, approximately 2000 pounds of carbon is injected through the door lance per heat during the refining period. By contrast, the entire charge of 150 tons of scrap steel and DRI only contained 1650 pounds of carbon. One ton of injected carbon should be capable of reducing 6 tons of iron oxide from the slag. Assuming the total slag weight for this operation ranges between 13 and 17 tons, a major reduction in the slag FeO should be achieved as a result of injected carbon. It should be pointed out that during refining oxygen is simultaneously injected with the carbon through the door lance. However, the maximum amount of injected oxygen observed for any of the trial heats at NSST would only combust approximately 15 to 20 percent of the injected carbon. Therefore, the quantity of injected carbon, which is available to react with the slag is of the same order of magnitude as the amount of carbon contained in the steel bath.

In a recent study, Kerr and Fruehan [55] investigated the rate of reaction of a slag containing 10% FeO and solid graphite. These researchers found the rate of reaction for their system to be on the order of 10^{-5} lb/cm^2.sec. Using this fundamental reaction rate, one can model the rate of reduction of FeO from the slag for different conditions. A model was constructed, which allow for variation of

- The grain size of the injected fines
- Injection rate
- Total quantity injected
- Initial slag FeO content
- Specific gravity of the injected carbon

Within this model, a system of ordinary differential equations is solved simultaneously using a numerical solver. This method allows for the evaluation of a number of interdependent parameters. The simulation shown below was generated assuming that carbon injection into the slag starts at t = 0. This basically describes the scenario where the carbon is turned on at the beginning of the refining period. Figure 99 displays the surface area of carbon available for reaction as a function of time assuming the injection of 2mm fines at a rate of 150 lbs/min.

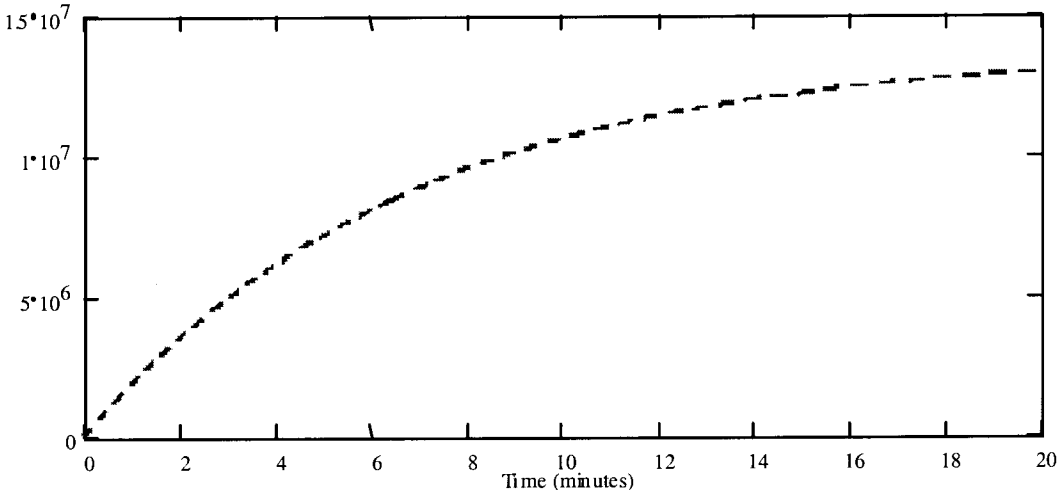

Figure 99: Interfacial area between the injected carbon and slag as function of time during refining.

After 20 minutes the reaction area approaches a steady state value as the rate of injection begins to balance the rate of consumption, which is in turn, a function of reaction area. This suggests that even the slag – carbon reaction area is a transient during the refine

period. Figure 100 displays the slag FeO as a function of time assuming an initial slag composition with 50wt% FeO.

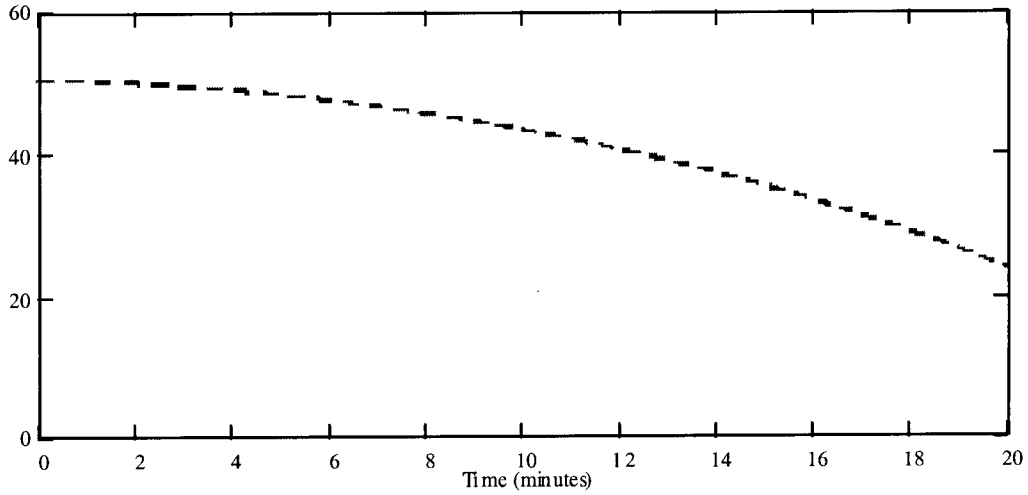

Figure 100: FeO in slag as function of time during refining.

The slag and metal weights used in the model were based on the NSST furnace. The model predicts a lag in the reaction rate, which is related to the area dependence of this reaction. A similar phenomenon was frequently observed during the trials at NSST. Often, when flat bath was reached, and carbon injection was commenced, there was an initial delay during which slag foaming was moderate at best. After several minutes of carbon injection, the slag – carbon reaction rate would suddenly surge, resulting in massive flushing of slag from the furnace. Even when the flow of carbon was stopped, the surge in the slag-carbon reaction took a minute or two to subside. This simulation most likely represents a fairly optimistic prediction of the actual conditions.

Despite this observation, the degree of iron oxide reduction predicted for carbon injected was not observed for any heats. Furthermore, the predicted trend of an accelerating rate of FeO reduction was also not observed. For these reasons, it is the opinion of the current author that solid carbon injected through a door lance is actually a very inefficient means of reducing carbon from the slag. In fact, careful observation of the slag, which was flushed from the furnace slag door at both PST and NSST revealed that the slag was 'burning' as it left the furnace. The most reasonable explanation for this phenomenon is that the injected carbon is only partially consumed before it is swept back out the slag door with the exiting slag. It is likely that the volume elements of slag, which benefit most from the injected carbon and obtain the highest degrees of FeO

reduction end up in the slag pit under the furnace. The lack of correlation between the actual slag chemistry data, and the calculated degree of reduction, which should be effected by injected carbon, suggest that this mechanism of iron oxide reduction has only a minor effect on the bulk slag chemistry.

6.1.2 Flux Additions and Slag Make During EAF Steelmaking

In addition to the formation and reduction of iron oxide during EAF steelmaking, behavior of the slag chemistry is complicated by several factors. For many electric furnace operations, flux additions of lime, dolomite, and/or magnesite are made early during the melting cycle to ensure the protection of furnace refractories from acid components of the slag make. In most cases, a large portion of these flux additions remains solid until well into the refining stage of the heat. Frequently, researchers estimate the total slag weight in a given furnace by dividing the total mass of flux additions by their mass fraction as determined chemical analysis. Because most slag sampling techniques will only give the chemical composition of the liquid slag phase, it becomes very difficult to estimate the total slag weight when a significant portion of the flux additions are likely in the solid state. At higher temperatures, late in the heat, nearly all flux additions will have dissolved for most flux practices. However, for many electric furnaces, significant slag flushing or slopping commences as soon as flat bath is achieved and slag foaming begins. All of these factors, contribute to make the simplest slag mass calculation, a complex guessing game.

For the above reasons, a series of crude models were constructed in attempt to mimic the observed trends in the experimental data presented in Chapter 5.

Slag Model 0

In the first model shown below, only the influence of FeO was considered:

- The total amounts of CaO, MgO, and SiO_2 were held constant
- The mass of FeO in the slag was increased at t = 15, then reduced assuming reduction by carbon in the steel bath only
- The total slag mass was unrestrained and allowed to vary with the changes in FeO

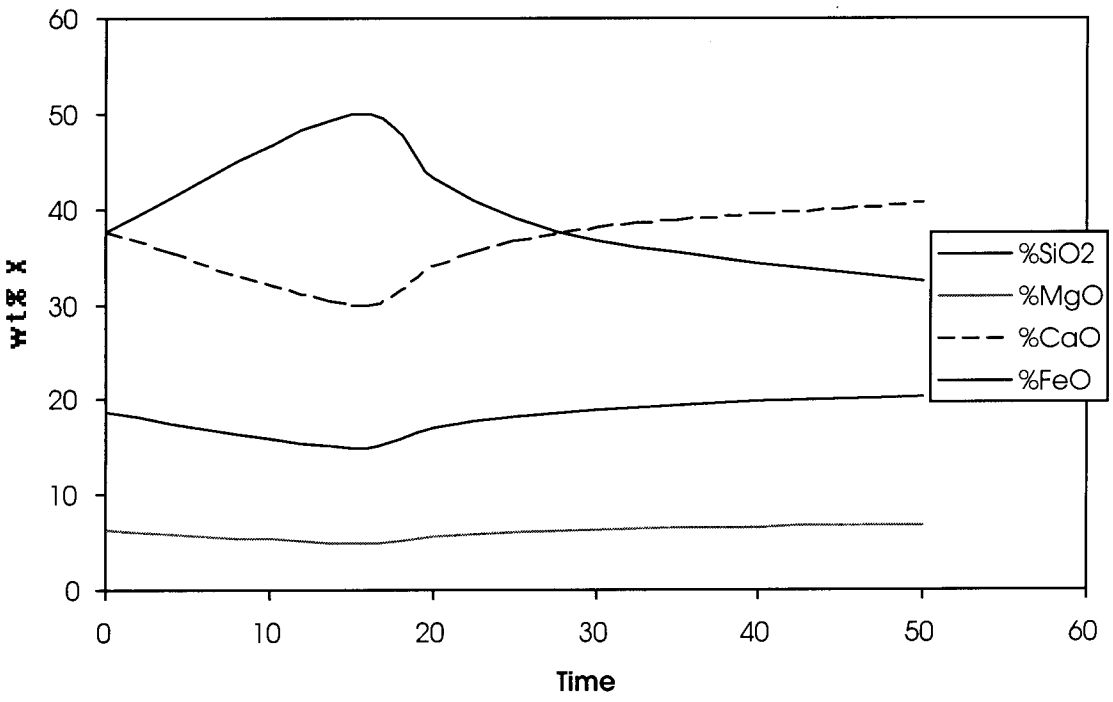

Figure 101: Slag model 0 – constant CaO, MgO, and SiO_2, with changing FeO and no slag flushing

The important attributes of Model 0 include:

- The change in the FeO is equal to the sum of the change of all other components
- The basicity and CaO/MgO and MgO/SiO_2 ratios remain constant

Slag Model 1

In the next case, the increase in FeO during melting was ignored, and the effect of increasing CaO in the final 30 minutes of the heat was studied. The thermodynamic temperature dependence of the solubilities of CaO and MgO, the kinetics of the dissolution phenomena, and the specific heating rate will all combine to determine the actual rates of dissolution of these components into the bulk slag. For the purposes of this exercise, detailed scientific predictions of the dissolution rates of CaO and MgO were not attempted. In this model:

- The masses of FeO and SiO_2 were held constant
- The mass of CaO increased proportionally to the square root of time, and the mass of MgO increased linearly with time.
- The slag weight was unrestrained and allowed to increase with the changes in lime and magnesia

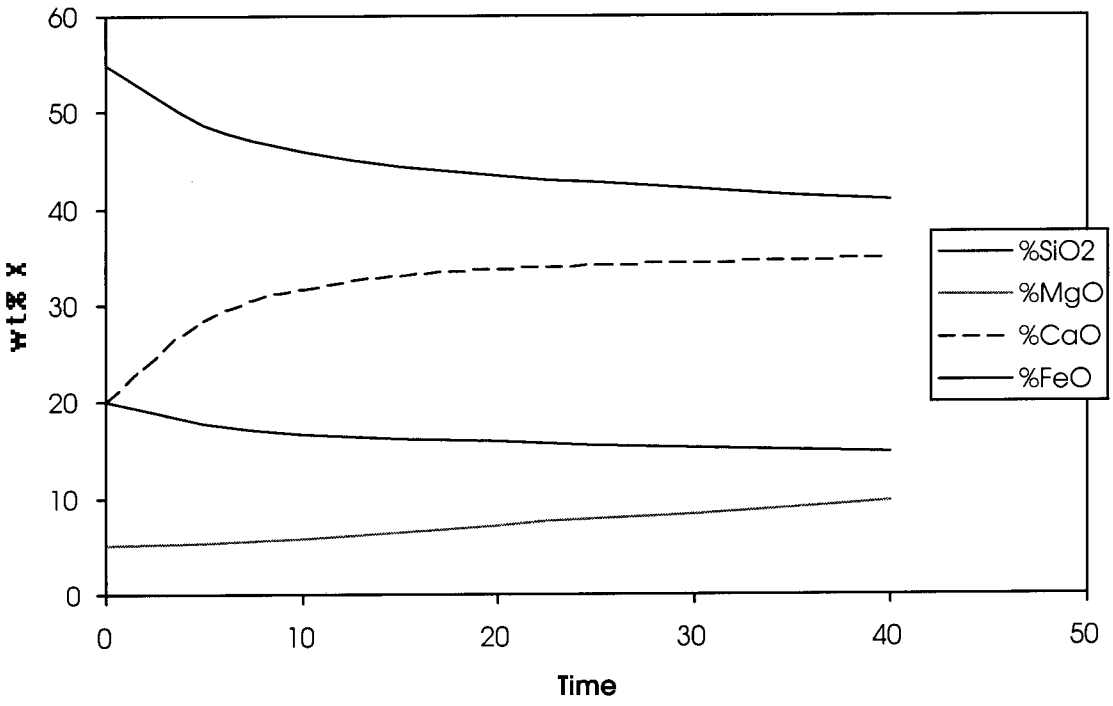

Figure 102: Slag Model 1 – Constant FeO and SiO_2, with increasing CaO and MgO and no slag flushing

The important attributes of Figure 102 are:

- The basicity is increasing
- The ratio of FeO/SiO_2 remains constant.
- Significant reductions in the observed wt % FeO can be effected by simply increasing the total lime

Slag Model 2

Slag Model 2 is the same as Slag Model 1 shown above, however, the total slag weight was restrained to simulate slag flushing. A weighted increment of each slag component was removed from the total slag weight at each time step in order to accommodate the additional CaO and MgO.

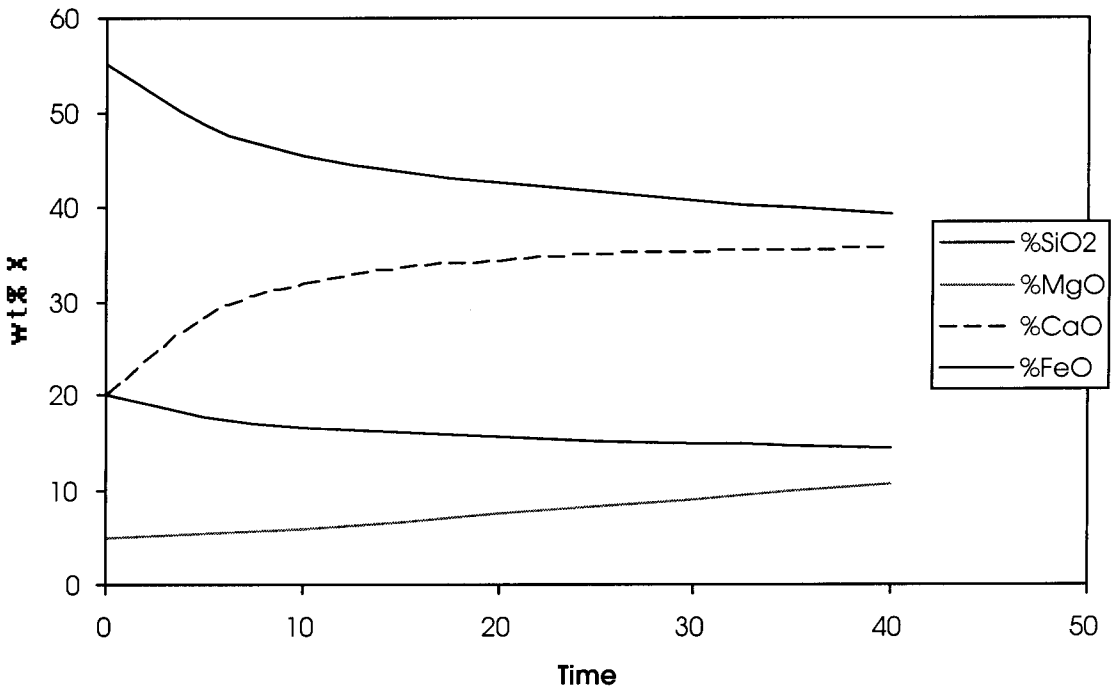

Figure 103: Slag Model 2- Constant FeO and SiO_2, with increasing CaO and MgO with slag flushing

The important attributes of Slag Models 1 and 2 are the same. Slag flushing will result in only a subtle shift in the final values of the different slag components.

Slag Model 3

In Slag Model 3, the variables modeled in Models 0-2 were combined. In this case:

- The weight of FeO in the slag was initially increased to represent scrap oxidation during melting, then allowed decay assuming reduction via carbon in the steel bath
- The weight of SiO_2 was increased at t = 15 then held constant.
- The mass of CaO increased proportionally with the square root of time, and the mass of MgO increased linearly with time.
- The total slag mass was restrained as in Simulation III to simulate slag flushing

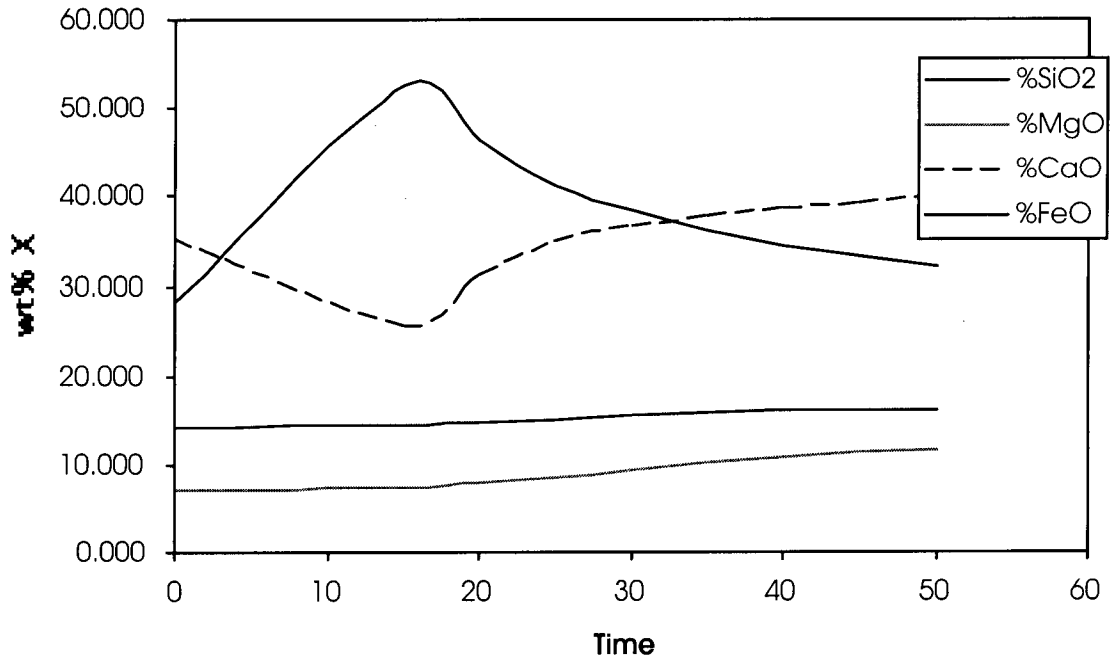

Figure 104: Slag Model 3 – FeO increase and reduction, SiO_2 increase, CaO and MgO increase, and slag flushing

In Slag Model 3, the mass of the dissolved lime in the slag roughly doubled and the mass of FeO decreased by roughly 40% in the last 45 minutes of the simulation. Although the absolute values of the slag components do not exactly match, the general trends observed in the data from the BHP furnace trials are fairly well reproduced in Figure 104.

Slag Model 3.1 – Continuous HBI Feeding

The effects of continuous feeding of HBI on the dynamics of the slag chemistry are also of great interest. The actual slag chemistry data from the BHP electric furnace trial with continuously fed HBI are reprinted below:

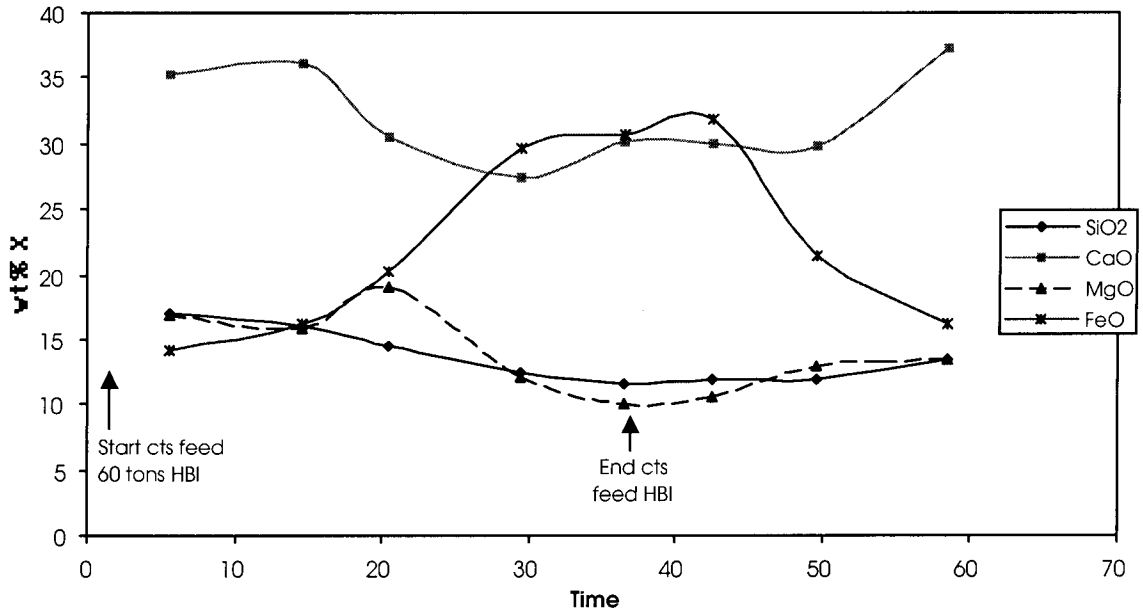

Figure 96: Slag chemistry versus time for a trial heat with 60 tons of continuously fed HBI.

The above data were simulated according to the following assumptions:

- After an initial transient period, the slag silica and FeO increase in proportion to the rate of HBI injection and the relative weight percents of those components in the HBI
- The mass of silica in the system remained constant after continuous feeding stopped
- FeO was reduced from the slag by carbon in the metal assuming a carbon content of 0.3 wt%C in the steel at the end of continuous feeding.
- Continuous lime and magnesia injection continued at a constant rate until the last 10 minutes of the heat
- The total slag weight was restrained to simulate slag flushing

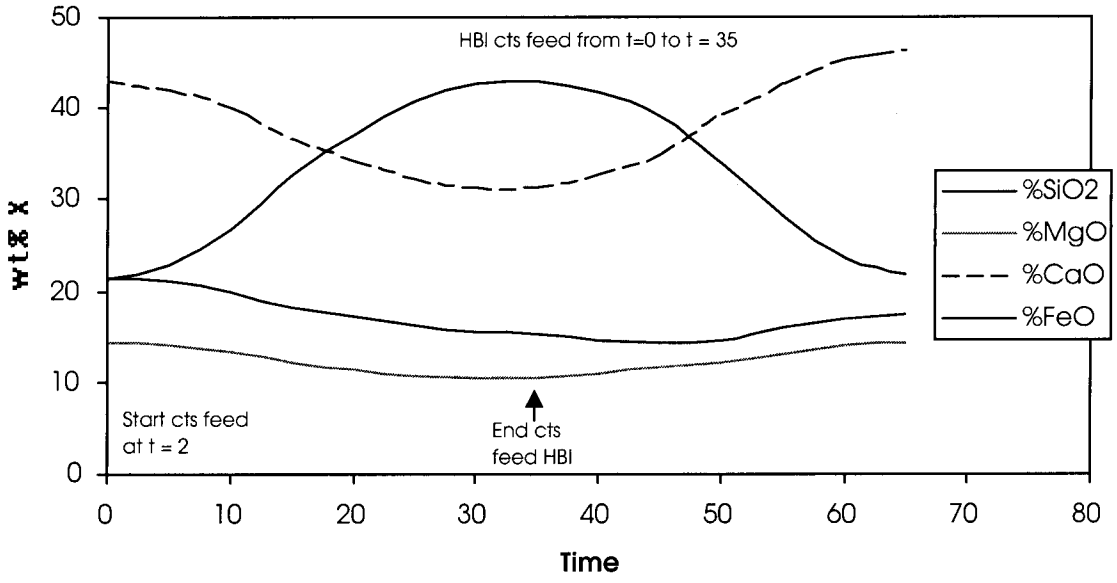

Figure 105: Slag Model 3.1- Simulation of HBI continuous feeding.

The results of continuous feeding slag model are not bad. Unfortunately, because no metal samples were available to compare with the changes in the slag chemistry, the carbon content of the steel was estimated based upon the rate and extent of iron oxide reduction.

The above exercise, though rather crude, made several important points clear:

- The initial rise in the slag wt% FeO, observed during melting is due primarily to an actual increase in the mass of iron oxide in the slag
- The decrease in the slag % FeO is due to both a decrease in the mass of iron oxide in the slag and an increase in the mass of dissolved lime and magnesia.
- It is very difficult to tell whether dilution, or actual reduction is dominating the slag chemistry.
- Tracking the ratios of the various slag components offers the most reliable way of deciphering what is happening.
- The primary mechanism of FeO reduction from the slag is believed to be via reaction with dissolved carbon in the steel bath. The observed rates of steel decarborization and slag reduction roughly agree with evaluation of the mass transfer conditions, which was presented in Chapter 5.

6.1.3 Furnace Temperature During EAF Steelmaking

Large thermal gradients are almost always present in the slag-metal system during EAF steelmaking. Therefore, it should be recognized that both experimental temperature measurements and/or thermal models, which assign a single temperature to the entire furnace are clearly not representative of the entire system. No attempt is made in the present study to model the thermal gradients between the slag and metal during steelmaking. However, separate measurements of the steel and slag temperatures indicate that the slag temperature can be more then 100°C higher than that of the metal during the refining period. However, because the steel temperature is the more important and more commonly monitored parameter during steelmaking, all "furnace" temperatures discussed in this paper imply the temperature of the metal bath. The general temperature profile during an EAF heat is shown schematically in Figure 106:

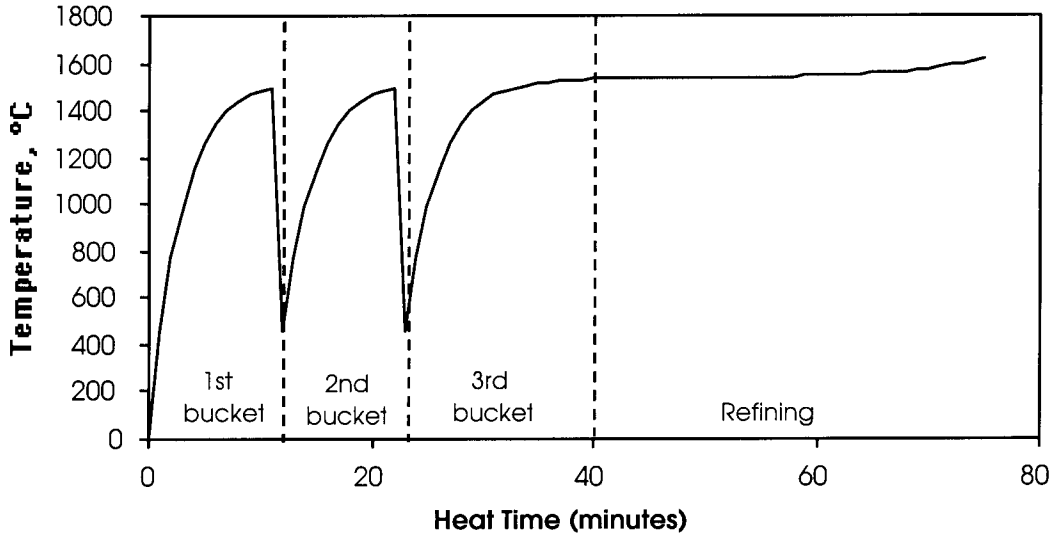

Figure 106: Steel temperature profile during a hypothetical EAF heat with a three bucket charge and a 75 minute tap to tap time.

During the melting stages of the cycle shown in Figure 106, heat transfer to the scrap pile from both oxy-fuel burners and the arc is very efficient, and the temperature of the scrap increases rapidly. As the heat approaches flat bath, heat transfer to the metal from the arc decreases. Also, the radiative heat transfer efficiency from the oxy-fuel burners to the scrap decreases rapidly as the furnace temperature increases. During the final melting stages of the heat, the temperature remains relatively constant until most of the steel is

molten. Toward the end of the refining period, nearly all the flux additions and all of the metallic charge are liquid and the temperature begins to increase rapidly once again. The last 30 minutes of Figure 106 are re-plotted in greater detail in Figure 107.

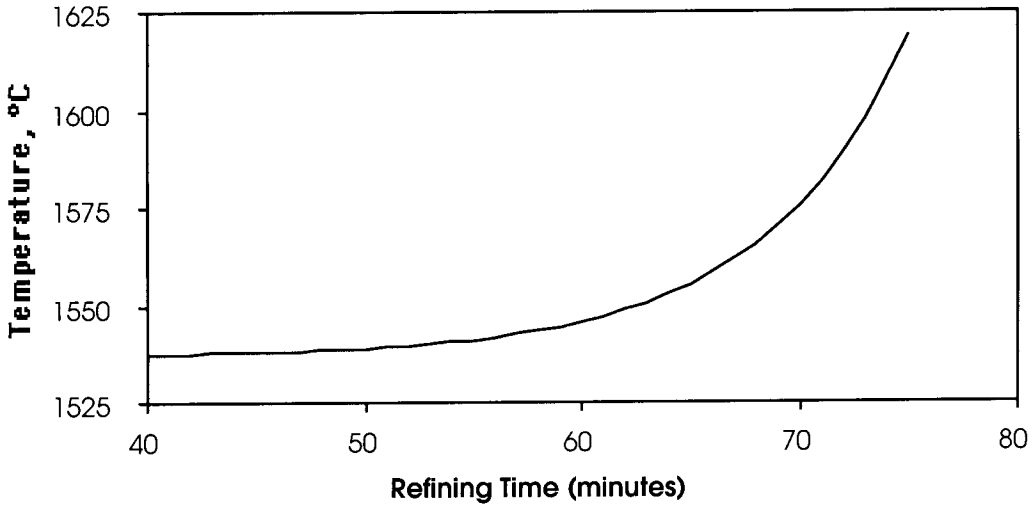

Figure 107: Steel temperature versus time during the refining period of the heat shown in Figure 106

The specific shape of the curve in Figure 107 will be influenced by several factors including the physical and chemical characteristics of the scrap charge and the power rating of the furnace. For a very high powered furnace such as the one at PST, the temperature increase at the end of the refining period will be fairly sharp as was seen in Figure 74 in Chapter 5. By contrast the furnace at NSST is a lower powered furnace and the temperature increase during the refining period was measured to be more linear. The measured steel temperature of one of the trial heats at NSST is plotted versus time in Figure 108.

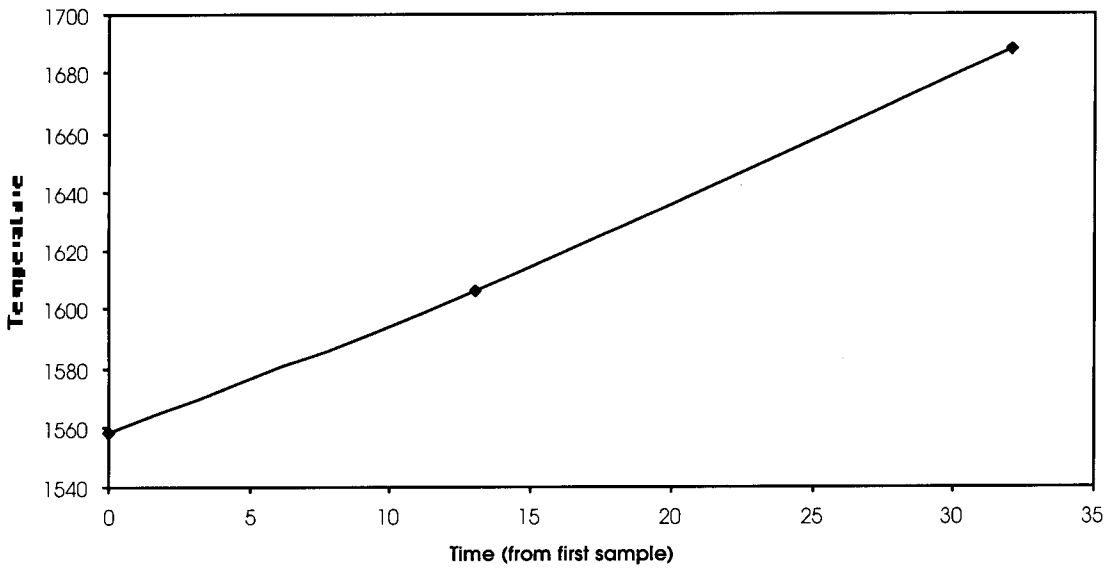

Figure 108: Steel bath temperature versus time for a 25% DRI – 75% scrap heat. The first sample was taken 7 minutes after the dropping of the third charge.

During most DRI/HBI continuous feeding practices, the feed rates of the iron bearing material and the required continuous flux additions are regulated to maintain a steady state condition of continuous melting at a constant temperature at a high power setting. The measured furnace temperature profile for the continuously fed heat shown in Figure 96 is plotted versus time in Figure 109 below.

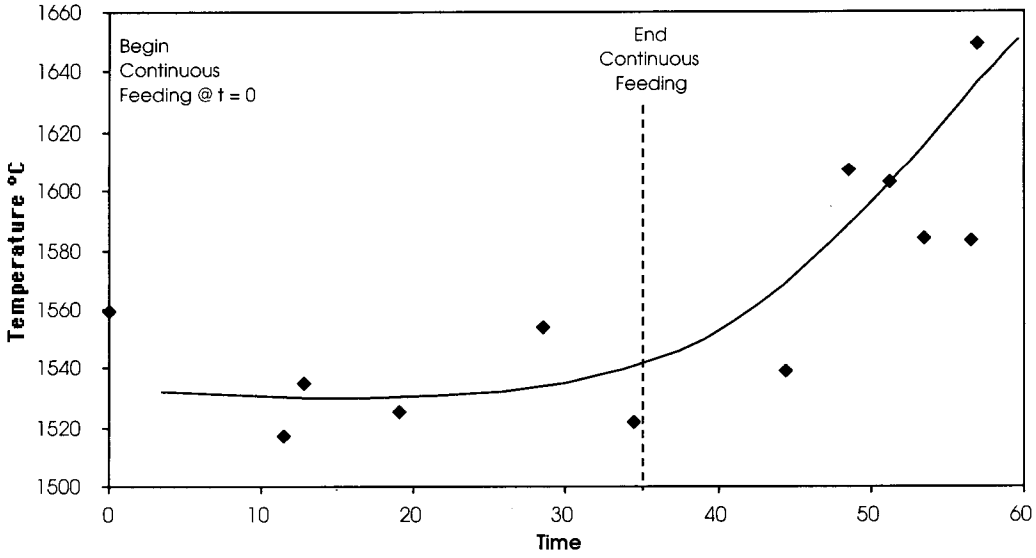

Figure 109: Temperature profile during continuous feeding of HBI into the BHP – Sydney electric furnace.

A schematic representation of the temperature profile for the duration of the entire heat of a continuously fed practice is shown in Figure 110.

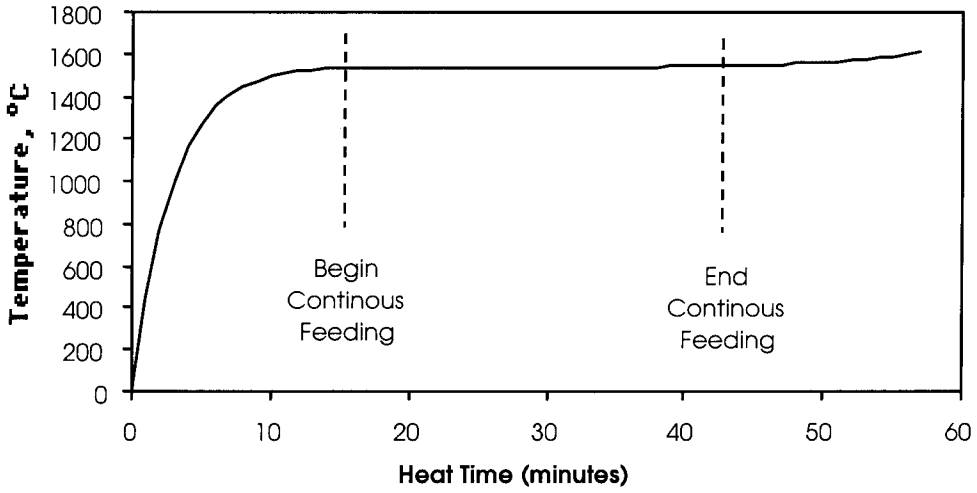

Figure 110: Steel temperature profile during a hypothetical continuously fed EAF heat.

Continuous feeding of a portion of the furnace charge in the form of DRI or HBI has been shown to offer many operating advantages over a completely batch fed practice. [5] One major effect of continuous feeding is to reduce the tap to tap cycle by extending the time during which the furnace is operated at full power. In such a practice, the melting and refining periods occur simultaneously. This generally extends the period of time at which the furnace is continuously at high temperature and slag metal reactions are in progress.

6.2 Numerical Process Model for Phosphorus Transfer During EAF Steelmaking

In order to evaluate the relative influence of different system parameters on the behavior of phosphorus in the electric furnace, a process model was developed. The mathematics of the process model are fundamentally very simple. Within the model, the two ordinary differential equations for phosphorus flux in the metal and slag given by:

$$\frac{\partial[\%P]}{\partial t} = -\frac{A\rho_m k_m}{W_m}\left[[\%P] - [\%P^i]\right] \qquad 28$$

and,

$$\frac{\partial(\%P)}{\partial t} = -\frac{A\rho_s k_s}{W_s}\left[(\%P) - (\%P^i)\right] \qquad 29$$

are solved simultaneously. If it is assumed that the interface is always at equilibrium, the interfacial phosphorus contents in the slag and metal are linked through the equilibrium phosphorus distribution. The equilibrium phosphorus distribution can be calculated as a function of temperature and slag chemistry according to any of the correlations listed in Appendix B. In the present model, the correlation of Ide et al. was used. As described in previous sections, both the slag chemistry and the temperature vary with time during a given heat. In Section 6.1 simple slag and temperature models were described, which can be used to express those system variables as algebraic functions of time. These algebraic expressions can then be combined with the Ide et al. correlation to calculate the slag-metal phosphorus distribution as a function of time. The simple system of the two differential equations expressed above, and the complex algebraic expression for phosphorus equilibrium can be solved using most commercially available numerical math software programs. For the present study, the symbolic mathematics software Mathcad© was used. The use of a symbolic math solver allowed for various iterations of the model to be developed and evaluated quickly. A representative worksheet from the model is shown in Appendix E. Because the equations are solved numerically, for specified increments of time, it is possible to vary the driving force for phosphorus transfer as a function of time, and solve for the slag and metal phosphorus concentrations in a very dynamic system.

6.2.1 NSST Electric Furnace Model

In order to test the numerical process model, an attempt was made to simulate the conditions of one of the trial heats from the DRI trials at NSST. Based upon the measured melt-in slag chemistry of the trial heat shown in Figure 111 and the actual scrap charge and flux additions, the slag model generated the following slag profile for the heat.

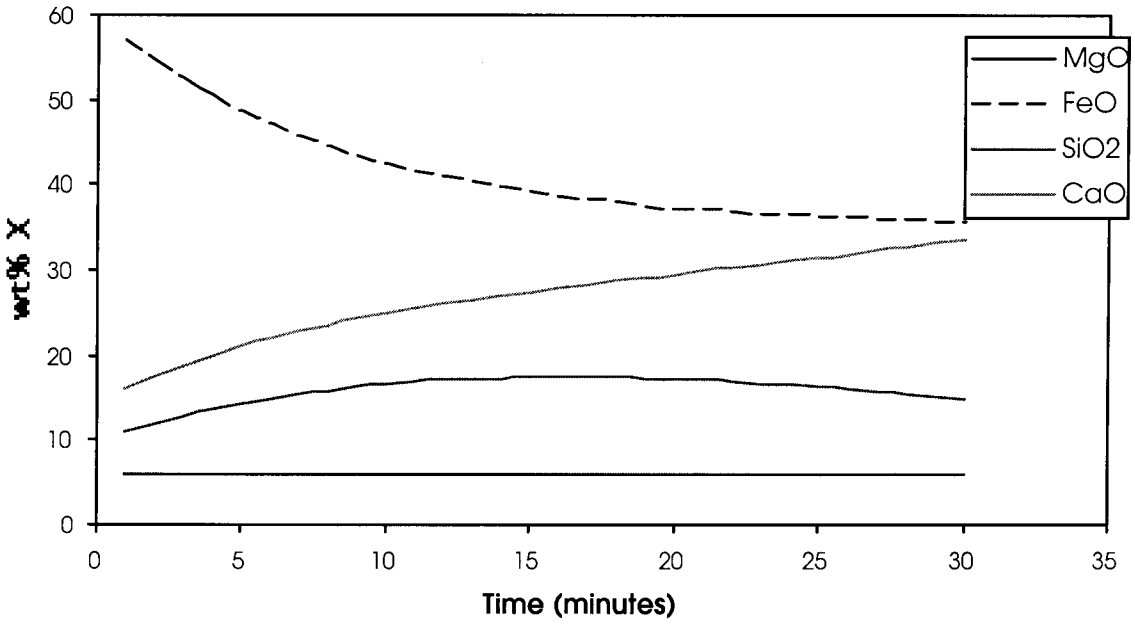

Figure 111: Predicted slag chemistry profile during the refining period of an electric furnace heat at NSST.

Based upon the temperature profile data for the NSST furnace, which was presented in Section 6.1.3, a simple linear temperature increase during the refining period was approximated. The equilibrium phosphorus distribution predicted by the Ide et al. correlation for the above temperature and slag chemistry profiles is plotted in Figure 112.

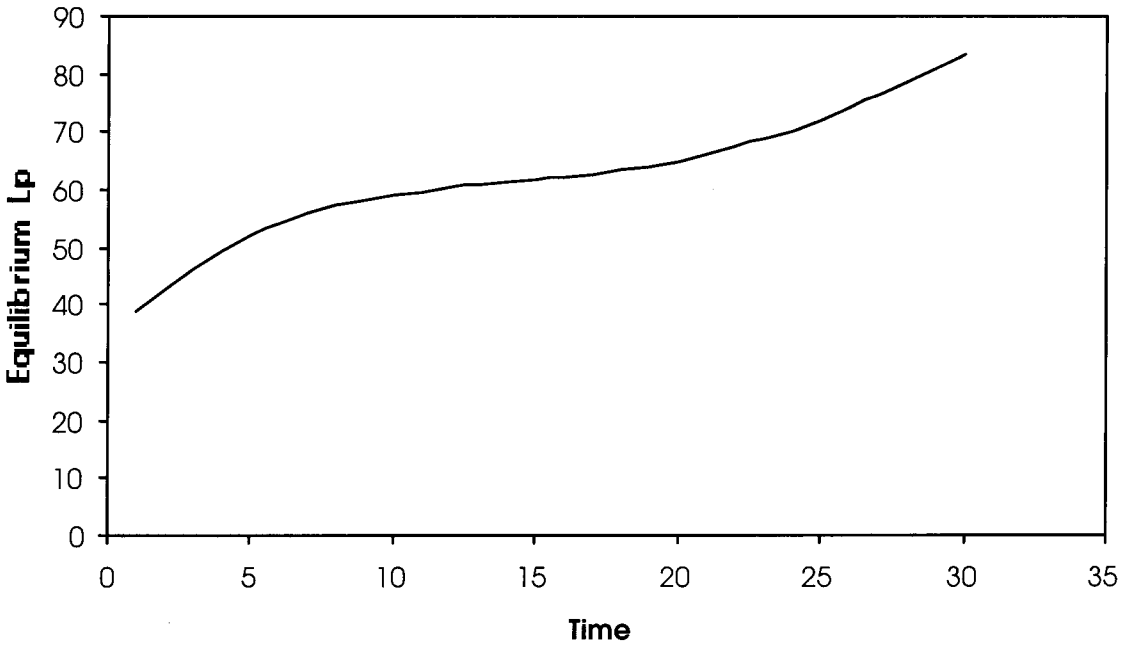

Figure 112: Slag-Metal equilibrium phosphorus distribution predicted by the Ide et al. correlation for the slag chemistry and temperature data of Figures 111 and 108.

The flux equations for phosphorus transfer in the slag and metal were solved assuming the dynamic equilibrium phosphorus distribution shown in Figure 112. For this particular simulation, the effect of slag flushing was ignored even though flushing did occur during the actual heat. Also, the kinetic term:

$$\frac{A\rho_m k_o}{W_m} \qquad 49$$

was assumed to be 0.13 min^{-1}. The calculated metal and slag phosphorus contents are plotted below versus time in Figures 113 and 114.

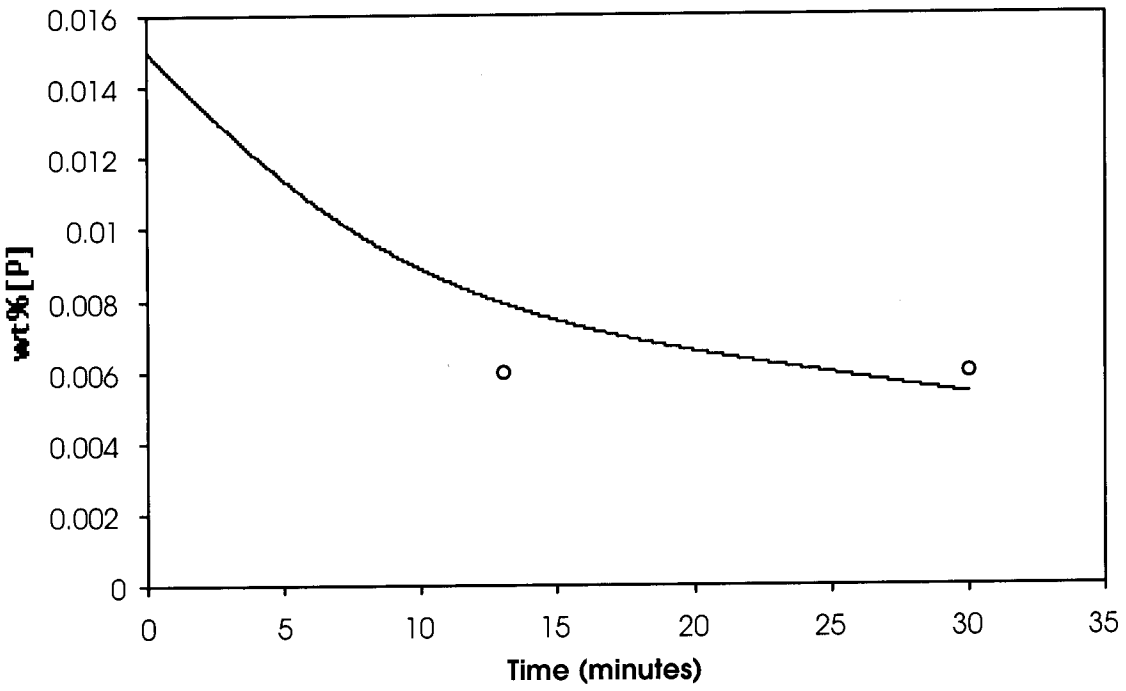

Figure 113: Metal phosphorus content predicted by the numerical process model for an EAF heat at NSST. The two discrete points are actual furnace chemistries.

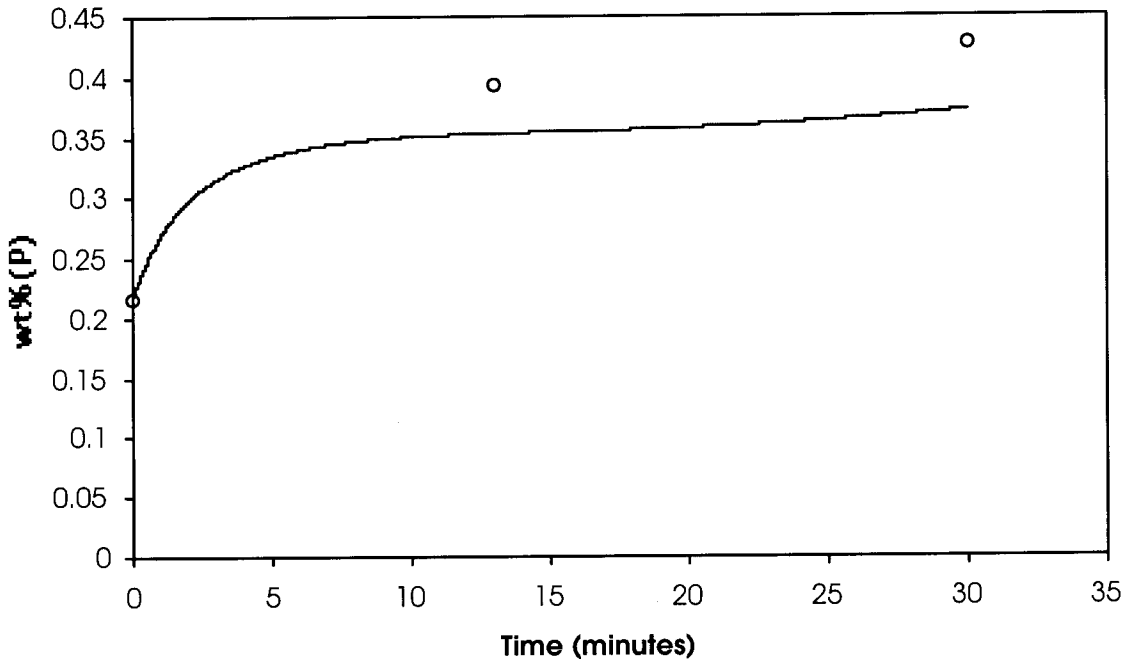

Figure 114: Slag phosphorus content predicted by the numerical process model for an EAF heat at NSST. The three discrete points are actual measured furnace slag chemistries.

The agreement between the predicted and calculated chemistries in Figures 113 and 114 is reasonably good. As described in Section 5.2, all of the early metal samples from the DRI trial heats at NSST showed fairly low metal phosphorus contents with only minor subsequent fluctuations. The simulation in Figure 113 suggests that a significant portion of the phosphorus mass transfer occurs early during the refining period. It is also interesting that with respect to phosphorus equilibrium, the positive influence of the slag chemistry changes, e.g. increasing CaO and decreasing FeO, more than make up for negative influence of the increasing temperature. As a result, the phosphorus distribution ratio remained high during the heat, and no period of reversion was observed.

6.2.2 BHP Electric Furnace Model – Continuous Feeding of HBI

The plant data from the BHP electric furnace trials with continuously fed HBI were also used to test the process model. A continuously fed electric furnace represents one of the most complex case studies, which can be evaluated by a model such as the present process model. During the actual and the simulated furnace heat, 60 tons of HBI were continuously fed into a 30 ton hot heal at an average rate of 1.7 tons per minute. Flux additions of lime and dolomite were fed concurrently with the metallic charge in order to balance the silica content of the HBI and maintain a slag V ratio of 2.5. The charging rate was selected such that the furnace power input matched the heat requirements for the heating and melting all of the charge materials. Therefore, during the period of continuous charging the furnace temperature nearly constant. When continuous feeding was terminated, the temperature increased exponentially. In order to model this system the following assumptions were made:

Slag:

- The initial slag weight was based upon an assumed 75 kilograms of slag per ton of steel on the heel.
- The initial slag chemistry was approximated from the experimental data in Figure 95.
- The mass of silica in the slag increased proportionally with the rate of feeding of HBI and the amount of silica in the HBI material according to Table 8.

- The mass of lime in the slag increased at a rate of 2.5 times the increase in slag silica.
- The mass of MgO of the slag increased linearly with time.
- Due to a lack of data regarding the chemistry of the steel heel, the change in the weight of iron oxide in the slag was approximated in a best fit manner. For the data in Figure 95, it was found that a harmonic equation could be used to roughly represent the profile of the FeO.
- The late in the heat, the above assumptions resulted in approximately 200 kg of slag per ton of metal. For a significant portion of the heat, however, the furnace was only partially filled. It was assumed that slag flushing would only become significant late in the heat when nearly all of the metallic charge had been fed into the furnace.

The above assumptions resulted in the following calculated slag profile for the continuously fed heat:

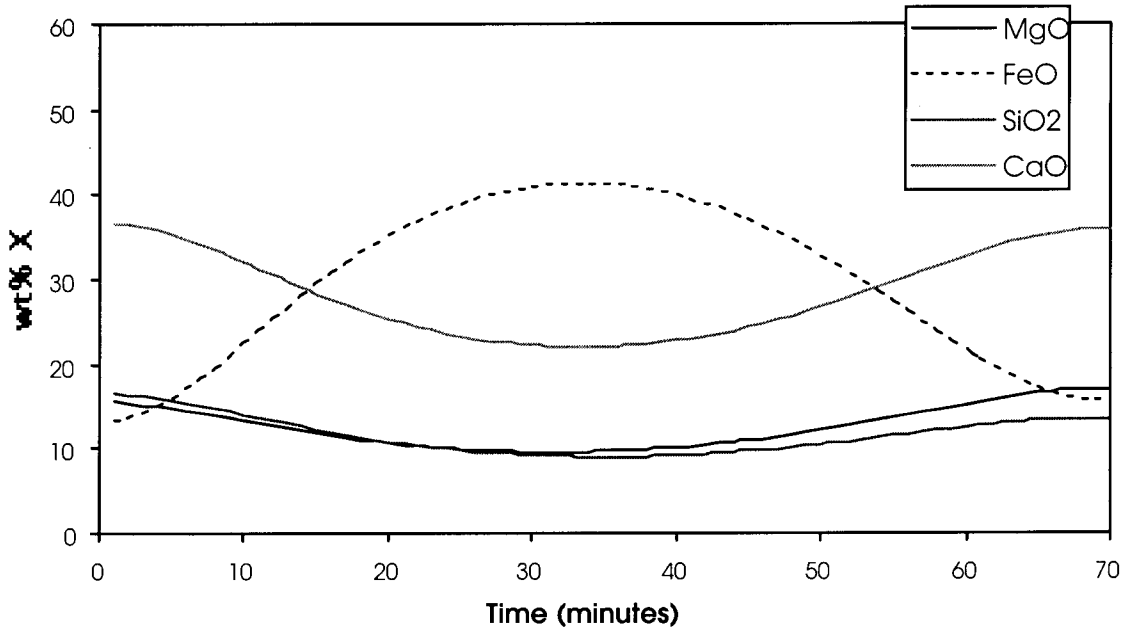

Figure 115: Modeled slag chemistry profile for the BHP electric furnace trial with continuously fed HBI. The actual slag chemistry profile is shown in Figure 97.

Figure 115 represents the major features of the actual measured slag chemistry profile reasonably well.

Temperature:

- The temperature was modeled after the general behavior observed in the in the actual data from the heat shown in Figure 109. The temperature basically followed a slowly developing exponential equation. The temperature profile used in this simulation is shown in Figure 116.

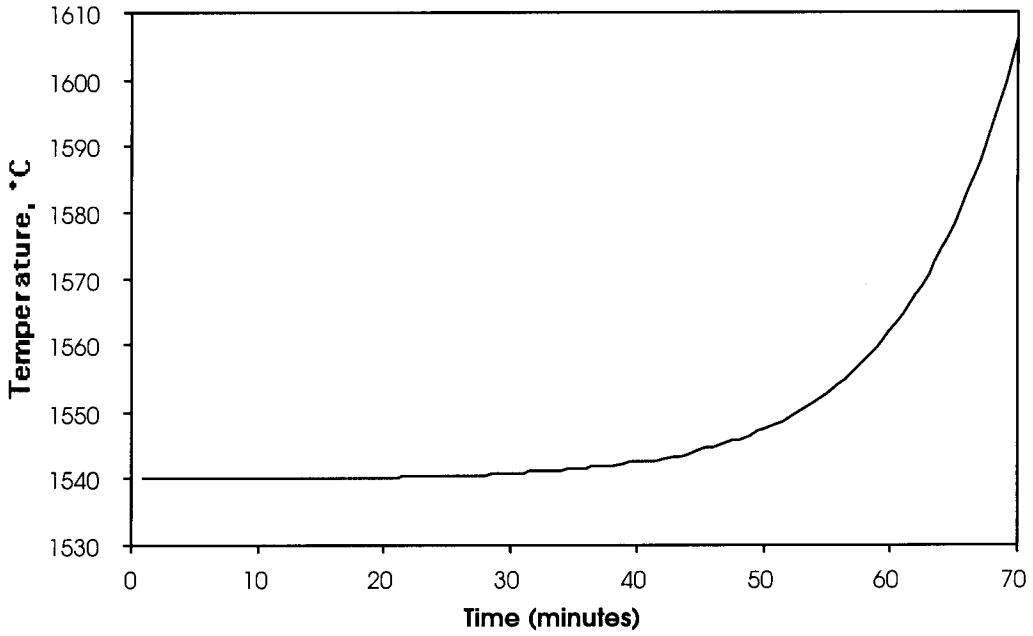

Figure 116: Simulated temperature profile for the BHP electric furnace trial with continuously fed HBI. The actual temperature profile is shown in Figure 109.

Based upon the slag chemistry and temperature profiles in Figures 115 and 116, the equilibrium phosphorus distribution was calculated according to the Ide et al. correlation.

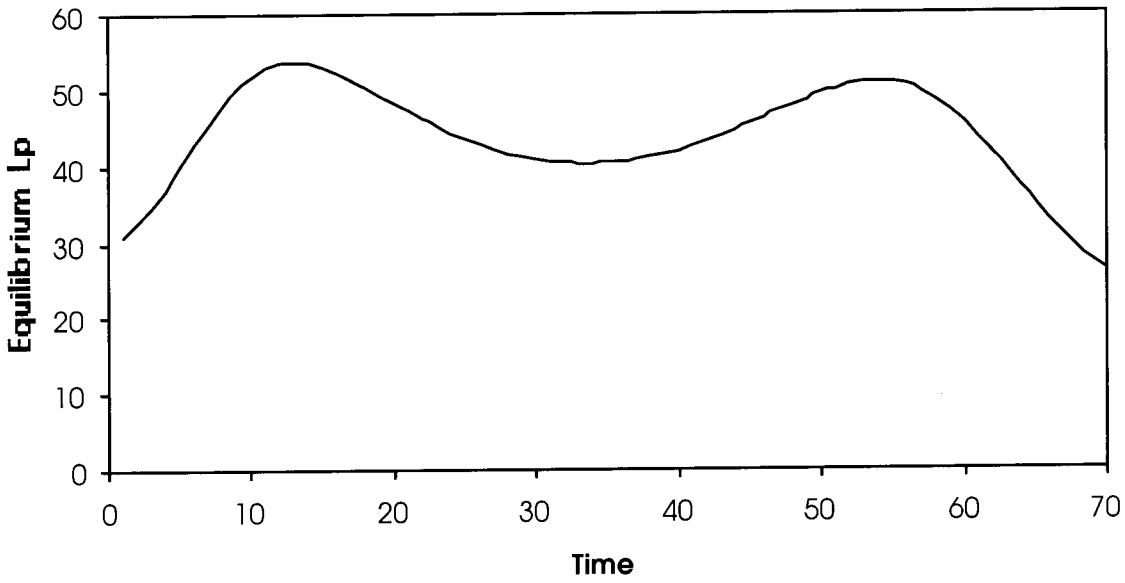

Figure 117: Slag-Metal equilibrium phosphorus distribution predicted by the Ide et al. correlation for the slag chemistry and temperature data of Figures 115 and 116.

Due to the continuous addition of phosphorus containing HBI, several additional assumptions had to be made. Based upon the laboratory results of the present research, it is believed that phosphorus reversion from HBI gangue to the surrounding bulk metal occurs on the same time scale as melting. Therefore, within the numerical model, the flux equation for phosphorus in the metal was modified to account for the phosphorus entering with the HBI. The flux equation for the slag phase remained the same. The changes in the liquid steel and slag weights were also incorporated into the model. The modified phosphorus flux equations were then solved. The calculated metal and slag phosphorus contents are plotted versus time in Figures 118 and 119 respectively.

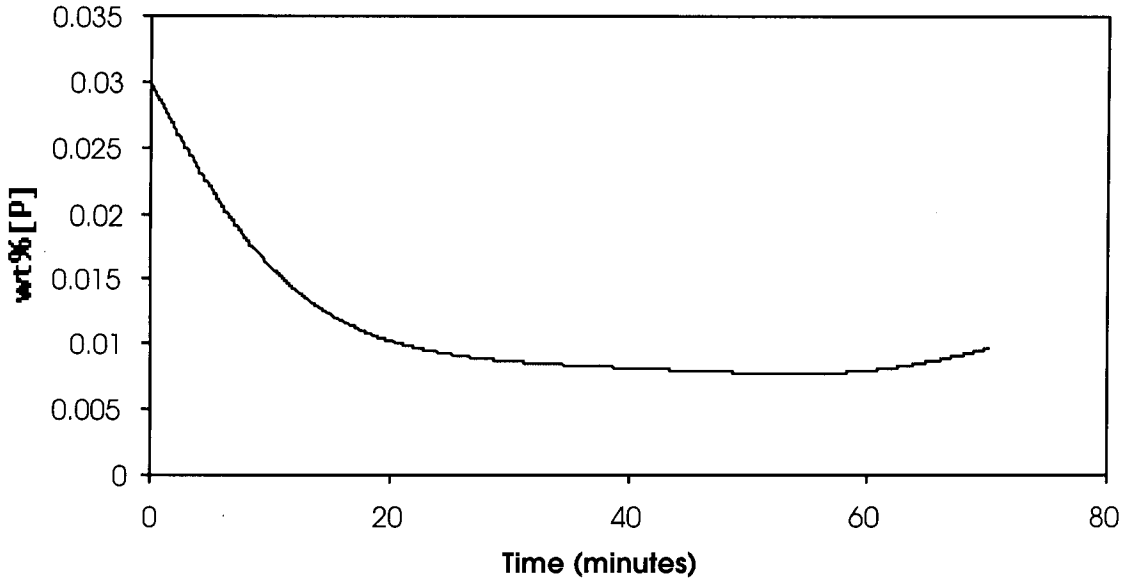

Figure 118: Metal phosphorus content predicted by the numerical process model for an EAF heat, which was continuously fed with 60 tons of HBI.

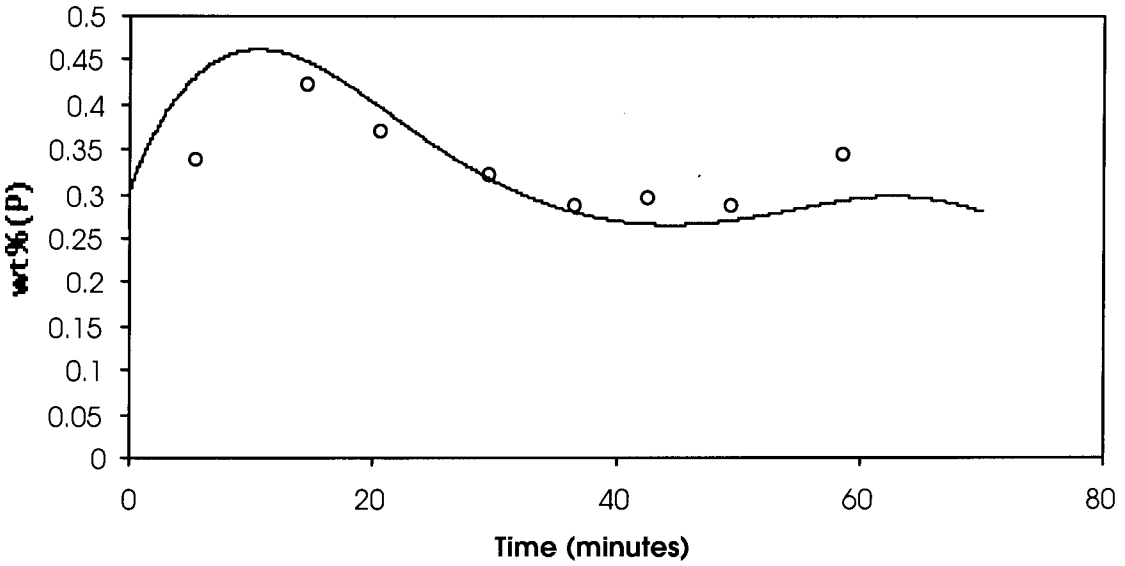

Figure 119: Slag phosphorus content predicted by the numerical process model for an EAF heat, which was continuously fed with 60 tons of HBI. The discrete points are actual measured furnace slag chemistries.

The agreement between the calculated and experimentally measured slag phosphorus content as shown in Figure 119 is excellent. Figure 119 suggests that extremely complex slag-metal systems can be described very accurately using the present simple model if the time dependant slag chemistry and temperature behaviors are known and can be

mathematically represented. With the appropriate data, the behavior of the slag chemistry during a given heat could be calculated from first principals accurately enough to suit the present model.

The calculations represented in Figures 118 and 119 were made assuming that all of the phosphorus in the continuously charged HBI initially enters the liquid metal melt. Phosphorus is then transferred between the slag and metal in response to the equilibrium conditions at each time step. As was discussed previously, many researchers believe that when HBI is melted, the phosphorus contained in the material will initially enter the slag phase and then transfer to the metal in response to equilibrium. The basic model used in the simulation shown in Figures 118 and 119 was modified such that all of the phosphorus contained in the HBI initially entered the slag phase rather than the metal. The calculated slag phosphorus content for the two cases, e.g. phosphorus initially entering the metal phase and phosphorus initially entering the slag phase, are plotted along with the experimental data in Figure 120.

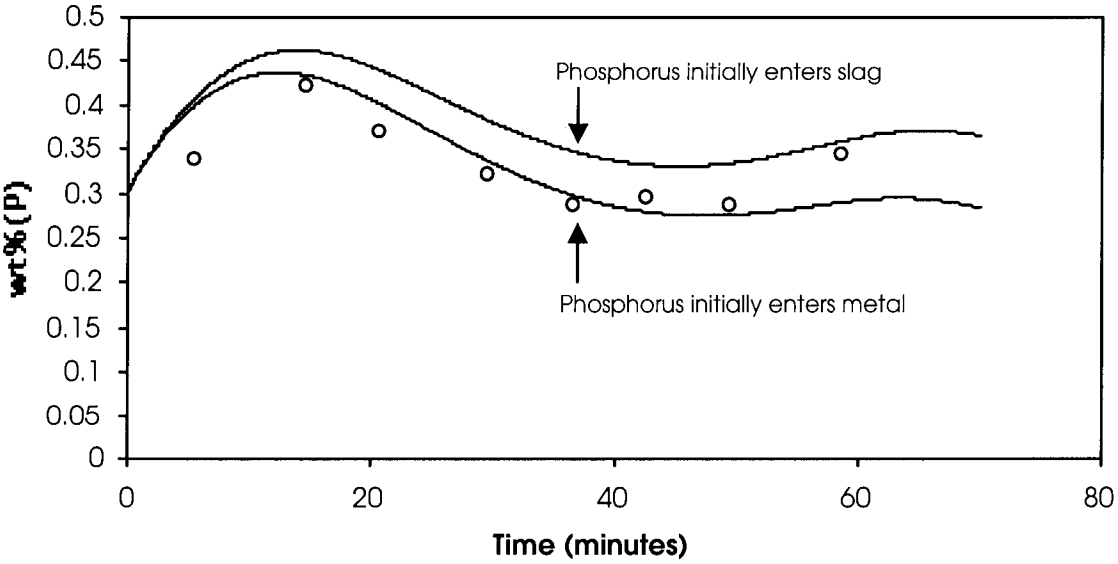

Figure 120: Slag phosphorus content predicted by the numerical process model for an EAF heat, which was continuously fed with 60 tons of HBI. The upper continuous curve was calculated assuming all phosphorus from the HBI initially reports to the metal phase. The lower continuous curve was calculated assuming all phosphorus from the HBI initially entered the slag phase. The discrete points are actual measured furnace slag chemistries.

Figure 120 suggests that there is almost no difference between whether the phosphorus contained in the HBI initially reports to the slag or metal. The HBI feed rate of 1.7 tons per minute delivers, roughly 0.92 kg of phosphorus per minute to either the slag or metal. Alternatively, during the first 10 minutes of the simulation, phosphorus is being transferred from the metal to the slag at a rate of approximately 0.4 to 0.5 kg per minute. The net build-up of .42 kg per minute represents only a 0.01 wt%(P) build-up in the slag. Under conditions where liquid phase mass transfer is extremely slow, and/or the feeding rate is very high, a significant build up in either phase might occur. However, continuous feeding of HBI results in rapid evolution of carbon monoxide at or just below the slag metal interface. As a result, the stirring conditions and the mass transfer parameter of a given furnace will be strongly related to the rate of continuous HBI charging. Therefore, it is likely that the conditions of low slag-metal stirring and high HBI feed rate will be mutually exclusive.

6.3 Value of a Predictive Process Model

A numerical process model for phosphorus transfer in the electric furnace was developed and tested in the previous sections. The general trends in slag chemistry and bath temperature, which were observed for three different electric furnace practices were also discussed in previous sections. A numerical process model as was described in Section 6.2 should be extremely useful in evaluating the influence of various furnace operating parameters upon the behavior of phosphorus during a given heat. Model simulations can be conducted as an alternative to expensive furnace trials in order to better optimize furnace practice for phosphorus control. Several comparative heat simulations are presented below, primarily as examples of how the process model can be used.

6.3.1 Influence of Mass Transfer Kinetics Upon Metal Phosphorus at Tap

Mass transfer kinetics will vary from one electric furnace to another. The present author speculates that the mass transfer parameter of the electric furnace can vary by at least an order of magnitude. The stirring conditions of the electric furnace will be most strongly influence by such factors as the use of bottom stirring, the melt-in metal carbon and slag FeO contents, continuous DRI/HBI feeding, etc. Under typical EAF

steelmaking conditions, some degree of dephosphorization will proceed during the refining stage of the heat. As tap to tap times become shorter, it may be necessary for some furnace operators to improve the mass transfer conditions of their furnaces in order to achieve acceptable phosphorus levels in the steel.

The process model was used to simulate three heats with different mass transfer parameters. Temperature and slag chemistry profiles were generated, which reflect the observations of actual plant data as discussed in previous sections. The temperature and slag chemistry profiles for the three simulated heats are shown in Figures 121 and 122.

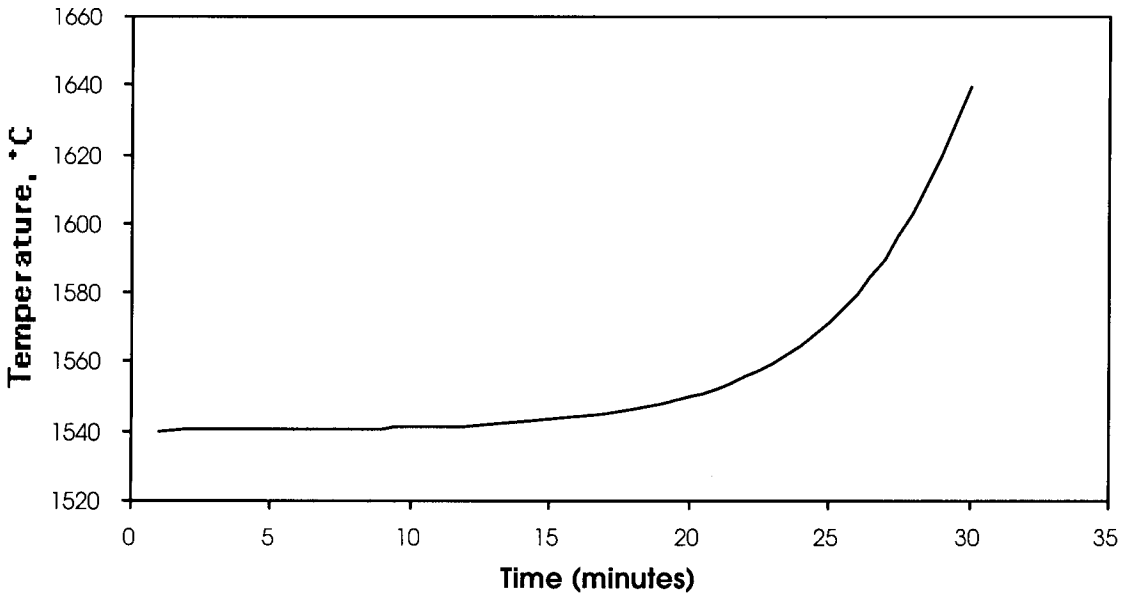

Figure 121: Metal temperature profile for the simulated EAF heats.

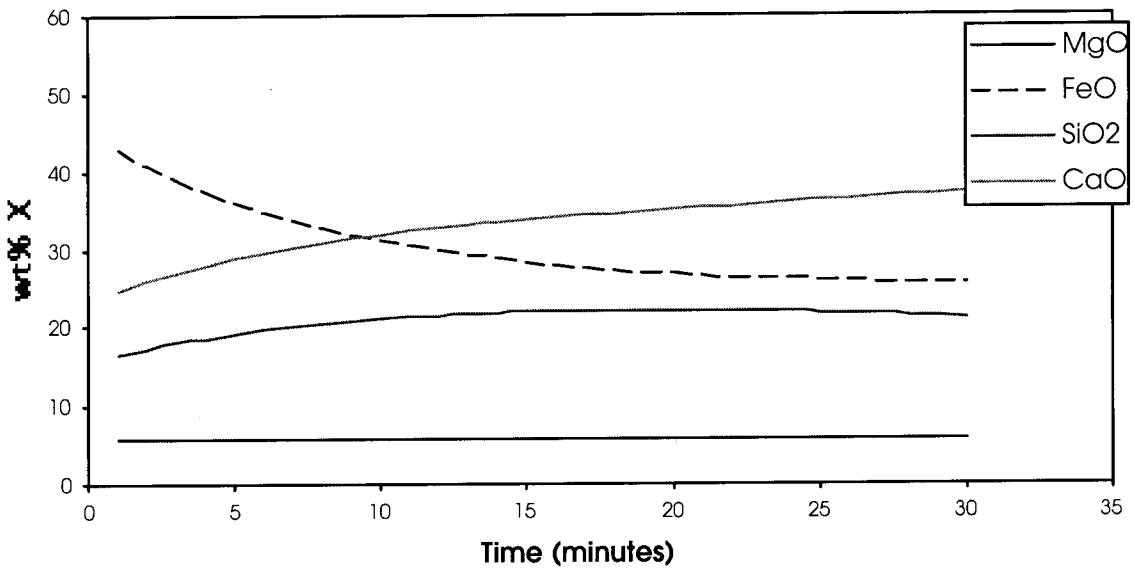

Figure 122: Slag chemistry profile for simulated EAF heats.

The equilibrium phosphorus distribution ratio was calculated for the above temperature and chemistry profiles, and is plotted versus time in Figure 123.

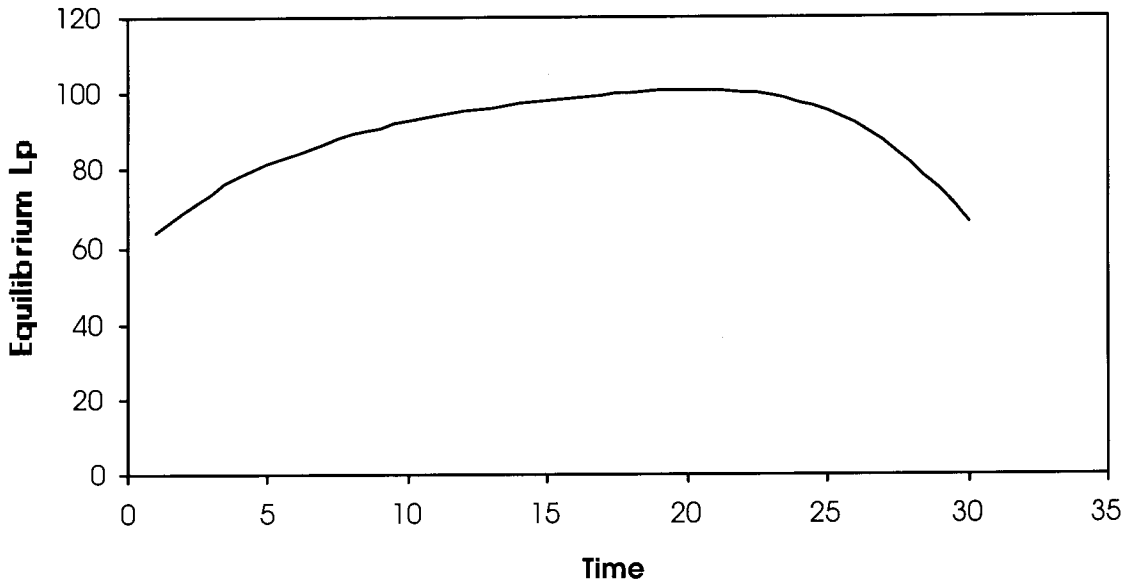

Figure 123: Equilibrium Phosphorus distribution ratio for simulated EAF heats based upon the temperature and slag chemistry profiles of Figures 121 and 122.

The equilibrium phosphorus distribution shown in Figure 123, is particularly useful in comparing mass transfer conditions because it peaks at some time in the middle of the heat. For very fast mass transfer conditions, the slag-metal system will closely follow the equilibrium profile. For slower mass transfer conditions, the specific shape of the

dynamic equilibrium profile will be less discernable. The numerical process model was used to calculate the metal phosphorus content versus time for three mass transfer conditions, which represent the limits of what was observed in the present study.

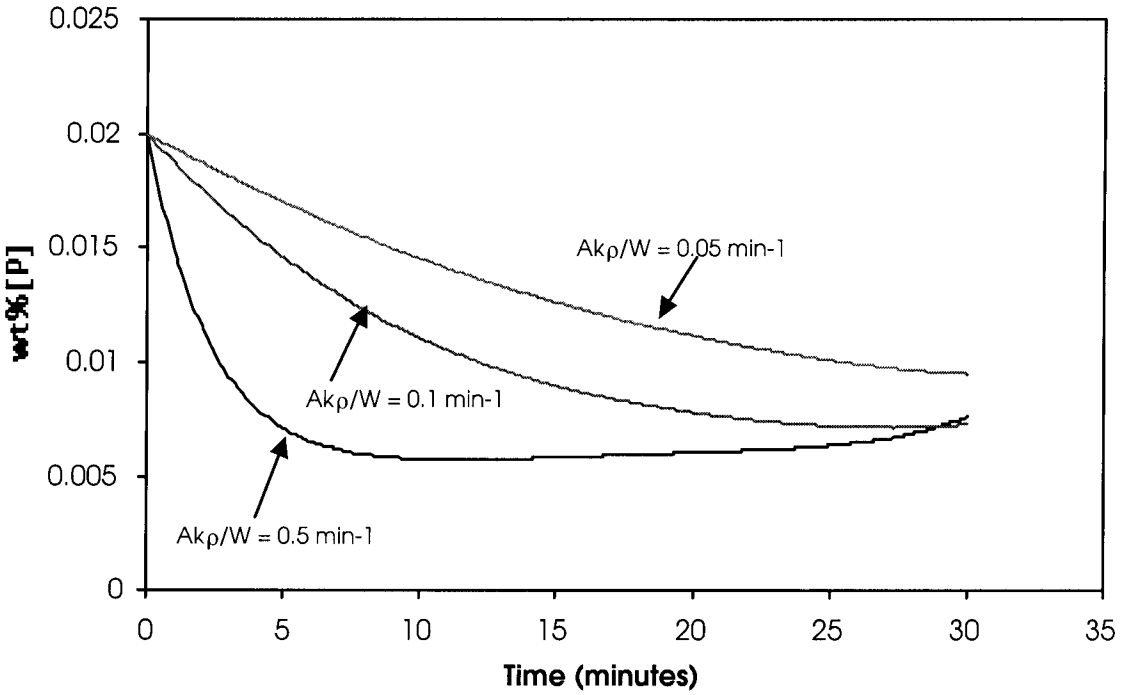

Figure 124: Simulated EAF metal phosphorus content versus time for three different mass transfer conditions.

The results of Figure 124 suggest that the kinetics of phosphorus mass transfer in the electric furnace has a strong effect on the metal phosphorus content of the steel during the course of a heat. For a tap to tap cycle with a 30 minute flat bath period, the three mass transfer conditions modeled in Figure 124 result in very similar final metal phosphorus contents in the steel. A 30 minute flat bath period is typical for a furnace with a 80 to 100 minute tap to tap time. If the refining period is reduced in length by 50 percent, the final metal phosphorus content will vary significantly for the three mass transfer conditions. For some electric furnace operations where the mass transfer conditions of the furnace can not be improved, the push toward shorter tap to tap cycles may be accompanied by restrictions in the chemical composition of the charge materials.

6.3.2 Effect of Melt-in FeO Upon Metal Phosphorus at Tap

Oxygen is used in electric furnaces today in ever increasing amounts in order to reduce electrical usage and accelerate melting. However, the amount of oxygen will have a direct effect upon the melt-in chemistry of the slag. In addition to compromises regarding metallic yield, increased oxygen usage may have an effect upon phosphorus control in the metal.

The behavior of FeO in electric furnace steelmaking slag was discussed at length in Section 6.1.1. It has been concluded by the present author that, for the furnaces examined in this study, the melt-in FeO content of the slag is most strongly influenced by the amount of injected oxygen used during melting. This assertion assumes DRI/HBI usage is less than 30% of the metallic charge, and that none of the charge materials exhibit exceedingly low metallizations. Subsequent to melt-down, iron oxide is reduced from the slag primarily via reaction with carbon in the steel bath. The degree of FeO recovery obtained for a given heat depends upon the slag flushing practice, the initial FeO content of the slag, the total slag weight, the melt-in carbon content of the steel, and the kinetics of mass transfer in the furnace.

Three electric furnace heats where simulated were the initial melt-in FeO content of the slag was varied from 30 wt%, 50 wt %, to 65 wt%. The final FeO content of the slag was held constant at 20wt% FeO, which implies that the heats also melted in with different metal carbon contents. The behavior of the other slag components followed the typical behavior observed in the plant trials of this study, e.g. increasing basicity due to continuous dissolution of lime and relatively constant magnesia content. The furnace temperature was increased from 1540°C near the beginning of the refining period to 1640°C at tap according to a slowly developing exponential function. The basic slag chemistry behavior for the heat containing 30 wt% FeO at melt-in is shown in Figure 125:

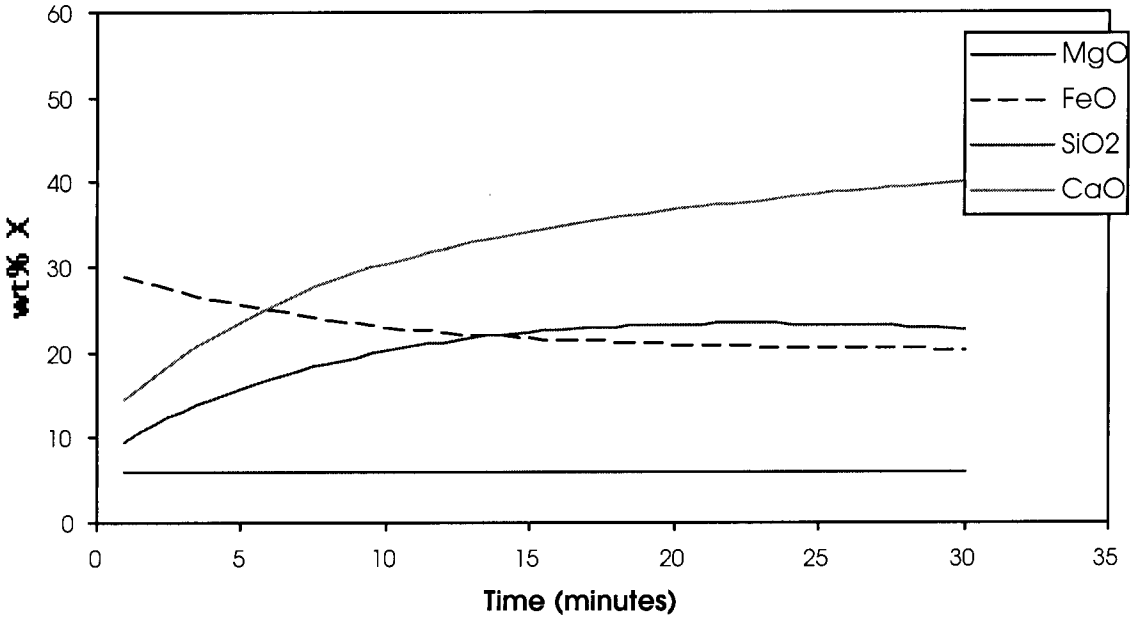

Figure 125: Slag chemistry profile for simulated heat with an initial FeO content of 30wt%

The other two heats with higher initial iron oxide contents showed the same basic slag chemistry profiles, e.g. the other slag components maintained the same ratios to one another. However, the slag FeO profiles for these heats differed as shown in Figure 126.

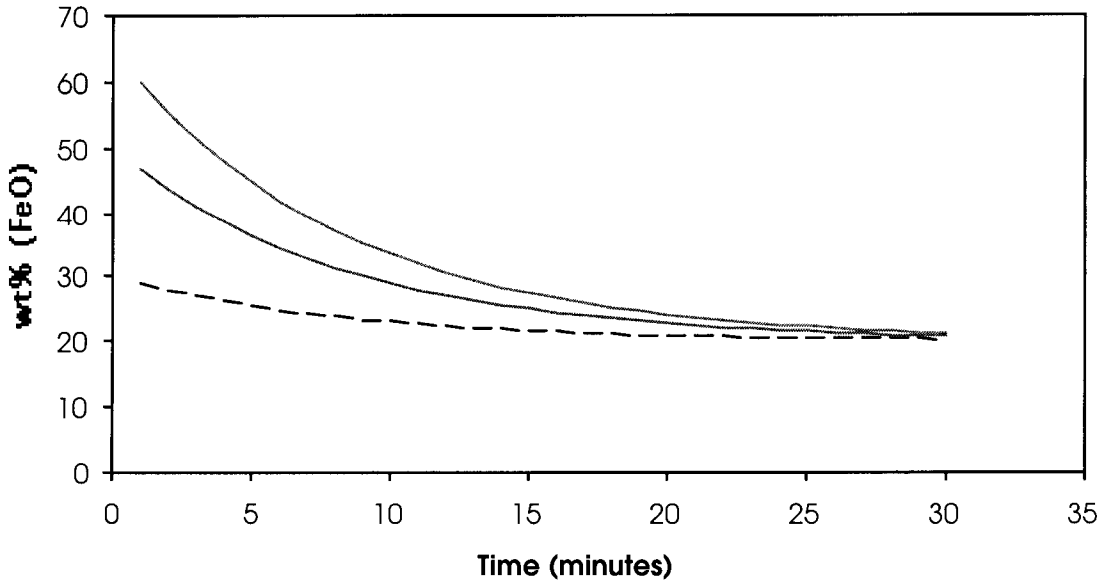

Figure 126: FeO profiles for three simulated heats.

Based upon the described temperature and slag chemistry profiles, the equilibrium phosphorus distribution was calculated as a function of time for the three heats.

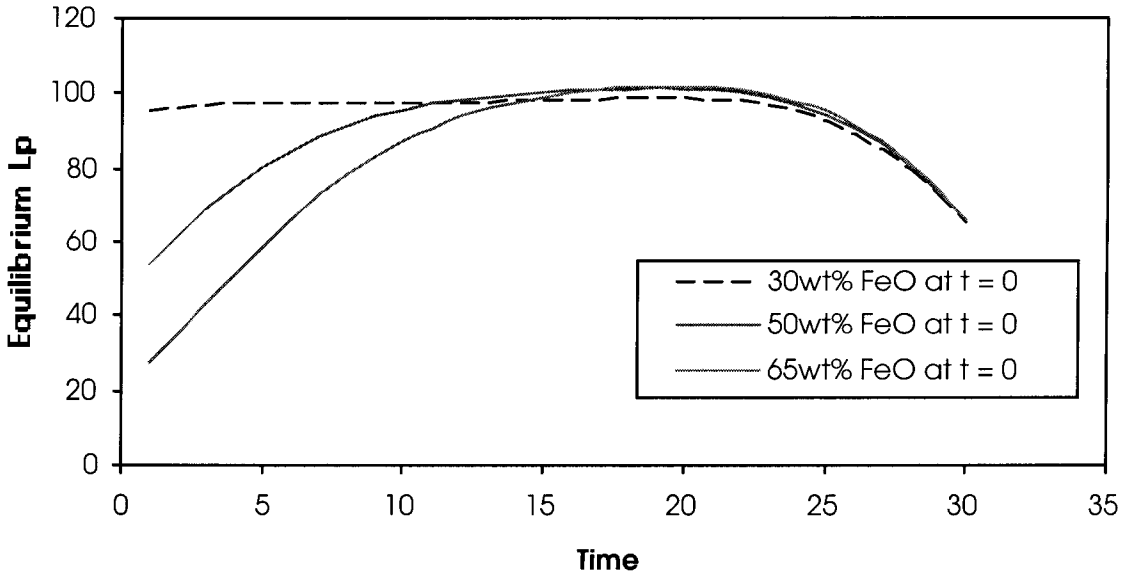

Figure 127: Calculated equilibrium phosphorus distribution for three heats with varying initial FeO contents in the slag.

Figure 127 shows that as the melt-in FeO content of the slag increases, the equilibrium phosphorus distribution early in the heat also decreases. The decrease in Lp toward the end of the heats is due to the rapid temperature increase just prior to tapping.

The numerical process model was used to calculate the phosphorus content of the steel as a function of time during the heat. The results for all three heats are shown in Figure 128.

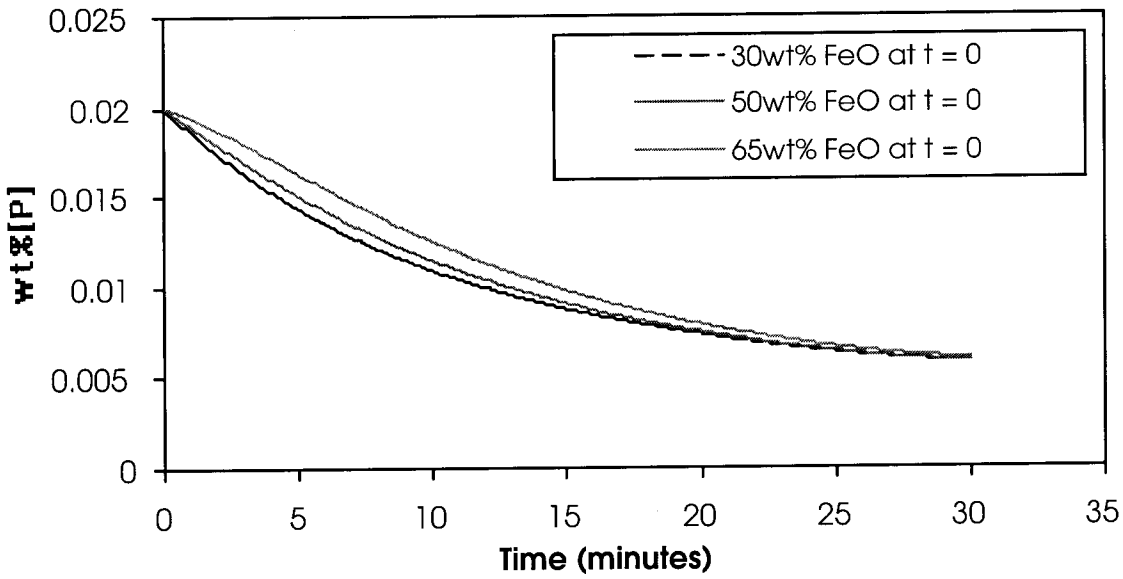

Figure 128: Predicted metal phosphorus content during the three simulated EAF heats.

Figure 128 indicates that despite differences in the phosphorus equilibrium early in the heat, the phosphorus content of the metal is not compromised if the iron oxide content of the slag is reduced to a reasonable level by the time of tap. Obviously, if the iron oxide content of the slag can not be reduced in the time allowed during the refining period, the equilibrium phosphorus distribution and metal phosphorus content at tap will be negatively effected. Because the kinetics of decarborization and dephosphorization are both liquid phase mass transfer limited for the conditions of this simulation, changes in the mass transfer conditions of the furnace should not significantly change the result of this simulation. If the slag is reduced primarily via direct carbon injection into the slag, the results of the present simulation may become invalid, though those conditions could just as easily be modeled.

6.3.3 V Ratio and the Phosphorus Mass Transfer

The relationship between slag V ratio and phosphorus control is common knowledge among those who make quality steels. Metal phosphorus decreases as a strong function of slag V ratio. Therefore, when making phosphorus sensitive grades from high phosphorus raw materials such as pig iron or DRI/HBI, a logical process modification is to increase the flux rate to the furnace in order to increase the V ratio of the slag.

However, it is most likely that there is a limit, beyond which further increases in the V ratio may negatively impact the final phosphorus content of the steel.

For a significant portion of the electric furnace steelmaking cycle, the furnace temperature is below 1600 °C. As was discussed in previous sections, investigation of actual furnace slag chemistry data shows that solid lime charged early in the melting cycle is continuously dissolving into the liquid slag late into the refining period. This is due in part to the kinetics of lime dissolution into the slag, but is primarily due to the temperature dependent solubility limit of lime in the CaO-SiO_2-FeO-MgO slag system. The maximum amount of lime present in the liquid portion of the slag will always be limited by this solubility limit. Lime additions in excess of the CaO solubility limit will result in either solid flux agglomerations frozen to the furnace side-wall or in second phase particles suspended in the slag. Both phenomena are seen in actual steelmaking practices, and both will have a direct effect upon mass transfer in the furnace. Large solid agglomerations in the slag or slag crusting, will significantly reduce the amount of stirring in the slag phase. Second phase particles have a strong effect on the bulk viscosity of slags. The dependence of the bulk viscosity of steelmaking slags upon second phase particles is fairly well know due to its relevance to slag foaming. [48] For the temperatures and V-ratios sometimes observed in EAF steelmaking, second phase particles may be responsible for a factor of 5 increase in the bulk viscosity of the slag. Because the slag mass transfer coefficient is inversely proportional to square root of viscosity, suspended second phase particles may appreciably reduce the rate of mass transfer in the EAF.

A series of three simulations were conducted where the V-ratio of the slag and the phosphorus mass transfer parameter were varied. The specific conditions of the simulations were as follows:

Table 11: Conditions of EAF Variable V-ratio and Mass Transfer Parameter Simulations

Simulation	V-Ratio	$\frac{A\rho_m k_o}{W_m}$
A	2	0.2
B	3	0.1
C	4	0.05

Assuming the temperature and iron oxide profiles used in Section 6.3.1 above, the equilibrium phosphorus distribution ratios were calculated as functions of time for the three slag conditions listed in Table 11.

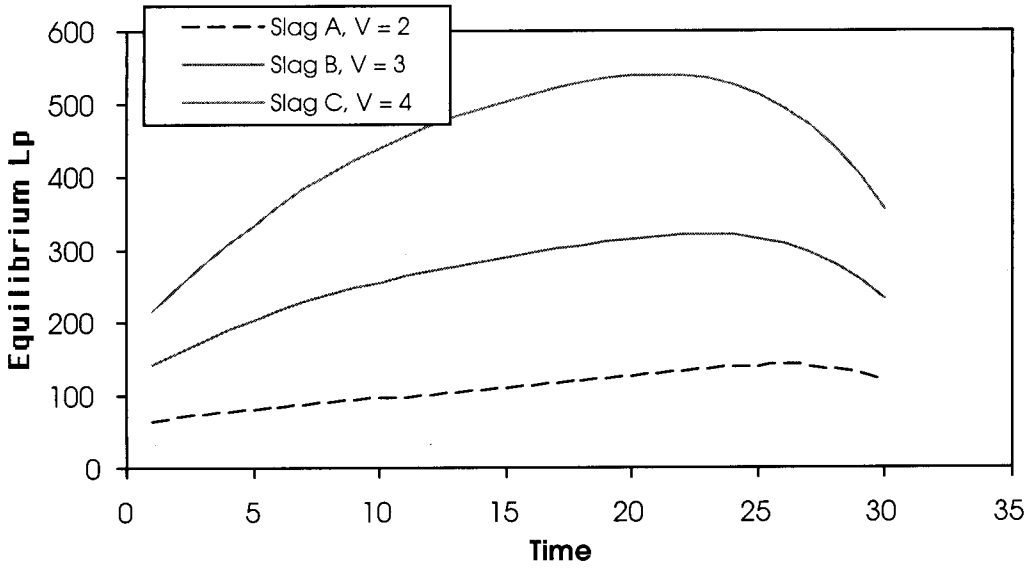

Figure 129: Equilibrium phosphorus distribution ratios for electric furnace simulations with different V-ratios.

Based on these calculated equilibrium conditions and the mass transfer conditions listed in Table 11, the phosphorus content of the steel bath was calculated using the numerical model. The results of the three simulations are shown in Figure 130.

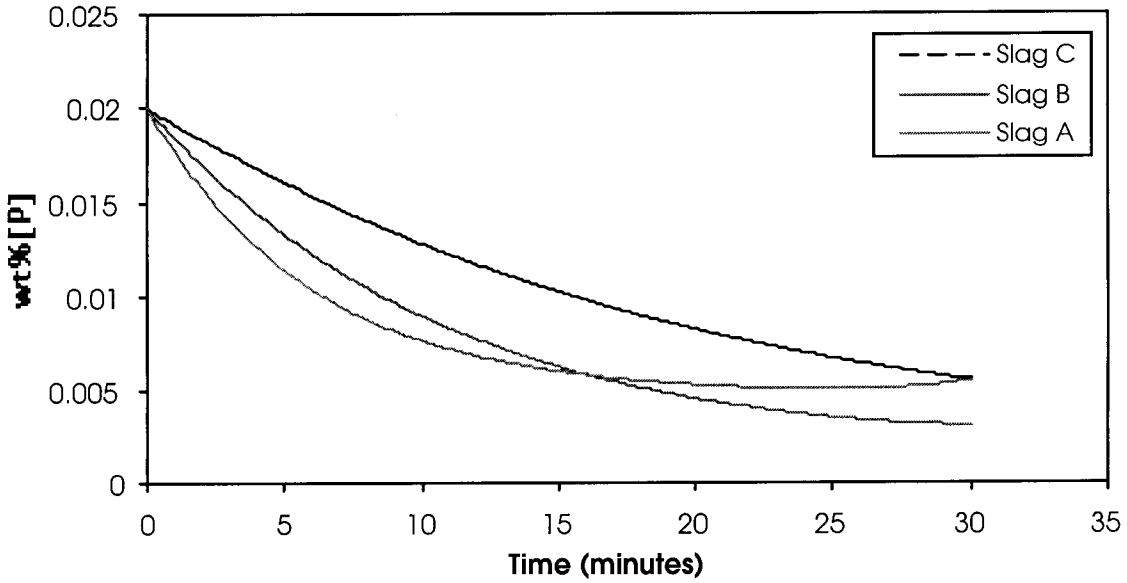

Figure 130: Predicted metal phosphorus content during the three simulated EAF heats.

Despite the very favorable phosphorus equilibrium conditions of Slag A, the slower mass transfer kinetics related to the suspended solids in the slag result in a final metal chemistry similar to that obtained with Slag C. Slag B, representing a compromise between viscosity and equilibrium phosphorus distribution ratio generates the lowest metal phosphorus content at tap. The relationship between V-ratio and the mass transfer parameter, which is proposed in Table 11 is not a fundamental calculated correlation. Therefore, the present author does not propose that slag B represents the ideal dephosphorizing slag. The simulations in Figure 130 are intended to be representative of phenomena, which are real, but not a precise and quantitative evaluation of those relationships. A diligent review of the literature would likely yield the data necessary to develop a more accurate correlation between excess solid lime and slag viscosity, and therefore mass transfer kinetics.

CHAPTER 7

CONCLUSIONS

The primary goal of the present research was to contribute to a better understanding of the behavior of phosphorus contained in DRI/HBI upon melting. The primary application of this research was aimed toward improved control of phosphorus in the EAF when using large amounts of DRI/HBI in the charge. The results of this research can be broken down into four basic components:

7.1 Investigation of Commercial DRI/HBI

An extensive investigation of the physical and chemical attributes of 7 different commercial DRI/HBI materials was completed. All components of this investigation were aimed toward the development of a fundamentally based understanding of the behavior of phosphorus in these materials upon melting. Some of the specific findings of this study include:

- Scanning electron microscopy indicates that phosphorus in DRI/HBI is present as a calcium phosphate phase.
- SEM investigation has shown that the gangue feature sizes present in DRI/HBI are very small. ($\approx$ 20-200 μm in size) The enormous area of contact between these fine gangue particles and the surrounding metal provides a large reaction area for phosphorus transfer from the gangue to metal upon melting.
- Fast melting experiments with DRI and HBI indicate that a significant amount of phosphorus is transferred from the gangue to the metal phase upon melting and that little phosphorus transfer occurs at times greater than one minute. The kinetics of phosphorus transfer from gangue to metal are much faster then the rate at which liquid oxide inclusions can physically separate from the liquid metal.
- Since the rate of equilibration between metal and the gangue phases in DRI/HBI is very fast, the melt-in phosphorus content of the metal can only be controlled by modifying the gangue chemistry to improve the equilibrium phosphorus distribution ratio of the gangue.

- Small additions of basic components to DRI/HBI materials can alter the melt in chemistry of the metal. However, this is also heavily dependant upon the amount of iron oxide and carbon in the material. The ideal DRI/HBI material with respect to phosphorus would melt in with a gangue chemistries very similar to that of a good steelmaking slag.
- In such an ideal material, enough carbon should be present to reduce 80% of the iron oxide present in the material at the time of use. As necessary flux additions should be made to the DRI or HBI such that the overall gangue material exhibits a V-ratio of 1.65 and an iron oxide content of 26%. Only minor flux additions would be required to from a good steelmaking slag as the DRI/HBI material melted.
- When DRI/HBI is continuously fed to the EAF, excess carbon in material can be very effective in promoting a foamy slag. When DRI/HBI is batch charged with scrap, the primary result of excess carbon in DRI is to increase the melt-in carbon content of the steel. In both cases excess carbon will reduce the FeO content of the gangue to effectively zero as the material is melted. This will result in a gangue/slag-make with a very low Lp (Lp < 1.) In the case of continuously fed DRI, the operational benefits of the excess carbon may out-weigh phosphorus considerations. In the case of a batch charged process, cheaper sources of carbon relative to excess carbon in DRI can be obtained. A DRI/HBI material, which contains enough carbon to consume 80% of the iron oxide in DRI and melts-in with a low metal phosphorus content, should be of greater value to a batch charged process as compared to a material, which contains excess carbon.

7.2 Laboratory Phosphorus Kinetics Study

A fundamental laboratory study was conducted for phosphorus transfer between metal and slag.

- Laboratory kinetic experiments have shown that the apparent rate of phosphorus transfer decreases as the dephosphorization and rephosphorization reactions progress.
- Both the average value of the apparent mass transfer coefficient and the extent to which it varies during dephosphorization, appear to be functions of interfacial

tension, which is in turn a function of the mass flux under conditions of intense mass transfer.

- For the present experimental conditions the apparent overall mass transfer coefficient for dephosphorization was on the order of 0.01cm/s at the start of reaction and decreased to approximately 0.001 cm/s toward the end of the reaction.
- The results of the present kinetic study are in good agreement with those of Mori et al.[34] and Seetharaman et al. [50]
- Review of the literature indicates that the observed variance of the mass transfer parameter may be related to a dynamic interfacial phenomenon, which is likely to enhance mass transfer when mass flux across the interface is high and to become less significant as phosphorus approaches equilibrium.
- A transient reduction in the slag-metal interfacial tension during dephosphorization could lead to either an increase in the reaction area due to emulsification, an enhancement of the mass transfer coefficient, or both. Based on data of the present study and information contained in the literature, it is impossible to isolate the effects of area changes or changes in the mass transfer coefficient within the mass transfer parameter.

7.3 EAF Plant trials

A series of electric furnace trials were conducted at Pennsylvania Steel Technologies in order to determine the mass transfer parameter for that furnace. Additional trials were conducted by North Star Steel – Texas to examine the effects of different types of DRI/HBI materials upon the furnace yield, slag chemistry, and metal phosphorus behavior.

- The mass transfer conditions of a 150 ton DC furnace were evaluated based on controlled furnace trials. The results of the trials are summarized in terms of several different kinetic parameters in Table 4 (shown here again):

Table 4: Results of Mass Transfer Trials at PST

	Mass Transfer Coefficient, ko (assuming furnace area) cm/s	Mass Transfer Parameter, A*ko cm^3/s	$\frac{A\rho_m k_o}{W_m}$ min^{-1}
High Value	0.99	$3.5*10^5$	1
Low Value	0.05	$1.7*10^4$	0.05
Best Fit Value	0.25	$8.7*10^4$	0.25
BOF Laboratory Expts.	--- ≈ 0.01	--- ≈ 0.07	1 ≈ 0.16

- It was determined that when enough operating variables were held constant or accurately measured, reasonable analysis of the experimental data yielded very realistic and reproducible numbers for the phosphorus mass transfer parameter.
- The most difficult variables to either control or measure, were the instantaneous weights of the liquid portion of the slag and metal.
- The trials at NSST suggest that the amount of injected oxygen used during melting has a more significant effect upon the FeO in the slag for a given heat, than does the FeO contained in DRI materials.
- Several general trends were observed in the NSST slag chemistry data behavior as a function of time during a given heat.
- The data from the NSST trials indicate that the unbalanced iron oxide units in Circal can be recovered by increasing the melt-in carbon content of the bath with pig iron additions. Indications are good that any source of carbon, which first melts or dissolves into the steel bath will be effective in recovering iron oxide units from the slag.
- Carbon, which remains suspended in the slag may be less effective in recovering iron units from a high FeO slag. This includes foamy-slag or injected carbon.
- Indications are that phosphorus mass transfer between the slag and metal is fast enough that the details of whether phosphorus from DRI/HBI first enters the slag or the metal is less relevant to the final metal phosphorus than are other operating parameters. Factors such as iron oxide content of the slag, excess superheat at tap, and slag carry over to the ladle have a much stronger influence on the final phosphorus content of the cast steel.

7.4 Process Model for Phosphorus control in the EAF

A process model based upon the plant trials and laboratory experiments was developed and tested using the plant data from the trials at NSST and data from trials conducted at BHP Steel Sydney.

- A semi-empirical model with a basis in fundamental phenomena was developed to describe the slag chemistry as a function for a given heat.
- It was found that the process model was able to reproduce the observed phosphorus mass transfer in both the NSST and BHP plant data when the slag chemistry and temperature profiles were known with accuracy.
- In the simulation of a heat, which was continuously fed with HBI for more than 60% of the charge, the process model indicated that it made very little difference whether the phosphorus in HBI first melts into the slag or the steel. After feeding 60 tons of material in a period of 35 minutes, the metal phosphorus content was predicted to be only 0.002wt% higher, when the phosphorus first entered the metal versus if it initially enters the sag.
- For illustrative purposes, the process model was used to simulate various operating conditions. The intent of the simulations was to show that the model could be used to evaluate the effects of various operating parameters on the behavior of phosphorus in the furnace.

CHAPTER 8

FUTURE WORK

8.1 Laboratory Experiments

- A better understanding of the fundamental phenomena, which lead to a dynamic mass transfer parameter during dephosphorization should be developed.
- A more precise definition of the mass transfer parameter, including the precise influence of parameters such as the slag-metal interfacial tension is needed.
- A better understanding of the structural aspects of molten salts is needed. With respect to the present study, a better understanding of the fundamental mechanism of phosphate ion formation at the slag-metal interface, and the precise mechanism of oxygen delivery to the interface from the slag is necessary to develop a better understanding of dynamic interfacial phenomena.
- A fundamental kinetic study should be conducted regarding the mass transfer of phosphorus, and other species in foamy slags. Most modern electric furnaces take advantage of the many operational benefits of a foamy slag practice. It is likely that the kinetics of mass transfer will be different in a highly agitated slag with 25% of its theoretical density.
- During UHP-DC electric furnace steelmaking, more than 10^5 coulombs per second (>100 kA) of charge are passed through the slag and across the slag metal interface. Alternatively, the charge transfer involved during typical conditions of dephosphorization is on the order of 10^4 or 10^3 coulombs per second. Because slag-metal reactions are electrochemical by nature, it would be interesting to examine the possible effects of arc current upon the thermodynamics and kinetics of slag-metal reactions important to steelmaking.

8.2 Plant Trials

- The plant trials conducted in conjunction with this study were an invaluable component of this project. Specific knowledge regarding the trends in slag chemistry

and temperature as functions of time during the steelmaking cycle are critical in arriving at the right answer.

- Efforts should continue to develop an understanding of the phenomena, which most strongly affect the bulk changes in slag chemistry which are observed in EAF steelmaking. The rate of scrap pile oxidation by oxidizing gasses in the furnace needs to be better understood. For these experiments, early sampling of the first slag to form in the furnace is required. Such samples were obtained for a few of the heats conducted at NSST. If good correlations can be established between various melting parameters, such as oxygen injection and the iron oxide content of the slag at melt-in, a more systematic evaluation of the reduction of iron oxide from slag can be realized.
- In addition to FeO behavior, a systematic study should be performed of the behavior of lime and magnesia in EAF slags. The specific relationships, which govern the rate of lime dissolution need to be better understood.
- If the flux dissolution and iron oxide formation and reduction processes are well understood for a given furnace, it should be possible to optimize the furnace practice with respect to yield, energy, carbon, and oxygen usage and melting time.
- If the normal process parameters, which affect the bulk slag chemistry are well understood a more systematic and controlled technique can be developed for comparing the performance of various raw materials in the furnace. With a more systematic evaluation process, more information can be gathered from fewer trial heats.
- Very large temperature gradients exist in the EAF during melting and refining. A better understanding of the temperature profiles in the slag and metal during an individual heat would very useful with respect to modeling of chemical reactions in the furnace

8.3 Process Model

- A useful tool was developed for evaluating the effects of various process parameters upon the behavior of phosphorus in the steel.
- The process relies heavily upon semi-empirical relationships describing the observed behavior or the bulk slag chemistry of the EAF during steelmaking, i.e. the dissolution rates of lime and MgO, and the melt in FeO content of the slag. Once the

fundamental processes, which govern the behavior of the slag chemistry are known, they should be included in the process model.

- In its present form, the process model can be executed in a symbolic math program. The model allows for a great deal of flexibility in how the slag chemistry and temperature data are introduced into the model. If the behavior of the slag chemistry can be understood from a fundamental perspective, such that its behavior becomes dependant upon only a few process parameters, the need for this flexibility may be diminished. Depending upon how the model is to be used in the future, it may be valuable to code the model such that it is a stand alone executable program. As an executable program, the model would be much more useful to electric furnace operators who wish to evaluate various conditions on their own.
- For furnaces with very short tap to tap cycles, a significant portion of the refining processes occur simultaneously with melting. The model should be modified to account for a continuously melting scrap charge.
- In its present form, the process model can be used to predict the phosphorus content of the steel as functions of time during a heat. With the basic framework of the phosphorus process model developed, it should be very simple to expand the model to predict the behavior of other slag metal reactions such as desulfurization.
- This model could be combined with others, developed for nitrogen transfer in steel to provide a very powerful tool for the optimization of electric furnace steelmaking.

Appendix A

Equilibrium Phosphorus Distribution Correlations

Phosphorus Distribution Equations

Investigator	Log (%P)/[%P]
Healy	$\frac{22,350}{T} + 0.08(\%CaO) + 2.5 \bullet \log(\%Fe_t) - 16.00$
Turkdogan	$\frac{21,740}{T} + 0.071 \bullet (\%CaO + 0.3\%MgO) + 2.5 \bullet \log(\%FeO) - 9.87$
Suito et al.	$\frac{10,730}{T} + 4.11 \bullet \log(\%CaO + 0.3\%MgO + \%CaF_2 - 0.05\%Fe_tO) + 2.5 \bullet \log(\%FeO) + 0.5\% \bullet \log(\%P2O5) - 13.87$
Zhang et al.	$\frac{11,000}{T} + \frac{1}{T}[162(\%CaO) + 127.5(\%MgO) + 28.5(\%MnO)] + 2.5 \bullet \log(\%FeO) - 6.28 \times 10^{-4} \bullet (\%SiO_2) - 10.76$
Ide and Fruehan	$\frac{10,730}{T} + 4.11 \bullet \log(\%CaO + 0.15\%MgO + \%CaF_2 - 0.05\%Fe_tO) + 2.5 \bullet \log(\%FeO) + 0.5\% \bullet \log(\%P2O5) - 13.87$

Appendix B

Chemical Composition of Slags Used by Mori et al. [34]

Slag Chemistries Examined by Mori et al. [27]

Designation By Mori et al.	Designation in Present Study	FetO	CaO	SiO_2	P_2O_5	MgO	Lp_{1600}*
D	1	33.2	34.9	30.6	0	12.0	100.6
E	2	45.0	18.1	28.5	0	27.9	21.7
C	3	23.1	40.2	35.2	0	10.7	75.3
A	4	42.0	35.3	20.7	0	6.5	164.1
L	5	25.1	25.8	43.8	5.1	23.6	45.45
I	6	69.0	12.0	11.6	7.4	7.5	8.61
F	7	47.3	29.8	16.9	5.3	8.0	245.4
H	8	48.1	25.7	18.6	7.0	9.4	160.1
H	9	48.1	25.7	18.6	7.0	9.7	161.3

*Lp calculated according to Ide and Fruehan [22] assuming T = 1600°C

Appendix C

Chemical Composition of Commercial DRI/HBI Materials Used in the Present Study

Chemical Composition of Investigated Commercial Materials

Material	Method of Reduction	Fe_t	FeO	C	SiO_2	Al_2O_3	CaO	P
Midrex DRI	Midrex	93.13	5.87	1.89	1.92	---	1.59	0.028
Midrex HBI	Midrex	92	10	< 0.5	1.8	---	---	0.06
BHP - HBI	Finmet	92	8	1.3	1.6	---	0.1	0.045
Mobile DRI	Midrex	91.2	7	2.43	1.14	0.36	0.3	0.037
Circal HBI	Circored	97	12	0	1.03	0.32	---	0.028
Sidor DRI	Midrex	93.76	7.6	>3	1.67	---	2.11	0.054
Opco HBI	Midrex	91.5	8.4	0.8	~2	---	---	0.053

Only limited compositional data were available from the suppliers of these materials. Shaded data were provided by the supplier of the material. The unknown quantities will be determined and reported in the final version of this report.

Appendix D

Methods and Results of Chemical Analysis of Experimental Slags

Methods of Chemical Analysis of Slag Components

SiO_2	Gravimetric (SiF_4 vaporization)
Total Iron	Stannous chloride reduction and dichromate titration
CaO	$KMnO_4$ titration
MgO	EDTA titration
P2O5	Phospho-Molybdenum-Blue photometric method

Chemical analysis of experimental slags

Slag Analysis for Dephosphorization Experiment #12

sample	Time (min)	%SiO2	%CaO	C/S	%MgO	%FetO	wt%(P)	Lp
12.11	11	22.58	48.36	2.14	error	20.36	1.41	46.32
12.6	60	22.82	44.48	1.95	error	12.55	1.23	116.63

Slag Analysis for Dephosphorization Experiment #13

sample	Time (min)	%SiO2	%CaO	C/S	%MgO	%FetO	wt%(P)	Lp
13.11	11	24.07	46.21	1.92	error	19.45	1.38	37.50
13.32	32	23.92	34.48	1.44	error	15.12	1.38	111.78

Slag Analysis for Dephosphorization Experiment #18

sample	time (min)	%SiO2	%CaO	C/S	%MgO	%FetO	wt%(P)	Lp
18.a	0	24.47	45.58	1.86	error	19.19	0.04	10.20
18.b	0.5	24.22	45.36	1.87	error	19.89	0.17	0.82
18.c	31	25.74	44.77	1.74	error	13.35	0.81	23.36
18.d	75	23.16	44.10	1.90	10.93	15.58	0.90	38.67

Slag Analysis for Dephosphorization Experiment #19

sample	time (min)	%SiO2	%CaO	C/S	%MgO	%FetO	wt%(P)	Lp
19.a	0	23.41	48.36	2.07	9.81	21.01	0.01	2.36
19.b	0.25	20.51	49.21	2.40	0.00	22.27	0.01	0.08
19.c	33	21.95	42.00	1.91	7.61	25.20	0.41	23.30
19.d	75	21.03	46.53	2.21	8.38	20.33	0.48	33.84

Slag Analysis for Dephosphorization Experiment #20

sample	time (min)	%SiO2	%CaO	C/S	%MgO	%FetO	wt%(P)	Lp
19.e	**0**	19.82	43.42	**2.19**	8.03	27.76	0.44	56.62
20.a	**0.5**	20.79	40.42	**1.94**	8.90	25.63	0.52	5.16
20.b	**31**	20.46	39.49	**1.93**	8.93	24.41	0.84	50.93
20.c	**76**	21.04	47.99	**2.28**	8.79	19.64	0.80	60.70

Slag Analysis for Dephosphorization Experiment #21

sample	time (min)	%SiO2	%CaO	C/S	%MgO	%FetO	wt%(P)	Lp
22a	**0**	25.71	43.63	**1.70**	12.88	20.30	0.42	44.40
22b	**30.5**	27.40	38.95	**1.42**	12.19	17.63	0.69	29.38
22c	**75**	27.83	37.70	**1.35**	13.76	17.49	0.71	45.57

Slag Analysis for Rephosphorization Experiment #16

sample	time (min)	%SiO2	%CaO	C/S	%MgO	%FetO	wt%(P)	Lp
16a	**8.3**	60.1	12.62	**0.21**	5.36	8.52	2.46	171.00
16b	**60**	38.3	21.01	**0.55**	17.23	17.18	1.68	65.97
16c	**90**	43.7	18.31	**0..42**	15.25	18.73	1.13	11.24

Appendix E

Example Worksheet for Phosphorus Process Model

Numerical Kinetic Model of NSST EAF Trials

$t := 0, 1 .. 30$

$T(t) := 1813 + 0.1 \cdot e^{.23 \cdot t}$

$C(t) := T(t) - 273$

$FeO(t) := 25 + 20 \cdot e^{-.12 \cdot t}$

B = C/S

$B(t) := \left(1.5 + 0.00001 \cdot t^3\right)$

$MgO := 6$

$SiO2(t) := \frac{(90 - MgO - FeO(t))}{(B(t) + 1)}$

$CaO(t) := SiO2(t) \cdot B(t)$

$Lp(t) := 10^{\left[\frac{11570}{T(t)}\right] + .072 \cdot (CaO(t) + 0.15 \cdot MgO) + 2.5 \cdot \log(FeO(t)) - 10.5}$

Initial Conditions (cgs)

$ko := 38$ $Dm := 7$ $Wm := 150 \cdot 10^6$ $Pm := .02$

$A := 2.8 \cdot 10^5$ $Ds := 2.7$ $Ws := 8 \cdot 10^6$ $Ps := .2$

$A \cdot Dm \cdot \frac{ko}{Wm} = 0.497$ **Mass Transfer Parameter (min-1)**

$Pi(t) := \frac{(Wm \cdot Pm + Ps \cdot Ws)}{(Ws \cdot Lp(t) + Wm)}$ **Interfacial Metal Phosphorus**

$P := \begin{bmatrix} Pm \\ Ps \end{bmatrix}$

$D(t, P) := \begin{bmatrix} -\left(A \cdot Dm \cdot \frac{ko}{Wm}\right) \cdot \left(P_0 - Pi(t)\right) \\ \left(A \cdot Ds \cdot \frac{ko}{Ws}\right) \cdot \left(Pi(t) \cdot Lp(t) - P_1\right) \end{bmatrix}$ **Slag and Metal Flux Equations**

$Z := rkfixed(P, 0, 30, 300, D)$ $n := 0 .. 300$

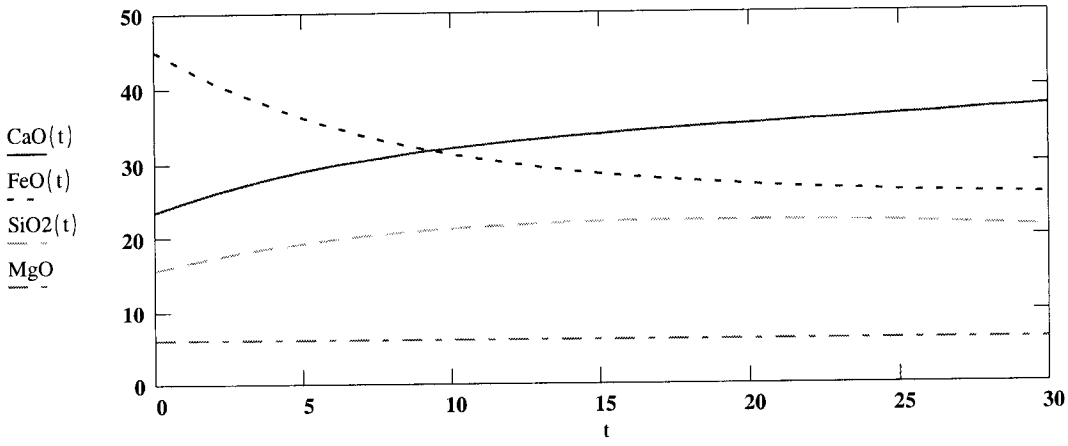
CaO(t)
FeO(t)
SiO2(t)
MgO
50
40
30
20
10
0
0
5
10
15
20
25
30
t

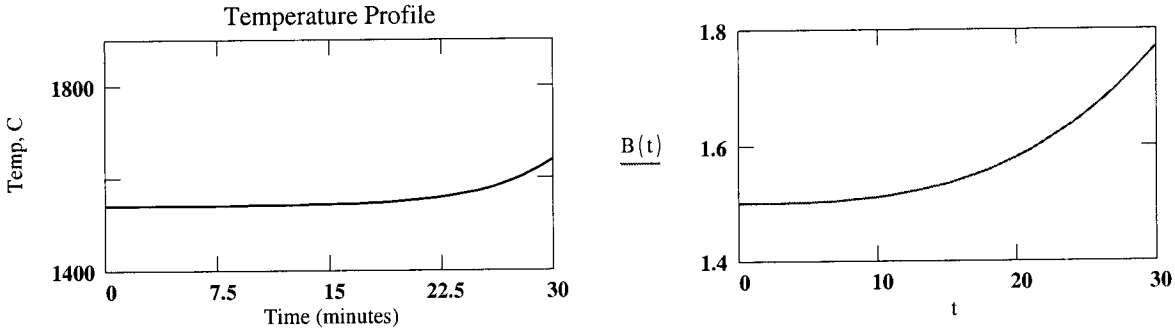
Temperature Profile
Temp, C
1800
1400
0
7.5
15
22.5
30
Time (minutes)
B(t)
1.8
1.6
1.4
0
10
20
30
t

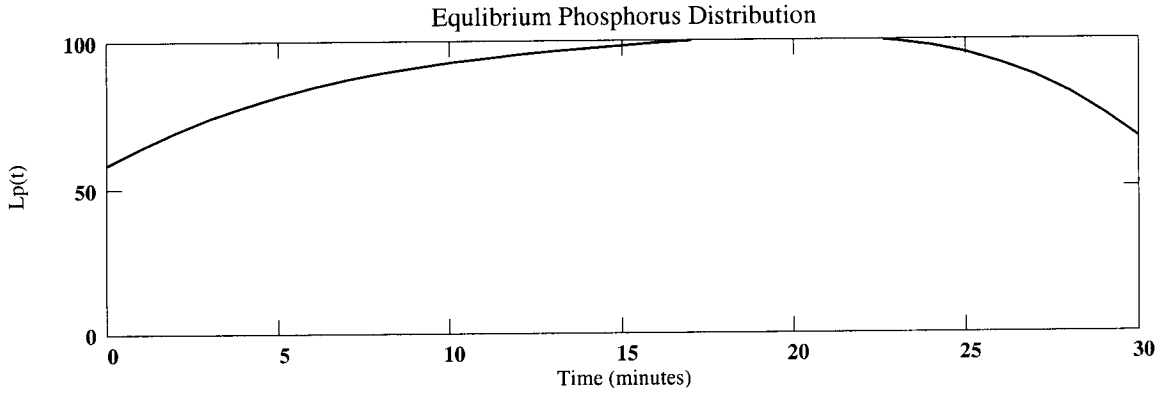
Equlibrium Phosphorus Distribution
Lp(t)
100
50
0
0
5
10
15
20
25
30
Time (minutes)

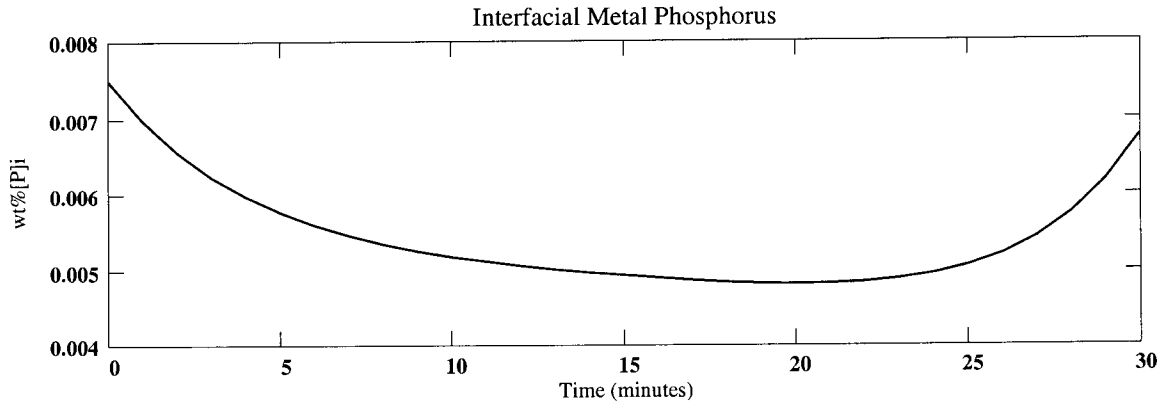
Interfacial Metal Phosphorus
wt%[P]i
0.008
0.007
0.006
0.005
0.004
0
5
10
15
20
25
30
Time (minutes)

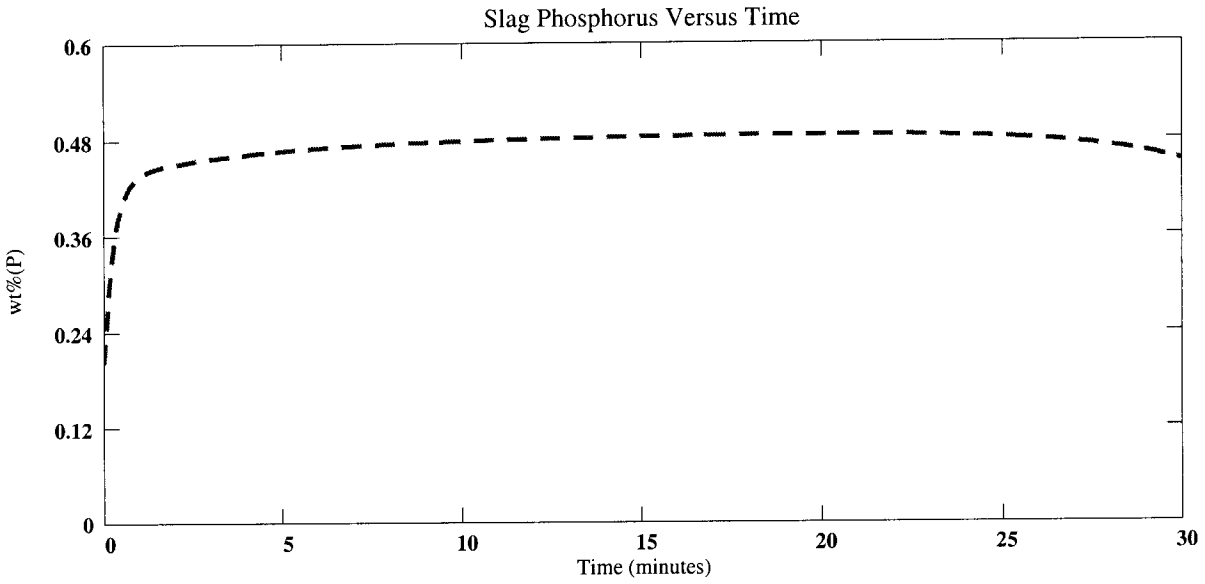
Slag Phosphorus Versus Time
wt%(P)
0.6
0.48
0.36
0.24
0.12
0
0
5
10
15
20
25
30
Time (minutes)

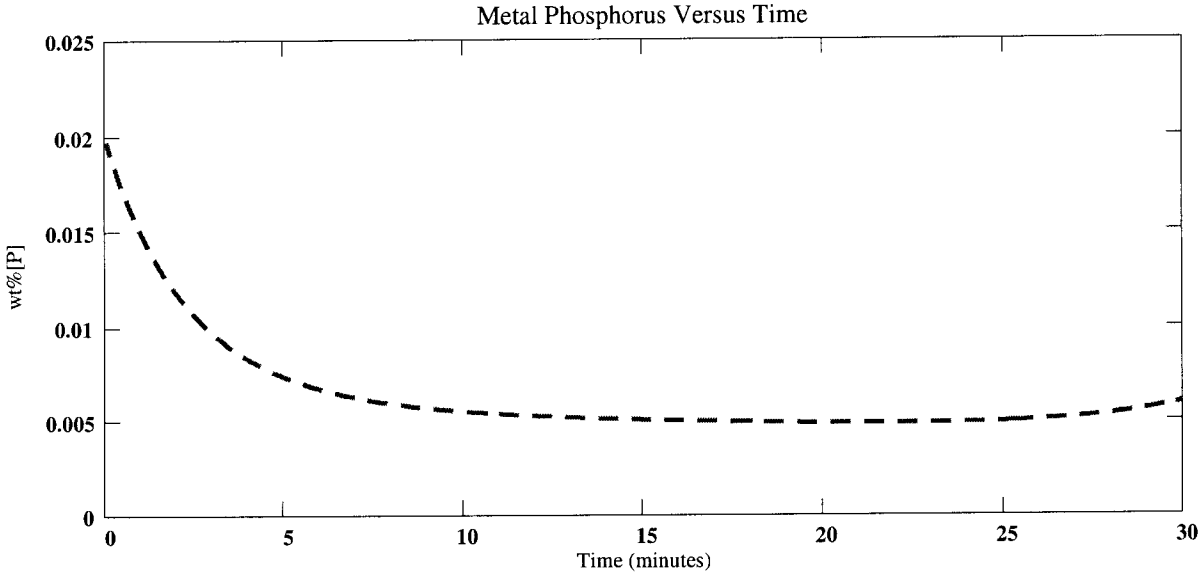
Metal Phosphorus Versus Time
wt%[P]
0.025
0.02
0.015
0.01
0.005
0
0
5
10
15
20
25
30
Time (minutes)

REFERENCES:

[1] M. Lee, D. Trotter, and O. Mazzei, "Production of Low Phosphorus and Nitrogen Steels Using HBI in the EAF", 1997 Electric Furnace Proceedings, 1997, pp. 467-472.

[2] "Phosphorus and DRI", *New Steel*, April 1994, p11.

[3] C. Queens, "The Behavior of Phosphorus at Melt-Down of Sponge Iron", Arch Eisenhuttenwes, Vol. 46, 1975, pp. 695-700..

[4] R. J. Fruehan and A. W. Cramb, "Fundamental Issues of Steel Refining," Procedings of the Julian Szekely Memorial Symposium, TMS, 1997, pp. 209-230.

[5] R. Smailer, H. Jensen, W. Scott "Utilization of Direct Reduction Iron in Electric Steelmaking", Proceedings of the Third Interregional Symposium on the Iron and Steel Industry, Brasilia, Brazil, October, 1973.

[6] R. Smailer, J.Price "Operating Benefits of Continuously Charging Prereduced Ore Briquetts to a 150-Ton Electric Furnace", OpenHearthProceedings, 1970, pp. 38-43.

[7] R. Smailer, H. Jensen, W. Scott "Utilization of Direct Reduction Iron in Electric Steelmaking", AISI 82nd General Meeting, May 22, 1974.

[8] K. McEuen, "History of Electric Furnace Trials Using Prereduced Iron Bearing Materials", Lukens Steel Company – Research and Development Report 73-2, April 1973.

[9] V. Joshi, "Value analysis of Direct Reduction Iron for Electric Furnace Steelmaking", Lukens Steel Company – Research and Development Report 76-3, March 1976.

[10] A. Lingras, "Some Aspects of Steelmaking with FIOR Briquettes", Lukens Steel Company – Research and Development Report 79-9, March, 1979.

[11] T. Fuwa, "Dephosphorization in Liquid Iron and Steel", I&SM, June 1981, pp. 18-25, I&SM, July 1981, pp. 25-31.

[12]R. Inoue and H. Suito, "Phosphorus Distribution Between Soda- and Lime-based Fluxes and Carbon-saturated Iron Melts", Trans. ISIJ, Vol. 25, 1985, pp. 118-126.

[13] H. Ishii and R.J. Fruehan, "Dephosphorization Equilibria Between Liquid Iron and Highly Basic CaO-Based Slags Saturated with MgO", ISS Transactions, Feb. 1997, pp. 47-54.

[14] K. Ito and N. Sano, "Phosphorus Distribution Between Basic Slags and Carbon-saturated Iron at Hot Metal Temperatures," Trans. ISIJ, Vol. 25, 1985, pp. 355-362.

[15] P. Johnston, *Effect of CaF_2 on Slags used for the External Dephosphorization of Hot Metal*, Masters Thesis, Department of Materials Engineering, The University of Wollongong, 1997.

[16] T. Mori, "On the phosphorus Distribution Between Slag and Metal", Trans. of the Japan Institute of Metals, Vol. 25, No. 11, 1984, pp. 761-771.

[17] R.J. Stubbles, "Phosphorus and Sulfur in Steelmaking", I&SM, March 1986 pp. 34-35, April 1986, pp. 44-45, May 1986 pp. 50-51, July 1986 pp. 60-61, Aug. 1986 pp. 47, Sept. 1986 pp. 68-70, Nov. 1986 pp. 50-51, Dec. 1986 pp. 34-35, Jan 1987 pp. 52-53, Feb. 1987 pp. 41, March 1987 pp. 45-46, April 1987 pp. 40-41.

[18] H. Suito and F. Inoue, "Effect of Calcium Fluoride on Phosphorus Distribution Between MgO Saturated Slags of the System CaO-MgO-FeO_x-SiO2 and Liquid Iron," Trans. ISIJ, Vol. 22, 1982, pp. 869-877.

[19] H. Suito, F. Inoue and M. Takada, "Phosphorus Distribution Between Liquid Iron and MgO Saturated Slags of the System CaO-MgO-FeOx-SiO2", Trans. ISIJ, Vol. 21, 1981, pp. 251-259.

[20] E.T. Turkdogan, *Steelmaking Fundamentals*, Institute of Materials, London, 1996, pp. 186-189.

[21] E.T. Turkdogan and J. Pearson, "Activities of Constituents of Iron and Steelmaking Slags", JISI, Vol. 173, 1953, pp. 217-223; vol. 175, 1953, pp. 393-401; vol 176, 1954, pp. 59-63.

[22] G.J.W. Kor, "Effect of Fluorspar and Other Fluxes on Slag-Metal Equilbria Involving Phosphorus and Sulfur", Metall. Trans., Vol. 8B, 1978, pp. 107-113.

[23] G.W. Healy, "A New Look at Phosphorus Distribution", JISI, Vol. 208, 1970, pp. 664-668.

[24] K. Balajiva, A.G. Quarrell, and P. Varjagupta, "A Laboratory Investigation of the Phosphorus Reaction in the Basic Steelmaking Process", JISI, Vol. 153, 1946, pp. 115-150.

[25] K. Balajiva, A.G. Quarrell, and P. Varjagupta, "The Effect of Temperature on the Phosphorus Reaction in the Basic Steelmaking Process", JISI, Vol. 155, 1947, pp. 563-567.

[26] O. Wijk, "The Phosphorus Problem in Iron and Steelmaking", Scandinavian Journal of Metallurgy, Vol. 22, 1993, pp. 130-138.

[27] T. Winkler and J. Chipman, "An Equilibrium Study of the Distribution of Phosphorus Between Liquid Iron and Basic Slags", Trans. AIME, Vol. 167, 1946, pp. 111-133.

[28] X.F. Zhang, I.D. Sommerville, and J. M. Tiger, "An Equation for the Equilibrium Distribution of Phosphorus Between Basic Slags and Steel", ISS Trans. Vol. 6, 1985, pp. 29-34.

[29] K. Ide, *Evaluation of Phosphorus Reaction Equilibrium Steelmaking and Kinetics in Foaming Slag*, Masters Thesis, Department of Materials Science and Engineering, Carnegie Mellon U., 1999.

[30] T. Forland, and K. Grjotheim, Met. Trans. B., Vol. 8, 1977, pp. 645-650.

[31] H.Flood and K. Grjotheim, J.Iron and Steel Inst., Vol. 171, 1952, pp. 64-70.

[32] C.Garlic, G.R. Belton and S. Jahanshahi, "A Thermodynamic Study of Metal/Slag Phosphorus Equilibria,"

[33] P. Johnston, *Effect of CaF_2 on Slags used for the External Dephosphorization of Hot Metal*, Masters Thesis, Department of Materials Engineering, The University of Wollongong, 1997.

[34] K. Mori, S. Doi, T. Kaneko, and Y. Kawai, "Rate of Transfer of Phosphorus Between Metal and Slag", Trans. ISIJ, Vol. 18, 1978, pp. 261-268.

[35] M. Motlagh, "Dephosphorization of Steel During Melting", ISS Trans. Vol. 6, 1985, pp. 202-213.

[36] W.K. Lewis and W. Whitman, Industrial and Engineering Chemistry. Vol. 16, 1924 pp 1215.

[37] D.R. Poireir and G. H. Geigger, *Transport Phenomena in Materials Processing*. TMS, Warrendale-PA, 1994, pp. 476-538.

[38] E.L. Cussler, *Diffusion - Mass Transfer in Fluid Systems*. Cambridge University Press, New York, 1984, pp. 215-307.

[39] A.H.P. Skelland, *Diffusional Mass Transfer*. John Wiley &Sons, New York, 1974, pp. 29-39 & 83-307.

[40] T.K. Sherwood and R.L. Pigford, *Boundary Layer Theory*., 7th ed., McGraw-Hill, New York, 1975.

[41] R. Higbie, Trans. AIChEJ. Vol. 31, 1935, p 365.

[42] H. Toor and J.M. Marchello, "Film-Penetration Model for Mass and Heat Transfer", AIChEJ, Vol. 4, No. 1 1958, pp. 97-101.

[43] S. Mukawa, and Y. Mizukami, "Effect of Stirring Energy and Rate of Oxygen Supply on the Rate of Jot Metal Dephosphorization", ISIJ International, Vol. 35, 1995, pp. 1374-1380.

[44] P. Wei, M. Sano, M. Hirasawa, and K. Mori, "Kinetics of Phosphorus Transfer Between Iron Oxide Containing Slag and Molten Iron of High Carbon Concentration Under Ar-O2 Atmosphere", ISIJ International, Vol. 33, No. 4, 1993, pp. 479-487.

[45] S. Ohguchi, D.G. Robertson, B. Deo, P. Grieveson, and J.H. Jeffes, "Simultaneous Dephosphorization and Desulfurization of Molten Pig Iron", Ironmaking and Steelmaking, 1984, Vol. 11, No. 4, pp. 202-213.

[46] S. Kitamura, T. Kitamura, K. Shibata, Y. Mizukami, S. Mukawa, and J. Nakagawa, "Effect of Stirring Energy Temperature and Flux Composition on Hot Metal Dephosphorization," ISIJ International, Vol. 31, 1991, No. 11, pp. 1322-1328.

[47] B.J. Monaghan, R.J. Pomfret, and L.S. Coley, "The kinetics of Dephosphorization of Carbon-Saturated Iron Using an Oxidizing Slag" Met. Trans B, Vol. 29B, 1998 pp111-118.

[48] Yongsug Chung and Alan Cramb, "Direct Observation of Spontaneous Emulsification and Associated Interfacial Phenomena at the Steel-Slag Interface," Phi. Trans. Royal Society of London, Vol. 356, 1998, pp.981-993.

[49] H. Gaye, L.D. Lucas, M. Olette, and P. V. Riboud, "Metal-Slag Interfacial Properties: Equilibrium Values and 'Dynamic' Phenomena," Canadian Metallurgical Quarterly, Vol. 23, No. 2, 1984, pp.179-191.

[50] A. Jakobsson, M. Nasu, J. Mangwiru, K.C. Mills, S. Seetharaman, "Interfacial Tension Effects on Slag-Metal Reactions," Phi. Trans. Royal Society of London, Vol. 356, 1998, pp.995-1001.

[51] A. Jakobsson, M. Nasu, B. Monaghan, K.C. Mills, S. Seetharaman, "Effect of Slag/Metal Interfacial on Kinetics of Dephosphorization," Iron and Steelmaking, Vol. 26, No. 5, 1999, pp.353-357.

[52] L. Gu, G. Irons, "Physical and Mathematical Modeling of Oxygen Lancing and Arc Jetting in EAF Furnaces," 1998 Electric Furnace Proceedings, 1998, pp. 269-277.

[53] D. Guo, L. Gu, G. Irons, "Evaluation of Stirring in Electric Arc Furnaces," 2000 Electric Furnace Proceedings, 2000, pp. 223-233.

[54] D. Goldstein, *Nitrogen Reactions In the EAF and OSM*, Doctoral Thesis, Department of Materials Science and Engineering, Carnegie Mellon U., 1996.

[55] J.Kerr, and R.J Fruehan, "Foamability of Stainless Steelmaking Slags in the EAF," 2000 Electric Furnace Proceedings, 2000, pp. 1049-1063.

[56]R.J Fruehan, ed., *The Making Shaping and Treating of Steel – 11th Edition– Steelmaking and Refining Volume,* AISE, Pittsburgh, 1998, P. 103.